EXPERIMENTAL AND NUMERICAL INVESTIGATIONS ON THE MECHANICAL BEHAVIOUR OF WELDED HIGH STRENGTH STEEL JOINTS UNDER TENSILE FORCE

SHENTAO ZHAO

PhD

The Hong Kong Polytechnic University

2025

The Hong Kong Polytechnic University

Department of Civil and Environmental Engineering

EXPERIMENTAL AND NUMERICAL INVESTIGATIONS ON THE MECHANICAL BEHAVIOUR OF WELDED HIGH STRENGTH STEEL JOINTS UNDER TENSILE FORCE

SHENTAO ZHAO

A thesis submitted in partial fulfilment of the requirements for the

Degree of Doctor of Philosophy

April 2025

CERTIFICATE OF ORIGINALITY

I hereby declare that this thesis is my own work and that, to the best of my knowledge and belief, it reproduces no material previously published or written, nor material that has been accepted for the award of any other degree or diploma, except where due acknowledgement has been made in the text.

_____(signed)

Shentao ZHAO (Name of Student)

Abstract

High strength steel (HSS) with nominal yield strength greater than 460 MPa is commercially available nowadays. Compared with normal strength steel (NSS), HSS has improved strength-to-weight ratio leading to cost saving. However, one major obstacle for the widespread use of HSS in construction industry is welding. During welding, thermal cycles can trigger phase transformations in HSS, resulting material deterioration in heat affected zone (HAZ) for HSS. In this study, three types of HSS welded joints were fabricated with different heat inputs and steel grades and were subjected to tension. These welded joints included butt-welded joints, single row T-stub joints and gusset plate to CHS X-joints.

Three steel grades including Q460, Q690 and Q960 were used to fabricate the butt-welded joints by robotic gas metal arc welding (GMAW). For each steel grade, four different heat inputs were adapted. Butt-welded tensile coupon tests and hardness tests were implemented. It was found that the fracture locations moved from the base metal (BM) of the Q460 to the HAZ of the Q960 butt-welded tensile coupons as the steel grades increased under the same heat input. Besides, as the heat input increased, the yield strength showed a more obvious reduction compared to the tensile strength. The hardness results showed that increasing the heat input could enlarge the HAZ widths for all steel grades. In addition, an iterative experimental-numerical method was adapted to calibrate the HAZ material properties based on the Hollomon model. According to the database consisting of calibrated HAZ material properties, two regression models were developed and validated.

For single row T-stub joints, Q460, Q690 and Q960 were welded together by robotic GMAW. Three different heat inputs were also adapted for each steel grade. These single row T-stub joints were axially loaded until the ultimate load was reached. The failure

modes of the single row T-stub joints at the ultimate state were mainly the flange punching shear failure and bolt hole failure. The load-displacement curves of the T-stub joints generally consisted of three stages. It was found that regardless of the steel grade and end distance, the plastic resistance decreased as the heat input increased, which may be attributed to the deterioration of HAZ. Under high heat inputs, the ultimate load could decrease as the steel grade increased. Besides, the end distance and steel grade could also affect the single row T-stub joint behaviours. Evaluations towards EN 1993-1-8 demonstrated that it gives conservative predictions for both plastic resistance and ultimate resistance. Numerical models were developed and validated for the tested single row T-stub joints. Furthermore, a parametric study was implemented to investigate the influence of end distance, flange thickness and heat input.

A total of 18 HSS gusset plate to circular hollow section (CHS) X-joints were fabricated by robotic GMAW with three steel grades and two heat inputs. These joints were loaded under brace tension. Current design codes for tubular joints, including ISO 14346, EN 1993-1-8 and Voth's method, were evaluated. According to the 3% d_0 deformation limit, most specimens failed by chord face failure. However, four transverse gusset plate to CHS X-joints failed before reaching to the limit. Steel grades, heat inputs and geometric parameters can affect both the joint strengths and ductility of the joints. Besides, it was found that current design methods usually underestimated the load at 3% d_0 deformation for the HSS gusset plate to CHS X-joints. Furthermore, the design methods were not accurate and reliable when predicting the load corresponding to chord punching shear. The numerical models were also developed and validated for the tested gusset plate to CHS X-joints. The plastic stage of load-deformation curves was affected by the HAZ. Based on the numerical techniques, a comprehensive parametric study was conducted for the longitudinal gusset plate to CHS X-joints under tension. The evaluated design methods showed conservativeness when predicting the load at 3% d_0 deformation.

List of publications

Conference papers:

Shentao Zhao, Junbo Chen & Tak-Ming Chan. 2024. Experimental Investigation on HSS Butt-welded Joints Made of 6 mm Plates. 10th International Conference on Steel and Aluminium Structures. Rio de Janeiro, Brazil.

Journal papers:

Shentao Zhao, Junbo Chen & Tak-Ming Chan. 2025. Effect of welding on behaviours of high strength steel: Review and outlook. Structures (in preparation).

Shentao Zhao, Junbo Chen & Tak-Ming Chan. 2025. Experimental and numerical investigations on the mechanical properties of high strength steel butt-welded joints (in preparation).

Shentao Zhao, Junbo Chen & Tak-Ming Chan. 2025. Experimental investigations on the mechanical behaviours of high strength steel gusset plate to circular hollow section X-joints fabricated by different heat inputs under tension (in preparation).

Shentao Zhao, Junbo Chen & Tak-Ming Chan. 2025. Experimental investigations on the mechanical behaviours of high strength steel single row T-stub joints fabricated by different heat inputs under tension (in preparation).

Acknowledgements

I would like to express my sincere and foremost gratitude to my Supervisor Prof. Tak-Ming Chan. His utmost guidance, generous support and patience throughout my whole PhD study really helped me build my research career. Every time I encounter difficulties in my PhD project, he is always patient and inspiring in guiding me to move forward. These concerns, support and motivations are highly appreciated together with his humility. I believe that these four years will be a precious and beneficial memory for my whole life. I would like to extend my gratitude to Prof Ahmed Youssef ELGHAZOULI for his support and guidance in my research.

I would also like to sincerely thank the technical staffs in the Concrete Technology Laboratory, Industrial Centre and Structural Engineering Research Laboratory for the support. I would also like to thank the technical support from Wo Lee Green Solutions Ltd. for helping fabricate the specimens. I would like to particularly mention Mr. Harry Lai, Mr. David Leung, Mr. Francis Yip, and Mr. Tom Cheung for their support during the experimental works.

Sincere thanks also go to my colleagues and friends who accompany me all the way in the PhD study. I would like to thank Dr Shuai Li, Dr Jiachen Guo, Dr Junbo Chen, Dr Partha Debnath, Dr Haixin Liu, Dr Qi Ma, Dr Yixun Wang, Dr Rui Yan, and Mr Mingjie Jiang not only for their assistance but also for their friendships.

Finally, I would like to express my deepest gratitude to my family. My parents have been giving me the greatest and everlasting love and support throughout my study. My wife, Dr Wenxin Zhang, has always been a strong and great support throughout my hard times. This thesis cannot be finished without all your love.

Table of Contents

List of Figures

List of Tables

Chapter 1 Introduction

1.1 Background

Arc welding is a popular connecting method for steel structures. In arc welding, the electric arc melts the connecting surfaces of two or more components by intense heat, joining the components together to achieve permanent connections after cooling and solidifying. Several factors, including the welding current, voltage, welding speed, wire stick out length of filler electrode, shielding gas, gas flow, filler electrode, as well as the welder's experience, can influence the weld appearance for arc welding.

Table 1.1 shows the influence of factors on the weld appearance mentioned above. As the welding current increases, the penetration depth increases, while increasing the welding voltage can broaden the weld width. However, the penetration depth, weld width and reinforcement can be reduced by improving the welding speed. The stability of arc during welding is mainly governed by the wire stick out length of filler electrode. If wire stick out length is too long, the shielding gas protection effect can be impaired, leading to instability of electric arc and resulting in an unsatisfactory weld shape. Finally, the welder's experience in choosing the welding gun traversal angle, welding gun work angle, and wire feed direction is of vital importance for a satisfactory weld appearance. The thermal effect of welding can be reflected by the heat input, an integrated index to reflect welding parameters, such as the welding current, voltage and speed. The heat input Q (in kJ/mm) of welding can be calculated through Eq. 1.1 (SSAB), in which k is the thermal efficiency, U is the voltage in V, I is the current in A, and v is the welding speed in mm/min. In a multi-layer and multi-pass, the inter-pass temperature, which is the temperature of the weld area between passes, should also be carefully controlled. The inter-pass temperature may influence the cooling time of materials, thus affecting the microstructure and material properties of heat affected zone

(HAZ). Therefore, the inter-pass temperature for high strength steel (HSS) should be carefully controlled, normally below 250 ℃ (Stroetmann et al., 2018, Gaspar and Balogh, 2013, Dusan Arsic, 2015, Gáspár, 2019).

$$Q = k\frac{UI}{v}\frac{60}{1000} \qquad \text{Eq. 1.1}$$

High strength steel (HSS) with a nominal yield strength greater than 460 MPa is commercially available due to the developments of metallurgical manufacturing procedures. Different processes exist to manufacture HSS. HSS manufactured by different processes may behave differently after welding (Amraei et al., 2019). HSS manufactured by different procedures has various phases induced by various heating temperature and cooling rate, such as martensite, bainite, austenite etc., and the phase fraction also varies. These phases are iron-carbon alloys with different microstructures and carbon contents, and they have different mechanical properties. Figure 1.1 shows the iron-carbon phase diagram, in which A_1, A_3 and A_{cm} are the critical transformation temperatures. When steel is heated up over or cooled down to PSK line (A_1), pearlite and austenite can be transformed into each other. Similarly, ferrite can be transformed to austenite if steel is heated up over GS line (A_3). Cementite can also be converted to austenite if the temperature is over ES line (A_{cm}). In practice, the actual transformation temperatures might be different with the critical transformation temperatures, and the actual transformation temperatures are denoted as A_{c1}, A_{c3} and A_{ccm}, respectively.

Figure 1.2 shows the quenching and tempering (QT) process in which the steel ingot is slowly cooled to the room temperature after hot rolling. Then, the steel is reheated above the A_3 temperature (the lower-temperature boundary of the austenite region at low carbon contents, i.e. the gamma/gamma and ferrite boundary) and transformed to austenite. Consecutively, it is quenched with an extreme high cooling rate. Finally, the steel is tempered under A_1 temperature (the minimum temperature for austenite) and

slowly cooled to ambient temperature (Song et al., 2013, Gaspar and Balogh, 2013). Based on the QT process, reheating, quenching and tempering (RQT) process, as illustrated in Figure 1.3, has a reheating process after tempering to achieve better homogeneity in through-thickness mechanical properties (Chen et al., 2019, Zhao et al., 2016). The direct quenching (DQ) process is depicted in Figure 1.4, in which the steel is directly quenched after the controlled rolling (Amraei et al., 2019), resulting in less energy consumptions (Gaspar and Balogh, 2013, Amraei et al., 2016). A mixture of bainite and martensite in which the bainite is fine sub-structured (Gaspar and Balogh, 2013, Javidan et al., 2016, Amraei et al., 2016) exists in DQ HSS.

Figure 1.5 presents the thermo-mechanical control process (TMCP) which contains controlled rolling, accelerated cooling and heat treatment processes. The controlled rolling aims to apply plastic deformation in the non-crystallization temperature range of austenite and form transformation nucleation sites at grain boundary and interior, and the strength of steel is increased. In addition, the accelerated cooling aims to gain martensite, and subsequent heat treatment can improve ductility and toughness of TMCP HSS (Chen, 2019, Gaspar and Balogh, 2013). Therefore, the thermo-mechanical rolling process produces a very fine grain structure with good toughness (Javidan et al., 2016, Gaspar and Balogh, 2013).

HSS can help reduce overall structure weight and carbon footprint. For example, when compared with web plates made of 350 MPa yield strength normal strength steel (NSS), web plates made of HSS600 has an improved strength-to-weight ratio, which can achieve more than 20% weight reduction by replacing conventional steel for steel structures (Sperle et al.). Thus, the cost of transportation, construction and foundation can be reduced. In addition, a storage tank made of steel with yield strength equal to 210 MPa was replaced by HSS with yield strength equal to 480 MPa, thus CO_2 emissions could be reduced by up to 31% (Sperle et al.). In summary, the application

of HSS will lead to thinner and lighter steel structures.

Although HSS has advantages over NSS, the application of HSS in engineering has not been quite widely spread. One major obstacle hindering the wide use of HSS is welding. During welding, thermal cycles including heating and cooling stage for materials in the heat-affected zone (HAZ) can trigger phase transformation in HSS. For example, bainite or martensite in HSS would transform to austenite during heating stage. At cooling stage, the transient austenite would transform from a mixture of martensite and bainite to a mixture of bainite, ferrite, pearlite and cementite, and the content of each component largely depends on the cooling time (Hu et al., 2013). The phase transformation in the HAZ would therefore affect its material properties when compared to base metal (BM). To minimize the welding influence on HSS, a heat input below 1.5 kJ/mm is recommended for S690 welded sections under compression with a thickness of 16 mm (Hu et al., 2022), which requires a good control on welding parameters. However, if the HSS components, such as butt-welded joint and T-stub joint, are subjected to tensile loading, the joint behaviours affected by welding and optimisation of welding parameters still need more investigations.

Design methods for tubular joints in current design codes are proposed based on the data of conventional normal strength steel (NSS). These design codes are ISO 14346 (ISO, 2013a), EN 1993-1-8 (CEN, 2005a), and CIDECT design guidelines (Wardenier et al., 2008) (Packer et al., 2009). To apply these design methods to calculate the joint strength of HSS tubular joints, additional reduction factors are stipulated. These reduction factors are regulated to consider the possible lower rotation and deformation capacity and to ensure the sufficient ductility (Cai et al., 2022b). Nevertheless, the suitability of these reduction factors for HSS tubular joints are debatable. Lee et al. (2017) evaluated the applicability of EN 1993-1-8 on the cold-formed HSS circular hollow section (CHS) X-joints under brace axial tension. It was found that the

adaptation of reduction factor led to overconservativeness for the joint strength prediction. Lee and Kim (2018) found that current design codes circumscribed the use of high strength steel to tubular joints as it prohibited the complete use of higher strength. In summary, the mechanical background behind the limitations are unclear (Lee and Kim, 2018). More research is imperatively needed to propose design method for HSS tubular joints.

There are many investigations focusing on the HSS tubular joints. Particularly, the effect of HAZ on the mechanical behaviours of HSS tubular joints was studied. Lan et al. (2019) explored the HAZ effect on the S960 RHS X-joints subjected to brace axial compression. Strength reductions were considered for the HAZ in the chord member. It was found that larger brace width-to-chord width ratio led to more significant joint strength reduction caused by the existence of HAZ. However, the strength reduction in this research was based on other research. Pandey and Young (2021) cut tensile coupons from fabricated S960 RHS T-joints made of different tube thicknesses from different locations near the welds to obtain mechanical properties of HAZ. Based on the tensile coupon results, a strength reduction model for HAZ was proposed. Then the model was applied to study the influence of HAZ on the S960 RHS T-joints under brace axial compression. It was found that the ignorance of HAZ in numerical models overestimated the joint strengths in the range of 12 to 34%. However, most studies on this topic investigated the HAZ effect on the HSS tubular joints under compression. Other loading cases, like brace axial tension, are still imperatively needed for further research.

1.2 Objectives

This thesis focused on the tensile behaviour of HSS welded joints. From simple to complicated, three types of HSS welded joints made of different steel grades and heat

inputs were experimentally and numerically studied, namely the butt-welded joint, T-stub joint and gusset plate to CHS X-joint. The influence of welding heat inputs on the tensile behaviour of these three joints were comprehensively studied.

The first part focuses on the HSS butt-welded joints. Three kinds of HSS (Q460, Q690 and Q960) were selected and various heat inputs were applied to fabricate the joints. The key objectives of this part are:

(1) to experimentally investigate the influence of heat inputs and steel grades on the mechanical properties of the HSS butt-welded tensile coupons. These mechanical properties included yield strength, ultimate strength, ultimate strain, elongation at fracture, the ratio of f_u/f_y and hardness.

(2) based on the HSS butt-welded tensile coupon test results, to calibrate the true stress-strain relationships for HAZ adapting the Hollomon model.

(3) to proposed polynomial regression models and linear regression models to predict the HAZ true stress-strain relationships in combination with Hollomon model.

The second part studies the HSS single row T-stub joints. Three kinds of HSS (Q460, Q690 and Q960) were selected and various heat inputs were applied to fabricate the joints. The key objectives of this part are:

(1) to experimentally investigate the influence of heat inputs, end distances and steel grades on the mechanical behaviours of the HSS single row T-stub joints, including plastic resistance, ultimate load and deformation ability.

(2) to obtain the hardness distributions of the flange for the single row T-stub joints. The linear regression models between heat inputs and HAZ widths were built for each steel grades.

(3) to access the applicability of current design equations for the single row T-stub joints.

(4) to develop reliable numerical models for the tested T-stub joints. Then the effect of HAZ on the joint behaviour was investigated.

(5) to conduct parametric study considering the effect of different heat inputs, end distances and flange thicknesses.

The third part investigates the HSS gusset plate to CHS X-joints. Three kinds of HSS (Q460, Q690 and Q960) were selected and various heat inputs were applied to fabricate the joints. The key objectives of this part are:

(1) to experimentally investigate the mechanical behaviours of the HSS gusset plate to CHS X-joints. The failure mode, load-deformation curve, and deformation characteristics were discussed with details.

(2) to evaluate the design methods in companion with the test results.

(3) to build the reliable numerical models for the tested specimens. The effect of HAZ was discussed based on the numerical simulations.

(4) to conduct a comprehensive parametric study for the longitudinal gusset plate to CHS X-joints. Based on the parametric study results, current design equations were evaluated for the longitudinal joints.

1.3 Outline of the thesis

This thesis contains eight chapters. The main content of each chapter is summarised as follows:

Chapter 1 demonstrates a brief introduction of the research work for the thesis, including the background, objectives and outline of the thesis.

Chapter 2 gives a comprehensive literature review about the effect of welding on behaviours of high strength steel. Several key concepts of welding, such as welding thermal cycle, phase transformation, peak temperature and cooling rate were explained. Then the effect of welding on the HSS in existing studies was thoroughly illustrated

and summarised. Particularly, the mechanical properties of HAZ were reviewed with details. Furthermore, the influence of welding on HSS joints were outlined in the literature review.

Chapter 3 concerns the HSS butt-welded joints fabricated by various steel grades and heat inputs. Tensile coupon tests and hardness tests were conducted for the joints. Then the HAZ material properties were calibrated based on the butt-welded tensile coupons via an iterative experimental-numerical method and a database for HAZ properties was built. Polynomial regression model and linear regression model were obtained for the prediction of HAZ properties according to the database.

Chapter 4 – 5 demonstrate the investigations of the HSS single row T-stub joints fabricated by different steel grades and heat inputs. The experiments concerned the mechanical behaviours of the joints regarding heat input, end distance, steel grade and boundary condition. Validated numerical models were developed and a parametric study was implemented to further investigate the influence of geometric and welding parameters.

Chapter 6 – 7 presents the investigations of the HSS gusset plate to CHS X-joints fabricated by varied steel grades and heat inputs. 18 specimens were used for the tensile tests in total. The test results were comprehensively discussed. Numerical models for the gusset plate to CHS X-joints were developed and validated. A comprehensive parametric study was conducted for the longitudinal gusset plate to CHS X-joints. Based on the parametric study results, design equations were evaluated for joint strength predictions.

Chapter 8 concludes the major findings obtained in this research. And the future research work was also listed.

Table 1.1 Influence of several factors on weld appearances (Ibrahim et al., 2012, Karadeniz et al., 2007, Singh and Singh, 2020)

Welding parameter	Weld appearance		Arc stability
	Penetration depth	Weld width	
Current ↑	↑	-	-
Voltage ↑	-	↑	-
Welding speed ↑	↓	↓	-
Wire stick out length ↑	-	-	↓

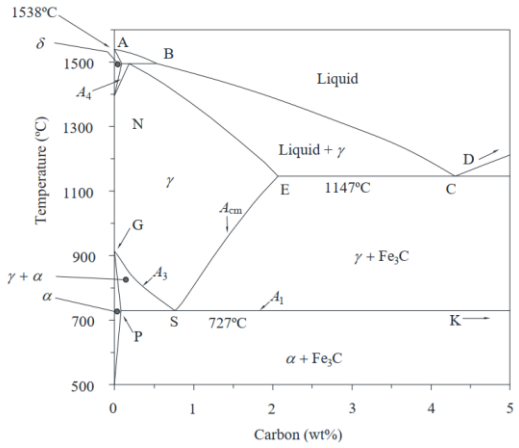

Figure 1.1 Iron-carbon equilibrium diagram (Chen, 2019)

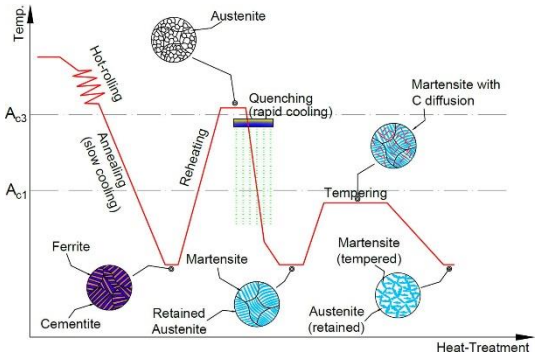

Figure 1.2 Quenching and tempering process (Xiong and Liew, 2020)

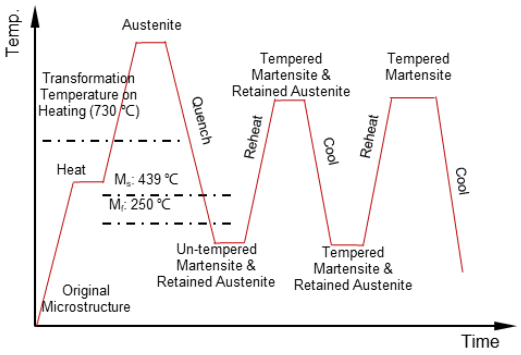

Figure 1.3 Reheating, quenching and tempering process (Chen, 2019)

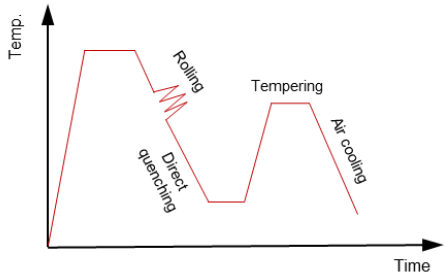

Figure 1.4 Direct quenching process (Song et al., 2013)

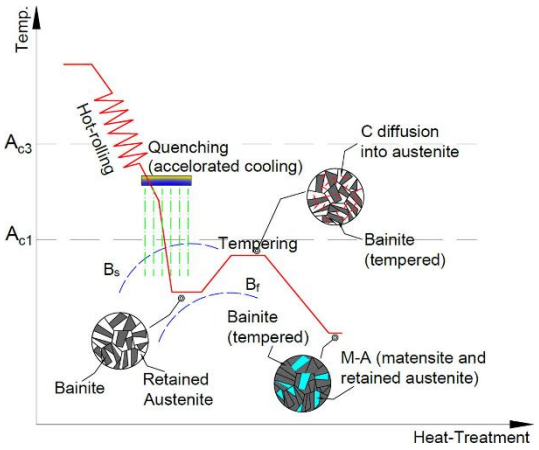

Figure 1.5 Thermo-mechanical control process (Xiong and Liew, 2020)

Chapter 2 Literature review

2.1 Introduction

This chapter demonstrates a comprehensive literature review on the research advances on the welding influence of HSS welded joints. Generally, arc welding contains three types: manual welding, semiautomated welding and robotic welding. Manual welding is flexible, traditional reliable. However, the welding quality, efficiency and accuracy may not be consistent. Semiautomated welding can achieve improved speed and precision compared to manual welding, but it requires an operator who has the skillset to run the machine. As for the robotic welding, it has enhanced weld quality, increased efficiency and accuracy too. However, it requires high initial investment and has limited versatility. In this chapter, welding thermal cycle was introduced first. Phase transformations happened due to welding thermal cycles, and HAZ formed because of phase transformations. The mechanical properties of HAZ were crucial in describing the behaviour of HSS welded joints, therefore relevant research was collated and summarised. The relationship between microstructures and mechanical properties for HAZ was reviewed. Finally, research on the influence of welding on HSS joints was analysed. The HSS welded joints included the butt joint, T-stub joint and tubular joint.

2.2 Influence of thermal cycles on HSS

2.2.1 Welding thermal cycle

Figure 2.1 demonstrates that different welding thermal cycles exist along the direction perpendicular to the welding centreline. Each welding thermal cycle consists of heating and cooling stages with different heating rates, peak temperatures (T_{max}) and cooling times (for instance $t_{8/5}$). If T_{max} surpasses A_1, A_3 or A_{cm} (counterpart boundary for high-carbon contents) temperatures, microstructures like pearlite, ferrite and cementite will transform to austenite. Subsequently, at cooling stage, austenite transforms to different

microstructures at different cooling rates. The cooling time $t_{8/5}$ (as shown in Figure 2.2), defined as the time to cool down from 800 ℃ to 500 ℃ (Chen et al., 2019) is commonly used as a representation of the cooling rate. Similarly, $t_{8.5/5}$ and $t_{6/4}$ are used as well to analogically represent the cooling times (Gaspar and Balogh, 2013, Chen, 2019). At the cooling stage, in the temperature interval roughly from 850 ℃ to 500 ℃, the cooling time $t_{8.5/5}$ significantly affects the final microstructure and mechanical properties (Gaspar and Balogh, 2013). Therefore, the peak temperature and cooling time are vital parameters for thermal cycles of HAZ (Gaspar and Balogh, 2013, Kaplan and Murry, 2008, Jiang et al., 2021). Furthermore, EN 1011-2 (CEN, 2001) recommends equations to calculate $t_{8/5}$ for unalloyed and low alloyed steels. Eq. 2.1 is for 3D heat flow, and Eq. 2.2 is for 2D heat flow, where T_0 is the initial plate temperature in ºC, Q is the heat input in kJ/mm, d is the plate thickness in mm, F_2 and F_3 are the shape factors for two-dimensional and three-dimensional heat flows, respectively. 2D or 3D models can be used as well to calculate $t_{8.5/5}$, as described in (Balogh et al., 1999). In addition, EN 1011-2 (CEN, 2001) also gives recommendations for welding of metallic materials. For thermo-mechanically treated fine grain and quenched and tempered steels, it applies to steels with yield stress larger than 360 MPa. As for limitations of chemical compositions for steels that are applicable to EN 1011-2 (CEN, 2001), they are regulated in groups 1 to 7 in ISO 15608 (CEN, 2000).

$$t_{8/5} = (6700 - 5T_o) \times Q \times (\frac{1}{500 - T_o} - \frac{1}{800 - T_o}) \times F_3 \quad \text{Eq. 2.1}$$

$$t_{8/5} = (4300 - 4.3T_o) \times 10^5 \times \frac{Q^2}{d^2} \times \left[\left(\frac{1}{500 - T_o}\right)^2 - \left(\frac{1}{800 - T_o}\right)^2\right] \times F_2 \quad \text{Eq. 2.2}$$

2.2.2 Phase transformations caused by welding thermal cycles

2.2.2.1 Formation of HAZ in HSS

During the heating stage of a welding thermal cycle, the peak temperature T_{max} of HSS around the molten pool usually is higher than A_{c1}, A_{c3} and A_{ccm}. Thus, various phase transformations happen in regions with different T_{max}. In the area where T_{max} is higher

than A_{c3}, primary phases such as martensite, bainite and pearlite, would be transformed to austenite (Chen, 2019). Subsequently, austenite experiences the cooling stage of welding. Depending on the cooling rate indicated in the continuous cooling transformation (CCT) diagram shown in Figure 2.3, austenite is transformed to different phases such as pearlite, bainite or martensite with different contents. Consequently, HAZ is generated by phase transformation around the weld (Śloderbach and Pająk, 2015). Figure 2.4 showcases different phases in a HAZ. Ferrite appears as grey patterns in BM, fine grain HAZ (FGHAZ), coarse grain HAZ (CGHAZ) and weld metal (WM); bainite appears as black blocks and strips; upper bainite appears as feather-like shape; pearlite appears as dots and strips. No martensite existed in this Q690 steel plate before and after welding.

2.2.2.2 Methods to distinguish the HAZ boundary

The microstructure observation and the hardness test are commonly used to distinguish HAZ subzones. Experimental apparatuses, including optical microscopy (OM), scanning electron microscopy (SEM), electron backscatter diffraction (EBSD), field emission scanning electron microscopy (FESEM), can be used to conduct microstructure observations for HSS. The microhardness tester can be used to obtain the hardness distribution along HAZ subzones. For both tests, the sample preparation includes grinding and polishing to obtain a smooth and clear surface. For the hardness test, Knoop, Brinell, Vickers and Rockwell hardness tests have been standardised in ISO 4545-1 (ISO, 2023a), ISO 6506-1 (ISO, 2014), ISO 6507-1 (ISO, 2018) and ISO 6508-1 (ISO, 2023b), respectively. The indentation line should be long enough from the welding centre line to cover different regions affected by welding (Chen, 2019). Multiple indentation lines are preferred to illustrate the hardness variation along the plate thickness (Chen, 2019, Kästner; and Stroetmann;, 2021, Amraei et al., 2019, Amraei et al., 2020, Khurshid et al., 2015, Neuvonen et al., 2021). In addition, Amraei et al. (2016) also tested the hardness distribution along the plate thickness, and the vertical hardness distribution may reflect the constraint effect along the thickness. As

for the microstructure observation, it is necessary to etch samples into $HCl \cdot FeCl_3 \cdot H_2O$ or 5% Nital solutions to distinguish microstructure details (Jiang et al., 2021, Zhao et al., 2017, Amraei et al., 2020, Afkhami et al., 2022a, Afkhami et al., 2019). After etching the weldment in chemical solutions for a proper period of time, the boundary between the HAZ and the weld metal (WM) can be visually observed (Chen, 2019, Liu et al., 2018), as shown in Figure 2.5. Furthermore, grains of the WM and the HAZ differed with each other under a light optical microscope (Chen et al., 2019), as shown in Figure 2.6. By combining microstructure observations and hardness tests , not only the boundary between the HAZ and the BM can be distinguished but also the HAZ can be divided into different subzones (Zhao et al., 2017, Chen et al., 2019). Zhao et al. (2017) used the hardness of BM as a standard to divide the HAZ into three different zones, including the CGHAZ , the FGHAZ , and the tempering zone (see Figure 2.7a). Microstructures under an optical microscope also proved the existence of different zones, as depicted in Figure 2.7b. In addition, other methods to distinguish the HAZ boundary have been proposed as well in existing literatures. Yan et al. (2021) proposed to use the digital image correlation (DIC) to identify HAZ boundaries by comparing the strain ratio in different regions. It was observed that the HAZ boundary identified by the strain ratio matched the hardness well (see Figure 2.8). Pandey and Young (2021) distinguished the HAZ by visual observations of steel surface colours after welding. However, it was difficult to accurately determine the actual HAZ size. In summary, it is a common practice in current studies to distinguish the HAZ boundary by microstructure and hardness measurements (Zhao et al., 2017, Chen et al., 2019, Afkhami et al., 2022b, Javidan et al., 2016, Afkhami et al., 2019, Neuvonen et al., 2021).

2.3 Effect of welding on HSS

2.3.1 Mechanical behaviours of HAZ

2.3.1.1 Relationship between microstructures and mechanical properties in HAZ

The material properties of HAZ could be influenced by many variables, such as the heat input, plate thickness, steel grade, manufacturing procedure, and chemical composition, as shown in Figure 2.9. The peak temperature, cooling rate, steel grade, manufacturing process and chemical composition can directly affect the microstructures, while the heat input and the plate thickness influence the HAZ indirectly by affecting the peak temperature and the cooling rate.

Softening usually happens in the HAZ of HSS. Some researchers attributed softening to the soft phase formation (such as pearlite, ferrite, tempered martensite, granular bainite and so on) in the HAZ during welding. Afkhami et al. (2022a) illustrated that the softening of heat-treated coupons made of S960-DQ and S1100-QT was caused by ferrite and granular bainite. Chen et al. (2019) demonstrated that the decomposition of the partially austenitised zone into ferrite, pearlite or cementite caused the soft layer in S690-RQT butt-joint. Other researchers, however, explained the softening from a micro-level. Softening occurs if the influence of solid solution hardening and precipitation hardening are significantly lower than that of the grain refinement from thermomechanical rolling (Stroetmann and Kästner, 2019).

Various phases in the HAZ can influence the mechanical properties of HSS. The fine tempered lath-like martensite had excellent strength (Gáspár, 2019). Amraei et al. (2020) found that for S960 steel made by DQ, the finer the prior austenite grain in the HAZ size was, the stronger 0.2% proof stress and tensile stress were. Fine-grained tempered martensite and bainite are beneficial for toughness (Bhadeshia and Honeycombe, 2017). In contrast, granular bainite, ferrite and tempered martensite in the HAZ resulted in the

decrease of 0.2% proof stress, tensile strength and hardness for HSS (Amraei et al., 2020, Javidan et al., 2016). Besides, the martensite-ferritic phase reduced the mechanical properties of S690 heat treated coupons (Ho et al., 2020). Afkhami et al. (2022a) found that for S1100, hindering and avoiding the ferrite formation can preserve the mechanical properties after welding.

2.3.1.2 Mechanical properties of HAZ

In current research, influences of the heat input, the peak temperature and the cooling time on the HAZ in HSS have been extensively investigated. It should be noted that they are coupled variables, among which the heat input is the most presentational variable because it influences the peak temperature and the cooling time.

The HAZ strengths of HSS, including yield strength and tensile strength, are significantly influenced by the heat input. Some research revealed that the heat input was negatively correlated to strengths (Jiang et al., 2021, Chen et al., 2019, Gaspar and Balogh, 2013). The yield strength of butt welded joint of HSS with a nominal yield strength of 690 MPa would have a strength reduction up to 30% compared with that of the BM when the heat input is higher than 1.6 kJ/mm (Jiang et al., 2021, Liu et al., 2018). However, if the heat input was properly controlled under 1.0 kJ/mm for HSS, satisfactory weldments can be achieved (Liu et al., 2018, Gaspar and Balogh, 2013, Skriko, 2018), as indicated in Figure 2.10. Figure 2.10 shows that the stress-stain relationship of S690 with heat input equal to 1.0 kJ/mm almost overlapped with that of the BM.

The cooling time also affects the HAZ strength. Stroetmann et al. (2018) studied the influence of the cooling time on HSS. Thermo-mechanically rolled steels S500M and S700M and quenched fine-grain steels S690Q and S960Q were investigated (Stroetmann et al., 2018). The experiment results conveyed that the tensile strength decreased as the cooling time increased for 20 mm thickness steel for all four kinds of

steel, shown in Figure 2.11. Further, Stroetmann et al. (2018) studied the cooling time influence on the properties of each subzone for S690Q. The CGHAZ had the most significant reduction of tensile strength at longer cooling time, followed by the inter-critical zone and the FGHAZ. Table 2.1 compares the cooling time of butt welded joints for different plate thicknesses according to EN 1011-2 (CEN, 2001). It can be observed that the cooling time significantly increases as the thickness reduces, which may cause microstructure deterioration. Therefore, HSS thin plates should be further investigated to clarify the welding effect.

The chemical composition can influence the HAZ mechanical properties in HSS by affecting solid solution hardening, precipitation hardening and grain refinement (Stroetmann and Kästner, 2019, Pandey and Young, 2021). Although S690Q and S700M had similar nominal yield strength, , the tensile strength of S690Q degraded when the cooling time was longer than 17 s, while that of S700M deteriorated even though the cooling time was very short after the thermal physical simulation (Stroetmann et al., 2018). The manufacturing process can also affect the HAZ mechanical properties. Usually as the steel grade increases, the strength reduction raises under the same heat input. However, in tests conducted by Amraei et al. (Amraei et al., 2019), both S700-QT and S1100-QT showed no major reductions of f_y and f_u after welding with the heat input ranging between 0.7~1.4 kJ/mm. In contrast, for S960-DQ, reductions in both f_y and f_u increased as the heat input increased. It was explained that the chemical composition and the manufacturing procedure of S1100-QT and S960-DQ were different, leading to significantly lower martensite start (M_s) and bainite start (B_s) temperatures for S1100 (Afkhami et al., 2022a, Amraei et al., 2020). Due to high hardenability of S1100 and its low M_s and B_s temperatures, austenite formed in the heating stage during welding transformed into a mixture of bainite and martensite. Therefore, the influence of the steel grade on f_y and f_u after welding was not linear considering the effect of the chemical composition and manufacturing procedure. For

further research, HSS welded plates with the same nominal yield strength but different manufacturing procedures should be compared and investigated.

Compared with NSS, HSS has a reduced deformation ability due to the existence of martensite and bainite (Ho et al., 2019). The deformation ability can be expressed in many forms, such as the plastic strain capacity, elongation at fracture, and ductility. For butt-welded S960-DQ, increasing the heat input can decrease the plastic strain capacity, which is the modulus of toughness (Amraei et al., 2016).The elongation at fracture for S700-QT, S960-DQ and S1100-QT reduced as the heat input increased (Amraei et al., 2019). Similarly, the elongation of S690Q-RQT butt joints decreased with the increase of heat input, which was caused by the localised deformation and the high concentration of the plastic strain in the soft layer (Chen et al., 2019). Ductility is a comprehensive indicator to reflect the deformation ability. EN 1993 1-12 (CEN, 2007) regulates ductility for steel based on three variables, shown as f_u/f_y, the elongation at failure and the ultimate strain ε_u. The ductility of butt joint was highly dependent on the heat input equal to 0.3~1.4 kJ/mm (Amraei et al., 2019). To date, comprehensive investigations into the HAZ deformation characteristics are still lacking. The influence of the steel manufacturing procedure, microstructure, and chemical composition should be further examined.

Toughness is the ability of a material to absorb energy and plastically deform without fracturing (Larson, 2001). The toughness of HSS butt joint could decrease significantly if rapid cooling was achieved during welding. It was caused by the increase of the prior austenite grain size as well as the volume fraction of bainitic ferrite and martensite-austenite island (Chen, 2019). As the heat input increased, the toughness gradually decreased until it reached to a stable value based on the tensile test of butt welded Q690-TMCP joints (Jiang et al., 2021). For the HAZ of S960QL, higher heat input lowered the impact energy (Gaspar and Balogh, 2013, Gáspár, 2019). Besides, the toughness

reduction in the HAZ of S960QL cannot be avoided by optimising welding parameters in the examined $t_{8/5}$ range (Gáspár, 2019). In particular, even though the toughness requirement was fulfilled, the observed failure mode of welded S960QL joint still showed a brittle characteristic (Gáspár, 2019). The influence of manufacturing procedure and microstructure on the fracture property of HAZ are still unclear.

Generally, hardness of HAZ in HSS would decrease due to welding caused phase transformations. Lower hardness value in FGHAZ was observed as higher heat input was applied due to the increase of pearlite for Q690-TMCP butt joint (Jiang et al., 2021). Besides, for V-N HSS, as the heat input increased, the content of ferrite increased, while the hardness of the coupons dropped (Hu et al., 2013). Usually, hardness and steel strength are positively correlated and ISO 18265 (ISO) provides equations to convert the hardness value into tensile strength. Besides, researchers proposed different hardness-strength conversion equations (Pavlina and Van Tyne, 2008, Murakami, 2002) Jiang et al. (2021) adopted the hardness-strength formula proposed by Pavlina and Van Tyne (2008) to calculate strengths for the HAZ in HSS Q690-TMCP steel. The results for the HAZ yield strength are satisfactory rather than for the HAZ ultimate strength. Amraei et al. (2020) showed that equations proposed by Murakami (2002) fairly predicted the tensile strength of each sub-zone for heat treated S960 and S1100 coupons compared to that proposed by Pavlina and Van Tyne (2008). It can be found that contradictory results exist when evaluating these hardness-to-strength conversion equations. These conversions cannot obtain an accurate tensile strength because the hardness test is quite different from the tensile test (ISO). The hardness test is empirical and used in practice when the tensile test is too involved or the piece to be examined cannot be destroyed (ISO).

2.3.1.3 Constraint effect

The metallurgical constraint is defined as the local disturbance of the stress state generated by adjacent zones for the HAZ (Neuvonen et al., 2021, Yan et al., 2022,

Rodrigues et al., 2004, Sun et al., 2018a), as shown in Figure 2.12. In the constraint effect, the region with the lowest yield strength will initiate the plastic deformation when adjacent zones are still in elastic states. Then adjacent regions will impose constraints, leading to a complex stress state in the lowest region and preventing the accumulation of the plastic strain. The constraint effect can result in a hydrostatic stress component in the HAZ (Amraei et al., 2016). Factors that influence the constraint effect include the ratio of the HAZ width to the plate thickness (Amraei et al., 2016), the mismatch ratio between the HAZ and adjacent materials and the hardening parameters of the adjacent materials (Yan et al., 2022, Rodrigues et al., 2004, Sun et al., 2018a).

HAZ with the constraint effect will obtain an increase in both the ductility and strength (Amraei et al., 2016, Cai et al., 2022a). For both plain strain and plain stress conditions, welded tensile coupons with the constraint effect yield at a larger nominal yield stress compared with the BM (Amraei et al., 2016). If the constraint effect was not eliminated, the predicted resistance of the S700 butt-welded coupon by the finite element analysis (FEA) would be higher than the experimental counterpart due to the transverse constraint in the 3D finite element (FE) model, and the predicted peak deformation corresponding to the onset of the HAZ necking could be overestimated by up to 30% (Yan et al., 2022). However, FE results in (Chen et al., 2019) showed that the tensile strength of S690-RQT butt joint predicted by numerical models was less than that of butt joint tested, and the peak deformation was underestimated by the FE model. This confliction indicates that more research should be carried out on the HAZ constraint effect.

2.4 Influence of welding on HSS joints

2.4.1 HSS butt-welded joints

In the design of weld, the directional method is currently adapted in EN 1993-1-8 (CEN,

2005a), in which a single parameter β_w is incorporated to consider the influences of BM, WM, processing parameters, joint type and stress on the weld strength. Stroetmann and Kästner (2021) proposed a new design model for welded joints, as expressed in Eq. 2.3. In this model, the design strength was calculated by the weld strength f_{wu} and the joint type α_w. The weld strength f_{wu} was determined considering the BM, the WM, the cooling time $t_{8/5}$, the number of layers and the opening angle.

$$\sigma_v = \sqrt{\sigma_\perp^2 + 3(\tau_\perp^2 + \tau_\parallel^2)} \leq \alpha_w \cdot \frac{f_{wu}}{\gamma_{M2}} \qquad \text{Eq. 2.3}$$

It was found that the butt-welded joint strength was mainly affected by the ratio of the soft layer strength to the base metal strength and the relative width of the softened zone (Wang and Li, 2022). Therefore, the applicability of current codes depends on the width of soft layer and the steel grade. Ran et al. (2019) concluded that the strengths of most mismatched HSS butt-welded joints up to Q890 were close to the strength calculated by EN 1993-1-8 (CEN, 2005a). Only for HSS butt-welded joints with the wide softened HAZ zone, the strength was significantly lower than the strength predicted by EN 1993-1-8 (CEN, 2005a). Sun et al. (2018b) concluded that EN 1993-1-12 (CEN, 2007) cannot be directly used to design a butt weld with a soft interlayer in the HAZ of HSS. Khurshid et al. (2015) recommended the correlation factor for designing butt-welded joints in S960 steels. However, no universal design methods have been proposed yet. Therefore, it is imperative to carry our comprehensive experimental programmes and numerical analyses to develop effective design methods for HSS structures incorporating the welding effect.

2.4.2 HSS T-stub joints

In the design of beam-column connections with endplates, the equivalent T-stub joint is commonly used to represent the tension zone, as shown in Figure 2.13. The typical load-displacement curve of the T-stub joint contains three branches, namely the elastic branch, the hardening branch and the second hardening branch, as depicted in Figure

2.14. Three possible failure modes and corresponding design resistance equations are provided in EN 1993-1-8 (CEN, 2005a), including complete yielding of flange (Figure 2.15(a)), bolt failure with yielding of the flange (Figure 2.15(b)) and bolt failure (Figure 2.15(c)).

For the T-stub joint made of HSS, since welding can generate the HAZ whose strength and ductility differ from those of BM along the weld toe where the plastic hinge forms under the large deformation, the joint strength and the failure mode may be affected. The HSS T-stub joint under tension showed that cracks formed in the HAZ area along the weld toe (Sun et al., 2018c). Besides, the T-stub joint made of S690 showed a more brittle failure mode in comparison with that made of S385 and S440 (Zhao et al., 2016). The ductility of the HSS T-stub joint decreased significantly compared to its NSS counterpart (Liang et al., 2019). In the engineering practice, HSS structures may be subjected to extreme loads during the service life, like explosions and earthquakes. Under these circumstances the beam-to-column joint would experience a large deformation which would cause the second order effect. Therefore, the overall load-displacement behaviour of a T-stub joint is of great significance in design because the collapse of the whole structure should be prevented (Zhang et al., 2022). Francavilla et al. (2022) proposed a step-by-step integration algorithm to predict the overall response of T-stub joints. However, this method neglected the influence of the HAZ on the HSS T-stub joint, which impaired the ductility of the joint.

Current design equations for the T-stub joint are developed based on NSS. The applicability for HSS should be checked. Liang et al. (2019) concluded that EN 1993-1-8 (CEN, 2005a) may not be applicable to predict the resistance of HSS welded T-stub joints when the flange fractured near the weld toe, which was caused by welding. Sun et al. (2018c) also concluded that the formulae in EN 1993-1-8 (CEN, 2005a) could not be directly used for the Q690 T-stub joint. In addition, Chen et al. (2017) reported that

EN 1993-1-8 (CEN, 2005a) overestimates the plastic resistance of the S690-RQT joint. In contrast, Chen et al. (2023) found that EN 1993-1-8 (CEN, 2005a) method 2 for the complete yielding of flange can predict the design plastic resistance of the HSS Q690 T-stub joint under tension with precision. The contradiction may be caused due to different heat inputs during welding. Apart from the heat input, the plate thickness may also affect the applicability of current design codes. Zhao et al. (2016) conducted tensile tests for the HSS S690-RQT welded T-stub joint (Figure 2.16). Table 2.2 shows the comparison between test results and EN 1993-1-8 (CEN, 2005a) predictions. There were 3 kinds of thicknesses. For the thinnest 8 mm flange, EN 1993-1-8 (CEN, 2005a) overestimated the joint strength largely compared to other two flange thicknesses. This indicated that for the thin plate, due to the longer cooling time, the HAZ deterioration may be larger.

Apart from evaluating current design codes, new design methods for the HSS T-stub joint are in progress. EN 1993-1-8 (CEN, 2005a) neglects the bolt bending stiffness when calculating the initial stiffness of the T-stub joint. However, it was found that when calculating the initial stiffness of the HSS T-stub joint (Q460, Q690, Q960), the bolt bending stiffness must be incorporated because neglecting it could cause a difference up to 21% (Qiang et al., 2020, Qiang et al., 2023). Besides, Zhao et al. (2016) derived the load-displacement relationship for the HSS S690-RQT T-stub joint under a small deformation based on the yield line theory. Nevertheless, the prying force was not considered, and the plastic resistance based on the model were larger than experimental results which may be caused by neglecting the HAZ effect. Therefore, Zhao et al. (2017) proposed a reduction factor for the design of S690-RQT T-stub joint which modified EN 1993-1-8 (CEN, 2005a) equations. Similarly, to better design the Q690 T-stub joint, a factor χ_{HAZ} that represents the HAZ effect was quantified (Sun et al., 2018c).

In summary, different opinions exist about the applicability of EN 1993-1-8 (CEN, 2005a) for the HSS T-stub joint. There is a lack of equation to predict the ultimate bearing capacity of HSS T-stub joint considering the HAZ. And more research is needed to describe the overall joint behaviour of the HSS T-stub joint.

2.4.3 HSS tubular joints

Tubular structures have been widely used in buildings, bridges, transmission towers and offshore platforms due to its lightweight, beauty and cost-saving (Lan et al., 2021). In tubular structures, the tubular joint is a crucial connection to transmit loads between members. Typical failure modes for tubular joints include chord plastification, chord sidewall failure, chord shear failure, chord punching shear, brace failure, and local buckling (CEN, 2005a). Design recommendations have also been standardised in the CIDECT design guides (Wardenier et al., 2008), the international standard ISO 14346 (ISO, 2013a), the American standard ANSI/AISC 360-22 (Construction, 2022) and the Eurocode EN 1993-1-8 (CEN, 2005a). The strength equations in these design guides and code provisions are in similar format but with different coefficients and partial factors or resistance factors. In general, the design recommendations are applicable to NSS joints. In Eurocode EN 1993-1-8 (CEN, 2005a), design recommendations for HSS joints are included, however reduction factors have been implemented. Additional reduction factors are regulated for HSS tubular joints to consider possible lower rotation, deformation capacity and sufficient ductility (Packer et al., 2009, Wardenier et al., 2008, Pandey and Young, 2019b). However, the effect of welding is not considered in these design equations. According to investigations of HSS tubular joints (Pandey and Young, 2019a, Lee et al., 2017, Kim and Lee, 2020, Kim et al., 2019), the suitability of the reduction factors remains further checking as it may generate conservative results when predicting the joint strength of the HSS tubular joint.

In recent years, researchers gradually begin to incorporate the welding effect on HSS

tubular joints. Hu et al. (2021) studied the cold-formed HSS circular hollow section (CHS) T joints made of S690-QT under brace compression and in-plane bending. It was concluded that if the welding procedure and welding parameters were properly controlled, the effect of welding onto the structural behaviour of T joints was small. Lan et al. (2019) numerically studied the HAZ influence on the structural behaviour of RHS and CHS S960 X-joint under brace compression. The results showed that the HAZ had no major impact on the initial stiffness. Since the heat input in this research was only 0.38 kJ/mm and the QT steel was used, the effect of welding was not considered in subsequent parametric studies. In contrast, Pandey et al. (Pandey et al., 2021a, Pandey et al., 2021b) numerically studied the cold-formed high strength steel rectangular hollow section (RHS) T joints under brace compression of S900-TMCP and S960-TMCP. The results revealed that ignorance of the HAZ in FE models overestimated the joint strengths in the range of 12 to 34%. Figure 2.17 shows the load-displacement curves for the T-joint with and without HAZ. In summary, a widely accepted design method considering the welding effect for HSS tubular joints has not been proposed yet.

For tubular joints, the joint strength is usually defined as the peak load or the load corresponding to the deformation limit, whichever occurs first (Hu et al., 2021, CEN, 2005a, ISO, 2013a, Lee et al., 2019). 3% deformation limit proposed by LU et al. (1994) is usually used. Most investigations mentioned above are targeted at HSS tubular joints under brace compression with the HAZ, in which the joint strength is deformation controlled by 3% deformation limit. While for HSS tubular joints under tension affected by the HAZ, it is likely that due to the existence of the HAZ which leads to the ductility reduction, their failure mode would switch from deformation control to strength control, for example, chord punching shear. For tubular joints with punching shear failure, the shear fracture is significant and should be incorporated in the fracture model (Ma et al., 2015). However, the fracture properties of HAZ in HSS are not systematically

investigated. Therefore, to facilitate the engineering practice of HSS tubular joints, it is urgent to study the HSS tubular joints under tension with the HAZ. Relevant design methods considering the HAZ should also be further developed.

2.5 Summary

This paper presents a comprehensive review on the effect of welding on the behaviours of HSS. Manufacturing and arc welding procedures of HSS were firstly introduced. The welding procedure specification by arc welding should be carefully prepared before welding HSS. Several factors, including the current, voltage, welding speed, stick-out length of electrode, and shielding gas, can influence the weld appearance and quality. Phase transformations occur in the HAZ due to the welding induced thermal cycles, which are characterised by the peak temperature T_{max} and cooling time $t_{8/5}$. HAZ can be divided into different subzones composed of various phases because of the thermal cycles. The mechanical properties of HAZ in HSS are strongly correlated to the microstructures. Recent investigations reveal that the strength, deformation ability, and microhardness of HSS are obviously impaired by the welding heat input. Therefore, the mechanical behaviours of HSS welded joints are affected by the HAZ caused by welding. Furthermore, related research on the mechanical behaviours of HSS welded joints considering the welding effect are summarised. Finally, numerical modelling techniques to simulate the heat transfer during welding and the coupled thermal-stress analysis for the welded HSS are introduced, and the research needs have been highlighted.

Table 2.1 Cooling time for different thicknesses of butt joints according to EN 1011-2 (CEN, 2001)

Q (kJ/mm)	T_0 (°C)	Plate thickness (mm)	$t_{8/5}$ (s)
0.5	25	3	29.00
	25	6	7.25
	25	16	2.41
1	25	3	116.01
	25	6	29.00
	25	16	4.08
1.5	25	3	261.03
	25	6	65.26
	25	16	9.18

Table 2.2 Test results of HSS S690-RQT T-stub joint with different flange thicknesses (Zhao et al., 2016)

Thickness (mm)	Test results-average (kN)	EN 1993-1-8: Method 1	EN 1993-1-8: Method 2	Difference 1 (%)	Difference 2 (%)
8	43.1	49.4	52.9	-12.9	-18.6
12	122.4	114.6	122.8	5.5	-1.6
16	218.7	210.3	225.6	4.0	-3.1

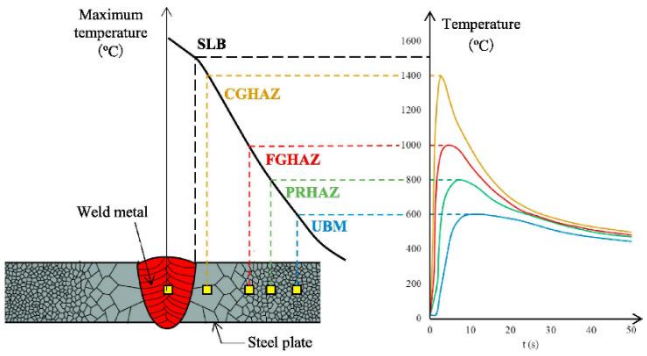

Figure 2.1 Different microstructures in HAZ (SLB: solid-liquid boundary, CGHAZ: coarse grain HAZ, FGHAZ: fine grain HAZ, PRHAZ: partially recyclised HAZ, UBM: unaffected BM) (Liu et al., 2018)

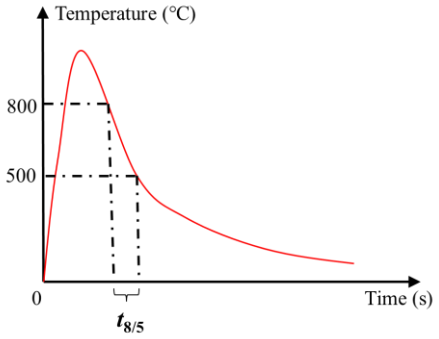

Figure 2.2 The definition of cooling time $t_{8/5}$ (Ho et al., 2020)

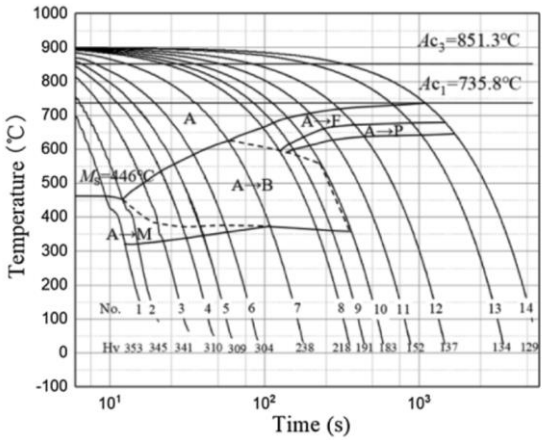

Figure 2.3 CCT curves of high strength S690 steel (Chung et al., 2020)

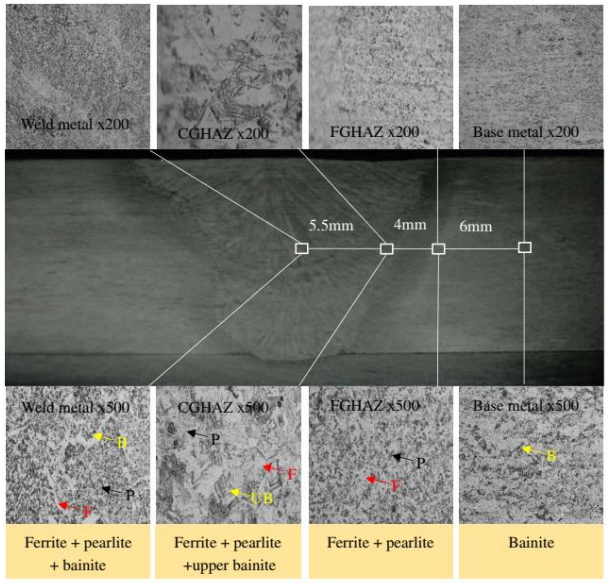

Note: F: ferrite, P: pearlite, B: bainite, UB: upper bainite.

Figure 2.4 Microstructure of Q690 butt joint (Jiang et al., 2021)

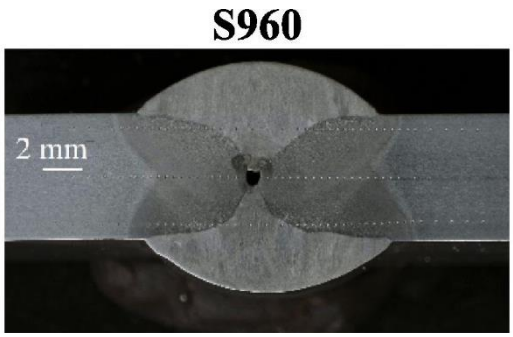

Figure 2.5 S960 butt-welded joint after chemical etching with distinguished HAZ/WM boundary (Amraei et al., 2019, Liu et al., 2018)

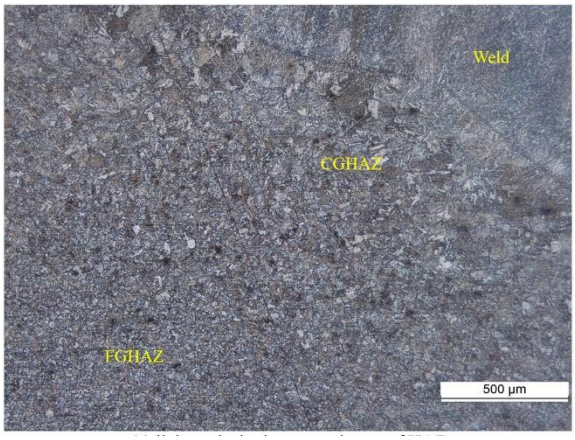

Figure 2.6 Boundary between WM and HAZ under light optical microscope

(Chen et al., 2019)

.

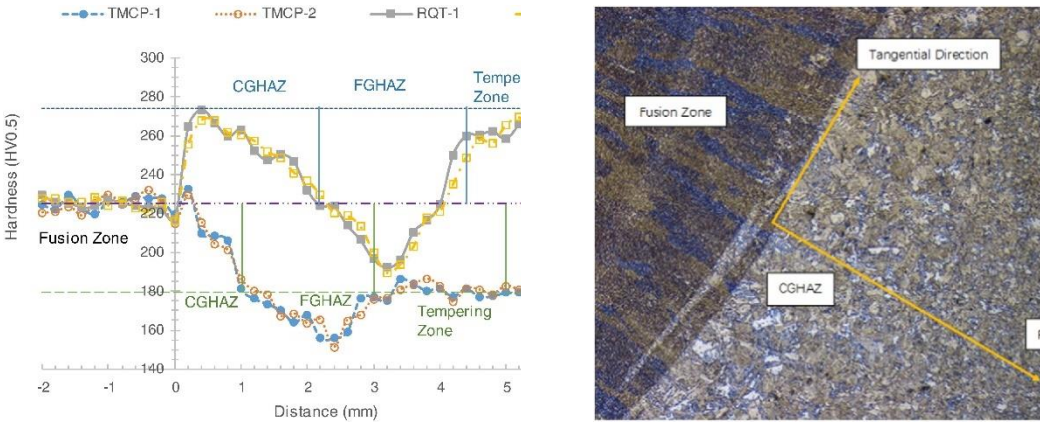

a) Hardness results

b) Microstructure under optical microscope

Figure 2.7 Metallurgical investigations (Zhao et al., 2017)

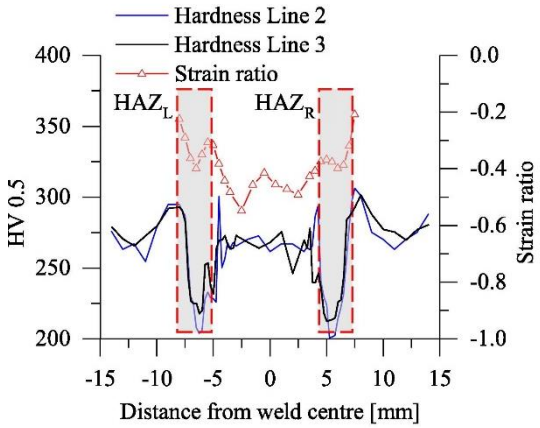

Figure 2.8 Identification of the HAZ boundary by strain ratio (Yan et al., 2022)

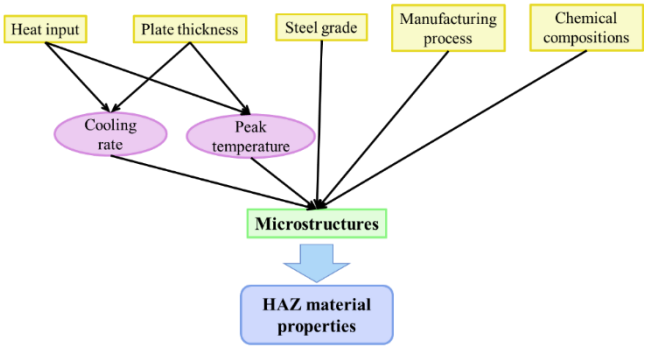

Figure 2.9 Relationships between different factors and HAZ material properties

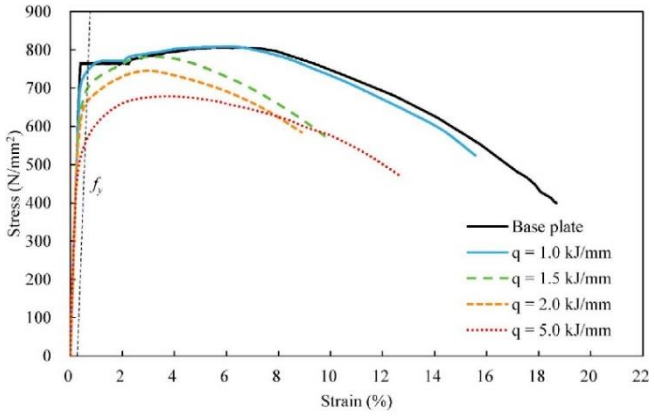

Figure 2.10 Stress-strain curves for S690 under different heat input (Liu et al., 2018)

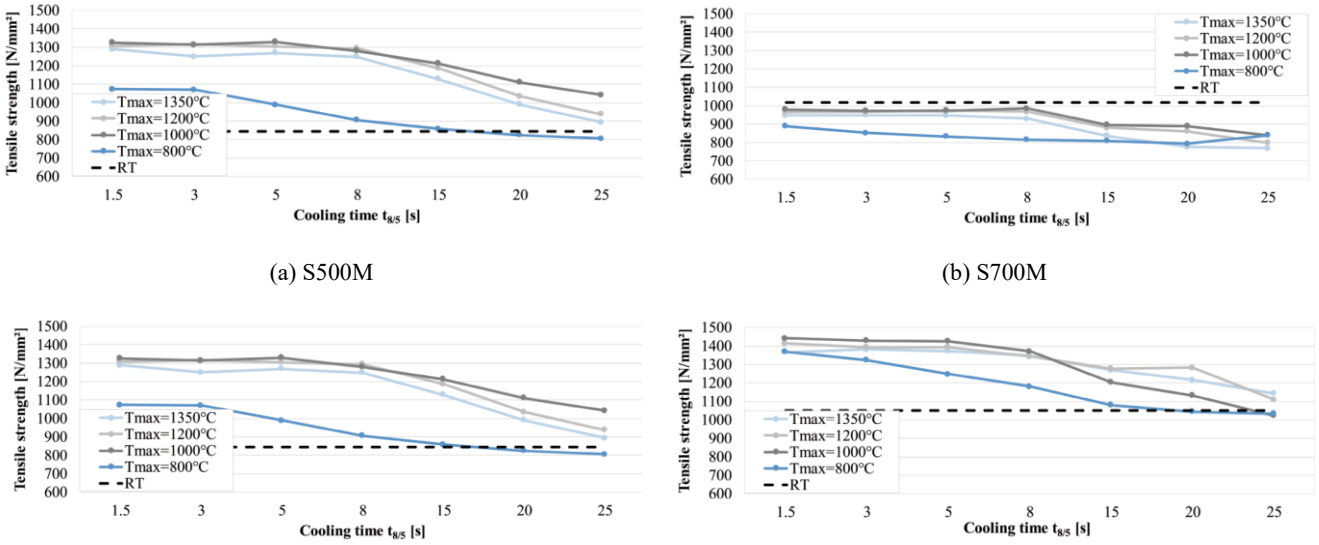

(a) S500M

(b) S700M

(c) S690Q

(d)S960Q

Figure 2.11 Tensile strength as a function of cooling time $t_{8/5}$

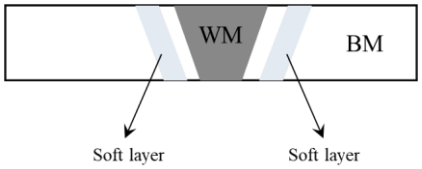

Figure 2.12 Constraint effect (Neuvonen et al., 2021, Yan et al., 2022, Rodrigues et al., 2004, Sun et al., 2018a)

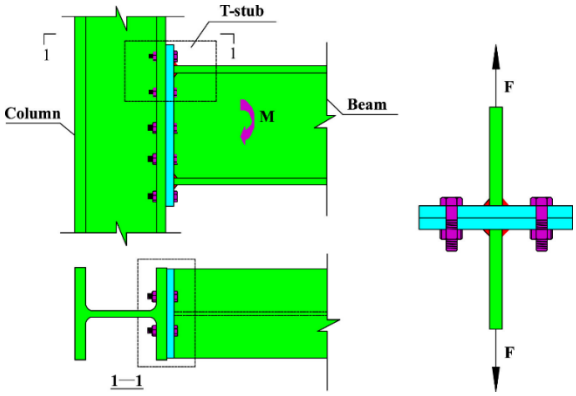

Figure 2.13 The T-stub in a beam to column connection (Guo et al., 2017)

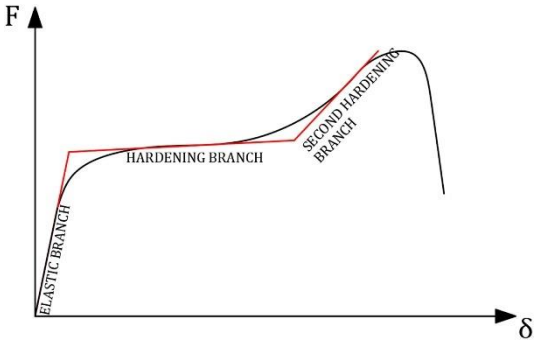

Figure 2.14 Three stages in load displacement curve for T-stub joint fixed at rigid support (Francavilla et al., 2022)

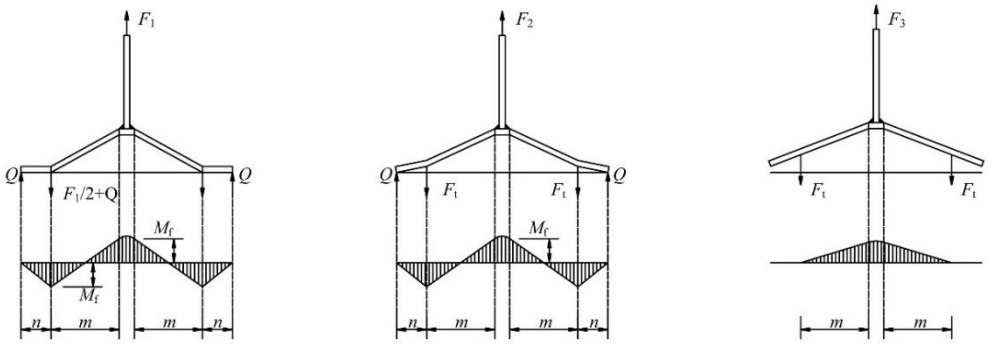

Figure 2.15 Failure modes in EN 1993-1-8 (Yuan et al., 2019)

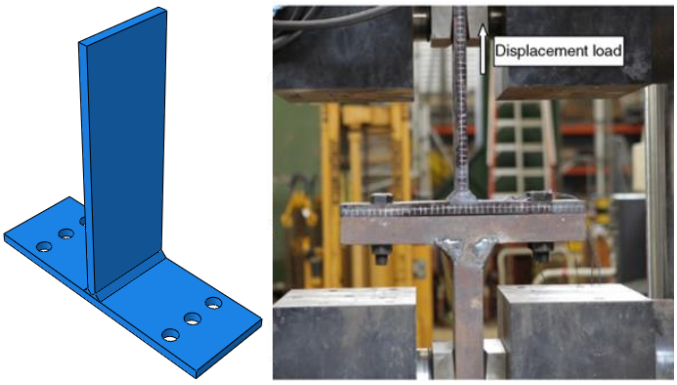

Figure 2.16 HSS S690-RQT welded T-stub joint under axial tension (Zhao et al., 2016)

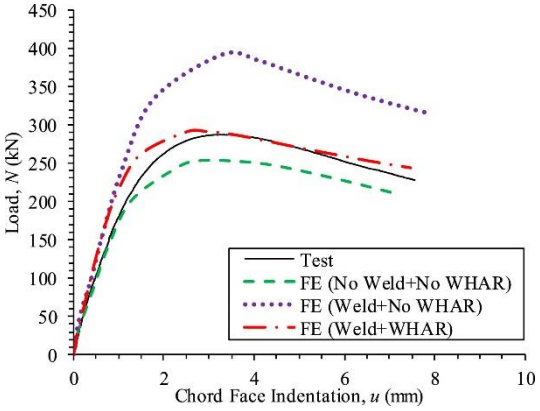

Figure 2.17 Weld and weld heat affected region (WHAR) effect on CHS-RHS T-joints (Pandey et al., 2021a)

Chapter 3 Experimental investigations of the HSS butt-welded joints

3.1 Introduction

The experimental investigations of the HSS butt-welded joints made of different steel grades and welded by various heat inputs were demonstrated in this chapter. Tensile coupons were cut from the butt-welded joints and tested under axial tension. Test blocks were utilised to acquire the hardness distributions in different plate depths. Based on the butt-welded tensile coupons results, an experimental-numerical iterative method was adapted to obtain the material properties for the heat affected zone (HAZ) with different steel grades and various heat inputs. The obtained HAZ material properties composed of a database, and two regression models were developed to predict the HAZ true stress-strain curves according to the database.

3.2 Experimental programme

3.2.1 Base material

There were 3 kinds of steel grades with the nominal plate thickness equal to 6 mm used in this study, including Q460, Q690 and Q960. For the delivery condition, the Q460 was as rolled (AR), and the Q690 and Q960 were quenched and tempered (QT). The nominal chemical compositions of these steels according to the mill certificate were illustrated in Table 3.1. Three flat coupons were wire-cut from each kind of steel plate for tensile coupon tests according to ISO 6892-1 (ISO, 2019), as shown in Figure 3.1. The obtained stress-strain curves were given in Figure 3.2. The nomenclature was introduced as follows: for example, in “460-T6-1”, “460” denoted the steel grade; “T6” denoted the nominal plate thickness was 6 mm, “1” denoted it was the first tensile coupon. The tested material properties of the base metal listed in Table 3.2 were obtained from the stress-strain curves, including the Young’s modulus (E), yield stress

(f_y), ultimate stress (f_u), ultimate strain (ε_u) and fracture strain (ε_f).

3.2.2 Specimens

3.2.2.1 Specimen information

This study investigated the influences of the heat inputs and steel grades on the mechanical behaviours of the butt-welded joints. Table 3.3 lists the HSS butt-welded joint groups varying in heat inputs and steel grades. The nomenclature for the HSS butt-welded joint was as follows: for "Q460-B6-H1", "Q460" represented the steel grade; "B6" represented the nominal plate thickness; "H1" represented the heat input. The weld details of the butt-welded joint was designed according to AWS D1.1/D1.1M (AWS, 2015). Figure 3.3 shows the joint configurations and weld details. 3 tensile coupons and 2 test blocks were wire-cut from the joint for each specimen, as shown in Figure 3.3 and Figure 3.4. The tensile coupon configurations were compliant with ISO 6892-1 (ISO, 2019), as shown in Figure 3.5. The average measured width and thickness of the butt-welded tensile coupons were shown in Table 3.4. "Q460-B6-H1-1" meant that it was the first tensile coupon for the butt-welded joint Q460-B6-H1

3.2.2.2 Specimen fabrication

Gas metal arc welding (GMAW) operated by a welding robot (brand: Panasonic G2-TA1400-VR006) was implemented to fabricate the HSS butt-welded joints. In this study, there were two welding passes for each specimen after a series of welding trials. The welding should be conducted in a windless room. The shielding gas consisted of 80% Ar and 20% CO_2. Matching welding was achieved by selecting the corresponding filler electrode for Q460 and Q690, as listed in Table 3.5. For Q960 high strength steel, the filler electrode ER 120S-G was selected for welding. This filler electrode had an ultimate strength no less than 830 MPa stipulated in AWS A5.28/A5.28M: 2005 (AWS, 2005), which was smaller than the nominal yield strength of Q960. Therefore, judging from this aspect, it was undermatched welding. It should be noted that usually if the

welding parameters were applicable for the filler electrode with higher classification, they could also be applied to the filler electrode with lower classification. During welding, the ceramic plates were attached at the bottom of the HSS butt-welded joint to prevent the drop of molten metal. Preheating was effective to prevent the hydrogen cracking (Sun and Dilger, 2023). However, since the nominal plate thicknesses of the butt-welded joint were only 6 mm, the method to determine the preheating temperature recommended in EN 1011-2 (CEN, 2001) indicated that the specimens in this experiment did not need preheating.

4 different heat inputs were determined according to an extensive welding trial, ranging from 0.9 to 1.8 kJ/mm. The base metal in this study had a nominal thickness of 6 mm. If further increasing the heat input above 2.0 kJ/mm, the steel plate could be penetrated and had reduced weld quality. In addition, every butt-welded joint had two welding passes to avoid the influence of welding passes on the joint behaviour. The heat input lower than 0.9 kJ/mm required three or more welding passes to achieve satisfactory weld quality according to the welding trials. Therefore, the heat input was chosen between 0.9 to 1.8 kJ/mm. Lower heat input, like 0.5 kJ/mm, was not chosen as the lack of fusion was found in the butt-welded joints adapting this heat input. A set of welding parameters was decided based on the previous welding parameters for the HSS butt-welded joints in the welding trial. The welding gun travel angle, welding gun work angle and wire stick out length were carefully adjusted before turning on the welding robot. Then several rounds of welding were implemented for the butt-welded joints to obtain satisfactory welds which exhibited good appearances and had no discontinuities. If weld discontinuities like porosity were found, the current, voltage or welding speed were adjusted as follows: the increase of current can increase the weld penetration depth; the increase of voltage can increase the weld width; the increase of speed can decrease the penetration depth and weld width. After several rounds of trial and error, 4 sets of welding parameters with different heat inputs were obtained, as shown in Table 3.6.

However, during fabricating the butt-welded joints, the actual welding parameters were slightly different from the welding parameters shown in Table 3.6. Panasonic G2-TA1400-VR006 could calculate the average voltage and current during welding. For each welding pass of the butt-welded joints, the average voltage and current were recorded. Table 3.3 lists the actual welding heat inputs based on the recordings. The examples of the fabricated specimen Q690-B6-H2 were shown in Figure 3.6. The welding quality was checked by visual inspections for the weld appearances and the cross-section observation after tensile coupon tests.

3.2.3 Test setup and procedure

The obtained HSS butt-welded tensile coupons were grinded to eliminate the weld reinforcement on both sides and to obtain flat surfaces, as shown in Figure 3.7. Each side of the tensile coupons was attached with a strain gauge. Then the butt-welded tensile coupons were installed on Instron 5982 and loaded under tension, as shown in Figure 3.8. An optical extensometer was utilised to measure the coupon deformation. For the loading rate, it was set as 0.1 mm/min; then when 0.2% proof stress was reached the loading rate was changed to 0.5 mm/min. After the tensile tests, all specimens were etched in Nital solution to observe the fracture locations. For the butt-welded joints made of Q460, 2% Nital solution was utilised for 1 min; for the butt-welded joints made of Q690 and Q960, 4% Nital solutions was used for 1.5 min.

Following steps were conducted to obtain the hardness distributions of the test blocks with different heat inputs and steel grades. BUEHLER EcoMet 30 in Figure 3.9 was used to grind and polish the test blocks. The rotating speed was between 250 and 450 rpm. Abrasive sandpapers with #100, #180, #400 and #600 were utilised in a sequence to grind the surface of the test blocks until it was flat. After grinding, polishing was implemented by the same EcoMet 30 with adding MasterPolish (Figure 3.10) which

had a diamond diameter of 0.05 μm. Finally, the test blocks obtained a mirror-like surface for the hardness tests.

The standard HV 0.5 hardness test was conducted by a Wilson Hardness tester manually (Figure 3.11). Figure 3.12 demonstrated the indentation lines on the test block cut from the butt-welded joint. Due to the symmetry of the hardness distributions, only half of the block was tested. There were three indentation lines for each test block. The distances between the indentation lines and between the surfaces of the block and the outer indentation lines complied with ISO 6507-1 (ISO, 2018). Two indentations had a distance of 0.5 mm between their centres. During testing, the full test force was lasted for 10 s. After hardness tests, the test blocks were immersed into the Nital solutions to obtain the boundaries of WM. The widths of the WM were measured at the depths corresponding to three indentation lines. The HAZ width then could be calculated combining the results of the measured WM widths and hardness distributions.

3.3 Experimental results of butt-welded tensile coupons

3.3.1 Stress-strain curves and mechanical characteristics for butt-welded tensile coupons

The stress strain curves of all the butt-welded tensile coupons and corresponding base metal tensile coupons in this study are presented in Figure 3.13 to Figure 3.15. The nomenclature was explained as follows: for “Q460-B6-H1-1”, “Q460” was the steel grade; “B6” denoted the nominal plate thickness was 6 mm; “H1” denoted the heat input; “1” denoted that it was the first tensile coupon for the butt-welded joint Q460-B6-H1. The mechanical properties for the butt-welded tensile coupons were obtained from the stress-strain curves. They included Young’s Modulus (E), yield stress (f_y), ultimate stress (f_u), ultimate strain (ε_u), fracture strain (ε_f) and elongation at fracture, as listed in Table 3.7.

All the butt-welded tensile coupons fractured at the end of tensile test. The fracture locations of all the specimens could be observed after etching in the Nital solution. Figure 3.16 illustrated several types of fracture locations: fracture at BM, fracture at HAZ/BM interface, fracture at HAZ and fracture at WM. Table 3.7 summarised the fracture locations of all the specimens. It can be observed that for the Q690 and Q960 butt-welded tensile coupons with heat input equal to M, the fracture locations were within HAZ. The ε_u and ε_f of these coupons were abnormally small compared to other coupons. The fracture surfaces showed porosity and multiple weld layers, as illustrated in Figure 3.17, which indicated that lack of fusion existed under this heat input. Therefore, heat input could not be too low, which could affect the formation of satisfactory welds. Besides, there existed a tendency that as the steel grades increased from Q460 to Q960, the fracture locations moved from the base metal of the Q460, to the HAZ/BM interface of the Q690, and to the HAZ of the Q960 butt-welded tensile coupons. This phenomenon indicated the influence of welding on the fracture initiation and damage evolution of the butt-welded joints got more significant for higher strength steels. For the butt-welded tensile coupons whose fracture location was BM, f_u was not obviously impaired, because it failed in BM. Since it was not ruptured at HAZ, that means the f_u of HAZ was greater than f_u of BM.

3.3.2 Variation of mechanical properties with heat inputs

3.3.2.1 Q460 butt-welded tensile coupons

Figure 3.18 presents the variations of the mechanical properties of Q460 butt-welded tensile coupons with heat inputs. In the figures, $f_{y,Butt}$ represented the yield strength of butt-welded coupons; $f_{y,BM}$ represented the ultimate strength of the base metal; ε_u represented the ultimate strain. The welding can improve the yield strengths of butt-welded joint, as $f_{y,Butt}/f_{y,BM}$ was greater than unity with corresponding heat input equal to 0.968 and 1.263 kJ/mm. But it dropped under unity when the heat input was increased

from 1.263 kJ/mm to 1.631 kJ/mm. Finally, under 1.752 kJ/mm, $f_{y,Butt}/f_{y,BM}$ was above unity. Therefore, $f_{y,Butt}/f_{y,BM}$ had a tendency to decrease with heat input between 0.968 to 1.631 kJ/mm, while it increased as heat input increased from 1.631 to 1.752 kJ/mm. It was likely that under 1.752 kJ/mm, the HAZ microstructures with the enhanced strength formed during welding. $f_{u,Butt}/f_{u,BM}$, in contrast, was almost unity no matter what the heat input was. It was because the fracture locations were at WM or BM rather than HAZ, which made $f_{u,Butt}$ close to $f_{u,BM}$. The deformation characteristics were also illustrated in Figure 3.18. The elongation at fracture and ε_u for butt-welded tensile coupons had similar trend that they both were parabolically related to the heat inputs. Finally, f_u/f_y was greater than 1.2, complying with the requirements in EN 1993-1-1 (CEN, 2005b) that this ratio should be greater than 1.1.

3.3.2.2 Q690 butt-welded tensile coupons

Figure 3.19 presents the variations of the mechanical properties of Q690 butt-welded tensile coupons with different heat inputs. It can be observed that welding had a significant negative influence on the yield stress of the Q690 butt-welded tensile coupons. If the heat inputs increased from 0.966 kJ/mm to 1.823 kJ/mm, $f_{y,Butt}/f_{y,BM}$ decreased from around 0.8 to 0.7, showing an obvious reduction compared to BM. Nevertheless, $f_{u,Butt}/f_{u,BM}$ was still close to unity, indicating that welding had neglectable effect on the tensile stress for Q690 butt-welded tensile coupons. It can be explained that the fracture locations of Q690 butt-welded tensile coupons were at HAZ/BM interface. Therefore, it can be concluded that the HAZ had minor effects on $f_{u,Butt}$. And f_u/f_y increased as heat input increased. In Figure 3.19(c), ε_u of Q690-B6-M-3 was deviated from other two tensile coupons greatly, therefore it was eliminated when considering the tendency for ε_u along with heat inputs. For the same reason, Q690-B6-M-3 was neglected when discussing the tendency for elongation at fracture along with heat inputs in Figure 3.19(d). It can be found that these deformation characteristics was also parabolically related to heat inputs for the Q690 butt-welded tensile coupons within

0.966 ~ 1.645 kJ/mm. But they were enhanced for the butt-welded tensile coupons with 1.823 kJ/mm heat input. f_u/f_y was greater than 1.2, complying with the requirements in EN 1993-1-1 (CEN, 2005b) that this ratio should be greater than 1.1.

3.3.2.3 Q960 butt-welded tensile coupons

Figure 3.20 presents the variations of mechanical properties of Q960 butt-welded tensile coupons with different heat inputs. f_y of Q960-B6-H1-1 exhibited great deviation from the other two counterparts. Therefore, it was eliminated when discussing f_y for the Q960 butt-welded tensile coupons. f_y of the Q960 butt-welded coupons exhibited a at least 20% remarkable reduction compared to that of the BM. For the Q960 butt-welded coupons with 1.592 kJ/mm, $f_{y,Butt}/ f_{y,BM}$ could even be around 0.6, experiencing a 40% strength reduction. However, enhancing heat input from 1.592 kJ/mm to 1.864 kJ/mm, $f_{y,Butt}/ f_{y,BM}$ increased from around 0.6 to 0.7. The increase may be caused by the formation of microstructures with higher strength during welding. On the other hand, in contrast to Q460 and Q690, $f_{u,\ Butt}/f_{u,\ BM}$ of the Q960 butt-welded joint was also impaired, which was likely related to its high steel grade. The ratio was almost 0.8 if increasing heat input to 1.864 kJ/mm. But it did not linearly diminish as the heat input increased. It can be explained that the fracture locations of Q960 butt-welded tensile coupons were HAZ. The reduction of $f_{u,\ Butt}$ indicated that $f_{u,HAZ}$ (the ultimate strength of HAZ) was impaired. As for the f_u/f_y, it was above 1.2 for almost all the Q960 butt-welded tensile coupons, satisfying the requirements that this ratio was recommended greater than 1.10, as listed in EN 1993-1-1 (CEN, 2005b). As for the deformation characteristics, Q960-B6-M-3 was eliminated from the discussion due to its great deviation. It can be observed that the elongation at fracture and ε_u both showed a parabolic relationship along with heat inputs.

In summary, for all steel grades, the yield strength f_y of butt-welded coupons were significantly impaired by increasing heat inputs, while the influence of welding on the

ultimate strength f_u depending on the fracture locations of butt-welded coupons. If fracture happened near BM, $f_{u,Butt}/f_{u,BM}$ was close to unity; if fracture happened in HAZ, $f_{u,Butt}/f_{u,BM}$ was less than one. The ductility of butt-welded coupons was represented by three indicators. For the deformation characteristics, represented by ε_u and elongation at fracture, they were parabolically related to the heat input. But for f_u/f_y, all the butt-welded coupons had a ratio above the value 1.10, which is the recommended value by EN 1993-1-1 (CEN, 2005b).

3.3.3 Variation of material properties with steel grades

3.3.3.1 Butt-welded tensile coupons with heat input equal to around 0.973 kJ/mm

Figure 3.21 shows the variations of the mechanical properties for the butt-welded tensile coupons by around 0.973 kJ/mm with various steel grades. It can be found that for higher steel grade, $f_{y,Butt}/f_{y,BM}$ and $f_{u,Butt}/f_{u,BM}$ would become smaller. The degree of reduction for $f_{y,Butt}/f_{y,BM}$ was more severe than that for $f_{u,Butt}/f_{u,BM}$. For the deformation characteristics, ε_u decreased greatly from 8% to 1% as steel grades of the butt-welded coupons increased from Q460 to Q960. Comparably, the elongation at fracture also was reduced apparently from around 13% to 2% with steel grades increasing from Q460 to Q960. As there were only two welding passes, Q690 and Q960 specimens with heat input lower than 1.0 kJ/mm exhibited large scatter of material properties as their welds exhibited porosity and lack of fusion.

3.3.3.2 Butt-welded tensile coupons with heat input equal to around 1.234 kJ/mm

Figure 3.22 exhibits the variations of mechanical properties of the butt-welded tensile coupons by around 1.234 kJ/mm with steel grades. Similar to the butt-welded tensile coupons made by 0.973 kJ/mm, under 1.234 kJ/mm, $f_{y,Butt}/f_{y,BM}$ showed a reduction up to 20% but $f_{u,Butt}/f_{u,BM}$ was only slightly reduced as the steel grade increased from Q460 to Q960. At the same time, ε_u decreased from 8.5% corresponding to Q460 to 4.0%

corresponding to Q960, and the elongation at fracture diminished from 18% corresponding to Q460 to 7% corresponding to Q960.

3.3.3.3 Butt-welded tensile coupons with heat input equal to around 1.546 kJ/mm

Figure 3.23 showcases the variations of mechanical properties of the butt-welded coupons by around 1.546 kJ/mm with various steel grades. $f_{y,Butt}/f_{y,BM}$ was reduced up to 40% as steel grades increased from Q460 to Q960. Under this heat input, $f_{u,\,Butt}/f_{u,\,BM}$ also exhibited small reduction with steel grades, as it was reduced from 1 for Q460 to around 0.9 for Q960. In addition, ε_u showed a significant reduction from 8% for Q460 to 4% for Q960 when it came to deformation characteristics. However, for the elongation at fracture, this decreasing trend was reversed at the Q690 butt-welded coupons which exhibited an increase as steel grades increased from Q690 to Q960.

3.3.3.4 Butt-welded tensile coupons with heat input equal to 1.760 kJ/mm

Figure 3.24 presents the variations of mechanical properties of the butt-welded tensile coupons by around 1.760 kJ/mm with various steel grades. With steel grades improved, apart from the obvious reduction of $f_{y,Butt}/f_{y,BM}$, the value of $f_{u,\,Butt}/f_{u,\,BM}$ was also lowered to around 0.85 for the Q960 specimens. Besides, both the elongation at fracture and ε_u were declined with increasing steel grades.

In summary, $f_{y,\,butt}/f_{y,\,BM}$ reduced significantly, indicating that the influence of welding increased as steel grades increased. $f_{u,\,butt}/f_{u,\,BM}$ showed a decrease with the heat input equal to around 0.973 kJ/mm as the steel grade increased to Q960. It was because under 0.973 kJ/mm, the weld of Q690 and Q960 had weld discontinuities like porosity. But remained close to unity with heat input equal to 1.234 kJ/mm and 1.546 kJ/mm. Then under 1.760 kJ/mm, $f_{u,\,butt}/f_{u,\,BM}$ exhibited significant drop when the steel grade was increased to Q960. It can then be concluded that as the heat input increased, the influence of steel grade on $f_{u,\,butt}$ amplified. The deformation characteristics, represented

by ε_u and elongation at fracture, decreased obviously as the steel grade increased, regardless of the heat input. This may imply that these two values were mainly controlled by steel grades.

3.3.4 Hardness results for butt-welded joints

Figure 3.25 to Figure 3.36 shows the hardness distributions of the specimens at different depths with respect to the upper plate surface. The BM hardness for each indentation line was calculated as the average hardness in the outer region of the indentation line far from the welds. The WM width at each indentation line was directly measured after etching the test blocks in the Nital solutions. To determine HAZ widths, the boundaries between HAZ and BM for each indentation line of the test block were taken as the crossing point between the BM hardness and the hardness distribution, as illustrated in Figure 3.37. The HAZ width for every indentation line was calculated by the *x*-coordinate HAZ/BM boundary minus the half of the WM width, as shown in Figure 3.37. The cross-section divisions of butt-welded joint were also demonstrated in Figure 3.25 to Figure 3.36 according to WM and HAZ widths. Table 3.8 exhibits the measured WM and HAZ widths at three levels of indentation lines. It can be observed that the variances of the HAZ widths between three lines for one specimen were within 3 mm since the nominal plate thickness was only 6 mm. Therefore, for each specimen, the average HAZ width was taken as the average value of the HAZ widths of three indentation lines. Figure 3.38 gives the variations of HAZ widths with heat inputs. It was clear that increasing heat input could widen the HAZ for all steel grades. Linear regression models were developed accordingly, as shown in Eq. 3.1 to Eq. 3.3, where W is the HAZ width in mm, Q is the heat input in kJ/mm. The slopes of Q690 and Q960 were greater than that of Q460, indicating a higher sensitivity of HAZ width toward heat inputs for higher strength steel.

$$W_{Q460} = 2.481 \times Q + 4.708 \qquad \text{Eq. 3.1}$$

$$W_{Q690} = 5.117 \times Q + 2.064 \quad \text{Eq. 3.2}$$

$$W_{Q960} = 5.183 \times Q + 2.368 \quad \text{Eq. 3.3}$$

The average hardness of WM and HAZ were calculated by averaging the indentations in the corresponding region. Table 3.9 demonstrates the average hardness of WM, HAZ and BM, denoted as H_{WM}, H_{HAZ} and H_{BM}. Besides, the ratios of the average hardness between different zones were also provided by Table 3.9. Figure 3.39 showcases the variations of H_{HAZ} along with heat inputs. It could be observed that for Q460 steel, increasing heat input could lead to the increase of HAZ hardness; for Q690 and Q960 steel, increasing heat inputs could impair the HAZ average hardness.

Figure 3.25 to Figure 3.36 exhibit the hardness distributions for the Q460, Q690 and Q960 butt-welded joints with different heat inputs. It can be found that the HAZs was inhomogeneous and consisted of the hardened and softened regions. As the heat input increased, both the hardened and softened regions expanded. For Q460 butt-welded joint, the hardness of the hardened regions was greater than the BM hardness. But for Q690 and Q960 butt-welded joint, the hardness of the hardened part was slightly larger or close to the BM hardness. The reason may be that the delivery condition of Q460 was as rolled, and the effect of cooling stage during welding could conduct equivalent but not finely controlled quenching and tempering on the material, thus resulting the improvement of hardness as well as strength as discussed previously. The delivery condition of Q690 and Q960 was quenched and tempered in the factory condition. Therefore, the cooling stage during welding conducted another round of equivalent quenching and tempering which was not finely controlled, which could not significantly improve the hardness of the material.

3.4 Calibration of HAZ material properties

Attempts were made to develop the models which can describe the material properties

of HAZ, since it can affect the performance of the HSS structures. Wang and Li (2022) applied the Ramberg-Osgood model to describe the HAZ stress-strain relationship for butt-welded joints. The strain hardening exponent n and strength coefficient K reflecting the HAZ were calibrated for Q550D-QT and Q690D-QT by trial and error through numerical simulations. Stroetmann et al. (Stroetmann et al., 2018, Stroetmann and Kästner, 2019) proposed regression models for the HAZ mechanical properties, including the hardness, yield strength, tensile strength and elongation at fracture. These properties were dependent on the peak temperature T_{max} and cooling time $t_{8/5}$, as indicated in Figure 3.40. However, many coefficients were introduced into these regression models and their physical meanings were unclear. Pandey and Young (2021) extracted HAZ tensile coupons from welded tubular joints at different locations and conducted tensile coupon tests. The results indicated that the Young's Modulus, yield strength, tensile strength and fracture strain were influenced by welding. However, the results only focused on S960-TMCP steel welded under specific welding parameters.

In the afore mentioned experiments, the butt-welded tensile coupons were tested. However, the butt-welded tensile coupons consisted of three regions, which were WM, HAZ and BM. The obtained stress-strain curves represented an average tendency of these regions, and the material properties of HAZ cannot be obtained directly. In this section, an experimental-numerical iterative method was adapted to acquire the HAZ material properties based on the butt-welded tensile coupons' test results. By this method, the true stress-strain curves corresponding to the engineering yield strength to engineering ultimate strength for the HAZ with various heat inputs and steel grades can be determined.

3.4.1 True stress-strain relationships

The conversion of the engineering stress-strain curve before necking to the true stress-strain curve assumes that the overall volume of the material remains constant. The true

strain increment $d\varepsilon_t$ can be calculated by Eq. 3.4 where L is the actual gauge length.

$$d\varepsilon_t = \frac{dL}{L} \quad \text{Eq. 3.4}$$

The initial gauge length is represented by L_0 and by integrating Eq. 3.4, the true strain can be expressed by Eq. 3.5 where ε_e is the engineering strain. Since the material volume is constant before necking, the true stress σ_t can be obtained by Eq. 3.6 where σ_e is the engineering stress.

$$\varepsilon_t = \ln(1 + \varepsilon_e) \quad \text{Eq. 3.5}$$

$$\sigma_t = \sigma_e(1 + \varepsilon_e) \quad \text{Eq. 3.6}$$

Eq. 3.5 and Eq. 3.6 were used to transfer the engineering stress-strain curves into the true stress-strain curves. Besides, there exists models proposed to depict the true stress-strain curves. Hollomon (Hollomon, 1945) described a power law to relate the true strain to the true stress, as shown in Eq. 3.7, where K and n denote the strength coefficient and the strain hardening exponent. This equation can be used to depict the true stress-strain relationship where the corresponding engineering stress-strain curve is between the yield and ultimate stress.

$$\sigma_t = K\varepsilon_t^n \quad \text{Eq. 3.7}$$

3.4.2 Experimental-numerical iterative method

Comparing the test results of the base metal and butt-welded tensile coupons, the Young's modulus of the butt-welded tensile coupons was not obviously affected by welding. Therefore, the Young's modulus of HAZ were taken as the Young's modulus derived from the stress-strain curves of the butt-welded tensile coupons. The plastic stage refers to the part of engineering stress-strain curve which exceeds the yield strength but ends at the ultimate strength. The true stress-strain curves of this stage for HAZ cannot be directly obtained from the engineering stress-strain curves of the butt-welded tensile coupons.

This investigation adapted an experimental-numerical iterative method to obtain the true stress-strain curves of HAZ for all the tested butt-welded coupons (Tu et al., 2019). It assumed that Hollomon model could be used to describe the true stress-strain relationship for HAZ in the plastic stage. The general finite element software ABAQUS was used to do numerical analysis for the butt-welded tensile coupons. The thickness of the numerical model was in accordance with the geometry of the physical entity. The gauge length was 50 mm for the numerical model. The Dynamic Explicit analysis was chosen to calculate the tensile coupon test. As shown in Figure 3.41, one end of the coupon was completely fixed in the model, and the other end was coupled to a reference point which was displacement-loaded in tension. Furthermore, the smooth step was utilised to exert the displacement load. An 8-node linear solid element with reduced integration (C3D8R) was adapted for the model. The mesh size was set as 2 mm to achieve both accuracy and computing efficiency according to the mesh sensitivity study. The numerical models were divided into WM, HAZ and BM three homogeneous regions. The widths of three regions were in accordance with the hardness results. The material properties of BM were set according to the base metal tensile coupon tests. The average hardness ratio of WM and HAZ was close to unity according to the hardness test results, therefore, the material properties of WM were assumed to be the same as that of HAZ. Four parameters needed to be determined for HAZ by utilising the Hollomon model, which were $f_{\text{True, y, HAZ}}$, $f_{\text{True, u, HAZ}}$, K_{HAZ} and n_{HAZ}, where $f_{\text{True, y, HAZ}}$ is the true stress of HAZ corresponding to the engineering yield stress, $f_{\text{True, u, HAZ}}$ is the true stress of HAZ corresponding to the engineering ultimate stress, K_{HAZ} is the strength coefficient of HAZ and n_{HAZ} is the strain hardening exponent of HAZ. $f_{\text{True, y, Butt}}$ and $f_{\text{True, u, Butt}}$ were taken as the initial values for $f_{\text{True, y, HAZ}}$ and $f_{\text{True, u, HAZ}}$. The initial value of strength coefficient K_{HAZ} was calculated by Eq. 3.8, where $H_{\text{HAZ}}/H_{\text{BM}}$ was the ratio of average hardness of HAZ and BM, K_{BM} was the average strength coefficient of BM. The initial strain hardening exponent n_{HAZ} was taken the same as that of BM, since

the strain hardening exponent between different steels did not vary significantly (Wang and Li, 2022, Ran et al., 2019).

$$K_{HAZ} = \frac{H_{HAZ}}{H_{BM}} \times K_{BM} \qquad \text{Eq. 3.8}$$

During the iterative process of numerical simulations, four parameters were adjusted as follows. $f_{\text{True, u, HAZ}}$ remained unchanged, because the butt-welded coupons fractured at HAZ or other regions. If the fracture location was HAZ, $f_{\text{True, u, HAZ}}$ could be represented by $f_{\text{True, u, Butt}}$ and there was no need to adjust it; if the fracture location was not HAZ, taking $f_{\text{True, u, Butt}}$ as $f_{\text{True, u, HAZ}}$ was safe as it underestimated $f_{\text{True, u, HAZ}}$. If the numerical stress-strain curves of butt-welded coupons differed from the experimental counterparts, K_{HAZ} was adjusted accordingly. Increasing K_{HAZ} could enhance the stress-strain curves. However, K_{HAZ} should not exceed the corresponding K_{BM} if HAZ was degraded compared to BM, which could be decided according to average hardness results. As for the strain hardening exponent n_{HAZ}, increasing it could weaken the stress-strain curves while decreasing it could enhance the stress-strain curves. $f_{\text{True, y, HAZ}}$ could only be reduced if HAZ was degraded compared to BM, which could be decided according to average hardness results. By adjusting the value of $f_{\text{True,y,HAZ}}$, K_{HAZ} and n_{HAZ}, the engineering stress-strain curves obtained from the numerical model gradually converged to the results obtained from the butt-welded tensile coupons, thus the best values of these parameters for the HAZ leading to the most fitted engineering stress-strain curves obtained from the FE model. For each iteration only one parameter was adjusted, and following sequence was adapted during several rounds of iterations: K_{HAZ}, n_{HAZ}, and finally $f_{\text{True, y, HAZ}}$. The iteration was finished when the numerical stress-strain curves were in good agreement with the experimental ones for the butt-welded tensile coupons.

Figure 3.42 to Figure 3.44 shows the comparisons between experimental and numerical

stress-strain curves for the butt-welded tensile coupons. The Hollomon model is used to describe the true stress-strain curves between yielding and necking. In this study, for the post-necking stage, no true stress-strain relationship was selected. The simulated stress-strain curves agreed well with tested engineering stress-strain curves before necking. After the ultimate stress, the deviation between FE and Test results became significant. Besides, the Hollomon model was proposed in 1945, when the high strength steel was not fabricated. For high strength steel like Q960, the effect of this model to describe the rounded region was not as satisfactory as Q460 and Q690, as illustrated in Figure 3.44. It can be concluded that by adapting the experimental-numerical iterative method, the material properties of HAZ, including $f_{\text{True, y, HAZ}}$, $f_{\text{True, u, HAZ}}$, K_{HAZ} and n_{HAZ} under various heat inputs and steel grades, could be obtained, as listed in Table 3.10. The calibration results of Q690-B6-M-1, Q690-B6-M-2, Q960-B6-M-1 and Q960-B6-M-2 were removed from Table 3.10 because these coupons had porosity in welds, which was observed from the fracture locations, as shown in Figure 3.45. Besides, the ratio $n_{\text{HAZ}}/n_{\text{BM}}$ was quite close to unity for all the specimens, which means that regardless of steel grade, heat input had little effect on the strain hardening exponent for HAZ. The data shown in Table 3.10 was used for the development of regression models which considered the influence of both steel grades and heat inputs.

3.5 Proposed material models for HAZ with different yield strengths and heat inputs

The true stress-strain relationship of steel material is of vital importance in describing the material behaviour for FE modelling. By referring to the engineering stress-strain curve, true stress-strain curve can be divided into three stages: elastic, plastic, and post-necking stage. Currently, there is a lack of material models which can describe the true stress-strain relationships for the HAZ in steel considering various yield strengths and heat inputs. In this section, based on the calibration results of HAZ material properties, regression models were developed for $f_{\text{True, y, HAZ}}$, $f_{\text{True, u, HAZ}}$ and K_{HAZ} incorporating the

influence of yield strengths and heat inputs. n_{HAZ}, however, was not significantly affected by heat input. Therefore, n_{HAZ} was set equal to n_{BM}. Combining the regression models with the Hollomon model, the plastic stage (from yielding to necking by referring to the engineering stress-strain curve) of the trues stress-strain curves for HAZ could be obtained.

3.5.1 Polynomial regression models considering BM strengths and heat inputs

The regression models developed relationships between HAZ material properties and two independent variables, which were the yield strength of BM and the heat input. The HAZ material properties included $f_{True,\ y,\ HAZ}$, $f_{True,\ u,\ HAZ}$ and K_{HAZ}. In this study, the HAZ material properties $f_{True,\ y,\ HAZ}$, $f_{True,\ u,\ HAZ}$ and K_{HAZ} were normalised by corresponding BM material properties $f_{True,\ y,\ BM}$, $f_{True,\ u,\ BM}$ and K_{BM}, respectively. Hence, the dependent variables of regression models were $f_{True,\ y,\ HAZ}/f_{True,\ y,\ BM}$, $f_{True,\ u,\ HAZ}/f_{True,\ u,\ BM}$ and K_{HAZ}/K_{BM}.

The polynomial regression analysis which can be treated as the linear regression analysis was adapted. The Ordinary Least Squares (OLS) method was utilised to fit the regression model. The minimum mean squared error between the test results and model predicted values was the goal of the regression analysis.

The database for the regression analysis to calculate $f_{True,\ y,\ HAZ}/f_{True,\ y,\ BM}$, $f_{True,\ u,\ HAZ}/f_{True,\ u,\ BM}$ and K_{HAZ}/K_{BM} included all the calibration results of HAZ, as listed in Table 3.10. Besides, the base metal material properties, whose $f_{True,\ y,\ HAZ}/f_{True,\ y,\ BM}$, $f_{True,\ u,\ HAZ}/f_{True,\ u,\ BM}$ and K_{HAZ}/K_{BM} were all one, were also included into the database with heat input equal to 0 kJ/mm. The regression models took the yield strengths of BM and heat inputs as the independent variables. The degrees of the polynomial regressions were set as 2, as overfitting would occur if the degree was 3 or larger. Besides, if the degree was set as 3 for the regression model whose independent variable was $f_{True,\ y,\ HAZ}/f_{True,\ y,\ BM}$,

the output for $f_{\text{True, y, HAZ}}/f_{\text{True, y, BM}}$ could be greater than unity in some ranges of heat inputs and yield strengths, as shown in Figure 3.46. To obtain a safer prediction for $f_{\text{True, y, HAZ}}$, the degree was set as 2.

Table 3.11 demonstrates the coefficients of determination for the quadratic polynomial regression in this study. It can be observed that when degree was 2, the R^2 indicated a good regression. Therefore, the quadratic polynomial model was applicable to describe the relationships between independent variables and dependent variables in the form of Eq. 3.9, where x represented the actual engineering yield strength, y represented the heat input, α_i represented the coefficients to be determined by regression analysis, $f(x, y)$ represented the ratios between the HAZ and BMs.

$$f(x,y) = \alpha_1 x^2 + \alpha_2 xy + \alpha_3 y^2 + \alpha_4 x + \alpha_5 y + \alpha_6 \quad \text{Eq. 3.9}$$

The obtained relationships between $f_{\text{True, y, HAZ}}/f_{\text{True, y, BM}}$ and independent variables were expressed in Eq. 3.10, where z_1 represented $f_{\text{True, y, HAZ}}/f_{\text{True, y, BM}}$. The obtained relationships between $f_{\text{True, u, HAZ}}/f_{\text{True, u, BM}}$ and independent variables were expressed in Eq. 3.11, where z_2 represented $f_{\text{True, u, HAZ}}/f_{\text{True, u, BM}}$. The obtained relationships between $K_{\text{HAZ}}/K_{\text{BM}}$ and independent variables were expressed in Eq. 3.12, where z_3 represented $K_{\text{HAZ}}/K_{\text{BM}}$. The curved surfaces for three obtained regression models were given in Figure 3.47. It can be observed that the characteristics of the surfaces were in accordance with the trends illustrated by the calibration results.

$$z_1 = 8.740 \times 10^{-7} x^2 - 2.349 \times 10^{-4} xy - 3.418 \times 10^{-2} y^2 - 1.422 \times 10^{-3} x + 8.299 \times 10^{-2} y + 1.537 \quad \text{Eq. 3.10}$$

$$z_2 = -4.344 \times 10^{-7}x^2 - 1.244 \times 10^{-4}xy - 2.653 \times 10^{-2}y^2 + 6.543 \times 10^{-4}x + 9.681 \times 10^{-2}y + 0.770$$

Eq. 3.11

$$z_3 = 7.300 \times 10^{-8}x^2 - 1.223 \times 10^{-4}xy - 1.952 \times 10^{-2}y^2 - 9.219 \times 10^{-5}x + 9.041 \times 10^{-2}y + 1.025$$

Eq. 3.12

By combining the regression models and the Hollomon model, the true stress-strain curve from yielding to necking for the HAZ with specific yield strengths of BM and heat input can be obtained. Firstly, the material properties including $f_{\text{True, y, BM}}$, $f_{\text{True, u, BM}}$, K_{BM} and n_{BM} for BM were obtained from tensile coupon tests, where $f_{\text{True, y, BM}}$ was the true yield stress of BM, $f_{\text{True, u, BM}}$ was the true ultimate stress of BM, K_{BM} was the strength coefficient of BM, and n_{BM} was the strain hardening exponent of BM. Then, based on the regression models, the ratios of $f_{\text{True, y, HAZ}}/f_{\text{True, y, BM}}$, $f_{\text{True, u, HAZ}}/f_{\text{True, u, BM}}$, and $K_{\text{HAZ}}/K_{\text{BM}}$ were calculated under certain heat input and yield strength, where $f_{\text{True, y, HAZ}}$, $f_{\text{True, u, HAZ}}$, and K_{HAZ} were the true yield stress, true ultimate stress, and strength coefficient of HAZ, respectively. Particularly, the strain hardening exponent n_{HAZ} was set as n_{BM}, since heat input had neglectable effect on n_{HAZ}. The material properties of HAZ were acquired, and the true strains corresponding to $f_{\text{True, y, HAZ}}$, $f_{\text{True, u, HAZ}}$ could be calculated by the Hollomon model. At last, the true stress-strain curves from yielding to necking for HAZ could be obtained.

3.5.1.1 Simulation of three butt-welded tensile coupon tests from HUST

Three butt-welded tensile coupon tests were done at Huazhong University of Science and Technology. This section validated the proposed HAZ material models by simulating these tests. Three butt-welded tensile coupons were 690-6-G2-1, 960-6-G1-2, and 690-10-G1-2. The nomenclature was illustrated as follows: for example, in 690-

6-G2-1, “690” denoted the steel grade was Q690; “6” denoted the nominal plate thickness was 6 mm; “G2” denoted the heat input; “1” denoted that it was the first specimen in the test group “690-6-G2”. The dimensions of these coupons were given by Figure 3.48. The gauge length for 690-6-G2-1 and 960-6-G1-2 was 50 mm. The gauge length for 690-10-G1-2 was 100 mm. Table 3.12 showcases the welding parameters for these butt-welded tensile coupons.

The material properties of the BM corresponding to these butt-welded joints were given by Table 3.13. 690-6, 960-6 and 690-10 were parent metal for 690-6-G2-1, 960-6-G1-2, and 690-10-G1-2, respectively. The HAZ material properties were calculated by the proposed material models. Specifically, $f_{\text{True, y, HAZ}}/ f_{\text{True, y, BM}}$, $f_{\text{True, u, HAZ}}/ f_{\text{True, u, BM}}$ and $K_{\text{HAZ}}/ K_{\text{BM}}$ were calculated based on the regression models. Then, $f_{\text{True, y, HAZ}}$, $f_{\text{True, u, HAZ}}$, and K_{HAZ} were obtained. The true stress-strain relationship for the HAZ was finally calculated by adapting the Hollomon model, as shown in Figure 3.49.

The HAZ widths were calculated based on the linear regression models between heat inputs and HAZ widths, as shown in Eq. 3.1 to Eq. 3.3. The calculated results are listed in Table 3.14. The general finite element software ABAQUS was utilised to do numerical simulations. The Dynamic Explicit solver was chosen. An 8-node linear solid element with reduced integration (C3D8R) was adapted for the model. The mesh size was set as 2 mm to achieve both accuracy and computing efficiency according to the mesh sensitivity study. WM and HAZ were set as a homogeneous region, and the obtained HAZ material properties were input.

The comparisons between experimental and numerical results were shown in Figure 3.50 and Table 3.15. Figure 3.50 shows that the elastic stage between experimental and numerical stress-strain curves were in good agreement with each other. For the plastic stage, however, the numerical models overestimated the stresses. Specifically, the yield

stress f_y given by numerical analysis was at least 10% larger than f_y given by experiments. In contrast, for the ultimate stress f_u, the numerical results were close to experimental results, varying within 3.0 %. It can be concluded that the proposed HAZ material model was applicable to be used for butt-welded joints, especially for the ultimate strength prediction.

3.5.1.2 Simulation of butt-welded joint tensile coupon tests from Chen (Chen, 2019)

Chen (Chen, 2019) conducted a batch of butt-welded tensile coupon tests made of Q690 steel. This section validated the proposed HAZ material properties by simulating 690-BJ16-3.2. In "690-BJ16-3.2", "690" denoted the steel grade was Q690; "BJ16" denoted the nominal thickness of the butt joint was 16 mm; "3.2" denoted the electrode diameter was 3.2 mm. The dimensions of the tensile coupon were shown in Figure 3.51. The gauge length for this coupon was 50 mm. Multi-pass welding was implemented for this specimen, and the average heat input was 1.14 kJ/mm. Table 3.16 gives the BM material properties. The HAZ material properties were calculated by the proposed material models, and the true stress-strain relationship for HAZ of Q690 was shown in Figure 3.52.

Due to the symmetry of the butt joint, the hardness distribution was demonstrated for half of the butt joint test block in Figure 3.53. The average HAZ width was obtained from the hardness distribution and it was 5.28 mm. The details of the numerical simulation were the same as in the last section.

Figure 3.54 and Table 3.17 show the comparison between experimental and numerical stress-strain curves for 690-BJ16-3.2. It can be observed that both the stress-strain curves had similar shapes. The difference between the yield stress f_y was greater than 10 %, while for the ultimate stress f_u the difference was less than 7%. Therefore, the proposed HAZ material model could be a useful tool to provide material properties for HAZ under certain

heat input and with specific yield strength.

3.5.2 Linear regression models considering only heat inputs

In the polynomial regression models for the HAZ material properties presented above, there were two independent variables, including the yield strength of BM and the heat input. The polynomial models predicted the true stresses corresponding to the engineering yield stress and ultimate stress, respectively. But for the true strain, the polynomial models adapted the Hollomon model to describe it. In the linear regression models presented in this section, in contrast, only one variable, heat input, was considered. For each steel grade Q460, Q690 and Q960, the relationships between the heat input and the normalised dependent variables, including $f_{\text{True, y, HAZ}}/ f_{\text{True, y, BM}}$ and $f_{\text{True, u, HAZ}}/ f_{\text{True, u, BM}}$, were developed. The true strain of the HAZ was taken as that of the BM. Besides, a plastic true strain-based regression was adapted to give the HAZ true stresses between $f_{\text{True, y, HAZ}}$ and $f_{\text{True, u, HAZ}}$ instead of using the Hollomon model.

The linear regression model was fitted by the Ordinary Least Squares (OLS) method, which aimed to obtain the minimum mean squared error between the test results and model predicted values. All the calibrated $f_{\text{True, y, HAZ}}$ and $f_{\text{True, u, HAZ}}$ in Table 3.10 were included into the database. Besides, the base metal material properties, whose $f_{\text{True, y, HAZ}}/ f_{\text{True, y, BM}}$, $f_{\text{True, u, HAZ}}/ f_{\text{True, u, BM}}$ and $K_{\text{HAZ}}/ K_{\text{BM}}$ were all one, were also included into the database with the heat input equal to 0 kJ/mm.

Figure 3.55 shows the linear regression models for the $f_{\text{True, y, HAZ}}/ f_{\text{True, y, BM}}$ and $f_{\text{True, u, HAZ}}/ f_{\text{True, u}}$ varying with the heat inputs for each steel. The equations for these models corresponding to different steel grades were expressed by Eq. 3.13 to Eq. 3.18 respectively, where Q represented the heat input in kJ/mm.

For Q460,

$$\frac{f_{True,y,HAZ}}{f_{True,y,BM}} = -0.0762Q + 1.0891 \quad \text{Eq. 3.13}$$

$$\frac{f_{True,u,HAZ}}{f_{True,u,BM}} = -0.0171Q + 1.0001 \quad \text{Eq. 3.14}$$

For Q690,

$$\frac{f_{True,y,HAZ}}{f_{True,y,BM}} = -0.1817Q + 1.0183 \quad \text{Eq. 3.15}$$

$$\frac{f_{True,u,HAZ}}{f_{True,u,BM}} = -0.0281Q + 1.0065 \quad \text{Eq. 3.16}$$

For Q960,

$$\frac{f_{True,y,HAZ}}{f_{True,y,BM}} = -0.1944Q + 0.976 \quad \text{Eq. 3.17}$$

$$\frac{f_{True,u,HAZ}}{f_{True,u,BM}} = -0.084Q + 1.0277 \quad \text{Eq. 3.18}$$

The true stress-strain curve corresponding to the engineering yield and ultimate stress-strain curve was obtained by following procedure. Based on the BM engineering stress-strain curve, $f_{\text{True, y, BM}}$ and $f_{\text{True, u, BM}}$ can be calculated. Different from previous polynomial regression model, this linear model did not incorporate the influence of yield stress. Therefore, these linear models are only applicable to the HAZ whose steel grade is Q460, Q690 and Q960. The ratios of $f_{\text{True, y, HAZ}}/f_{\text{True, y, BM}}$ and $f_{\text{True, u, HAZ}}/f_{\text{True, u, BM}}$ can be calculated by these linear models incorporating the heat input, thus the $f_{\text{True, y, HAZ}}$ and $f_{\text{True, u, HAZ}}$ can be obtained. For the values of $f_{\text{True, HAZ}}$ between $f_{\text{True, y, HAZ}}$ and $f_{\text{True, u, HAZ}}$, they were calculated by Eq. 3.19, where $f_{\text{True, BM}}$ represented the corresponding values in the BM true stress-strain curve and C represented the reduction factor. The reduction factor C can be calculated by the linear interpolation based on $f_{\text{True, y, HAZ}}/f_{\text{True, y, BM}}$ and $f_{\text{True, u, HAZ}}/f_{\text{True, u, BM}}$ which takes the true plastic strain of BM as the weight, considering that the HAZ material deterioration was related to the plastic

deformation represented by the true plastic strain. Finally, the true stress-strain curves for the HAZ with specific heat input can be obtained.

$$f_{True,HAZ} = C \times f_{True,BM} \quad \text{Eq. 3.19}$$

3.5.2.1 Simulation of three butt-welded tensile coupon tests from HUST

The test results already introduced in Section 4.1.2 were again utilised here to validate the linear regression models. Most numerical model information related to the three butt-welded tensile coupons is the same as section 4.1.2. However, it should be emphasised that the HAZ material properties were obtained differently. The true stress-strain relationship for the HAZ was shown in Figure 3.56.

The comparisons between experimental and numerical results were given in Figure 3.57 and Table 3.18. Figure 3.57 demonstrated that the elastic and hardening stage before necking between experimental and numerical stress-strain curves were in good agreement. Both the yield stress f_y and ultimate stress f_u obtained from numerical analysis were almost within 5% deviation from the values from experiments. It can be concluded that the proposed HAZ material model was applicable to be used for butt-welded joints.

3.5.2.2 Simulation of butt-welded joint tensile coupon tests from Chen (Chen, 2019)

The test results illustrated in Section 4.1.3 were adapted here to validate the linear regression models. The numerical model information was the same as listed in Section 4.1.3. The HAZ material properties here were calculated based on the linear regression models. The true stress-strain relationship for the HAZ was shown in Figure 3.58.

Figure 3.59 and Table 3.19 demonstrated the comparison between experimental and numerical results. It can be found that the elastic and part of plastic stage of the stress-

strain curves overlapped with each other. The difference between the yield stress f_y was less than 2% and the difference between ultimate stress f_u were within 7.5%. In conclusion, the proposed linear regression model was applicable to provide material properties for HAZ under certain heat input.

3.6 Summary

This chapter investigated the mechanical behaviours of the HSS butt-welded joints made of different steel grades and heat inputs. Tensile coupons cut from the butt-welded joints were used to conduct tensile tests. The stress-strain curves were obtained and typical material properties like Young's Modulus (E), yield stress (f_y), ultimate stress (f_u), ultimate strain (ε_u), fracture strain (ε_f) and elongation at fracture were carefully examined to observe the influence of heat inputs and steel grades. Test blocks were also cut from the butt-welded joints to acquire the hardness distributions at different plate depths. Based on the test results of the butt-welded tensile coupons, corresponding HAZ material properties were obtained based on an iterative experimental-numerical method. Two kinds of regression models including polynomial regression model and linear regression model were used to obtain the HAZ material properties. These two models were validated against the butt-welded tensile coupon tests implemented by other researchers.

The butt-welded tensile coupons fractured at several locations: BM, HAZ/BM interface, HAZ and WM. A tendency was observed that the fracture locations moved from the BM of the Q460, to the HAZ/BM interface of the Q690 and to the HAZ of the Q960 butt-welded tensile coupons as the steel grades increased from Q460 to Q960. It indicated that the influence of welding on the fracture initiation and damage evolution of the butt-welded joints got more significant for higher strength steels. According to the test results, generally, as the heat inputs increased, $f_{y,\,Butt}$ decreased significantly for all the butt-welded tensile coupons. For $f_{u,\,Butt}$, however, only for the Q960 butt-welded

tensile coupons there showed a significant reduction while for the Q460 and Q690 butt-welded tensile coupons $f_{u,\,Butt}$ remained almost unchanged. It was interesting to find that ε_u and elongation at fracture showed a parabolic correlation with the heat inputs. Another indicator of ductility, f_u/f_y, was above 1.2 for almost all the butt-welded tensile coupons, conforming to the requirements that this ratio was recommended greater than 1.10, as listed in EN 1993-1-1 (CEN, 2005b). In addition, as the steel grades increased, the strength reduction of $f_{y,Butt}$ caused by welding deteriorated under the same heat inputs. Similarly, the deformation characteristics of higher steel grades, represented by ε_u and elongation at fracture, deteriorated more significantly under the same heat inputs.

The widths of WM and HAZ were calculated combining the hardness distributions and etching results. It was found that increasing the heat input could enlarge the HAZ widths for all steel grades in this investigation, and high steel grade exhibited a larger influence. Corresponding linear regression models were developed to predict the HAZ width under specific heat input. There were also differences between steel grades. Increasing heat input could lead to the increase of HAZ average hardness for Q460 while lead to the decrease of HAZ average hardness for Q690 and Q960. Besides, the HAZ consisted of hardened zones and softened zones. For Q460 butt-welded joint, the hardness of the hardened regions was greater than the BM hardness. But for Q690 and Q960 butt-welded joint, the hardness of the hardened part was slightly larger or close to the BM hardness. These differences could be attributed to different manufacturing methods for Q460, Q690 and Q960.

The test results were for butt-welded tensile coupons. To obtain the true stress-strain curves of the HAZ, an iterative experimental-numerical method combining with the Hollomon model was implemented. The HAZ material properties obtained from the method included $f_{True,\,y,\,HAZ}$, $f_{True,\,u,\,HAZ}$, K_{HAZ} and n_{HAZ}. Apart from n_{HAZ} which was taken as n_{BM}, $f_{True,\,y,\,HAZ}$, $f_{True,\,u,\,HAZ}$, and K_{HAZ} were calibrated by trial and errors until the

engineering stress-strain curves obtained from the numerical model converged to the results obtained from the butt-welded tensile coupons. The comparisons between the experimental and numerical stress-strain curves agreed well before necking, demonstrating that by adapting the experimental-numerical iterative method, the material properties of HAZ, including $f_{\text{True, y, HAZ}}$, $f_{\text{True, u, HAZ}}$, K_{HAZ} and n_{HAZ} under various heat inputs and steel grades, could be obtained.

Based on the calibration results of HAZ material properties, two regression models were developed for $f_{\text{True, y, HAZ}}$, $f_{\text{True, u, HAZ}}$ and K_{HAZ}, one was polynomial regression model, the other was linear regression model. For the polynomial regression model, the HAZ material properties were dependent on the BM yield strength and heat input. For the linear regression model, the only independent variable was heat input for the HAZ material properties. Both regression models were obtained by the Ordinary Least Squares (OLS) method. And they were validated against HSS butt-welded tensile coupon tests by other researchers. The validation results exhibited that both regression models can be used to determine the HAZ material properties.

Table 3.1 Nominal chemical compositions of base material (%)

	Nominal thickness (mm)	C	Si	Mn	P	S	V	Nb	Ti	Cr	Ni	Cu	Mo	Al	N	B	CEV
Q460	6	0.17	0.12	1.63	0.013	0.006	0.002	0.012	0.001	0.03	0.02	0.02	-	-	-	0.0003	0.45
Q690	6	0.08	0.24	1.79	0.015	0.009	0.001	0.01	0.001	0.04	0.02	0.01	-	-	-	0.0004	0.39
Q960	6	0.18	0.25	1.03	0.006	0.001	0.043	0.023	0.013	0.35	0.02	0.02	0.46	-	-	0.0015	0.52

Table 3.2 The tested average material properties

Specimen	E (MPa)	f_y (MPa)	f_u (MPa)	f_u/f_y	ε_y (%)	ε_u (%)	$\varepsilon_u/\varepsilon_y$	ε_f (%)
460-T6-1	187850	428.41	615.04	1.44	0.23	7.88	34.53	14.64
460-T6-2	208060	445.25	625.85	1.41	0.21	8.18	38.22	18.81
460-T6-3	196520	442.50	626.69	1.42	0.23	8.72	38.74	18.73
Average	197477	438.72	622.53	1.42	0.22	8.26	37.17	17.39
690-T6-1	198270	731.10	762.56	1.04	0.37	6.06	16.45	12.66
690-T6-2	190090	726.85	758.04	1.04	0.38	6.61	17.29	13.85
690-T6-3	193100	734.77	765.05	1.04	0.38	6.72	17.65	14.54
Average	193820	730.91	761.88	1.04	0.38	6.46	17.14	13.68
960-T6-1	214800	949.96	997.81	1.05	0.44	7.41	16.75	14.95
960-T6-2	209160	947.12	999.76	1.06	0.45	5.88	12.99	13.51
960-T6-3	194290	963.57	1010.26	1.05	0.50	5.39	10.87	12.46
Average	206083	953.55	1002.61	1.05	0.46	6.23	13.46	13.64

Table 3.3 Butt-welded joint groups

Specimen	Steel grade	Heat input (kJ/mm)
Q460-B6-M	Q460	0.968
Q460-B6-H1	Q460	1.263
Q460-B6-H2	Q460	1.631

Q460-B6-H3	Q460	1.752
Q690-B6-M	Q690	0.966
Q690-B6-H1	Q690	1.257
Q690-B6-H2	Q690	1.645
Q690-B6-H3	Q690	1.823
Q960-B6-M	Q960	0.995
Q960-B6-H1	Q960	1.222
Q960-B6-H2	Q960	1.592
Q960-B6-H3	Q960	1.864

Table 3.4 The average measured width and thickness of the butt-welded tensile coupons

Label of specimens	true average width (mm)	true average thickness (mm)	Label of specimens	true average width (mm)	true average thickness (mm)
Q460-B6-M-1	12.51	6.12	Q690-B6-H2-1	12.54	5.91
Q460-B6-M-2	12.60	6.14	Q690-B6-H2-2	12.44	5.85
Q460-B6-M-3	12.45	6.19	Q690-B6-H3-1	12.60	5.90
Q460-B6-H1-1	12.55	6.23	Q690-B6-H3-2	12.57	5.95
Q460-B6-H1-2	12.53	6.15	Q690-B6-H3-3	12.38	5.92
Q460-B6-H1-3	12.41	6.25	Q960-B6-M-1	12.51	6.79
Q460-B6-H2-1	12.50	6.13	Q960-B6-M-2	12.44	6.72
Q460-B6-H2-2	12.51	6.20	Q960-B6-M-3	12.40	6.82
Q460-B6-H2-3	12.40	6.24	Q960-B6-H1-1	12.74	6.76

Q460-B6-H3-1	12.61	6.20	Q960-B6-H1-2	12.69	6.73
Q460-B6-H3-2	12.39	6.29	Q960-B6-H1-3	12.39	6.84
Q460-B6-H3-3	12.29	6.23	Q960-B6-H2-1	12.53	6.67
Q690-B6-M-1	12.53	5.90	Q960-B6-H2-2	12.66	6.71
Q690-B6-M-2	12.45	5.95	Q960-B6-H2-3	12.43	6.68
Q690-B6-M-3	12.39	5.93	Q960-B6-H3-1	12.52	6.71
Q690-B6-H1-1	12.54	6.00	Q960-B6-H3-2	12.63	6.74
Q690-B6-H1-2	12.48	5.95	Q960-B6-H3-3	12.36	6.70
Q690-B6-H1-3	12.44	5.97			

Table 3.5 Filler electrodes for butt-welded joints

Steel grade	Filler electrode	Yield strength (MPa)	Ultimate strength (MPa)
Q460	AWS A5.28 ER 80S-G	N/A	550
Q690	AWS A5.28 ER 110S-G	N/A	760
Q960	AWS A5.28 ER 120S-G	N/A	830

Table 3.6 Welding parameters with different heat inputs

Heat input type	Q (kJ/mm)	current (I)	voltage (V)	speed (mm/min)
Medium (M)	0.973	190	16	150
High heat input 1 (H1)	1.234	200	18	140
High heat input 2 (H2)	1.546	210	23	150
High heat input 3 (H3)	1.760	220	25	150

Table 3.7 Material properties for butt-welded tensile coupons

Specimen	fracture location	E (MPa)	f_y(MPa)	f_u (MPa)	ε_u (%)	ε_f (%)	elongation at fracture (%)

Q460-B6-M-1	WM	191200	474.52	608.46	8.16	13.30	14.58%
Q460-B6-M-2	WM	192370	479.35	611.47	7.41	10.61	11.29%
Q460-B6-M-3	WM	182570	478.62	618.38	7.46	11.08	12.99%
Q460-B6-H1-1	BM	204430	474.84	607.87	8.21	16.51	19.04%
Q460-B6-H1-2	BM	198630	437.64	604.28	9.03	16.52	16.49%
Q460-B6-H1-3	BM	192760	477.50	619.26	8.43	17.18	18.57%
Q460-B6-H2-1	BM	210560	379.40	609.40	8.57	17.47	18.74%
Q460-B6-H2-2	BM	197110	402.07	612.35	8.15	17.02	19.01%
Q460-B6-H2-3		217740	422.05	614.80	8.09	18.16	18.45%
Q460-B6-H3-1	WM	205810	435.70	592.44	6.74	12.70	13.44%
Q460-B6-H3-2		216230	467.08	609.55	9.70	18.21	19.56%
Q460-B6-H3-3		211990	456.88	598.43	6.56	11.14	11.30%
Q690-B6-M-1	HAZ	214380	600.87	743.95	2.40	5.41	5.54%
Q690-B6-M-2	WM	191730	594.83	721.55	2.53	6.08	6.84%
Q690-B6-M-3		219840	651.40	757.45	4.30	9.99	13.93%
Q690-B6-H1-1	HAZ/BM interface	228980	612.66	756.58	4.99	11.21	11.11%
Q690-B6-H1-2	HAZ/BM interface	204790	613.44	766.97	4.58	10.58	10.99%
Q690-B6-H1-3	HAZ/BM interface	202280	626.91	757.03	4.92	10.22	11.83%
Q690-B6-H2-1	HAZ/BM interface	215800	578.40	738.58	4.53	7.91	9.70%
Q690-B6-H2-2	HAZ/BM interface	201890	580.38	738.70	4.78	8.41	8.80%

Q690-B6-H3-1	HAZ/BM interface	217170	491.57	728.36	5.42	9.01	9.62%
Q690-B6-H3-2	HAZ/BM interface	239030	510.04	731.81	5.28	8.94	10.26%
Q690-B6-H3-3	HAZ/BM interface	208710	525.39	737.72	5.81	10.09	11.18%
Q960-B6-M-1	WM	208460	749.51	912.65	1.34	1.96	1.99%
Q960-B6-M-2	WM	192370	729.53	883.05	1.27	1.36	2.30%
Q960-B6-M-3		210030	724.49	960.85	3.38	4.24	4.54%
Q960-B6-H1-1	HAZ	213880	720.38	964.86	4.21	5.93	6.91%
Q960-B6-H1-2	HAZ	224090	724.37	970.72	4.49	6.91	7.50%
Q960-B6-H1-3	HAZ	195080	842.68	973.41	4.14	5.34	5.96%
Q960-B6-H2-1	HAZ	225000	588.88	939.61	4.35	12.30	13.72%
Q960-B6-H2-2	HAZ	218530	612.30	938.95	4.06	10.13	9.69%
Q960-B6-H2-3	the fracture surface crossed HAZ and WM	195170	619.95	921.18	3.72	11.76	12.52%
Q960-B6-H3-1	WM	223170	713.08	873.33	3.45	10.94	11.35%
Q960-B6-H3-2	the fracture surface crossed HAZ and WM	215460	639.08	861.11	3.66	10.58	10.67%
Q960-B6-H3-3	WM	203740	642.31	863.31	3.52	11.11	11.16%

Table 3.8 Measured WM and calculated HAZ widths at three levels of depths

Specimen	Width of WM at 1.5 mm	Width of WM at 3.0 mm	Width of WM at 4.5 mm	Average WM width	Calculated HAZ widths at 1.5 mm	Calculated HAZ widths at 3.0 mm	Calculated HAZ widths at 4.5 mm	Average HAZ widths
-	mm	mm	mm	mm	mm	mm	mm	mm
Q460-B6-M	7.2	4.56	5.49	5.75	6.9	8.72	7.255	7.63
Q460-B6-H1	8.02	5.32	6.41	6.58	5.99	7.84	7.30	7.04
Q460-B6-H2	11.02	6.61	5.49	7.71	6.99	9.20	9.76	8.65
Q460-B6-H3	11.81	6.49	5.02	7.77	7.60	10.26	10.49	9.45
Q690-B6-M	7.36	5.40	5.70	7.34	6.82	6.30	8.65	7.26
Q690-B6-H1	9.05	5.36	5.75	9.20	7.98	9.32	8.63	8.64
Q690-B6-H2	10.93	7.61	6.57	10.01	7.04	9.70	9.72	8.82
Q690-B6-H3	12.95	7.32	5.76	10.25	10.03	14.84	13.12	12.66
Q960-B6-M	7.59	6.40	7.21	8.00	8.21	7.30	6.40	7.30
Q960-B6-H1	7.93	5.96	5.94	8.05	7.54	8.52	8.03	8.03
Q960-B6-H2	9.70	6.23	4.52	8.69	11.65	13.39	13.74	12.93
Q960-B6-H3	12.29	8.14	5.85	9.77	8.86	10.93	12.08	10.62

Table 3.9 Average hardness of WM, HAZ and BM

Specimen	Heat input	H_{WM}	H_{HAZ}	H_{BM}	H_{HAZ}/H_{BM}	H_{WM}/H_{HAZ}
-	kJ/mm	HV0.5	HV0.5	HV0.5	-	-
Q460-B6-M	0.968	245.471	222.4	216.8	1.026	1.103
Q460-B6-H1	1.263	215.927	227.5	227.0	1.002	0.949
Q460-B6-H2	1.631	233.929	234.2	226.1	1.036	0.999
Q460-B6-H3	1.752	200.752	229.8	225.0	1.021	0.874

Q690-B6-M	0.966	283.467	268.4	281.6	0.953	1.056
Q690-B6-H1	1.257	278.928	266.2	286.4	0.929	1.048
Q690-B6-H2	1.645	267.796	264.6	284.4	0.930	1.012
Q690-B6-H3	1.823	255.599	259.4	291.7	0.889	0.985
Q960-B6-M	0.995	344.671	359.1	370.2	0.970	0.960
Q960-B6-H1	1.222	322.972	339.6	368.1	0.923	0.951
Q960-B6-H2	1.592	292.246	336.0	377.3	0.891	0.870
Q960-B6-H3	1.864	285.706	338.1	379.1	0.892	0.845

Table 3.10 Calibration results of HAZ material properties

				HAZ material properties				
Specimen	$f_{y,BM}$	heat inputs	n_{BM}	$f_{True,y,HAZ}$	$f_{True,u,HAZ}$	K_{HAZ}	n_{HAZ}	n_{HAZ}/n_{BM}
-	MPa	kJ/mm	-	MPa	MPa	-	-	-
Q460-B6-M-1	438.72	0.968	0.141	465.000	658.111	975.000	0.141	1.000
Q460-B6-M-2	438.72	0.968	0.141	481.506	656.754	989.338	0.141	1.000
Q460-B6-M-3	438.72	0.968	0.141	480.830	664.496	1000.000	0.141	1.000
Q460-B6-H1-1	438.72	1.263	0.141	460.000	657.762	966.364	0.141	1.000
Q460-B6-H1-2	438.72	1.263	0.141	420.000	658.840	960.000	0.150	1.064
Q460-B6-H1-3	438.72	1.263	0.141	465.000	671.476	966.364	0.141	1.000
Q460-B6-H2-1	438.72	1.631	0.141	380.000	661.655	970.000	0.145	1.028
Q460-B6-H2-2	438.72	1.631	0.141	380.000	662.282	970.000	0.141	1.000
Q460-B6-H2-3	438.72	1.631	0.141	400.000	664.534	990.000	0.141	1.000
Q460-B6-H3-1	438.72	1.752	0.141	410.000	632.353	960.000	0.145	1.028

Q460-B6-H3-2	438.72	1.752	0.141	450.000	668.705	970.000	0.145	1.028
Q460-B6-H3-3	438.72	1.752	0.141	440.000	637.692	970.000	0.145	1.028
Q690-B6-M-3	730.91	0.966	0.083	620.000	789.993	990.000	0.085	1.028
Q690-B6-H1-1	730.91	1.257	0.083	590.000	794.300	980.000	0.078	0.944
Q690-B6-H1-2	730.91	1.257	0.083	595.000	802.064	980.000	0.077	0.931
Q690-B6-H1-3	730.91	1.257	0.083	600.000	794.246	985.000	0.080	0.968
Q690-B6-H2-1	730.91	1.645	0.083	560.000	772.021	970.000	0.090	0.000
Q690-B6-H2-2	730.91	1.645	0.083	550.000	774.035	980.000	0.087	0.000
Q690-B6-H3-1	730.91	1.823	0.083	470.000	767.822	950.000	0.095	1.149
Q690-B6-H3-2	730.91	1.823	0.083	490.000	770.486	950.000	0.087	1.052
Q690-B6-H3-3	730.91	1.823	0.083	500.000	780.573	960.000	0.087	1.052
Q960-B6-M-3	953.55	0.995	0.066	710.000	993.293	1230.000	0.072	1.091
Q960-B6-H1-1	953.55	1.222	0.066	695.000	1005.506	1200.000	0.066	1.000
Q960-B6-H1-2	953.55	1.222	0.066	700.000	1014.291	1210.000	0.066	1.000
Q960-B6-H1-3	953.55	1.222	0.066	800.000	1013.684	1200.000	0.066	1.000
Q960-B6-H2-1	953.55	1.592	0.066	570.000	980.468	1180.000	0.070	1.061
Q960-B6-H2-2	953.55	1.592	0.066	580.000	977.051	1190.000	0.070	1.061
Q960-B6-H2-3	953.55	1.592	0.066	580.000	955.421	1170.000	0.070	1.061
Q960-B6-H3-1	953.55	1.864	0.066	680.000	903.427	1139.380	0.080	1.212
Q960-B6-H3-2	953.55	1.864	0.066	610.000	892.607	1110.000	0.072	1.091

Q960-B6-H3-3	953.55	1.864	0.066	615.000	893.740	1110.000	0.072	1.091

Table 3.11 Coefficient of determination (R^2) for polynomial regression

	R^2	Adjusted R^2
$f_{True,\ y,\ HAZ}/f_{True,\ y,\ BM}$	0.882	0.856
$f_{True,\ u,\ HAZ}/f_{True,\ u,\ BM}$	0.851	0.818
K_{HAZ}/K_{BM}	0.946	0.934

Table 3.12 Welding parameters for three butt-welded tensile coupons

Specimen	Welding pass	Current (A)	Voltage (V)	Speed (mm/s)	Heat input (kJ/mm)	Average heat input (kJ/mm)
690-6-G2-1	1	235	25.9	4.1	1.26	1.16
	2	247	25.9	5.1	1.06	
960-6-G1-2	1	211	24	3.3	1.3	1.27
	2	218	24	3.6	1.25	
690-10-G1-2	1	218	23.9	3.3	1.34	1.36
	2	218	23.9	3.3	1.34	
	3	221	23.9	3.2	1.41	

Table 3.13 Material properties of BM

Base metal	E (MPa)	f_y (MPa)	f_u (Mpa)	$f_{true,y}$ (MPa)	$f_{true,u}$ (Mpa)	K (MPa)	n
690-6	200259	771.79	809.96	776.17	852.03	977.92	0.04880
960-6	206090	1026.84	1075.49	1034.09	1118.91	1270.90	0.03960
690-10	199770	795.45	835.26	803.49	885.30	1022.60	0.05610

Table 3.14 HAZ widths for butt-welded joints

Specimen	HAZ width (mm)
690-6-G2-1	8.00
960-6-G1-2	8.95
690-10-G1-2	9.02

Table 3.15 Comparisons between experimental and numerical strengths based on polynomial regression model

Specimen	f_y (MPa)	f_u (MPa)
690-6-G2-1	625.76	762.43
Sim-690-6-G2-1-curve1	745.07	782.47
Differences	19.07%	2.63%
960-6-G1-2	828.64	983.14
Sim-960-6-G1-2-curve1	982.98	993.41
Differences	18.63%	1.04%
690-10-G1-2	693.43	795.01
Sim-690-10-G1-2-curve1	758.02	790.07
Differences	9.31%	0.62%

Table 3.16 Q690 BM material properties

Base metal	E (MPa)	f_y (MPa)	f_u (Mpa)	$f_{true,y}$ (MPa)	$f_{true,u}$ (Mpa)	K (MPa)	n
Q690	208900	765.12	850.86	769.48	912.11	1070.5	0.06280

Table 3.17 Comparisons between experimental and numerical strengths

Specimen	f_y (MPa)	f_u (MPa)
690-BJ16-3_2	649.93	772.74
Sim-690-BJ16-3_2-curve1	761.54	823.68
Differences	17.17%	6.59%

Table 3.18 Comparisons between experimental and numerical strengths based on linear regression model

Specimen	f_y (MPa)	f_u (MPa)
690-6-G2-1	625.76	762.43
Sim-690-6-G2-1-curve1	645.36	790.51
Differences (%)	3.13%	3.68%
960-6-G1-2	828.64	983.14
Sim-960-6-G1-2-curve1	805.86	988.46
Differences (%)	2.75%	0.54%
690-10-G1-2	693.43	795.01
Sim-690-10-G1-2-curve1	643.48	810.59
Differences (%)	7.20%	1.96%

Table 3.19 Comparisons between experimental and numerical strengths based on linear regression model

Specimen	f_y (MPa)	f_u (MPa)
690-6-G2-1	649.93	772.74
Sim-690-6-G2-1-curve1	667.01	828.50
Differences (%)	2.63%	7.22%

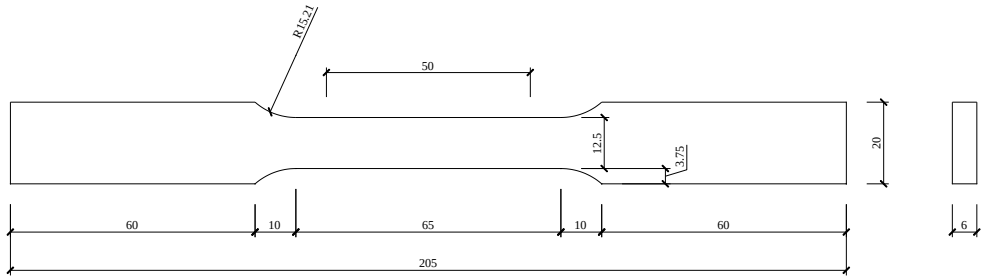

Figure 3.1 Tensile coupon configurations for all steel grades (mm)

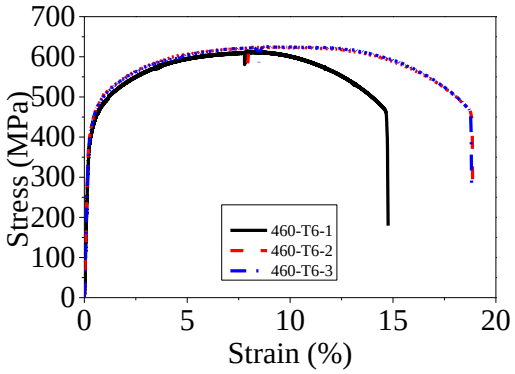

(a) Q460

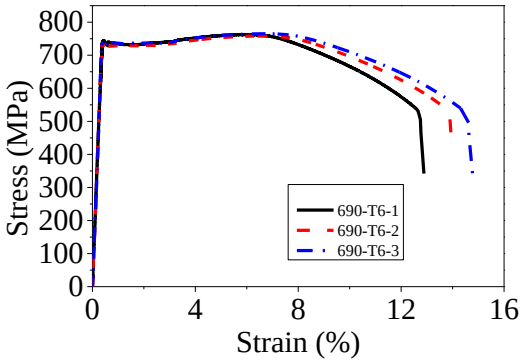

(b) Q690

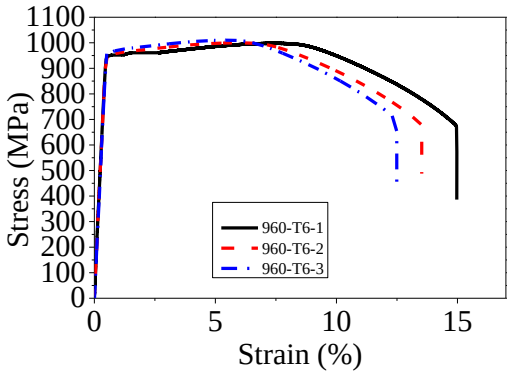

(c) Q960

Figure 3.2 Stress-strain curves of tensile coupons

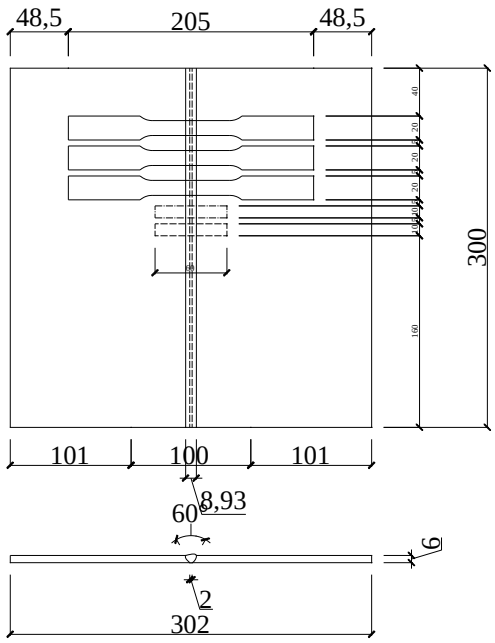

(a) Overall configuration

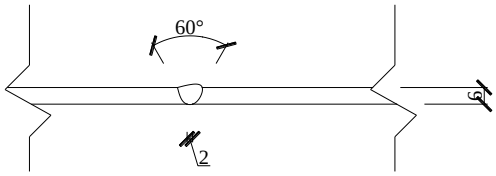

(b) Weld details

Figure 3.3 Butt-welded joint configuration (mm)

Figure 3.4 Butt-welded tensile coupons cut from butt-welded joints

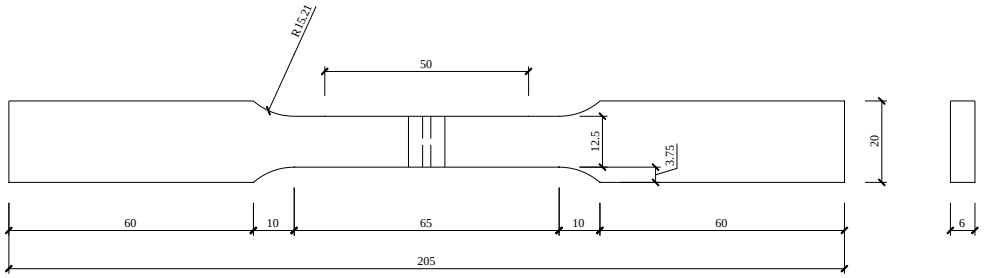

Figure 3.5 Butt-welded tensile coupon configurations (mm)

(a) Front view (b) Back view

Figure 3.6 Specimen Q690-B6-H2

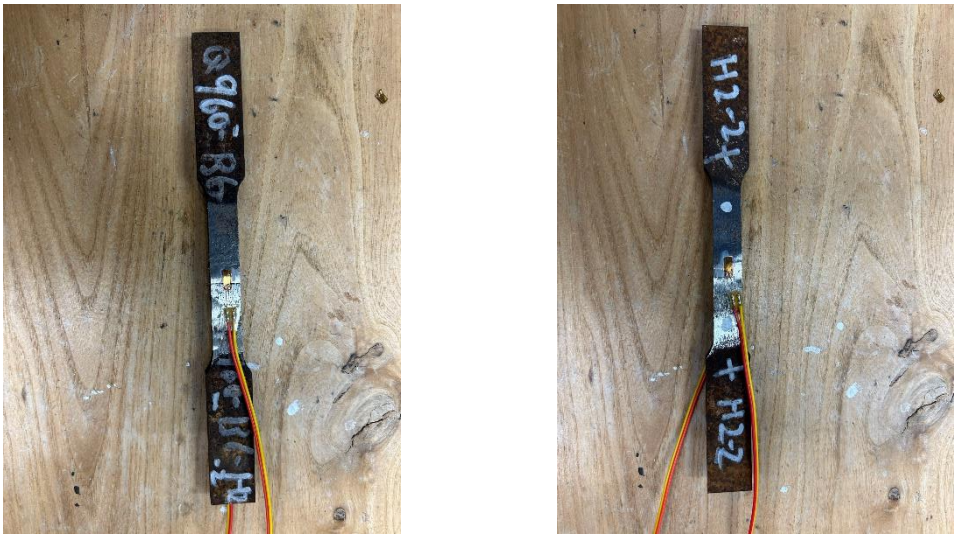

Figure 3.7 Strain gauges on both sides

Figure 3.8 Instron 5982 installed with tensile coupons

Figure 3.9 BUEHLER EcoMet 30

Figure 3.10 Polishing material MasterPolish

Figure 3.11 Wilson hardness tester

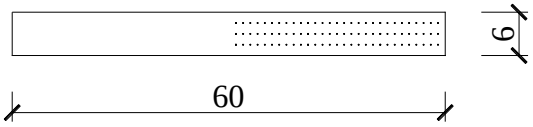

Figure 3.12 Indentation lines on test block (mm)

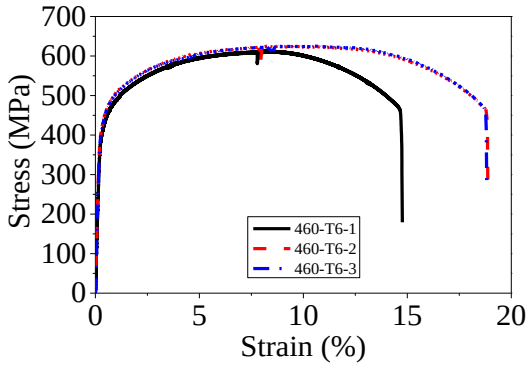

(a) BM

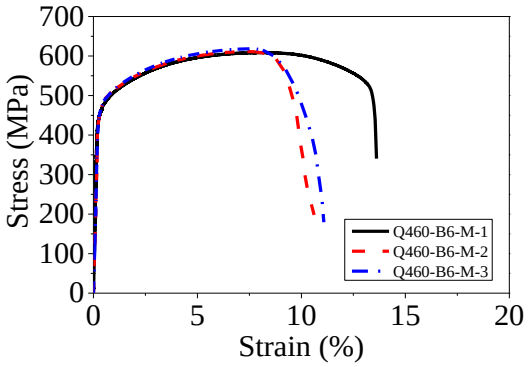

(b) Heat input equal to 0.968 kJ/mm

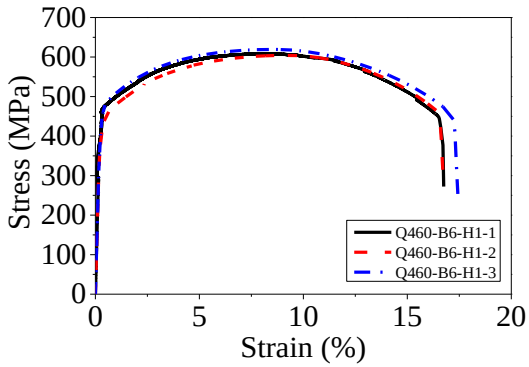

(c) Heat input equal to 1.263 kJ/mm

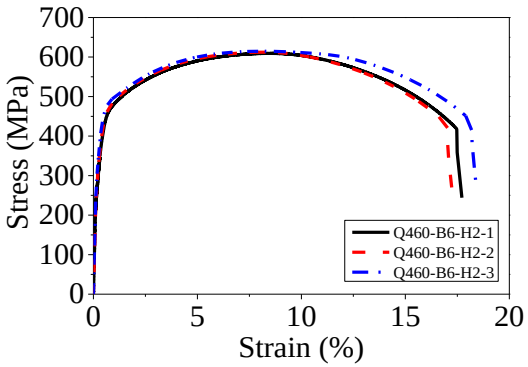

(d) Heat input equal to 1.631 kJ/mm

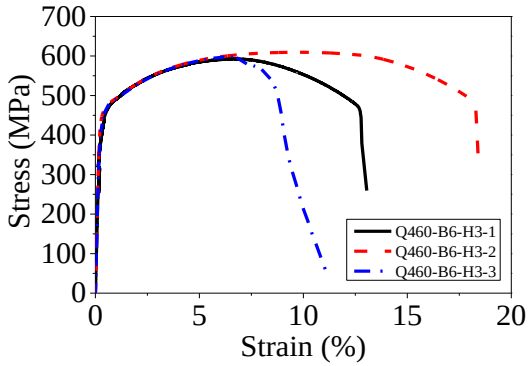

(e) Heat input equal to 1.752 kJ/mm

Figure 3.13 Stress-strain curves for the Q460 butt-welded tensile coupons

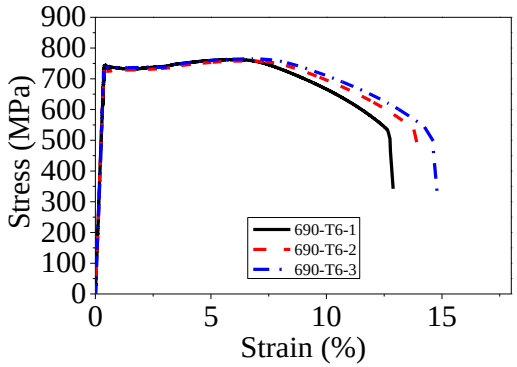

(a) BM

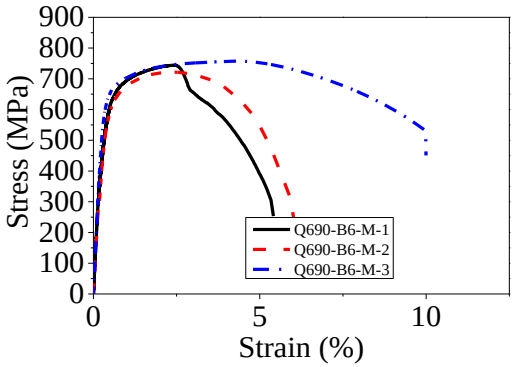

(b) Heat input equal to 0.966 kJ/mm

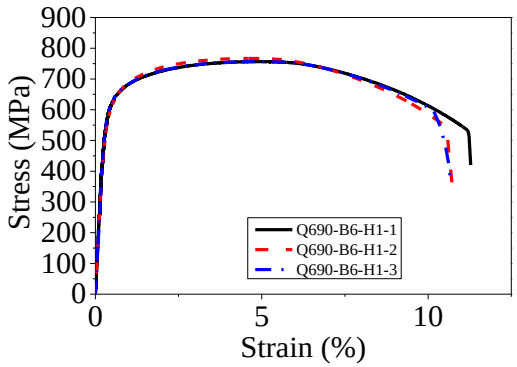

(c) Heat input equal to 1.257 kJ/mm

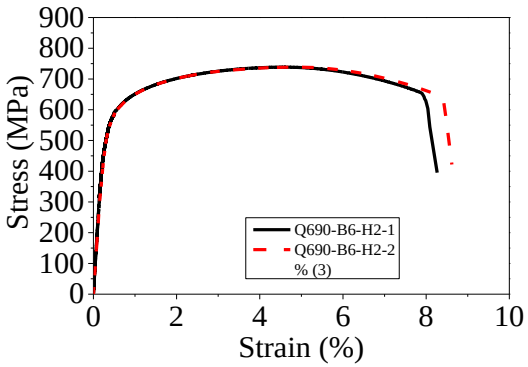

(d) Heat input equal to 1.645 kJ/mm

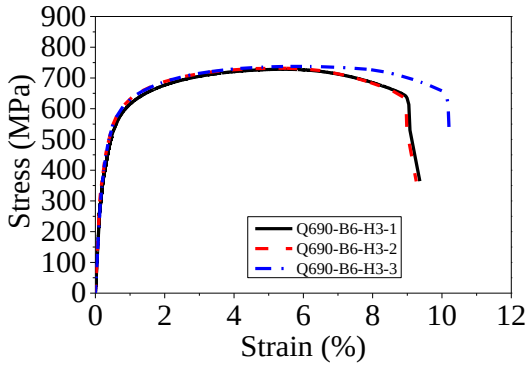

(e) Heat input equal to 1.823 kJ/mm

Figure 3.14 Stress-strain curves for the Q690 butt-welded tensile coupons

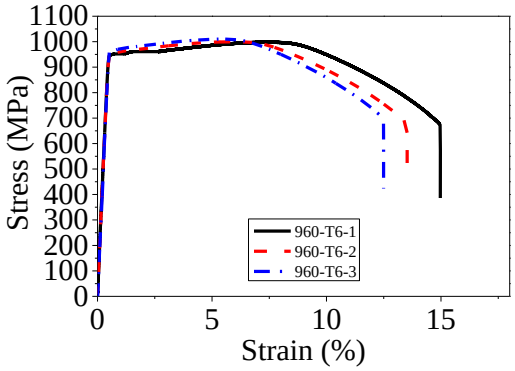

(a) BM

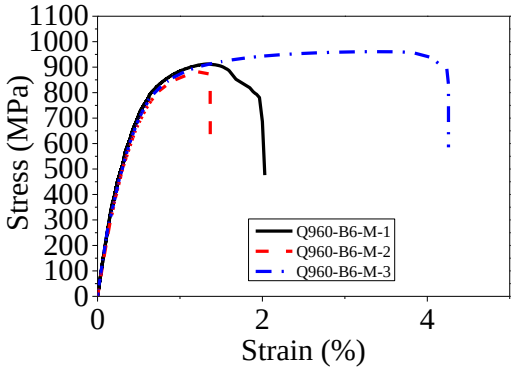

(b) Heat input equal to 0.995 kJ/mm

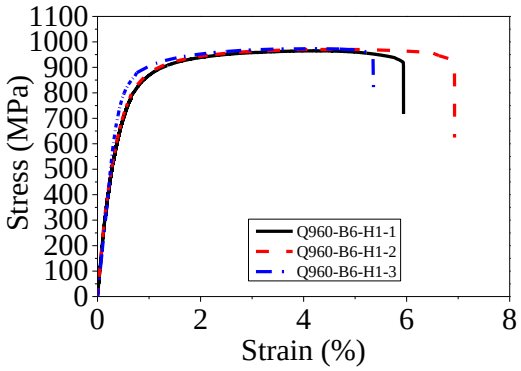

(c) Heat input equal to 1.222 kJ/mm

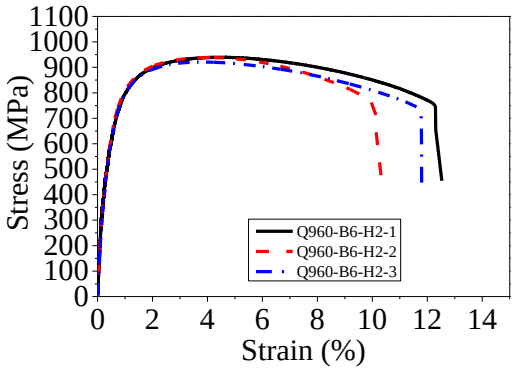

(d) Heat input equal to 1.592 kJ/mm

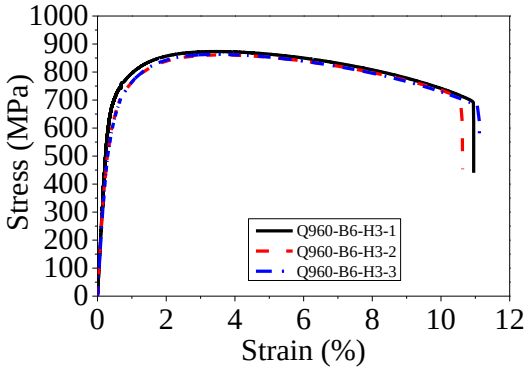

(e) Heat input equal to 1.864 kJ/mm

Figure 3.15 Stress-strain curves for the Q960 butt-welded tensile coupons

(a) Fracture at BM: Q460-B6-H1-1

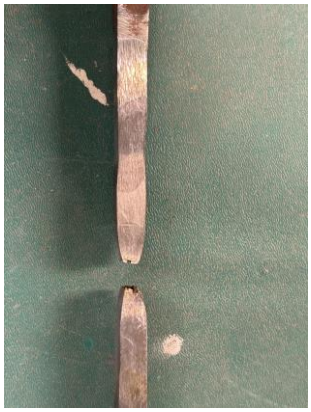

(b) Fracture at HAZ/BM interface: Q690-B6-H1-2

(c) Fracture at HAZ: Q960-B6-H1-2

(d) Fracture at WM: Q460-B6-M-2

Figure 3.16 Several fracture types for HSS butt-welded tensile coupons

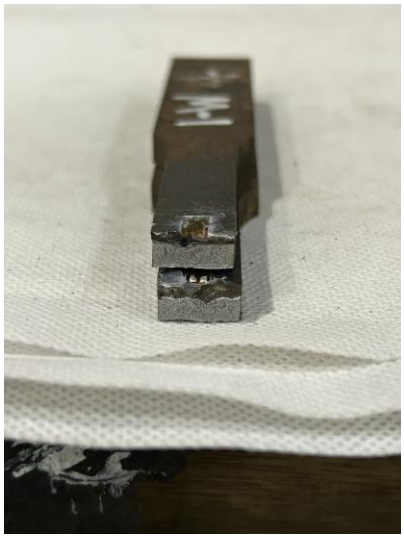

(a) Q690-B6-M-1

(b) Q960-B6-M2

Figure 3.17 Fracture surfaces for Q690 and Q960 butt-welded coupons under heat input M

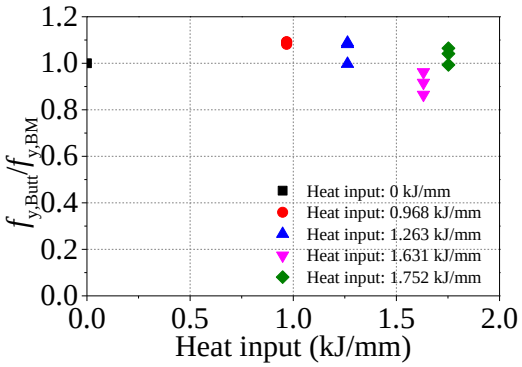

(a) $f_{y,\,butt}/f_{y,\,BM}$

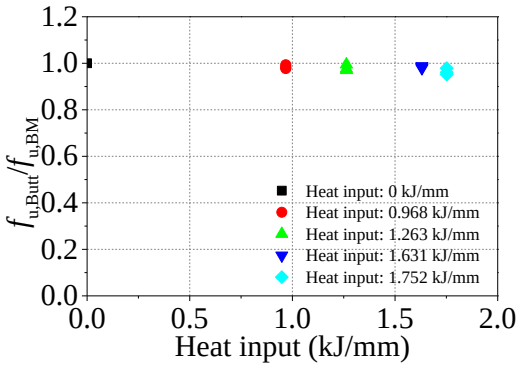

(b) $f_{u,\,butt}/f_{u,\,BM}$

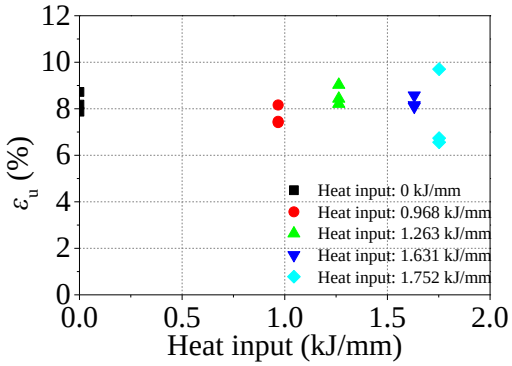

(c) ε_u

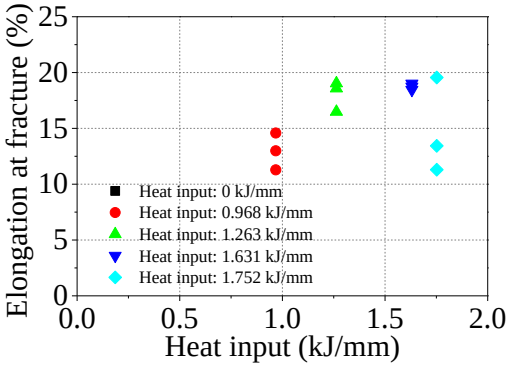

(d) Elongation at fracture

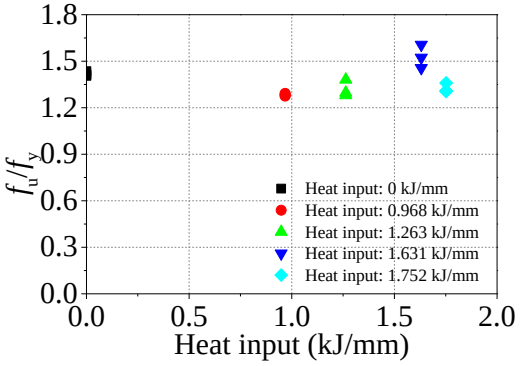

(e) f_u/f_y

Figure 3.18 Variation of mechanical properties of Q460 butt-welded tensile coupons with heat inputs

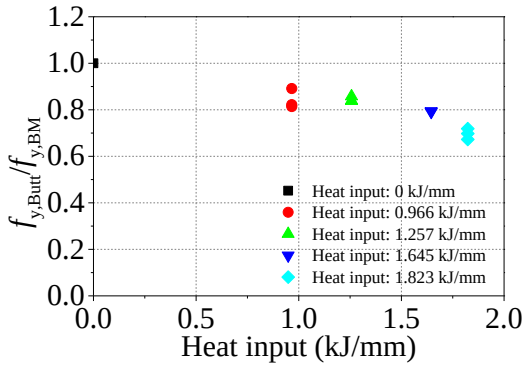

(a) $f_{y,\ butt}/f_{y,\ BM}$

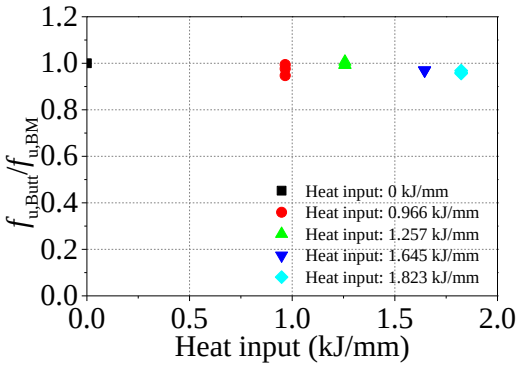

(b) $f_{u,\ butt}/f_{u,\ BM}$

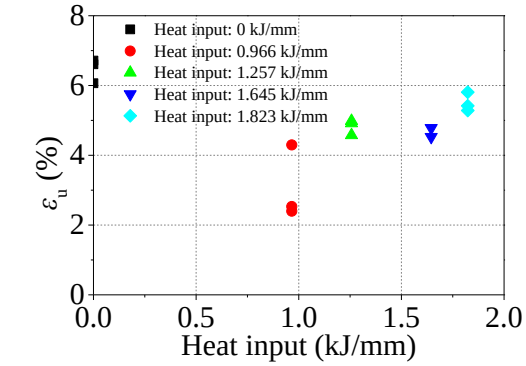

(c) ε_u

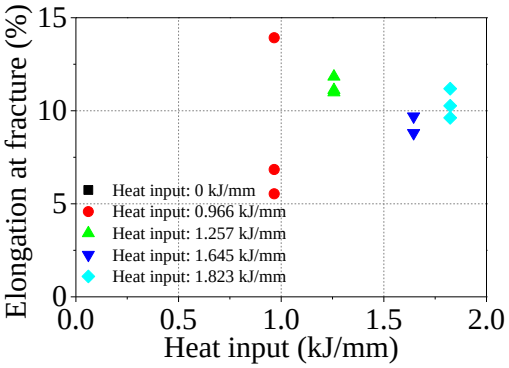

(d) Elongation at fracture

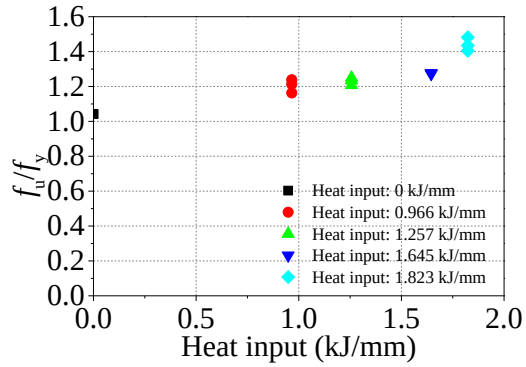

(e) f_u/f_y

Figure 3.19 Variation of mechanical properties of Q690 butt-welded tensile coupons with heat inputs

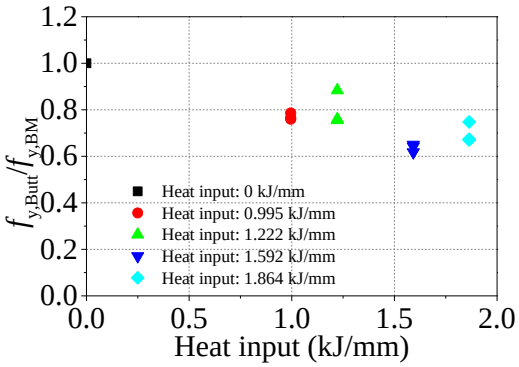

(a) $f_{y,\,butt}/f_{y,\,BM}$

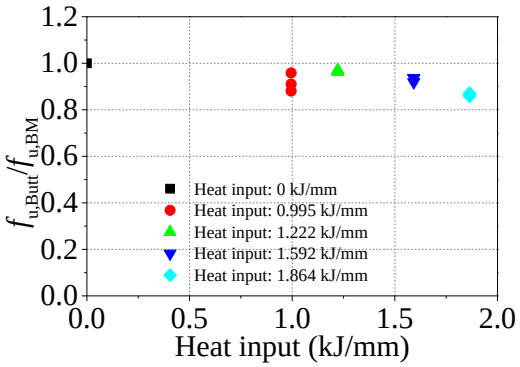

(b) $f_{u,\,butt}/f_{u,\,BM}$

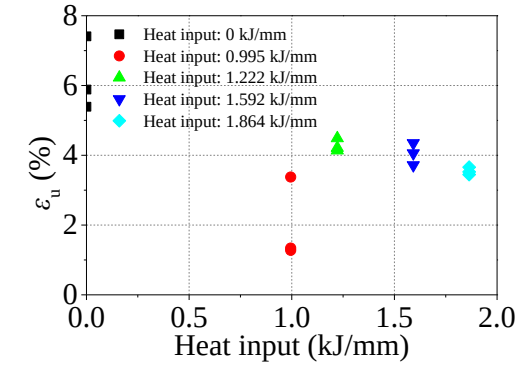

(c) ε_u

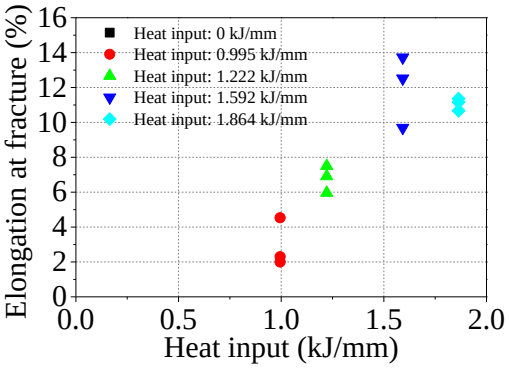

(d) Elongation at fracture

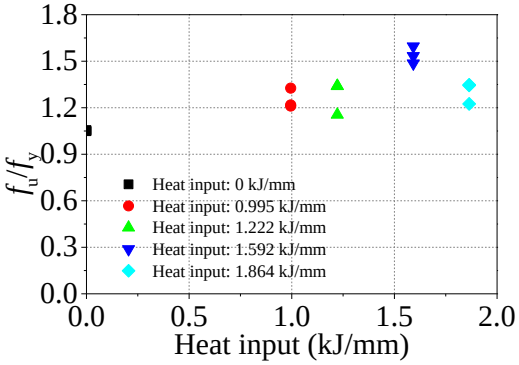

(e) f_u/f_y

Figure 3.20 Variation of mechanical properties of Q960 butt-welded tensile coupons with heat inputs

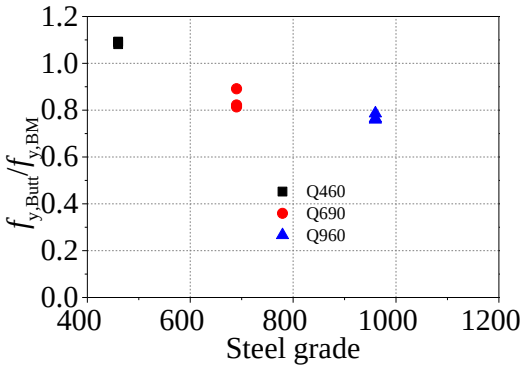

(a) $f_{y,\,butt}/f_{y,\,BM}$

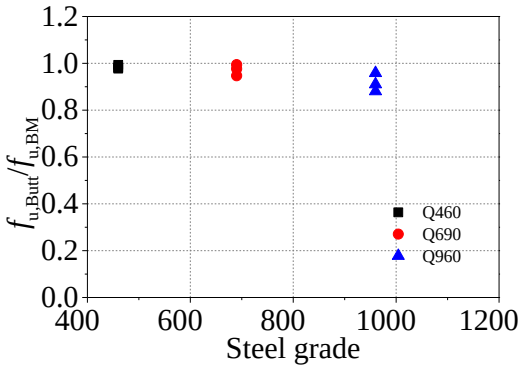

(b) $f_{u,\,butt}/f_{u,\,BM}$

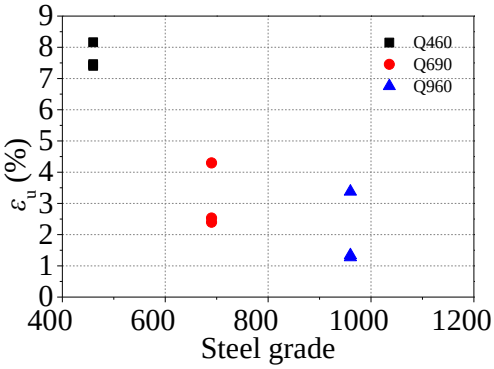

(c) ε_u

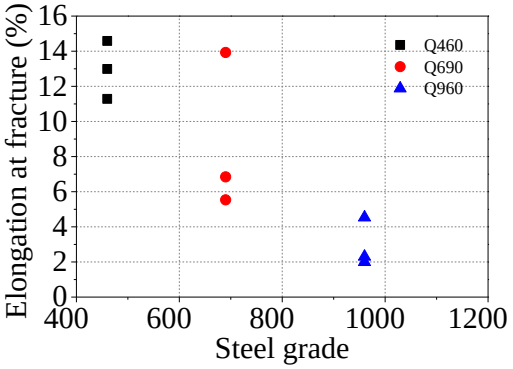

(d) Elongation at fracture

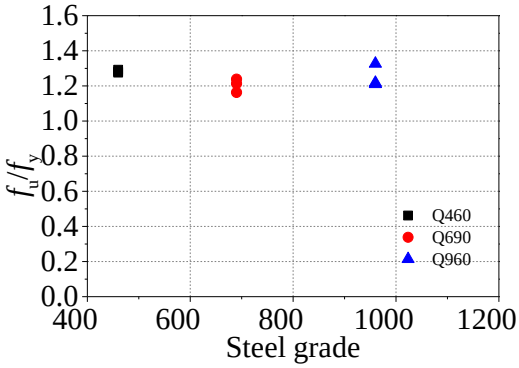

(e) f_u/f_y

Figure 3.21 Variation of mechanical properties of butt-welded tensile coupons by 0.973 kJ/mm with steel grades

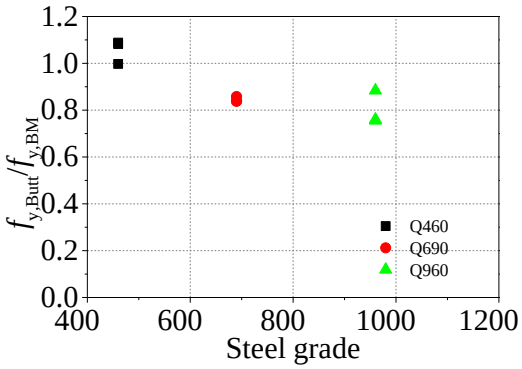

(a) $f_{y,\,butt}/f_{y,\,BM}$

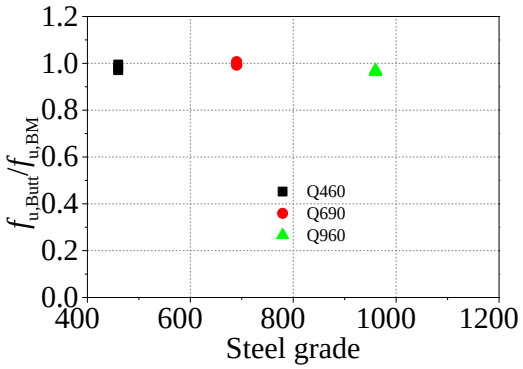

(b) $f_{u,\,butt}/f_{u,\,BM}$

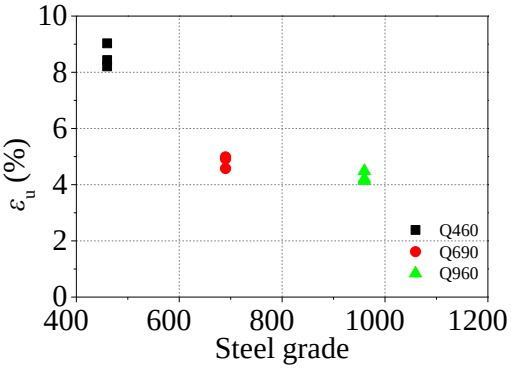

(c) ε_u

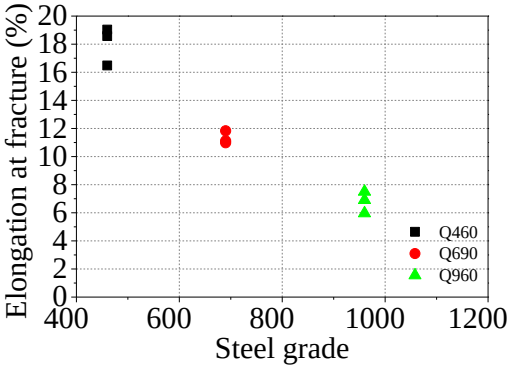

(d) Elongation at fracture

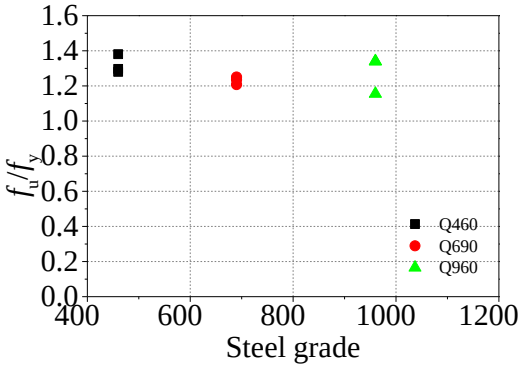

(e) f_u/f_y

Figure 3.22 Variation of mechanical properties of butt-welded tensile coupons by 1.234 kJ/mm with steel grades

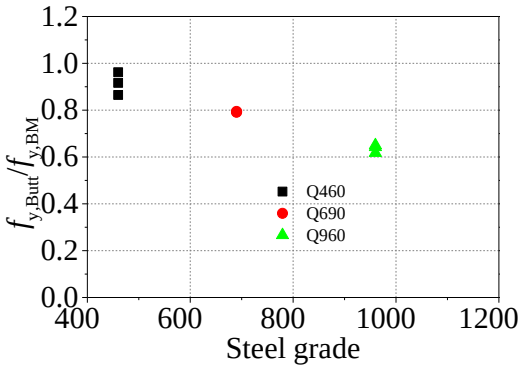

(a) $f_{y,\,butt}/f_{y,\,BM}$

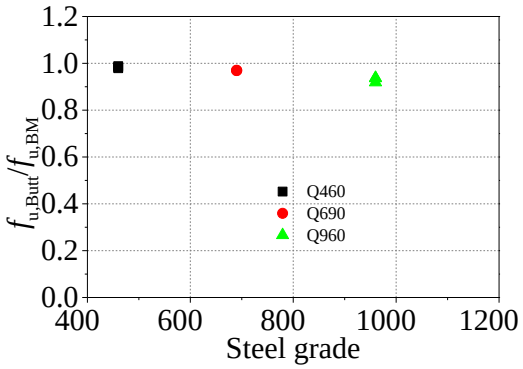

(b) $f_{u,\,butt}/f_{u,\,BM}$

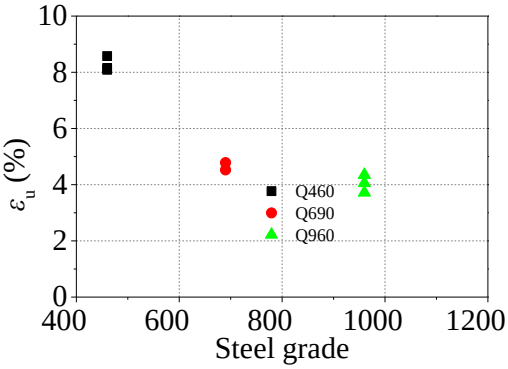

(c) ε_u

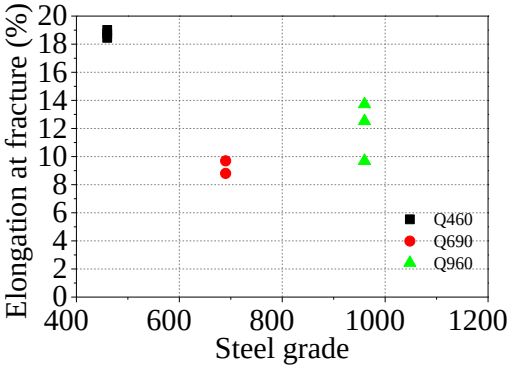

(d) Elongation at fracture

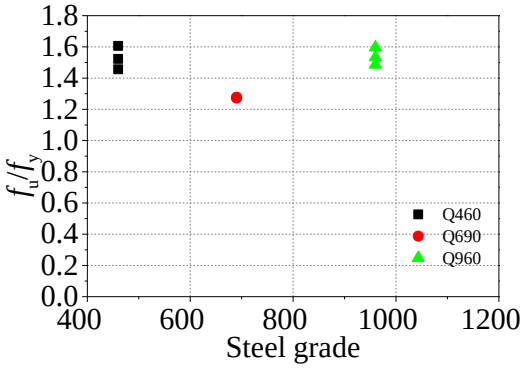

(e) f_u/f_y

Figure 3.23 Variation of mechanical properties of butt-welded tensile coupons by 1.546 kJ/mm with steel grades

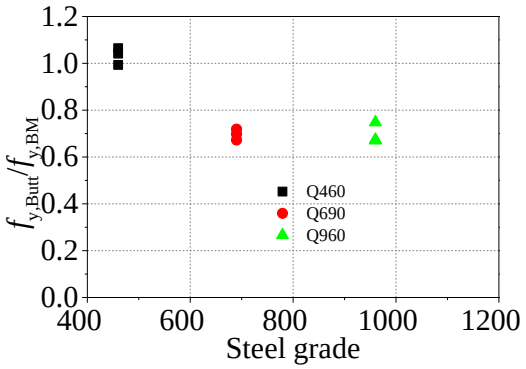

(a) $f_{y,\,butt}/f_{y,\,BM}$

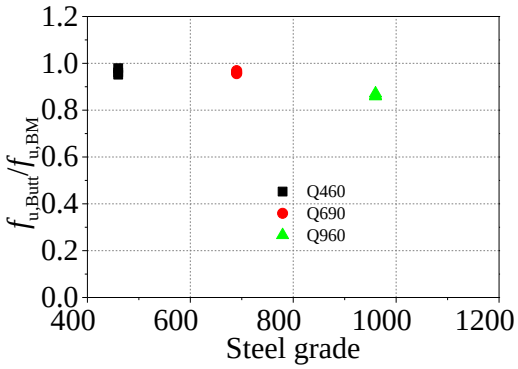

(b) $f_{u,\,butt}/f_{u,\,BM}$

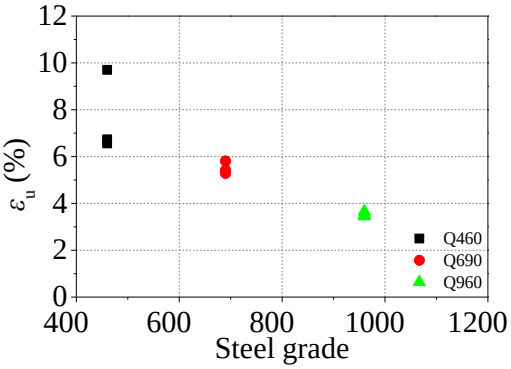

(c) ε_u

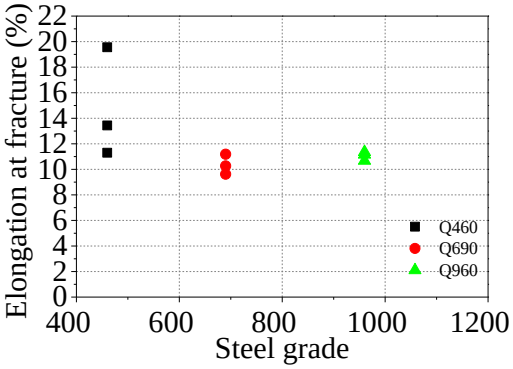

(d) Elongation at fracture

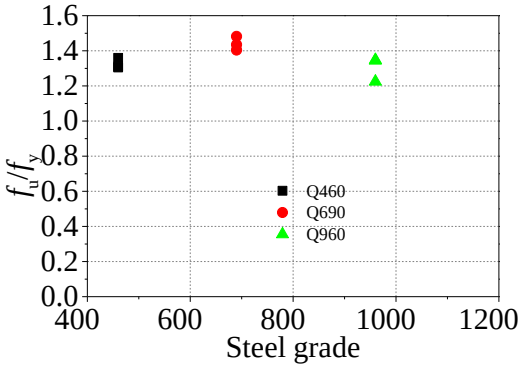

(e) f_u/f_y

Figure 3.24 Variation of mechanical properties of butt-welded tensile coupons by 1.760 kJ/mm with steel grades

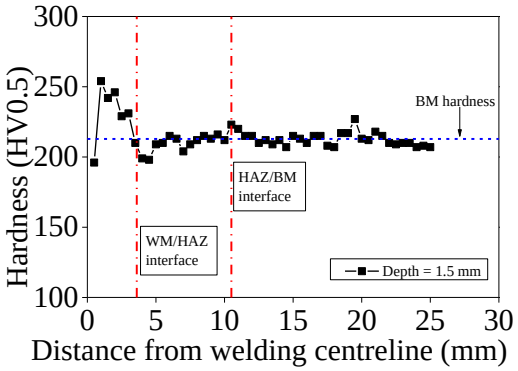

(a) Indentation line at 1.5 mm

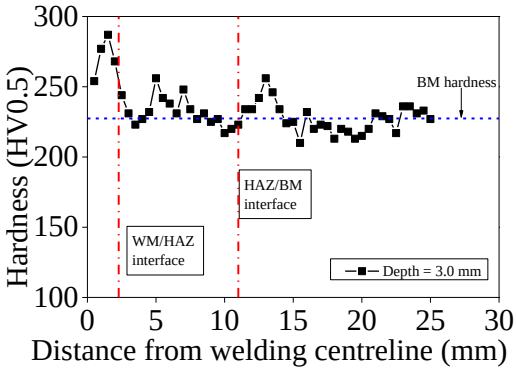

(b) Indentation line at 3.0 mm

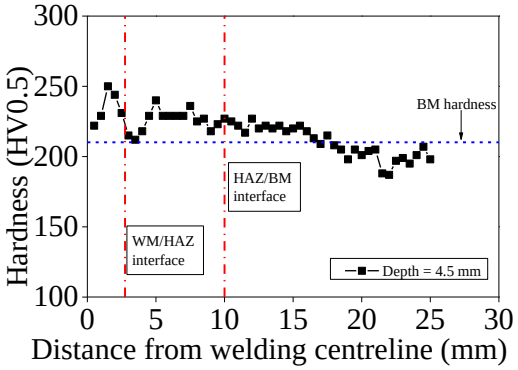

(c) Indentation line at 4.5 mm

Figure 3.25 Hardness distributions of Q460-B6-M

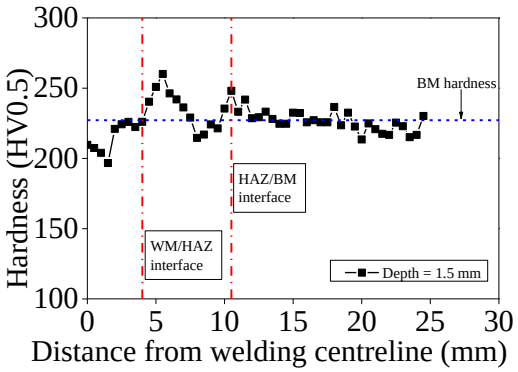

(a) Indentation line at 1.5 mm

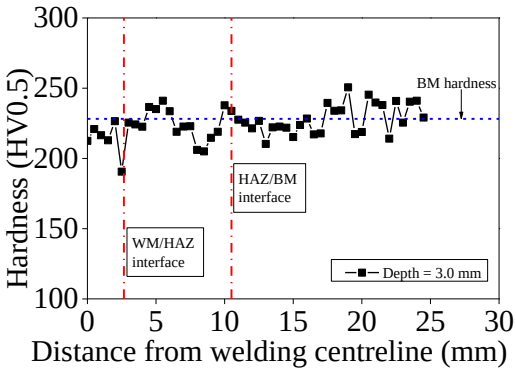

(b) Indentation line at 3.0 mm

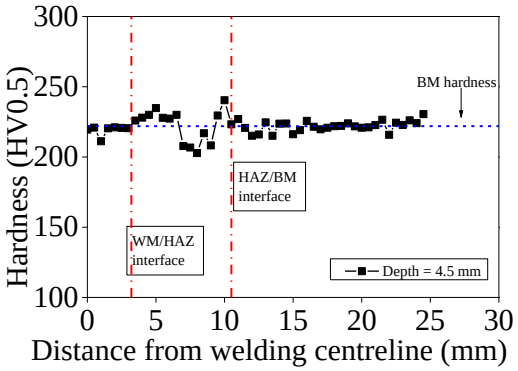

(c) Indentation line at 4.5 mm

Figure 3.26 Hardness distributions of Q460-B6-H1

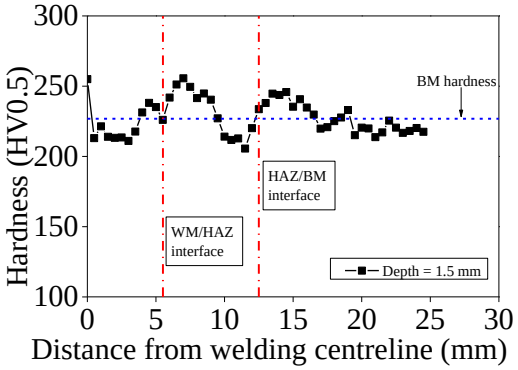

(a) Indentation line at 1.5 mm

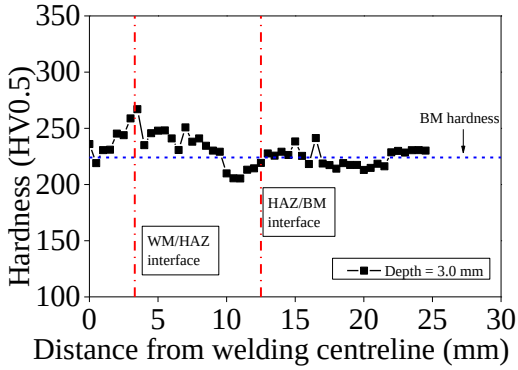

(b) Indentation line at 3.0 mm

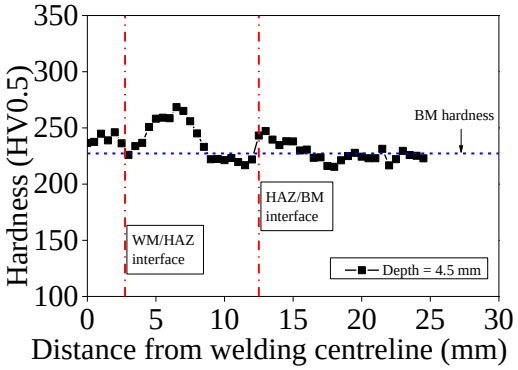

(c) Indentation line at 4.5 mm

Figure 3.27 Hardness distributions of Q460-B6-H2

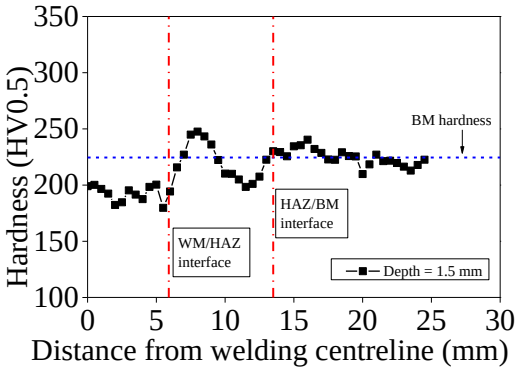

(a) Indentation line at 1.5 mm

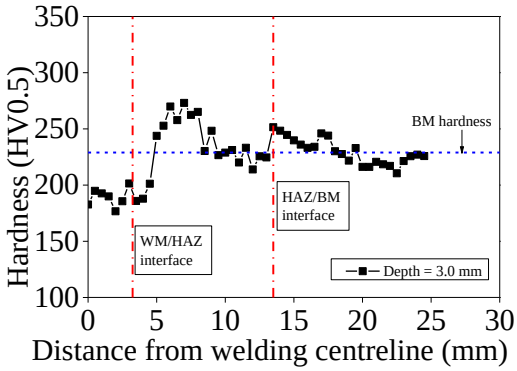

(b) Indentation line at 3.0 mm

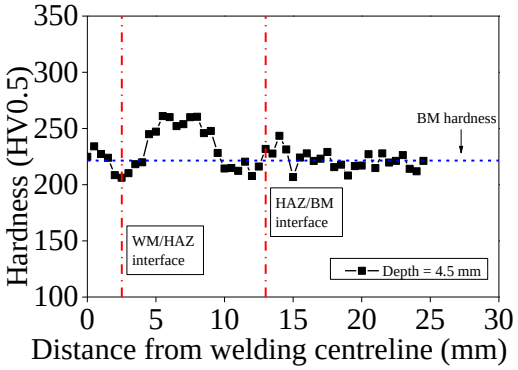

(c) Indentation line at 4.5 mm

Figure 3.28 Hardness distributions of Q460-B6-H3

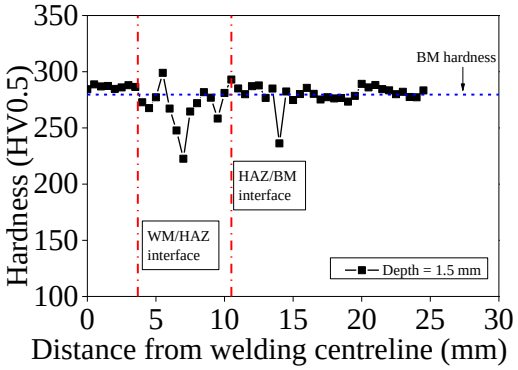

(a) Indentation line at 1.5 mm

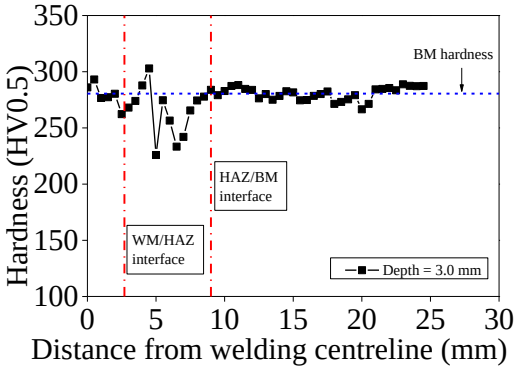

(b) Indentation line at 3.0 mm

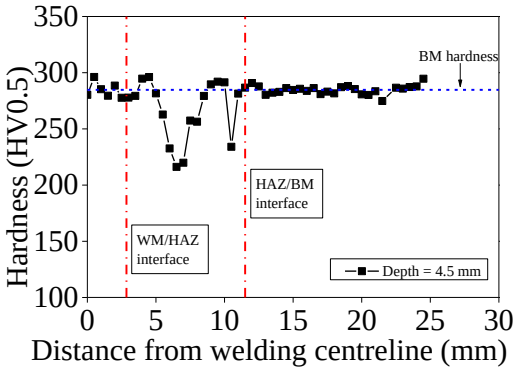

(c) Indentation line at 4.5 mm

Figure 3.29 Hardness distributions of Q690-B6-M

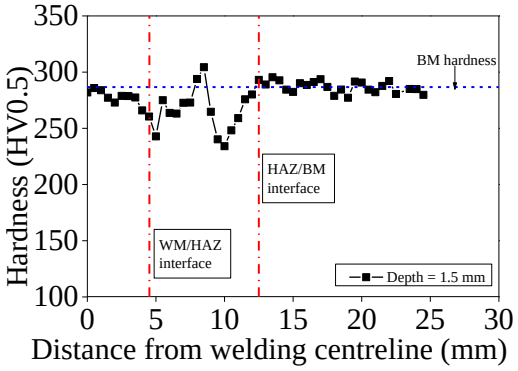

(a) Indentation line at 1.5 mm

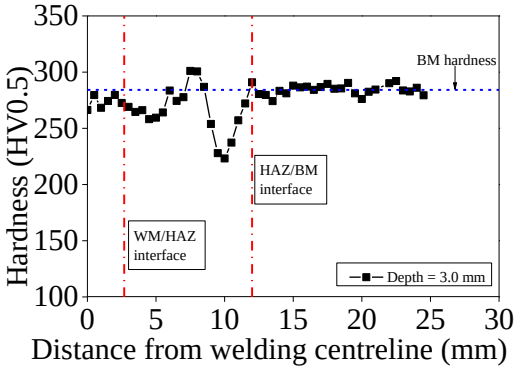

(b) Indentation line at 3.0 mm

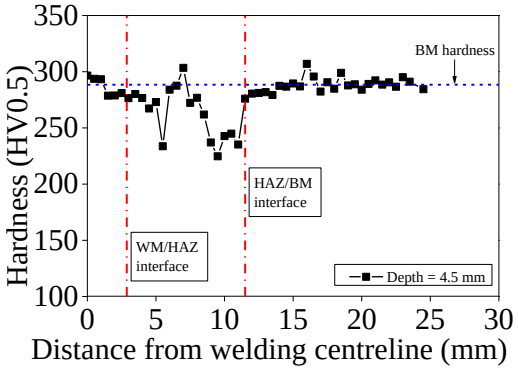

(c) Indentation line at 4.5 mm

Figure 3.30 Hardness distributions of Q690-B6-H1

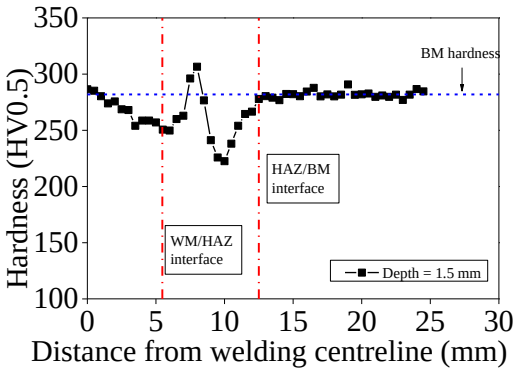

(a) Indentation line at 1.5 mm

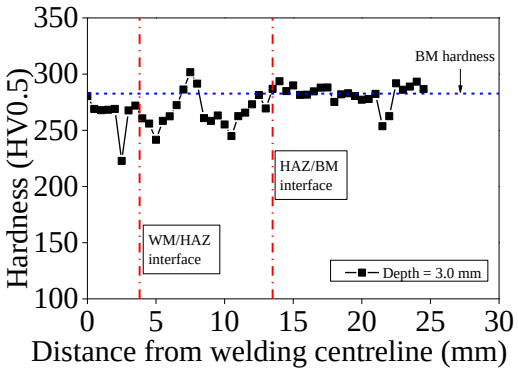

(b) Indentation line at 3.0 mm

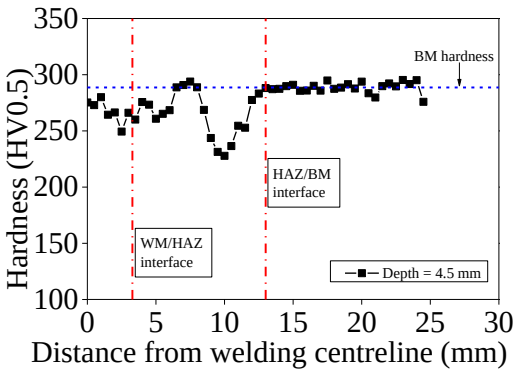

(c) Indentation line at 4.5 mm

Figure 3.31 Hardness distributions of Q690-B6-H2

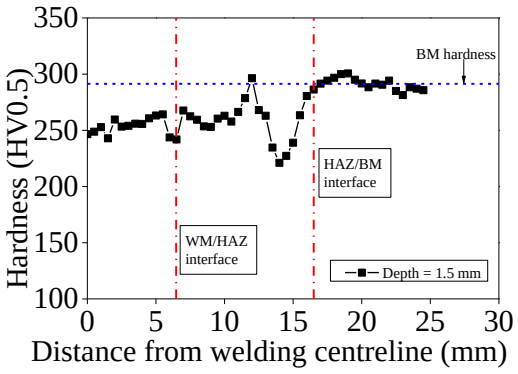

(a) Indentation line at 1.5 mm

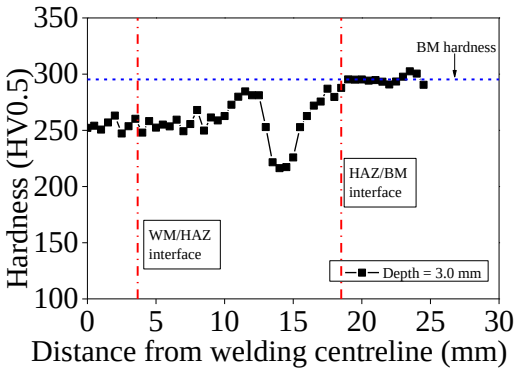

(b) Indentation line at 3.0 mm

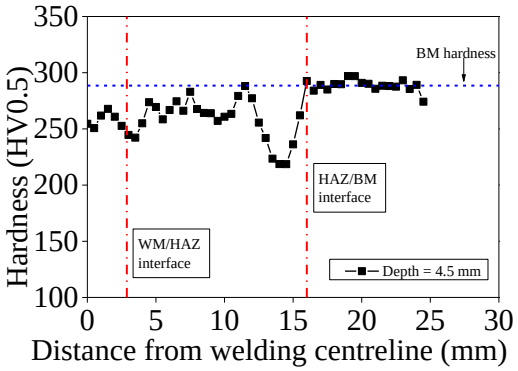

(c) Indentation line at 4.5 mm

Figure 3.32 Hardness distributions of Q690-B6-H3

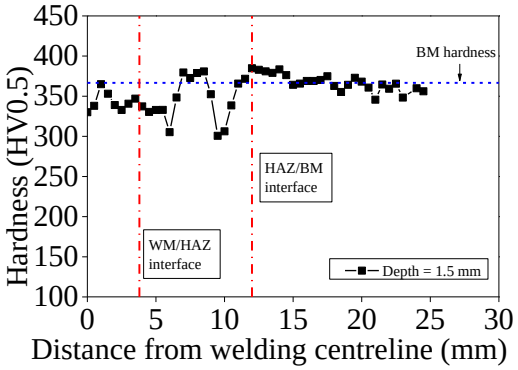

(a) Indentation line at 1.5 mm

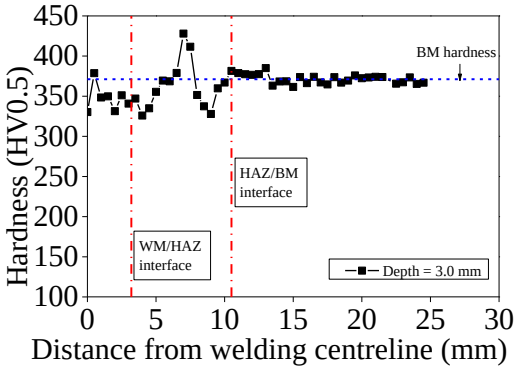

(b) Indentation line at 3.0 mm

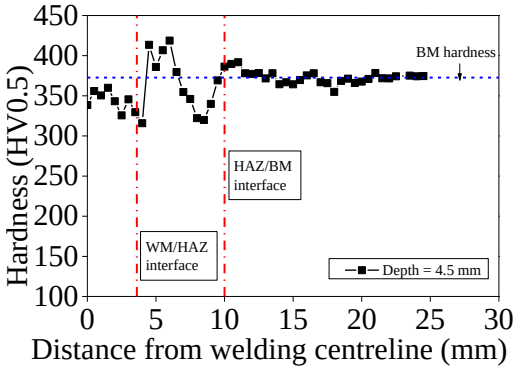

(c) Indentation line at 4.5 mm

Figure 3.33 Hardness distributions of Q960-B6-M

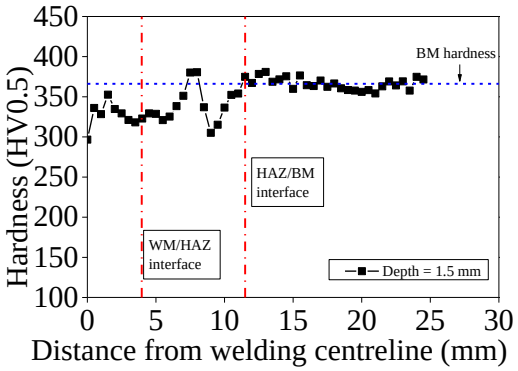

(a) Indentation line at 1.5 mm

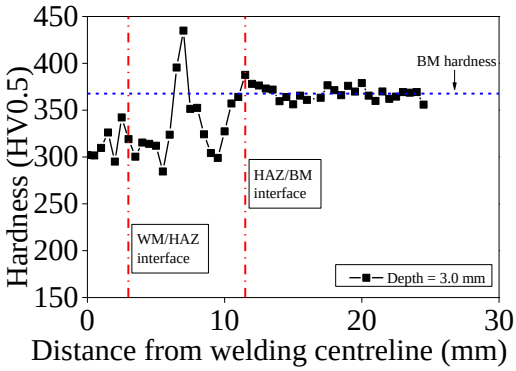

(b) Indentation line at 3.0 mm

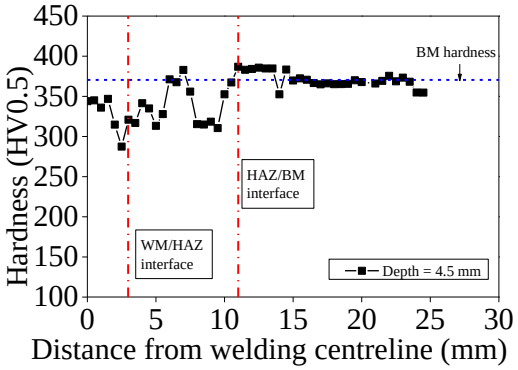

(c) Indentation line at 4.5 mm

Figure 3.34 Hardness distributions of Q960-B6-H1

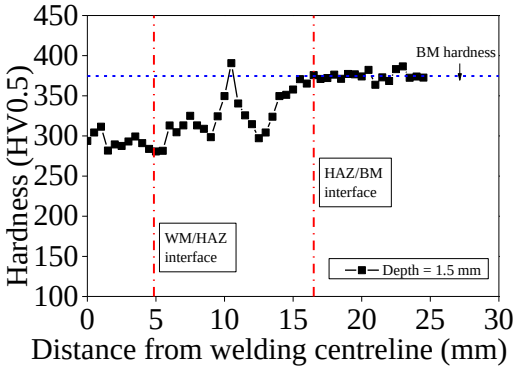

(a) Indentation line at 1.5 mm

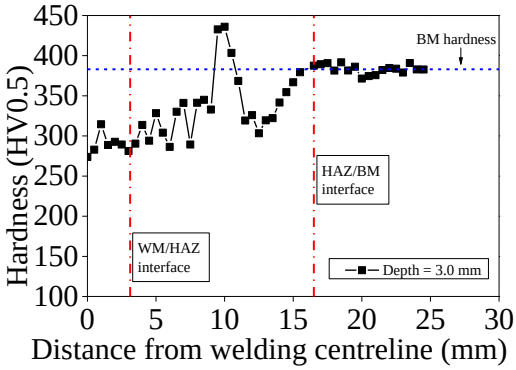

(b) Indentation line at 3.0 mm

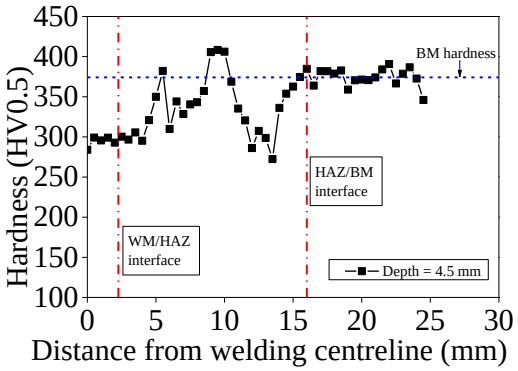

(c) Indentation line at 4.5 mm

Figure 3.35 Hardness distributions of Q960-B6-H2

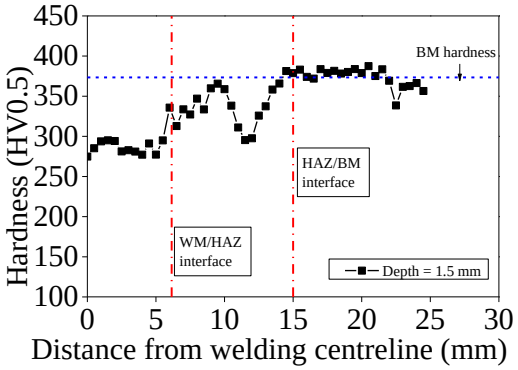

(a) Indentation line at 1.5 mm

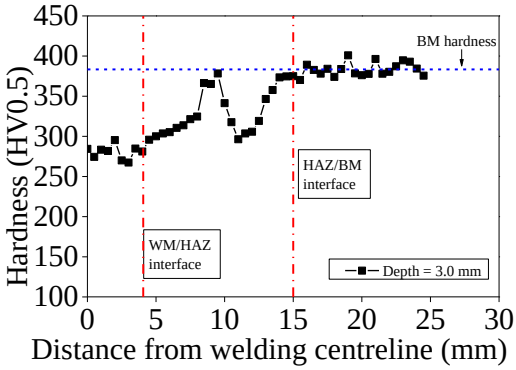

(b) Indentation line at 3.0 mm

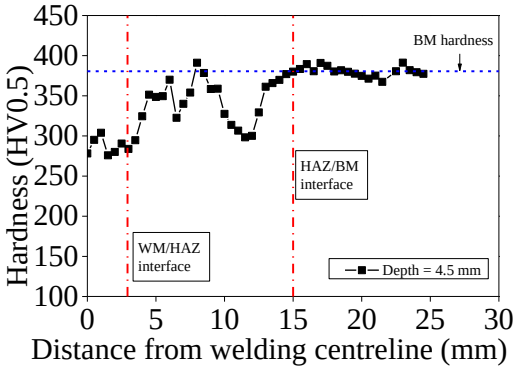

(c) Indentation line at 4.5 mm

Figure 3.36 Hardness distributions of Q960-B6-H3

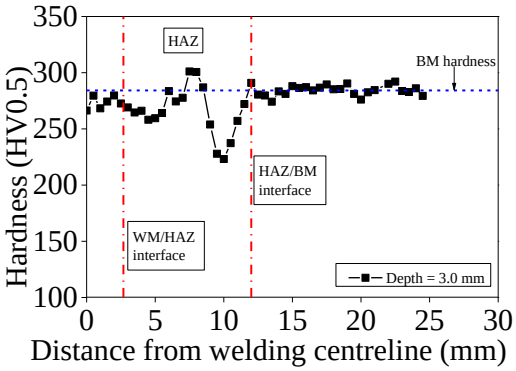

Figure 3.37 Boundaries along indentation lines at certain depth level

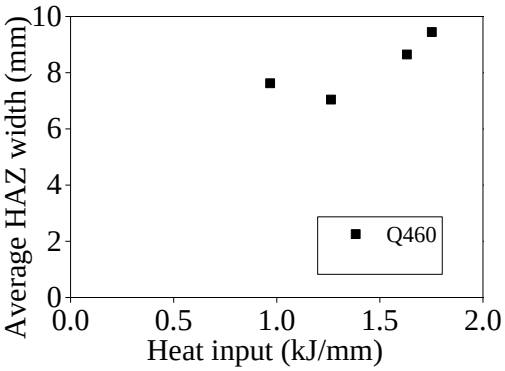

(a) Q460 butt-welded joint

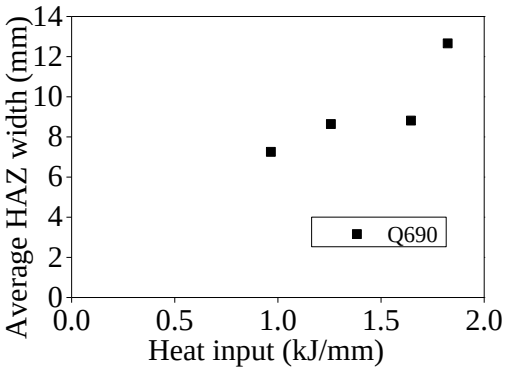

(b) Q690 butt-welded joint

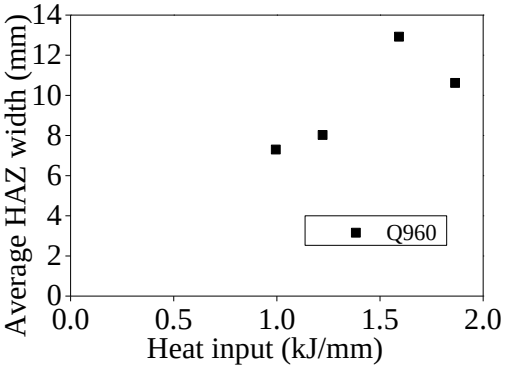

(c) Q960 butt-welded joint

Figure 3.38 HAZ widths vs. heat inputs for butt-welded joints

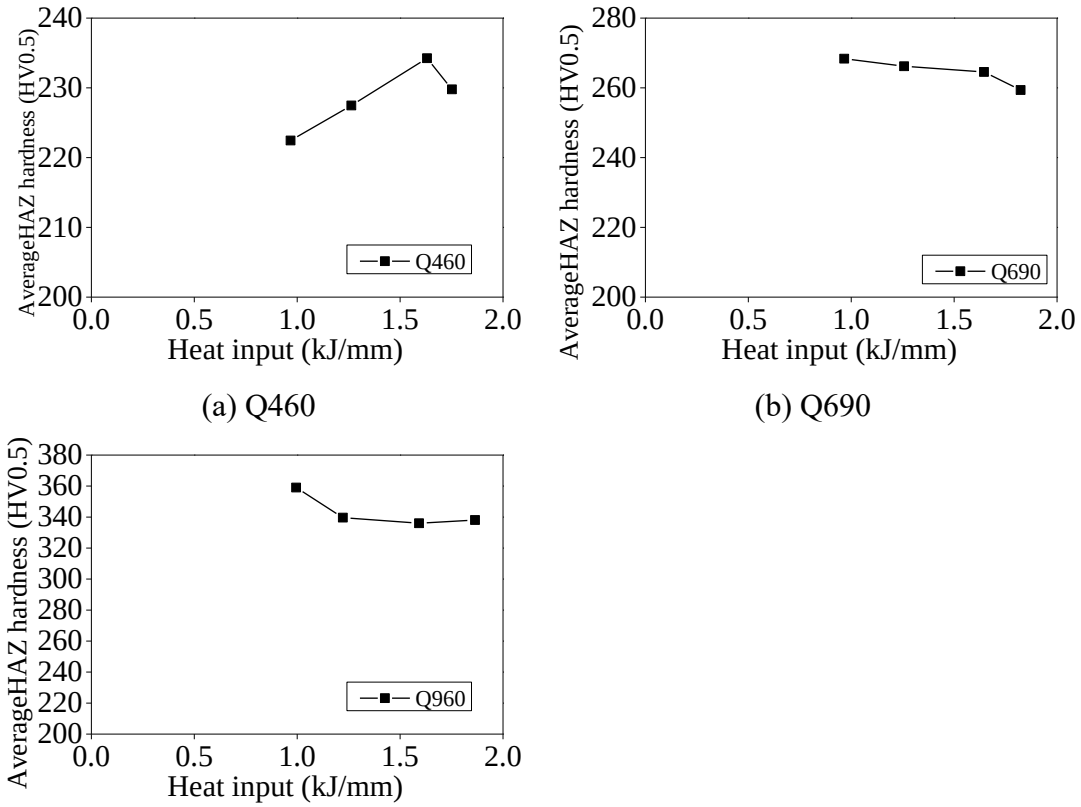

(a) Q460 (b) Q690

(c) Q960

Figure 3.39 HAZ hardness vs. heat inputs for butt-welded joints

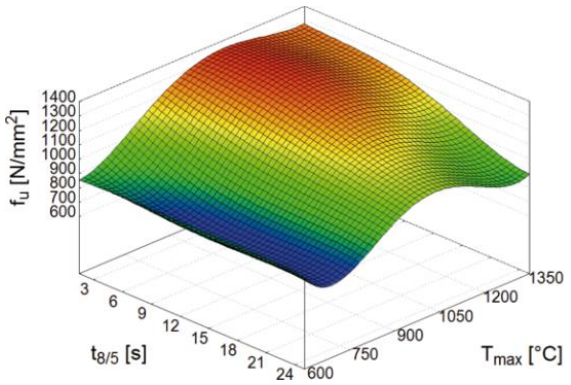

Figure 3.40 Polynomial function of the tensile strength depending on cooling time $t_{8/5}$ and peak temperature T_{max} of steel S690Q

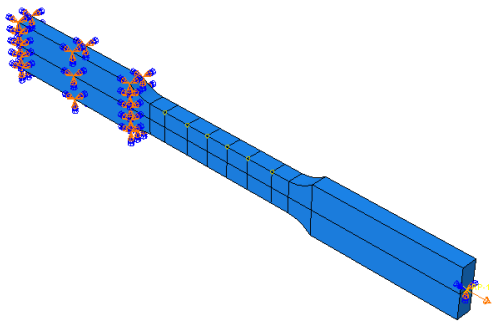

Figure 3.41 Numerical models for butt-welded tensile coupon

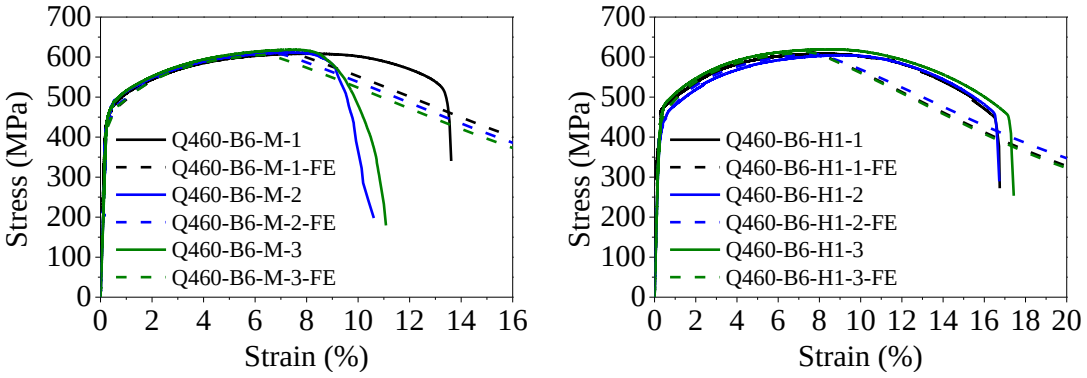

(a) Heat input equal to 0.968 kJ/mm (b) Heat input equal to 1.263 kJ/mm

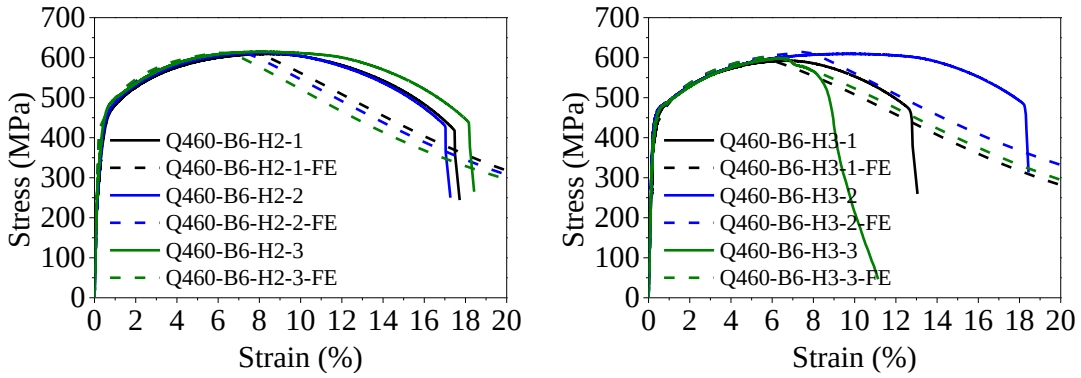

(c) Heat input equal to 1.631 kJ/mm (d) Heat input equal to 1.752 kJ/mm

Figure 3.42 Comparison between experimental and numerical stress-strain curves for Q460 butt-welded tensile coupons

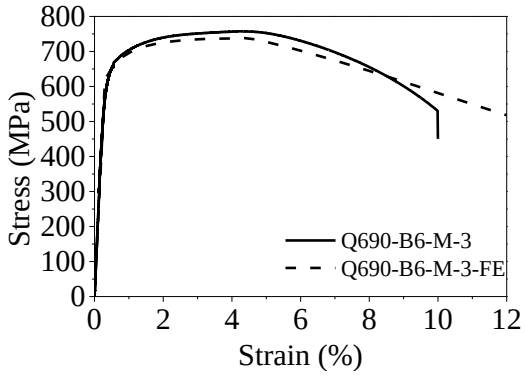

(a) Heat input equal to 0.966 kJ/mm

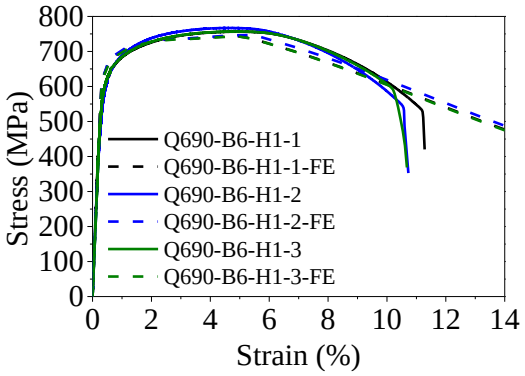

(b) Heat input equal to 1.257 kJ/mm

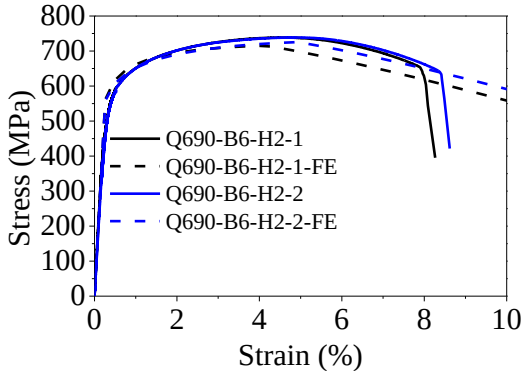

(c) Heat input equal to 1.645 kJ/mm

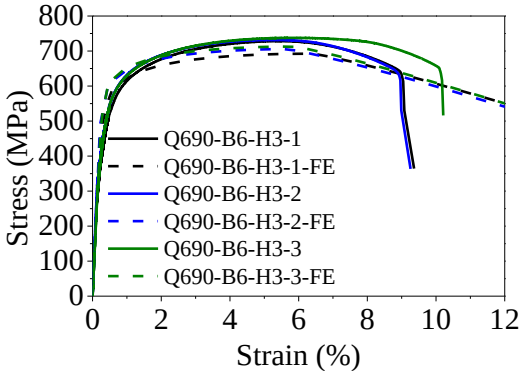

(d) Heat input equal to 1.823 kJ/mm

Figure 3.43 Comparison between experimental and numerical stress-strain curves for Q690 butt-welded tensile coupons

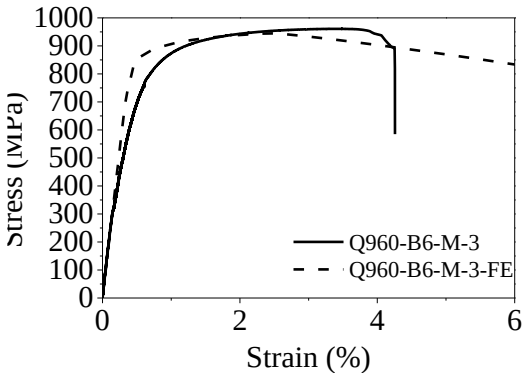

(a) Heat input equal to 0.995 kJ/mm

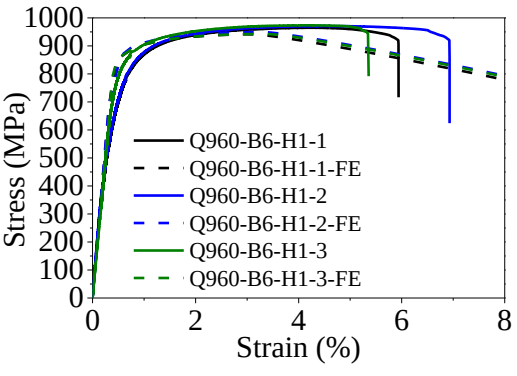

(b) Heat input equal to 1.222 kJ/mm

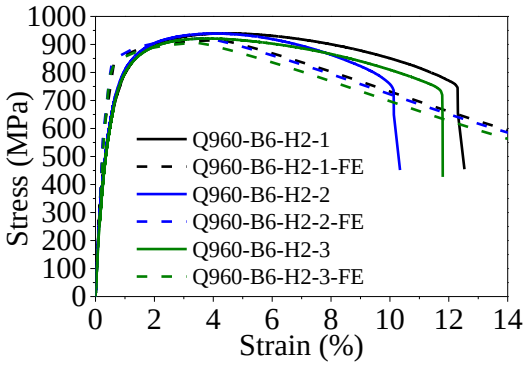

(c) Heat input equal to 1.592 kJ/mm

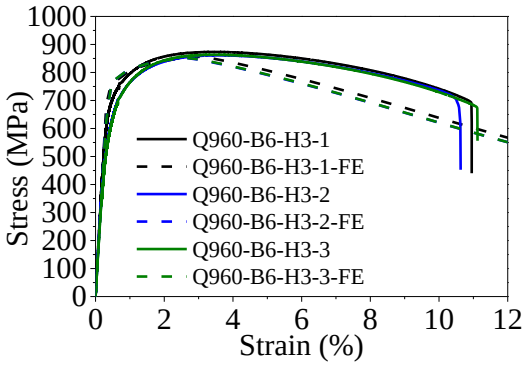

(d) Heat input equal to 1.864 kJ/mm

Figure 3.44 Comparison between experimental and numerical stress-strain curves for Q960 butt-welded tensile coupons

(a) Q690-B6-M-1

(b) Q690-B6-M-2

(c) Q960-B6-M-1 (d) Q960-B6-M-2

Figure 3.45 Weld discontinuities for Q690 and Q960 with heat input < 1 kJ/mm

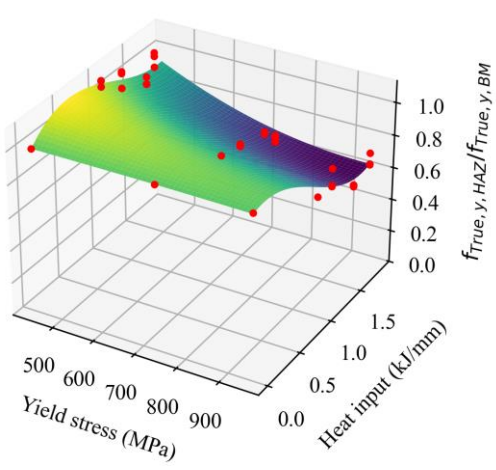

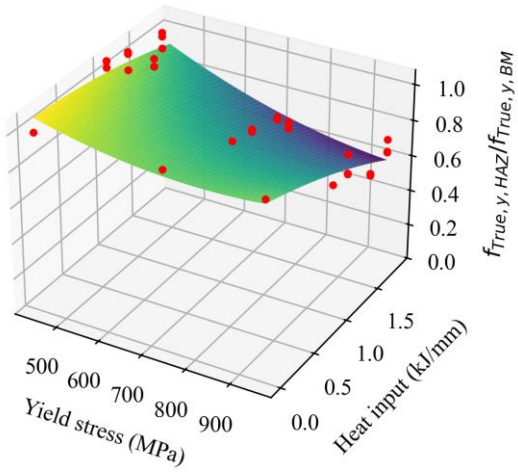

(a) Degree = 3 (b) Degree = 2

Figure 3.46 Polynomial regression analysis for $f_{\text{True, y, HAZ}}/f_{\text{True, y, BM}}$ under different degrees

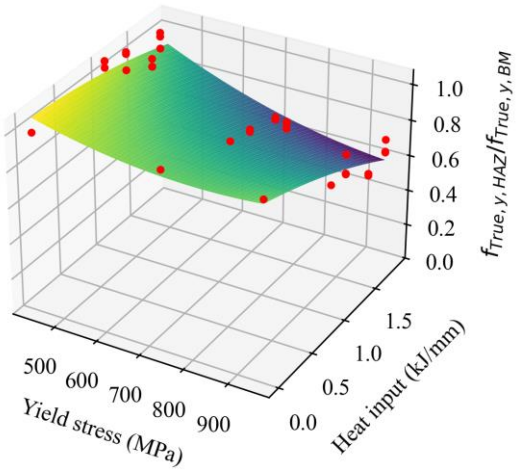

(a) Surface for $f_{\text{True, y, HAZ}}/f_{\text{True, y, BM}}$

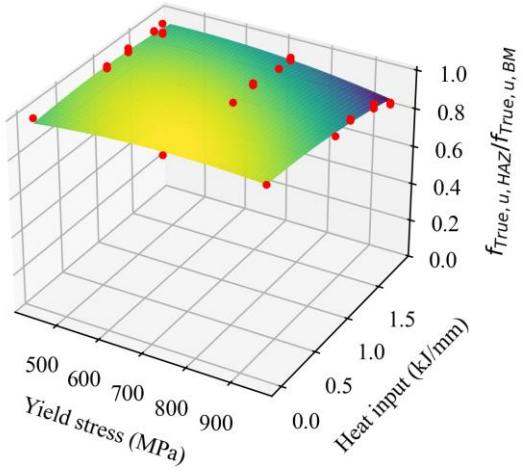

(b) Surface for $f_{\text{True, u, HAZ}}/f_{\text{True, u, BM}}$

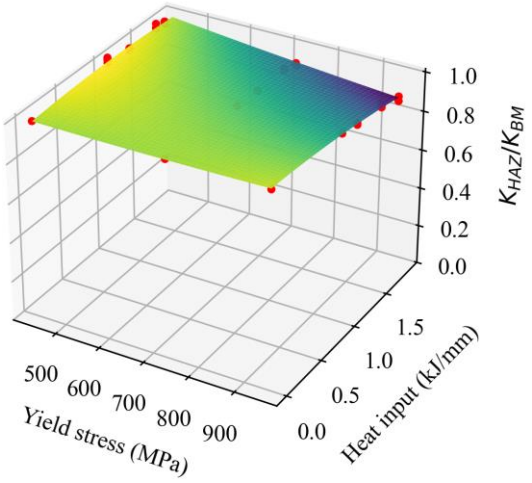

(c) Surface for $K_{\text{HAZ}}/K_{\text{BM}}$

Figure 3.47 Curved surfaces for quadratic regression models

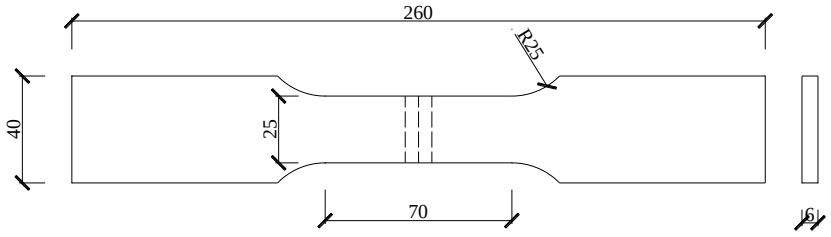

(a) 690-6-G2-1

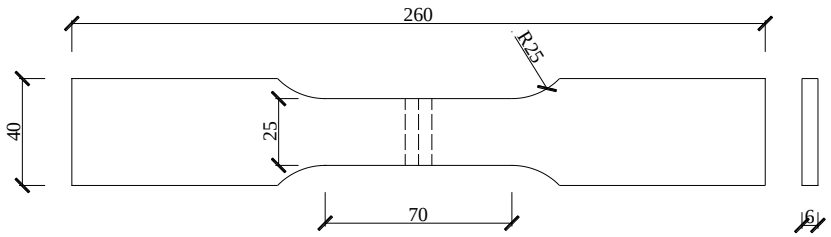

(b) 960-6-G1-2

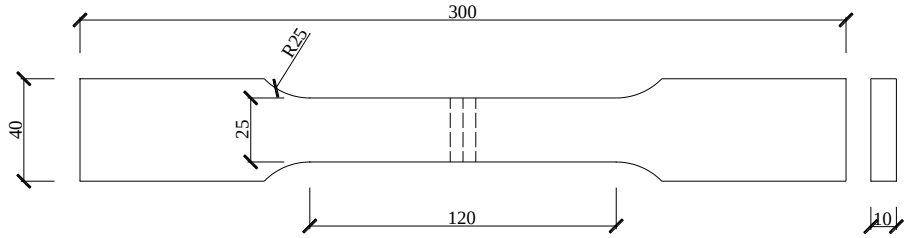

(c) 690-10-G1-2

Figure 3.48 Dimensions of butt-welded tensile coupons for validation (Unit:mm)

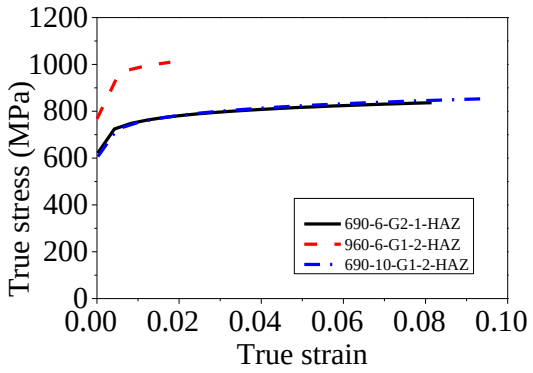

Figure 3.49 True stress strain curves for HAZs

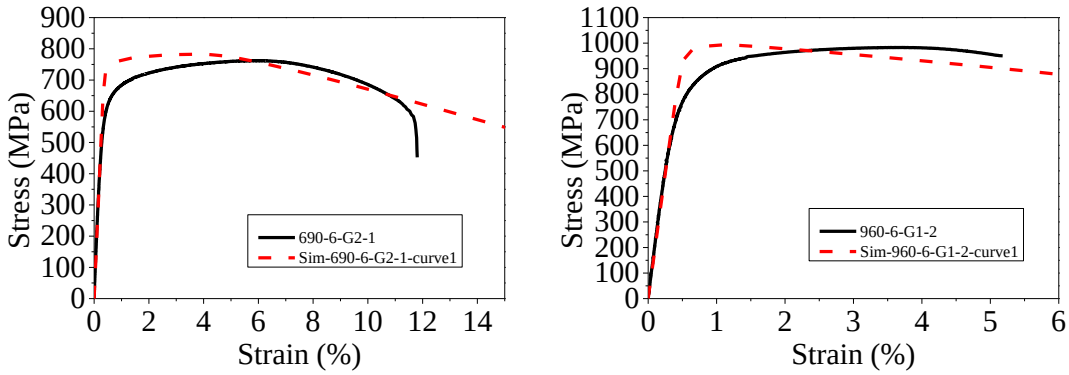

(a) 690-6-G2-1 (b) 960-6-G1-2

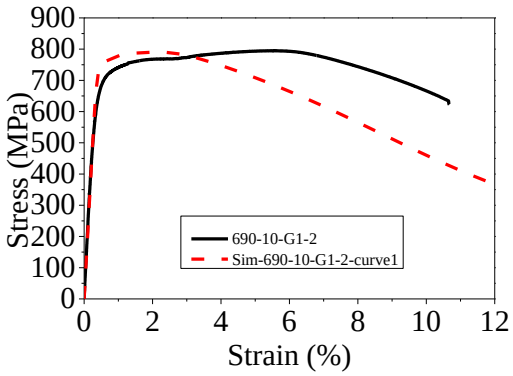

(c) 690-10-G1-2

Figure 3.50 Comparisons between experimental and numerical stress-strain curves based on polynomial regression model

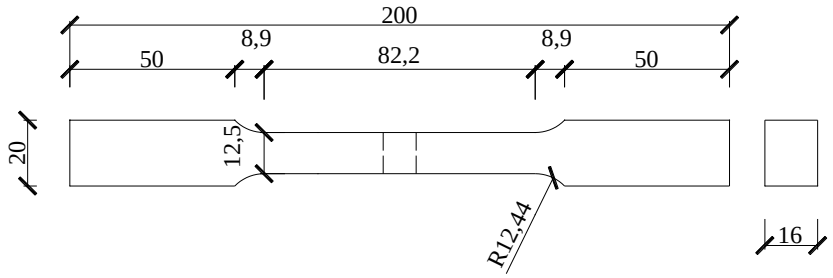

Figure 3.51 Dimensions of 690-BJ16-3.2 (Unit: mm)

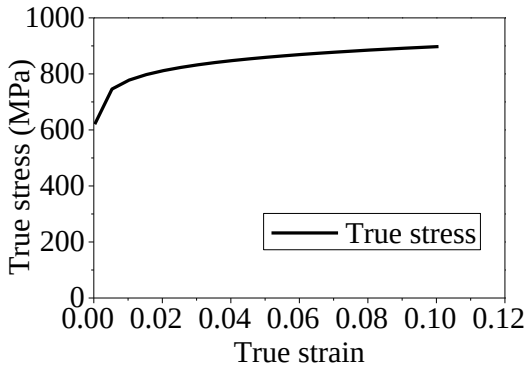

Figure 3.52 True stress-strain curve for HAZ of 690-BJ16-3.2 based on polynomial regression model

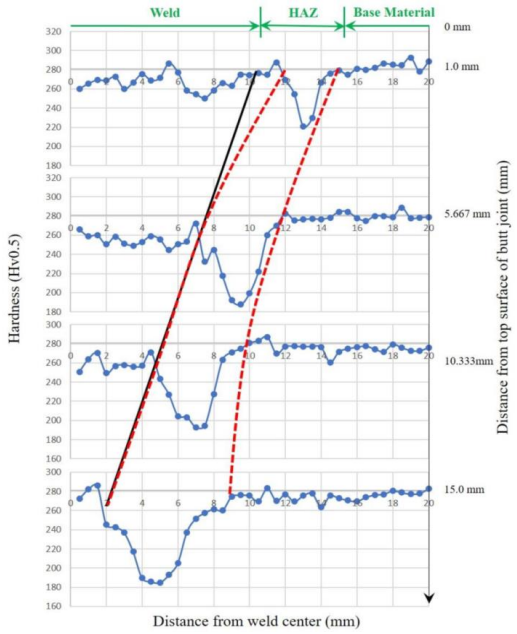

Figure 3.53 Hardness distribution for 690-BJ16-3.2

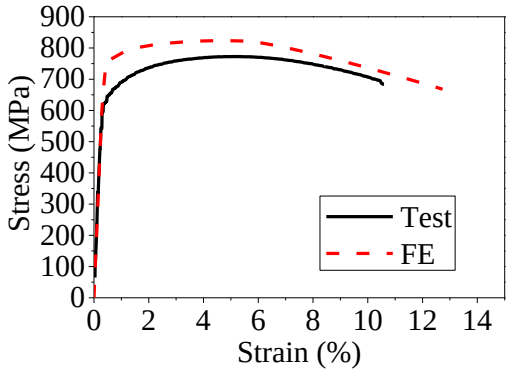

Figure 3.54 Comparisons between experimental and numerical stress-strain curves for 690-BJ16-3.2

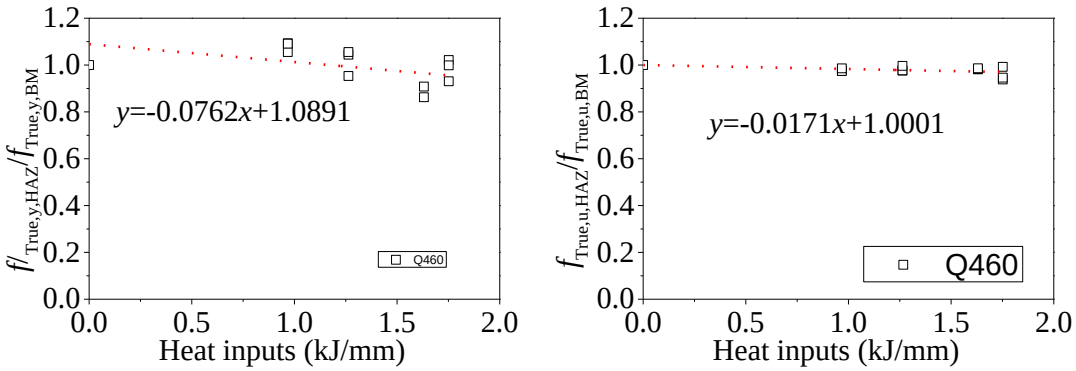

(a) Q460, $f_{True,\ y,\ HAZ}/f_{True,\ y,\ BM}$ (b) Q460, $f_{True,\ u,\ HAZ}/f_{True,\ u}$

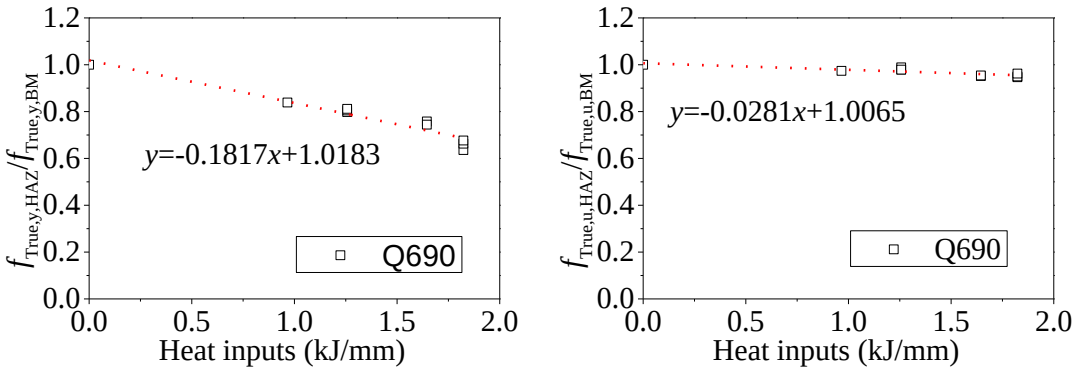

(c) Q690, $f_{True,\ y,\ HAZ}/f_{True,\ y,\ BM}$ (d) Q690, $f_{True,\ u,\ HAZ}/f_{True,\ u}$

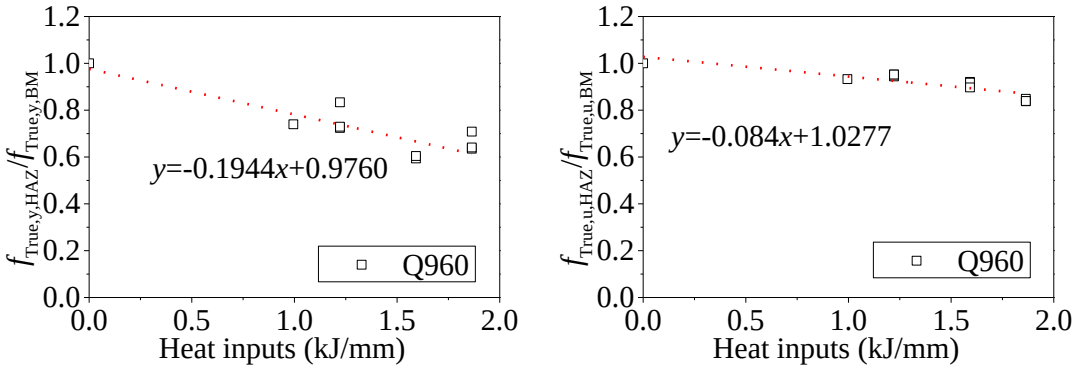

(e) Q960, $f_{True,\ y,\ HAZ}/f_{True,\ y,\ BM}$ (f) Q960, $f_{True,\ u,\ HAZ}/f_{True,\ u}$

Figure 3.55 Linear regression models for $f_{True,\ y,\ HAZ}/f_{True,\ y,\ BM}$ and $f_{True,\ u,\ HAZ}/f_{True,\ u}$ with different heat inputs

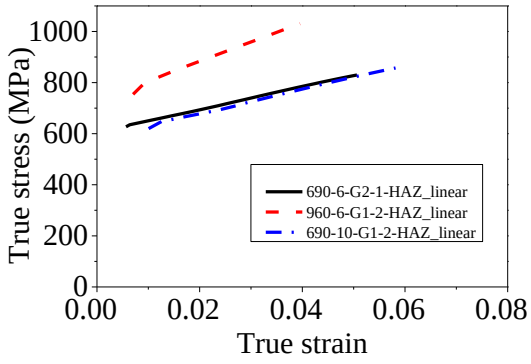

Figure 3.56 True stress-strain curves for HAZs by linear regression model

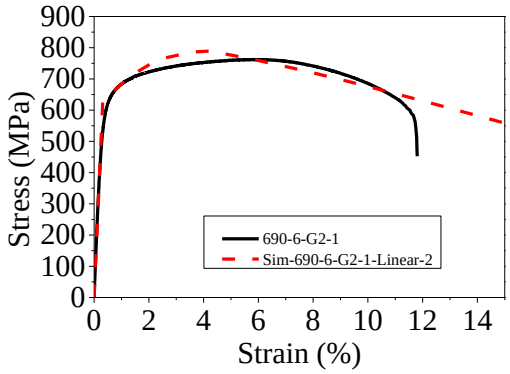

(a) 690-6-G2-1

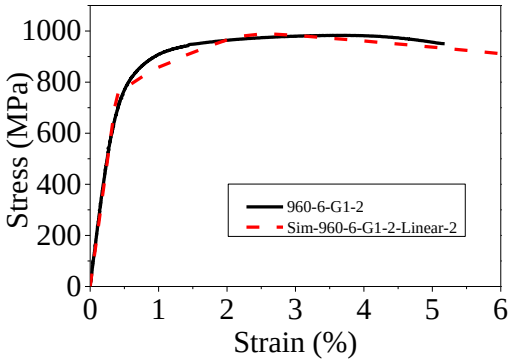

(b) 960-6-G1-2

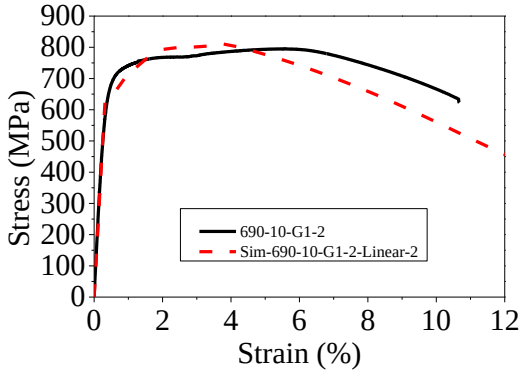

(c) 690-10-G1-2

Figure 3.57 Comparisons between experimental and numerical stress-strain curves based on linear regression model

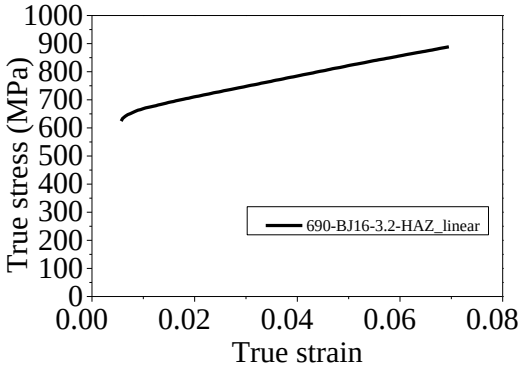

Figure 3.58 True stress-strain curve for HAZ of 690-BJ16-3.2 based on linear regression model

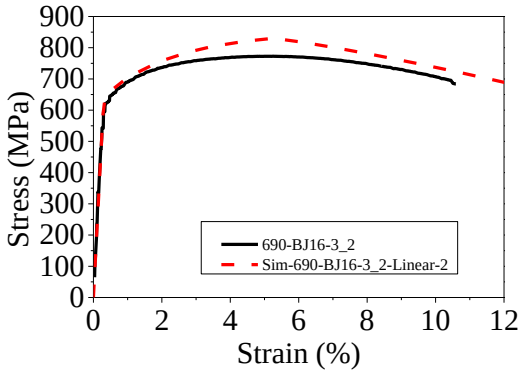

Figure 3.59 Comparisons between experimental and numerical stress-strain curves for 690-BJ16-3.2 based on linear regression model

Chapter 4 Experimental investigations of HSS single row T-stub joints

4.1 Introduction

This chapter demonstrated the experimental investigations of the HSS single row T-stub joints. HSS single row T-stub joints were cut from the long T-stub joints fabricated by different steel grades and heat inputs. Tensile tests were implemented for the HSS single row T-stub joints until the ultimate failure happening. Hardness distributions were obtained from the test blocks cut from the long T-stub joints by an automatic hardness tester. Based on the test results, the influence of welding on the single row T-stub joints were discussed with details, including plastic resistance, ultimate resistance, deformation ability and failure modes. Finally, the design equations in EN 1993-1-8 (CEN, 2005a) were introduced and the applicability of these equations on the tested HSS single row T-stub joints was evaluated.

4.2 Experimental programme

4.2.1 Base material

In this test, there were 3 kinds of high strength steel, including Q460, Q690 and Q960. For each steel grade, two kinds of nominal plate thicknesses were applied, which were 6 mm and 20 mm. Table 4.1 demonstrates the nominal chemical compositions for all the base metals according to the mill certificates. The tensile coupons were cut from the base metal for coupon tests. The dimensions were designed according to ISO 6892-1 (ISO, 2019), as shown in Figure 4.1. The tested stress-strain curves were given by Figure 4.2. Taking “460-T20-1” as an example to illustrate the nomenclature: “460” denoted the steel grade; “T20” denoted the nominal plate thickness was 20 mm, “1” denoted it was the first tensile coupon in the “460-T20” group. The average Young’s modulus (E), yield stress (f_y), ultimate stress (f_u), ultimate strain (ε_u) and fracture strain

(ε_f) were listed in Table 4.2.

4.2.2 Specimens

4.2.2.1 Specimen information

The study emphasised the effects of the heat inputs and steel grades on the mechanical behaviours of the single row T-stub joint made of HSS. The single row T-stub joint was shown in Figure 4.3. It consisted of a web and a flange. The nomenclature for the geometry was as follows: t_w represented the web thickness. h_w represented the web height. w_f represented the width of the joint. t_f represented the flange thickness. l represented the flange length. e_1 represented the end distance. d_i represented the bolt hole diameter. t_H and t_V denoted the horizontal and vertical weld leg size for the welds, respectively. In this investigation, there are two configurations of end distances (e_1), as shown in Figure 4.4(a)(b). The weld details were also shown in Figure 4.4(c), where the gap width was 1.2 mm and the blunt edge was 0 mm. These weld details complied with AWS D1.1 (AWS, 2015). Besides, for each steel grade, 3 kinds of heat input were adapted to fabricate the single row T-stub joint. The specimen groups were illustrated in Table 4.3. Taking Q460-H1-E80-Rig as an example to illustrate the nomenclature: "Q460" denoted the steel grade; "H1" denoted the heat input, H1<H2<H3; "E80" denoted the end distance was 80 mm; "Rig" denoted the boundary condition was rigid. The heat input in Table 4.3 was obtained by calculating the average heat input of all the welding passes in this T-stub joint as described by Eq. 4.1 (Sun et al., 2018b, Gharibshahiyan et al., 2011), where Q is heat input in kJ/mm, N is the total number of welding passes, U is voltage in V, I is current in A, and s is the welding speed in mm/min . The measured dimensions for all the single row T-stub joint were listed in Table 4.4. For the single row T-stub joint with a flexible boundary condition, two identical T-stub were installed together. Therefore, the dimensions included both T-stubs for this kind of joint.

$$Q = \frac{1}{N}\sum \frac{60UI}{1000s} \qquad \text{Eq. 4.1}$$

4.2.2.2 Specimen fabrication

A series of procedures were conducted to fabricate the single row T-stub joints. The webs and flanges for the long T-stub joints were cut from parent plates by laser cutting first. The webs were then milled to form the weld bevel conforming to the weld details. Milling did not have heat effect on the webs, as the temperature was not high during and after milling.

There were 3 steel grades, and for Q460 and Q690, matching welding was achieved by selecting corresponding filler electrode, shown in Table 4.5. For Q960 high strength steel, the filler electrode ER 120S-G was selected for welding. This filler electrode had an ultimate strength no less than 830 MPa stipulated in AWS A5.28/A5.28M: 2005 (AWS, 2005), which was smaller than the nominal yield strength of Q960. Therefore, judging from this aspect, it was undermatched welding. The web and flange were spot welded to form a long T-stub joint. It should be noted that the gaps between the web end and flange surface should be 1.2 mm, as depicted in weld details. In addition, several clamps were utilised to fix the long T-stub joint to prevent distortion during welding, as shown in Figure 4.5. Before welding, the T-stub joint was preheated to around 200 ℃, shown in Figure 4.6. The interpass temperature was no more than 200 ℃, shown in Figure 4.7. Grinding and cleaning for the previous welding pass were conducted before welding next welding pass. For welding position, flat welding was adapted. The welding was conducted in a windless environment to prevent the formation of porosity.

Gas metal arc welding (GMAW) was used for welding. The shielding gas consisted of 80% Ar and 20% CO_2. The wire stickout length of filler electrode was around 15 mm and should be kept stable during the overall welding process. There were 3 different

heat inputs ranging between 0.5 - 1.3 kJ/mm, whose welding parameters were shown in Table 4.6. If higher heat input was adapted, it would penetrate the 6 mm flange plate. For each heat input, multi-pass welding was adapted. For each welding pass, it was located at different locations on the web bevel. Therefore, welding parameters were slightly adjusted to achieve satisfactory welding (considering the effect of gravity). This may cause that the welding parameters for each welding pass were slightly different for each long T-stub joint. During welding, the welding angle and placement of welding gun were carefully controlled and adjusted by two experienced welders, shown in Figure 4.10. Two welding robots were used to conduct welding at two sides, shown as Figure 4.8. This can avoid carbon arc gauging, thus improving fabricating efficiency and achieving full penetration. The brand numbers of the welding robots were Panasonic TM-1400GIII and TM-1400WGIII. Two different welding robots were adapted because they have different current modes, thus preventing electromagnetic interference. During welding, one robot was initiated first and after 1 second the other robot was initiated too, also aiming to reduce electromagnetic interference.

After welding, ultrasonic detection was implemented for all the long T-stub joints. The results demonstrated that all the long T-stub joints achieved satisfactory welds without discontinuity inside. Therefore, further procedures can be implemented to acquire the single row T-stub joints.

The parts of the long T-stub joint corresponding to the start and end the welds were cut and abandoned because there would exist discontinuity in these regions. The single row T-stub joint was cut from the long T-stub joint by sawing machine (Figure 4.11). Besides, small test blocks for hardness tests were also cut by sawing machine from the long T-stub joints, whose dimensions were shown in Figure 4.12. Finally, bolt holes on the flange of the single row T-stub joints were drilled by laser cutting.

4.2.3 Test setup and instrumentation

A servo-hydraulic universal testing machine (UTM) with a capacity of 2000 kN was adapted to apply the axial tension for the single row T-stub joints. For the rigid boundary condition, a steel T-support was installed on the UTM. The flange of the T-support was thick and rigid. Therefore, its flange had almost no deformation during loading. The single row T-stub joint was installed onto the T-support by two 12.9 M30 bolts. The test setup was shown in Figure 4.13(a)(b). For the flexible boundary condition, two identical single row T-stub joints were connected by two 12.9 M30 bolts, shown in Figure 4.13(c)(d). In Table 4.3, the rigid boundary was represented by "Rigid", and the flexible boundary condition was represented by "Flexible".

There were 2 LVDTs which measured the displacement at both sides of the single row T-stub joint. A L-shaped aluminium alloy member was clamped on the web for the specimen to facilitate 2 LVDTs on both sides. The upper surface of the L-shaped aluminium alloy member was 103 mm away from the surface of the T-support, so that 2 LVDTs can measure the deformation of T-stub at the 100 mm height of the web because the thickness of the L-shaped timber was 3 mm. The instrumentations for joints with different end distances were given in Figure 4.14. A grinder was used to remove rust before sticking strain gauges. After grinding, white straight lines were marked on the single row T-stub joint to make deformation more visible. Then, strain gauges were installed on the T-stub joint by glue. They were installed along the possible plastic hinges. After instalment of measurement systems, the wires of LVDTs, strain gauges, load channel, and displacement channel were all connected to the data logger. The loading rate was set as 1mm/min.

BUEHLER EcoMet 30 in Figure 4.15 was used to grind and polish the test blocks. The rotating speed was between 250 and 450 rpm, and the grinding load was between 5 and 20 N. Abrasive sandpapers with 60#, 120#, 180#, 240#, 320#, 600# and 1000# were

utilised in a sequence to grind the surface of the test blocks until it was flat. After grinding, polishing was implemented by the same EcoMet 30 with adding MasterPolish (Figure 4.16) which had a diameter of 0.05 μm. Finally, the test blocks obtained a mirror-like surface for hardness tests. The two surfaces of the sample should be parallel, thus the automatic hardness tester could recognise the size and dimension of indentations.

The standard HV0.5 hardness test was conducted by an automatic hardness tester DURAMIN-40 A3 (Figure 4.17). There was one indentation line for each test block, located at the centre of the plate thickness. The distance between the indentation lines and between the surfaces of the block and the outer indentation lines complied with ISO 6507-1 (ISO, 2018). Two indentations had a distance of 0.5 mm between their centres. During testing, the full test force 500gf was lasted for 10 s.

4.3 Experimental results of single row T-stub joints

4.3.1 Failure modes and load-displacement curves

The failure modes were determined when the ultimate capacity of the single row T-stub was reached, which means the joint ruptured and thus the UTM stopped. The failure modes for all the single row T-stub joints were summarised in Table 4.7. The observed failure modes of single row T-stub joints at the ultimate state included flange punching shear failure, bolt hole failure, complete yielding of flange with stripping out of nut, and a combination of bolt hole failure and weld toe cracking, as shown in Figure 4.18.

Specimen Q690-H3-E80-Rig showed a complete yielding of flange along with nut stripping. The stripping out of nut was caused by the failure of thread on the bolt shank, shown in Figure 4.19. It can be deduced that if the thread had kept integral, this specimen would fail in flange punching shear, because the flange cracks near the weld

toe were deep and wide while the flange near bolt hole did not neck.

The overall load-displacement curves for the single row T-stub joints under axial tension were shown in Figure 4.20. There were usually three stages in the load-displacement curves in Figure 4.20 (a-d) and (f): elastic stage, plastic stage and second hardening stage. In the second hardening stage, significant membrane forces had developed in the flange regardless of end distances and boundary conditions. In Figure 4.20 (e), severe flange cracks developed along the weld toe, which impaired the flange thickness. After the stress redistribution, Q960 single row T-stub joint with nominal 6 mm flange thickness went into the second hardening stage and the membrane action developed, behaving like a T-stub joint with smaller flange thickness. The repeated specimens Q690-H3r-E80-Rig-Repeat and Q960-H2-E80-Rig-Repeat indicated that the test results were reliable because their load-displacement curves agreed well with Q690-H3-E80-Rig and Q960-H2r-E80-Rig, respectively.

4.3.2 Influence of heat input on test results

Generally, the heat input during welding can influence the load-displacement curves. Except specimens with Q960, elastic stages of single row T-stub joints with the same steel grade and end distances overlapped with each other, indicating that the heat input did not affect initial stiffness significantly for these specimens. For single row T-stub joints made of Q460, Q690 and Q960 with e_1 = 80 mm, plastic stages were parallel for the same steel grade. For example, for Q460 single row T-stub joints, Q460-H1-E80-Rig had the lowest heat input, but its plastic stage was higher than other two specimens. This phenomenon was more obvious for Q690 and Q960 single row T-stub joints, which implied that welding could affect plastic stages, and this effect got more significant for higher steel grades. However, for single row T-stub joints made of Q460 and Q690 with e_1 = 40 mm, the plastic stages with different heat inputs also overlapped with each other, which may be attributed to the small end distance. It may because for T-stub joints with

long end distances, the yield lines near the weld leg developed more significantly than T-stub joints with short end distances. Nevertheless, for Q960 single row T-stub joint with e_1 = 40 mm, the plastic stage of Q960-H3-E80-Rig was significantly lower than the other two specimens as its heat input was highest. As for the second hardening stage, except specimens made of Q460 and Q690 with e_1 = 40 mm, the second hardening stages for other specimens descended as the heat input increased for the same steel grade, especially for Q960. Besides, Figure 4.20 (e) and (f) show that as the heat inputs increased, the moment that flange near weld toe cracked got advanced, represented by the sudden drop of load-displacement curves in the plastic stages.

Figure 4.21 to Figure 4.26 showcase the influence of heat inputs on the failure modes. Generally, all the specimens showed cracks on the flange along the weld toe. For Q460 single row T-stub joints, the shape and depth of crack did not vary significantly with heat inputs regardless of end distances, as shown in Figure 4.21 and Figure 4.22. For Q690 single row T-stub joints with 80 mm end distance, the failure mode switched from bolt hole fracture to flange punching shear as the heat input increased. Besides, the flange cracks near the weld toe became wider and deeper for Q690 and Q960 single row T-stub joints with the increase of heat inputs, as shown in Figure 4.23 to Figure 4.26. The yield stress of butt-welded tensile coupons was reduced with the increase of heat inputs. Assuming the von Mises yield criterion is applicable, and the equivalent stress-strain curve of butt-welded tensile coupon is applicable for other loading cases. For the T-stub joint under tension, the equivalent stress along the weld toe on the flange yielded earlier for joints with higher heat inputs. After yielding, the equivalent plastic strain began to accumulate and reached to the fracture initiation earlier. Then, damage developed, and the cracks got wider and deeper. Therefore, the flange cracks near weld toe became wider and deeper for Q690 and Q960 T-stub joints with the increase of heat input at the ultimate state.

Table 4.7 shows that for all Q960 single row T-stub joints, the failure modes were flange punching shear failure, regardless of end distances and heat input. This implied that the material deterioration of Q960 was more severe than Q460 and Q690, because for Q460 and Q690, single row T-stub joint with e_1 = 40 mm failed in bolt hole fracture.

Table 4.8 exhibits the experimental results of the plastic resistance, ultimate load, elastic stiffness and displacement ductility coefficient of all single row T-stub joints. The plastic resistance was determined as the load corresponding to the intersection point between slope lines of elastic and plastic stages. The ultimate load was defined as the peak load during the overall loading process. The elastic stiffness was defined as the slope of elastic stage. The displacement ductility coefficient was calculated as the ratio between displacement corresponding to ultimate load and displacement corresponding to plastic resistance. They were all obtained from the load-deformation curves of the tested single row T-stub joints.

4.3.2.1 Plastic resistance

First yield resistance can be obtained from tested load-displacement curves by intersecting the slopes of elastic and plastic stages, shown in Figure 4.27. It is also named as the plastic resistance (Liang et al., 2019, Coelho, 2004) . It is controlled by the yield stress of the plastic hinge. It is widely accepted as the design plastic resistance of the joint before large deformation appears (CEN, 2005a).

Figure 4.28 shows the effect of heat input on the plastic resistance of single row T-stub joints. It reveals that regardless of steel grade and end distance, the plastic resistance decreased as the heat input increased. The reason may be that welding could reduce the yield stress for HAZ; the yield strength reduction got more obvious as the heat input increased.

4.3.2.2 Ultimate load

The ultimate load in this study is defined as the maximum load that the component can resist before losing the ability to bear load. In this study, the ultimate load was the peak load during the overall loading process for most specimens. While for Q960 single row T-stub joint with e_1 = 80 mm, the ultimate load was the peak load before severe cracks along the weld toe developed. It was because the cracks were so severe that the deformations were obvious, and the joint was not proper to resist more load.

For single row T-stub joints failed in flange punching shear, the ultimate load is controlled by flange cracks near the weld toe. The flange near weld toe ruptured immediately after reaching ultimate load, therefore the load-displacement curves had a sharp drop. In contrast, for single row T-stub joints failed in bolt hole fracture, the ultimate load needs to be discussed. As shown in Figure 4.20, Q460-H1-E40-Rig, Q460-H2-E40-Rig and Q460-H3-E40-Rig failed in bolt hole fracture immediately when reaching ultimate load. Their ultimate load was controlled by bolt hole fracture. Q690-H1-E80-Rig, Q690-H1-E40-Rig, Q690-H2-E40-Rig and Q690-H3-E40-Rig also failed in bolt hole fracture. However, they did not rupture immediately when reaching peak load. Instead, the load dropped and the flange cracks near weld toe kept developing after peak load. Then during the load descending process, the bolt hole suddenly ruptured. For this situation, although their failure mode was bolt hole failure, their ultimate load was still determined by the flange cracks near the weld toe, which was influenced by the heat input.

Figure 4.29 presents the influence of the heat input on ultimate loads of single row T-stub joints. In Figure 4.29 (a), the ultimate load of Q460 single row T-stub joint with e_1 = 80 mm did not simply reduce as the heat input increased. In Figure 4.29(b), the ultimate load of Q460 single row T-stub joints with e_1 = 40 mm reduced as the heat input increased. Although the ultimate load of these joints was controlled by bolt hole

fracture, the yield line of the flange along the weld toe formed at the ultimate state. Since the yield strength decreased as the heat input increased, the ultimate load was reduced finally.

Figure 4.29 (c) (e) and (f) reveals that for Q690 and Q960 single row T-stub joint, the ultimate load descended remarkably as the heat input increased. This may be attributed to the fact that for HSS, the welding induced reduction in the tensile strength got more severe for Q690 and Q960, as illustrated in Chapter 3. For these T-stub joints in Figure 4.29 (c) (e) and (f), their ultimate loads were controlled by the flange rupture near the weld toe, which got more significant for higher heat input.

4.3.3 Influence of end distance on test results

End distances can influence the single row T-stub joint behaviours. In Figure 4.20(e), in the plastic stage, all the Q960 single row T-stub joints with e_1 = 80 mm developed cracks near the weld toe severely as the load-displacement curves dropped significantly. In contrast, the Q960 single row T-stub joints with e_1 = 40 mm did not crack severely in plastic stage. Besides, there existed a tendency in Table 4.7 that if the end distance increased, the failure mode switched from flange punching shear to bolt hole failure, especially for the Q460 and Q690 T-stub joints.

4.3.3.1 Deformation ability

Figure 4.30 compared load-displacement curves of single row T-stub joints with different end distances. It was shown that longer end distances could improve the initial stiffness significantly. Besides, the maximum displacement corresponding to the ultimate state increased if the end distance was reduced. The deformation ability could be quantified by the ductility coefficient, which was defined in Figure 4.31 (Liang et al., 2019). It was the ratio of the displacement corresponding to the ultimate load and the displacement corresponding to the plastic resistance. Figure 4.32 shows the tendency that displacement ductility coefficients varied with end distance. It could be

observed that generally, for the Q460 and Q960 single row T-stub joints, reducing the end distances could enlarge the deformation ductility coefficients. Since the ultimate load definitions varied for Q960 T-stub joints with different end distances, this improvement was quite significant. For Q690 T-stub joints, however, reducing the end distances could reduce the deformation ductility coefficients.

4.3.2.2 Plastic resistance

Figure 4.33 shows the effect of end distance on the plastic resistance of single row T-stub joints. Larger end distance can enhance the plastic resistance, as the plastic resistances of T-stub joints with e_1 = 80 mm were two times than that of T-stub joints with e_1 = 40 mm. This phenomenon was in accordance with the design equation EN 1993-1-8 (CEN, 2005a). In addition, the influence of heat input on plastic resistance may get lighter if end distance was reduced, as the slope in Figure 4.33 decreased if the end distance was reduced to 40 mm.

4.3.3.3 Ultimate load

Figure 4.34 shows the influence of end distance on the ultimate load. For Q460 and Q690 single row T-stub joints made of H1 and H2, reducing end distance can reduce the ultimate load. However, for the Q690 single row T-stub joints made of H3, the joint with e_1 = 40 mm had higher ultimate load than the joint with e_1 = 80 mm. For Q960 single row T-stub joints with the same level heat input, joint with e_1 = 40 mm had higher ultimate load than joint with e_1 = 80 mm. The reason was that for Q690 and Q960 T-stub joints with e_1 = 80 mm, the welding effect was so significant that the HAZ deteriorated severely. Therefore, when the flange cracked along the weld toe, it ruptured immediately, thus reaching to the ultimate load. While for Q690 and Q960 joints with e_1 = 40 mm, the membrane action developed, and the ultimate load was achieved when flange punching shear happened. Therefore, the increase of ultimate load caused by the membrane action surpassed the decrease of ultimate load induced by the HAZ deterioration.

4.3.4 Influence of steel grade on test results

4.3.4.1 Plastic resistance

Figure 4.35 presents the influence of steel grade on the plastic resistance. It was revealed that the plastic resistance increased as the steel grade increased under all heat inputs.

4.3.4.2 Ultimate load

Figure 4.36 presents the influence of steel grade on the ultimate load. The tendency revealed by Figure 4.36 showed that under certain circumstances, especially high heat inputs, the ultimate load could decrease as the steel grade increased. In all groups, the ultimate load of the Q960 T-stub joints was the minimum. This can be attributed to the welding induced material deterioration for Q960. For the Q960 single row T-stub joints with e_1 = 80 mm, the ultimate load is defined as the peak load before severe flange cracking. No membrane action was considered. In addition, welding could also impair the steel strength of the HAZ. Therefore, the ultimate load of the Q960 joints with e_1 = 80 mm was less than that of Q460 and Q690. For the Q960 single row T-stub joints with e_1 = 40 mm, although the membrane action developed and was included in the ultimate load, the flange near the weld toe cracked and impaired the thickness. Therefore, the ultimate load was less than that of Q460 and Q690. In particularly, Figure 4.36 (e) shows that the ultimate load decreased as the steel grade increased. The reason for Q690 behind this is similar to Q960. This fact implied that for the HSS single row T-stub joints, if the heat input was large, it would offset the advantage of HSS and cause strength degradation for the joints.

4.3.4.3 Deformation ability

Figure 4.37 shows the influence of steel grade on the displacement ductility coefficient. In Figure 4.37 (a – d), the displacement ductility coefficients increased as the steel grade increased from Q460 to Q690. Nevertheless, the coefficients decreased as the steel grade increased to Q960. For Q960 joints with e_1 = 80 mm, the ultimate state was

defined as the moment the flange cracked, which was prior to flange punching shear. Therefore, its coefficients degraded. For Q960 joints with e_1 = 40 mm, the actual flange thickness was less than 6 mm as a result of the flange cracks, thus reducing its coefficient even though the membrane action developed. The coefficients of Q960 were minimum in all groups. In Figure 4.37 (e) and (f), the displacement ductility coefficients decreased as the steel grades increased with the heat input equal to around 1.3 kJ/mm. Under this heat input, Q690 and Q960 both cracked which impaired flange thickness. Therefore, the joints behaved with a thinner flange, whose displacement ductility was reduced.

4.3.5 Influence of boundary conditions

Figure 4.38 compares the load displacement curves with different boundary conditions. For the same steel grade, the elastic stages almost overlapped with each other, indicating that the boundary condition did not affect initial stiffness significantly. Figure 4.38 (a) shows that for the Q690 single row T-stub joints with flexible boundary condition, the peak load reduced significantly, while the deformation ability increased observably. Figure 4.38 (b) shows that for the Q960 single row T-stub joints with flexible boundary condition, the flange near the weld toe also cracked significantly in plastic stage, and the ultimate load was also defined as the peak load before severe cracking. Therefore, the deformation ability was not prominent for Q960 joints with flexible boundary.

4.3.6 Hardness distributions of single row T-stub joints

Figure 4.39 to Figure 4.41 demonstrate the hardness distributions of the flange for the single row T-stub joints. The regions between the red dash lines were HAZ. It was found that the hardness distribution within the HAZ was not uniform. For the Q460 T-stub joints, the hardened regions existed in the HAZ with higher hardness compared to the BM. And the softened regions were near the hardened region with lower hardness compared to the BM. For the Q690 and Q960 T-stub joints, only softened regions existed. But the central regions at the HAZ had higher hardness than two sides. In this

study, the delivery condition of Q460 was as rolled, while for Q690 and Q960 the delivery condition was quenching and tempering (QT). After welding thermal cycles, Q460 experienced a not strictly controlled process of quenching and tempering, which caused hardened regions in the HAZ. Q690 and Q960, in contrast, underwent a needless heat treatment without strict control, which impaired their harnesses.

The nominal flange thickness was only 6 mm. Therefore, the hardness distribution along the plate thickness was assumed to be homogeneous. Table 4.9 shows the HAZ width and average hardness of the T-stub joints. Figure 4.42 and Figure 4.43 plot the test results in Table 4.9. It was found that the relationship between the HAZ width and the heat input was linear for all steel grades, as expressed in Eq. 4.2 to Eq. 4.4, where W is the HAZ width in mm, Q is the heat input in kJ/mm. Besides, the HAZ average hardness did not completely reduce as the heat input increased. For example, the tendency of the Q460 T-stub joints was opposite to that of the Q690 and Q960 T-stub joints.

$$W_{Q460,T-stub} = 10.767 \times Q + 18.432 \quad \text{Eq. 4.2}$$

$$W_{Q690,T-stub} = 6.980 \times Q + 37.141 \quad \text{Eq. 4.3}$$

$$W_{Q960,T-stub} = 5.502 \times Q + 32.902 \quad \text{Eq. 4.4}$$

4.4 Current design equation evaluation

4.4.1 Introduction to current design methods for T-stub joint

EN 1993-1-8 (CEN, 2005a) provides the design method to calculate the plastic resistance for the T-stub joint. There are three possible failure modes: complete yielding of flange, bolt failure with yielding of flange and bolt failure. In the complete yielding of flange, four plastic hinges form in which two are located at the bolt axes and two are

located at the flange near weld toes. In the bolt failure with yielding of flange, two plastic hinges developed at the flange near the weld toes, and prying forces cause the premature of bolt fracture. In the bolt failure, only the bolt fractured (Francavilla et al., 2015). Corresponding design equations are regulated for them, as illustrated in Table 4.10, where m and n are presented in Figure 4.44, $F_{t, Rd}$ is the plastic resistance of the bolt. The plastic moment of the flange is expressed by Eq. 4.5, where $f_{y, f}$ is the yield stress of the flange, t_f is the flange thickness, b_{eff} is the effective width for single row T-stub joint, as illustrated in Table 4.11. The plastic resistance of the T-stub joint is taken as the minimum resistance among $F_{T, 1, Rd}$, $F_{T, 2, Rd}$ and $F_{T, 3, Rd}$.

$$M_{pl,Rd} = \frac{t_f^2}{4} f_{y,f} b_{eff} \qquad \text{Eq. 4.5}$$

Actually, EN 1993-1-8 (CEN, 2005a) regulates a bi-linear curve which had an elastic-perfect plastic response of the T-stub joint (Zhao et al., 2021), as it neglects the material strain hardening effect of the T-stub joint. This design method assumes that once the T-stub joint reaches its plastic resistance, the load will remain the plastic resistance while the displacement will keep increasing. Therefore, by adapting the design recommendations in EN 1993-1-8 (CEN, 2005a), the ultimate resistance of the T-stub joints has the same value as the plastic resistances.

4.4.2 Applicability of current design equations according to test results

Table 4.12 shows the plastic resistance and ultimate resistance of the single row T-stub joints obtained from tests and design methods in EN 1993-1-8 (CEN, 2005a). $F_{p, test}$ and $F_{u, test}$ represent the plastic resistance and ultimate resistance obtained from test results, respectively. $F_{p, EC3}$ and $F_{u, EC3}$ represent the plastic resistance and ultimate resistance obtained from EN 1993-1-8 (CEN, 2005a), respectively. It was found that EN 1993-1-8 (CEN, 2005a) could give safe predictions of both plastic resistance and ultimate resistance, because all the $F_{p, test}/ F_{p, EC3}$ and $F_{u, test}/ F_{u, EC3}$ were greater than unity.

Figure 4.45 shows the influence of steel grade and heat input on $F_{p,\,test}/\,F_{p,\,EC3}$. Except single row T-stub joint made of Q690 with e_1 = 40 mm, the ratio steadily dropped as the heat input increased for all other specimens. This is because the $F_{p,\,test}$ dropped as the heat input increased. For single row T-stub joint with the same end distance, as the steel grade increased, $F_{p,\,test}/\,F_{p,\,EC3}$ dropped under the same heat input level. Particularly, for the Q960 single row T-stub joint, $F_{p,\,test}/\,F_{p,\,EC3}$ was close to 1. It reflected the fact that welding had the most significant influence on this steel grade. The EN 1993-1-8 was safe to predict the plastic resistances of the joint, and as steel grade increased, the degree of overestimation was reduced.

Figure 4.46 presents the influence of heat input and steel grade on $F_{u,test}\,/\,F_{u,\,EC3}$. For all the specimens, the ratio was larger than 1, ensuring a safe design. However, the ultimate load predictions by EN 1993-1-8 (CEN, 2005a) were greatly conservative, for example, the ratio was greater than 8 for the Q460 and Q690 single row T-stub joints with e_1 = 40 mm. This conservativeness was caused by the fact that design equations in EN 1993-1-8 (CEN, 2005a) are not applicable for the T-stub joint under large deformation. In this circumstance, the material strain hardening and membrane action develop in the flange of T-stub joint, thus improving the ultimate resistance under large deformation (Tartaglia et al., 2020). However, the Q960 single row T-stub joints with e_1 = 80 mm had reduced conservativeness for $F_{u,test}\,/\,F_{u,\,EC3}$. For this joint configuration, the ultimate load was defined as the peak load before severe flange cracks developed near the weld toe. Thus, this joint configuration did not experience large deformation compared with other specimens.

End distance could influence $F_{u,test}\,/\,F_{u,\,EC3}$ significantly. For the single row T-stub joint under the same heat input level, $F_{u,test}\,/\,F_{u,\,EC3}$ of joint with e_1 = 40 mm was more than 1.5 times than that of joint with e_1 = 80 mm. The load-displacement curves showed that

shorter end distance could experience larger deformations, thus the degree of ultimate load enhancement caused by material hardening and membrane action was more significant, leading to conservativeness when applying EN 1993-1-8 (CEN, 2005a) to predict the ultimate load.

4.5 Summary

This chapter presented the experimental investigations of the HSS single row T-stub joints under axial tension fabricated by different steel grades and heat inputs. The long T-stub joints were matching welded by integrating a web and a flange plate carefully to achieve complete penetration welds. The shielding gas, preheating, interpass temperature, welding parameters and welding positions were carefully controlled to obtain satisfactory welds without disadvantages, checked by the ultrasonic detection. The single row T-stub joints were then cut from the long T-stub joints and drilled for holes, which had different configurations varying in end distances, steel grades, boundary conditions and heat inputs. Tensile tests were implemented for these single row T-stub joints on a servo-hydraulic universal testing machine (UTM). Test blocks for hardness tests were also cut from the long T-stub joints. Then automatic hardness tester was utilised to obtain the hardness distribution along the centreline of the flange thickness direction. Finally, the design equations in EN 1993-1-8 were evaluated based on the test results.

The observed failure modes of the single row T-stub joints at the ultimate state included flange punching shear failure, bolt hole failure, complete yielding of flange with stripping out of nut, and a combination of bolt hole failure and weld toe cracking. In the load-displacement curves, three stages were observed for most specimens: the elastic stage, plastic stage and second hardening stage. In the second hardening stage, significant membrane forces developed in the flange. The heat input could affect the joint behaviours. For the single row T-stub joints with e_1 = 80 mm, as the heat input

increased, the load at the plastic stage decreased, especially for higher steel grade. For Q690 single row T-stub joints with 80 mm end distance, the failure mode switched from the bolt hole fracture to flange punching shear as the heat input increased. Besides, the flange cracks near the weld toe became wider and deeper for the Q690 and Q960 joints with the increase of heat inputs. Furthermore, regardless of the steel grade and end distance, the plastic resistance decreased as the heat input increased, which may be attributed to the deterioration of HAZ. The influence of heat inputs on the ultimate loads was not consistent. It was observed that for the Q690 and Q960 single row T-stub joint, the ultimate load descended remarkably as the heat input increased.

The end distance could affect the single row T-stub joint behaviours. If the end distance increased, the failure mode tended to switch from the flange punching shear failure to bolt hole failure, especially for the Q460 and Q690 joints. For the Q960 single row T-stub joints, increasing end distance could lead to more severe cracks along the weld toe. For single row T-stub joints made of Q460 and Q690 with e_1 = 40 mm, different from the joints with e_1 = 80 mm, the plastic stages with different heat inputs also overlapped with each other, which may be attributed to the small end distance. Longer end distances could improve the initial stiffness but reduce the overall displacement of the joint. Meanwhile, reducing the end distances could enlarge the deformation ductility coefficients. In addition, increasing the end distance can enhance the plastic resistance. But for the ultimate load, the Q960 single row T-stub joint was an exception which showed higher ultimate load with shorter end distance. This phenomenon was attributed to the fact that the definition for the ultimate state was severe cracking along the weld toe for joints with e_1 = 80 mm, which neglected the membrane action developed furthermore.

The single row T-stub joint was influenced by steel grades. The plastic resistance increased as the steel grade increased. However, under high heat inputs, the ultimate

load could decrease as the steel grade increased. This fact implied that for the HSS single row T-stub joints, if the heat input was large, it would offset the advantage of HSS and cause strength degradation for the joints. For the deformation ability, the influence of steel grade was not simply linear, except that when the heat input was high, the displacement ductility coefficient was linearly reduced as the steel grade increased. As for the boundary condition, it would reduce the ultimate load but improve the deformation ability for Q690 T-stub joints. For Q960 T-stub joints, however, since the definition of ultimate state was different, the deformation ability was not prominent for Q960 joints with flexible boundary.

The hardness distributions of the flange of the single row T-stub joints within HAZ was not uniform. HAZ widths and average HAZ hardness were calculated based on the hardness distributions. Regression models were developed which could be utilised to predict the HAZ width based on the heat inputs. However, the HAZ average hardness did not completely reduce as the heat input increased, since for Q460, as the heat inputs increased, the average HAZ hardness increased.

The design equations in EN 1993-1-8 (CEN, 2005a) were introduced and evaluated. It was found that EN 1993-1-8 (CEN, 2005a) could give conservative predictions of both plastic resistance and ultimate resistance, because all the $F_{p,\,test}/\,F_{p,\,EC3}$ and $F_{u,\,test}/\,F_{u,\,EC3}$ were greater than unity. With the increase of heat inputs, the degree of underestimation for $F_{p,\,test}/\,F_{p,\,EC3}$ was reduced. This is because the $F_{p,\,test}$ dropped as the heat input increased. Besides, for the single row T-stub joints with higher steel grades but the same end distance, $F_{p,\,test}/\,F_{p,\,EC3}$ dropped under the same heat input level. Particularly, for the Q960 single row T-stub joint, $F_{p,\,test}/\,F_{p,\,EC3}$ was close to 1. In contrast, $F_{u,test}\,/\,F_{u,\,EC3}$ was much greater than unity, leading to a great conservative strength prediction for the ultimate load. This conservativeness was caused by the fact that design equations in EN 1993-1-8 (CEN, 2005a) are not applicable for the T-stub

joint under large deformation, in which material strain hardening and membrane action were neglected. Therefore, design methods for the ultimate capacity of the single row T-stub joints should be further investigated.

Table 4.1 Nominal chemical compositions of base material

	Nominal thickness (mm)	C	Si	Mn	P	S	V	Nb	Ti	Cr	Ni	Cu	Mo	Al	N	B	CEV
Q460	6	0.17	0.12	1.63	0.013	0.006	0.002	0.012	0.001	0.03	0.02	0.02	-	-	-	0.0003	0.45
Q690	6	0.08	0.24	1.79	0.015	0.009	0.001	0.01	0.001	0.04	0.02	0.01	-	-	-	0.0004	0.39
Q960	6	0.18	0.25	1.03	0.006	0.001	0.043	0.023	0.013	0.35	0.02	0.02	0.46	-	-	0.0015	0.52
Q460	20	0.18	0.24	1.68	0.015	0.004	0.001	0.01	0.002	0.04	0.02	0.02				0.0004	0.47
S690	20	0.14	0.24	1.28	0.008	0.0003	0.041	0.016	0.014	0.51	0.05	0.02	0.292	0.031	0.0037	0.0013	0.53
Q960	20	0.16	0.25	1.17	0.005	0.001	0.044		0.011	0.35	0.01	0.01	0.57			0.0014	0.55

Table 4.2 The tested average material properties

Steel grade	Thickness (mm)	E (MPa)	f_y (MPa)	f_u (Mpa)	ε_u (%)	ε_f (%)
Q460	6	197477	438.72	622.53	8.26	17.39
Q690	6	193820	730.91	761.88	6.46	13.68
Q960	6	206083	953.55	1002.61	6.23	13.64
Q460	20	199987	498.40	592.53	13.81	25.72
S690	20	193690	822.43	867.15	5.92	12.68
Q960	20	194780	975.88	1017.05	6.83	17.22

Table 4.3 Specimen groups

Specimen No.	Heat input (mm)	End distance (mm)	Boundary condition
Q460-H1-E80-Rig	0.531	80	Rigid
Q460-H1-E40-Rig	0.531	40	Rigid
Q460-H2-E80-Rig	0.775	80	Rigid
Q460-H2-E40-Rig	0.775	40	Rigid
Q460-H3-E80-Rig	1.267	80	Rigid

Q460-H3-E40-Rig	1.267	40	Rigid
Q690-H1-E80-Rig	0.548	80	Rigid
Q690-H1-E40-Rig	0.548	40	Rigid
Q690-H1r-E80-Flex	0.542	80	Flexible
Q690-H2-E80-Rig	0.775	80	Rigid
Q690-H2-E40-Rig	0.775	40	Rigid
Q690-H2r-E80-Flex	0.775	80	Flexible
Q690-H3-E80-Rig	1.126	80	Rigid
Q690-H3-E40-Rig	1.126	40	Rigid
Q690-H3r-E80-Rig-Repeat	1.267	80	Rigid
Q960-H1r-E80-Rig	0.547	80	Rigid
Q960-H1r-E40-Rig	0.547	40	Rigid
Q960-H2-E80-Rig-Repeat	0.775	80	Rigid
Q960-H2r-E80-Rig	0.775	80	Rigid
Q960-H2r-E40-Rig	0.775	40	Rigid
Q960-H3-E80-Rig	1.267	80	Rigid
Q960-H3-E40-Rig	1.267	40	Rigid
Q960-H3r-E80-Flex	1.267	80	Flexible

Table 4.4 Measured dimensions for single row T-stub joints

Specimen	t_w (mm)	h_w (mm)	t_f (mm)	w_f (mm)	l (mm)	*e1 (mm)*	$t_{H,\ left}$ (mm)	$t_{V,\ left}$ (mm)	$t_{H,\ right}$ (mm)	$t_{V,\ right}$ (mm)
Q460-H1-E80-Rig	20.77	297.6	6.26	69.5	299.0	18.5	6.7	10.2	7.2	8.5
Q460-H1-E40-Rig	20.77	298.0	6.27	71.2	298.8	19.6	6.1	10.0	7.0	9.3
Q460-H2-E80-Rig	20.91	298.1	6.24	69.3	298.2	18.7	7.1	8.9	5.1	10.0
Q460-H2-E40-Rig	20.95	297.7	6.23	68.8	299.3	17.2	5.2	8.1	6.8	7.3
Q460-H3-E80-Rig	20.91	297.2	6.26	70.0	298.0	18.2	5.4	10.5	4.5	10.2
Q460-H3-E40-Rig	20.91	297.8	6.27	69.5	298.9	18.2	5.3	10.2	4.8	10.0
Q690-H1-E80-Rig	20.44	297.0	6.13	69.3	297.3	18.8	8.8	10.5	10.0	10.0
Q690-H1-E40-Rig	20.52	296.5	6.23	70.1	298.4	18.8	10.3	11.2	8.6	10.5
Q690-H1r-E80-Flex-up	20.39	296.1	6.11	70.0	299.0	18.6	9.0	10.8	7.3	11.0
Q690-H1r-E80-Flex-down	20.38	297.0	6.13	71.0	298.8	19.1	7.4	11.0	9.0	11.1
Q690-H2-E80-Rig	20.27	297.2	6.16	69.5	298.9	17.0	8.5	9.0	7.5	9.0
Q690-H2-E40-Rig	20.31	296.7	6.15	69.8	299.0	19.2	7.2	9.0	8.5	9.0
Q690-H2r-E80-Flex-up	20.35	297.0	6.07	70.5	298.5	18.9	7.5	10.0	6.3	8.0
Q690-H2r-E80-Flex-down	20.38	296.8	6.08	69.1	298.9	18.4	6.3	9.0	8.0	10.0
Q690-H3-E80-Rig	20.34	297.1	6.09	69.3	297.5	19.5	9.0	10.5	9.9	13.8
Q690-H3-E40-Rig	20.41	297.0	6.08	70.5	298.2	18.4	9.1	11.5	9.8	14.5
Q690-H3r-E80-Rig-Repeat	20.32	297.0	6.23	70.5	298.6	17.7	4.9	9.6	5.3	11.3
Q960-H1r-E80-Rig	22.03	298.0	6.97	69.1	299.2	18.3	6.0	10.2	6.2	12.8
Q960-H1r-E40-Rig	22.03	298.3	6.94	68.1	298.3	19.0	7.0	10.0	7.0	10.0
Q960-H2-E80-Rig-Repeat	21.97	298.1	6.96	69.9	298.9	18.8	6.2	8.0	4.8	9.3
Q960-H2r-E80-Rig	22.16	297.3	6.87	69.5	298.5	16.5	5.4	15.2	4.8	12.5
Q960-H2r-E40-Rig	22.12	297.4	6.89	70.6	298.1	18.9	6.0	14.0	5.7	12.5
Q960-H3-E80-Rig	22.1	298.0	7.08	71.1	299.0	18.4	4.0	9.5	3.5	10.1
Q960-H3-E40-Rig	22.09	297.5	6.95	68.6	298.8	17.3	3.0	10.1	5.0	10.0
Q960-H3r-E80-Flex-up	22.06	296.8	6.99	69.1	298.5	18.3	3.2	9.0	3.9	10.8

Q960-H3r-E80-Flex-down	22.06	297.9	6.95	68.6	299.0	17.0	3.7	10.2	3.7	10.0

Table 4.5 Filler electrode for each steel grade

Steel grade	Filler electrode	Yield strength (MPa)	Ultimate strength (MPa)
Q460	AWS A5.28 ER 80S-G	N/A	550
Q690	AWS A5.28 ER 110S-G	N/A	760
Q960	AWS A5.28 ER 120S-G	N/A	830

Table 4.6 Welding parameters for T-stub joints

(a) Welding parameters for low heat input

side	No. of layer	No. of pass	type	k	I (A)	U (V)	s (mm/min)	Q (kJ/mm)
left	1	1	straight	0.800	200	22.0	300	0.704
		2	straight	0.800	180	21.0	550	0.330
		3	straight	0.800	200	22.4	350	0.614
		4	straight	0.800	180	21.0	550	0.330
		5	straight	0.800	200	22.4	350	0.614
		average						0.519
right	1	1	straight	0.800	200	24.5	300	0.784
		2	straight	0.800	180	24.0	550	0.377
		3	straight	0.800	200	24.5	350	0.672
		4	straight	0.800	180	24.0	550	0.377

		5	straight	0.800	200	24.5	350	0.672
		average						0.576

(b) Welding parameters for medium heat input

side	No. of layer	No. of pass	type	k	I (A)	U (V)	s (mm/min)	Q (kJ/mm)
left	1	1	straight	0.800	220	21.2	250	0.895
		2	straight	0.800	190	21	550	0.348
		3	straight	0.800	220	21.2	250	0.895
		average						0.713
right	1	1	straight	0.800	220	25	250	1.056
		2	straight	0.800	190	24	550	0.398
		3	straight	0.800	220	25	250	1.056
		average						0.837

(c) Welding parameters for high heat input

side	No. of layer	No. of pass	type	k	I (A)	U (V)	s (mm/min)	Q (kJ/mm)
left	1	1	straight	0.800	220	23.0	200	1.214
		2	straight	0.800	220	23.0	200	1.214
		average						1.214
right	1	1	straight	0.800	220	25.0	200	1.320
		2	straight	0.800	220	25.0	200	1.320
		average						1.320

Table 4.7 Tested failure modes for the single row T-stub joints

Specimen	failure mode
Q460-H1-E80-Rig	flange punching shear
Q460-H1-E40-Rig	bolt hole failure and weld toe cracking
Q460-H2-E80-Rig	flange punching shear
Q460-H2-E40-Rig	bolt hole failure and weld toe cracking
Q460-H3-E80-Rig	flange punching shear
Q460-H3-E40-Rig	bolt hole failure
Q690-H1-E80-Rig	bolt hole failure and weld toe cracking
Q690-H1-E40-Rig	bolt hole failure and weld toe cracking
Q690-H1r-E80-Flex	flange punching shear
Q690-H2-E80-Rig	flange punching shear
Q690-H2-E40-Rig	bolt hole failure and weld toe cracking
Q690-H2r-E80-Flex	flange punching shear
Q690-H3-E80-Rig	complete yielding of flange, stripping out of nut
Q690-H3-E40-Rig	bolt hole failure and weld toe cracking.
Q690-H3r-E80-Rig-Repeat	flange punching shear
Q960-H1r-E80-Rig	flange punching shear
Q960-H1r-E40-Rig	flange punching shear
Q960-H2-E80-Rig-Repeat	flange punching shear
Q960-H2r-E80-Rig	flange punching shear
Q960-H2r-E40-Rig	flange punching shear
Q960-H3-E80-Rig	flange punching shear

Q960-H3-E40-Rig	flange punching shear
Q960-H3r-E80-Flex	flange punching shear

Table 4.8 Test results of single row T-stub joints

Specimen	heat input (kJ/mm)	$F_{y,t}$, plastic resistance (kN)	ultimate load (kN)	Elastic stiffness (N/mm)	Δ_e (mm)	Δ_u (mm)	Δ_u/Δ_e
Q460-H1-E80-Rig	0.531	44.29	205.06	11657.2	3.42	28.86	8.44
Q460-H1-E40-Rig	0.531	19.36	172.71	2769.9	6.85	47.09	6.87
Q460-H2-E80-Rig	0.775	42.67	171.30	8922.5	3.69	24.53	6.64
Q460-H2-E40-Rig	0.775	17.56	159.59	2394.6	6.26	44.86	7.17
Q460-H3-E80-Rig	1.267	39.08	205.17	10207.5	3.53	29.98	8.49
Q460-H3-E40-Rig	1.267	16.56	159.75	3538.7	3.92	44.55	11.37
Q690-H1-E80-Rig	0.547	55.50	247.83	17801.8	3.11	30.72	9.89
Q690-H1r-E80-Flex	0.542	56.05	164.03	12511.4	2.77	71.27	25.68
Q690-H1-E40-Rig	0.547	24.46	200.16	5173.9	4.91	43.86	8.93
Q690-H2-E80-Rig	0.775	45.40	223.06	18643.8	2.43	27.92	11.48
Q690-H2r-E80-Flex	0.775	50.33	149.63	12924.7	3.65	76.03	20.82
Q690-H2-E40-Rig	0.775	23.69	185.76	4941.0	5.00	43.92	8.77
Q690-H3-E80-Rig	1.126	49.18	170.99	12089.0	3.45	22.99	6.67
Q690-H3r-E80-Rig-Repeat	1.267	44.45	189.18	15562.6	2.88	26.49	9.19
Q690-H3-E40-Rig	1.126	24.78	196.88	3485.3	6.66	43.59	6.54
Q960-H1r-E80-Rig	0.547	84.02	126.32	20896.5	5.11	13.08	2.56
Q960-H1r-E40-Rig	0.547	38.85	154.70	6747.4	6.83	32.30	4.73

Q960-H2-E80-Rig-Repeat	0.775	81.92	108.87	21011.5	3.72	12.03	3.23
Q960-H2r-E80-Rig	0.775	75.73	108.59	22517.6	3.65	13.62	3.73
Q960-H2r-E40-Rig	0.775	34.08	162.28	6550.2	5.32	34.34	6.46
Q960-H3-E80-Rig	1.267	67.84	88.78	18335.2	3.92	9.00	2.29
Q960-H3r-E80-Flex	1.267	57.83	74.76	12406.2	4.19	8.29	1.98
Q960-H3-E40-Rig	1.267	34.00	138.18	5673.1	5.66	33.30	5.88

Table 4.9 HAZ width and average HAZ hardness of the T-stub joints

Specimen	Steel grade	Average heat input	HAZ width	Average HAZ hardness
-	-	kJ/mm	mm	HV0.5
Q460-H1	Q460	0.531	24.0	214
Q460-H2	Q460	0.775	27.0	219
Q460-H3	Q460	1.267	32.0	228
Q690-H1	Q690	0.548	41.0	247
Q690-H2	Q690	0.775	42.5	234
Q690-H3r	Q690	1.267	46.0	232
Q960-H1	Q960	0.556	34.0	296
Q960-H2r	Q960	0.775	40.0	316
Q960-H3	Q960	1.267	39.0	307

Table 4.10 Design equations in EN 1993-1-8 (CEN, 2005a)

Failure modes	Design equation
Complete yielding of flange	$F_{T,1,Rd} = \frac{4M_{pl,Rd}}{m}$
Bolt failure with yielding of flange	$F_{T,2,Rd} = \frac{2M_{pl,Rd} + n\sum F_{t,Rd}}{m+n}$

Bolt failure	$F_{T,3,Rd} = \sum F_{t,Rd}$

Table 4.11 Effective width for single row T-stub joint

	Non-circular	Circular	Beam
Individual bolt row	$4m+1.25n$	$2\pi m$	W

Table 4.12 Comparison of plastic and ultimate resistance between test results and predicted results by EN 1993-1-8 (CEN, 2005a)

Specimen	$F_{p,\,test}$ (kN)	$F_{u,\,test}$ (kN)	$F_{p,\,EC3}$ (kN)	$F_{u,\,EC3}$ (kN)	$F_{p,\,test}/F_{p,\,EC3}$	$F_{u,\,test}/F_{u,\,EC3}$
Q460-H1-E80-Rig	44.29	205.06	22.67	22.67	1.95	9.05
Q460-H1-E40-Rig	19.36	172.71	13.10	13.10	1.48	13.18
Q460-H2-E80-Rig	42.67	171.30	22.11	22.11	1.93	7.75
Q460-H2-E40-Rig	17.56	159.59	12.48	12.48	1.41	12.79
Q460-H3-E80-Rig	39.08	205.17	21.98	21.98	1.78	9.33
Q460-H3-E40-Rig	16.56	159.75	12.57	12.57	1.32	12.71
Q690-H1-E80-Rig	55.50	247.83	37.97	37.97	1.46	6.53
Q690-H1r-E80-Flex	56.05	164.03	36.87	36.87	1.52	4.45
Q690-H1-E40-Rig	24.46	200.16	21.84	21.84	1.12	9.16
Q690-H2-E80-Rig	45.40	223.06	36.78	36.78	1.23	6.07
Q690-H2r-E80-Flex	50.33	149.63	35.64	35.64	1.41	4.20
Q690-H2-E40-Rig	23.69	185.76	20.90	20.90	1.13	8.89

Q690-H3-E80-Rig	49.18	170.99	37.66	37.66	1.31	4.54
Q690-H3r-E80-Rig-Repeat	44.45	189.18	36.07	36.07	1.23	5.24
Q690-H3-E40-Rig	24.78	196.88	21.03	21.03	1.18	9.36
Q960-H1r-E80-Rig	84.02	126.32	59.51	59.51	1.41	2.12
Q960-H1r-E40-Rig	38.85	154.70	33.87	33.87	1.15	4.57
Q960-H2-E80-Rig-Repeat	81.92	108.87	59.61	59.61	1.37	1.83
Q960-H2r-E80-Rig	75.73	108.59	57.74	57.74	1.31	1.88
Q960-H2r-E40-Rig	34.08	162.28	34.33	34.33	0.99	4.73
Q960-H3-E80-Rig	67.84	88.78	60.96	60.96	1.11	1.46
Q960-H3r-E80-Flex	57.83	74.76	57.78	57.78	1.00	1.29
Q960-H3-E40-Rig	34.00	138.18	33.17	33.17	1.02	4.17

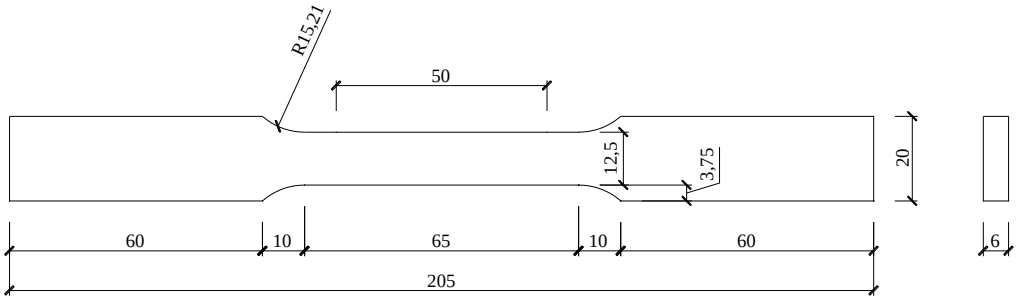

(a) Plate thickness: 6 mm

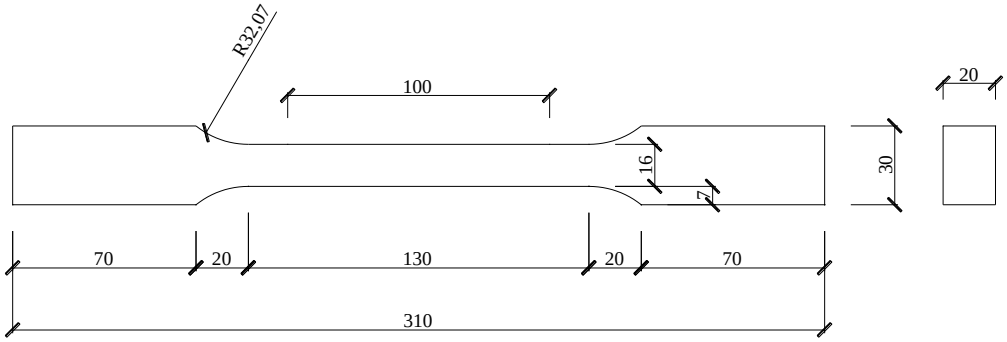

(b) Plate thickness: 20 mm

Figure 4.1 Dimensions for tensile coupons with different plate thicknesses

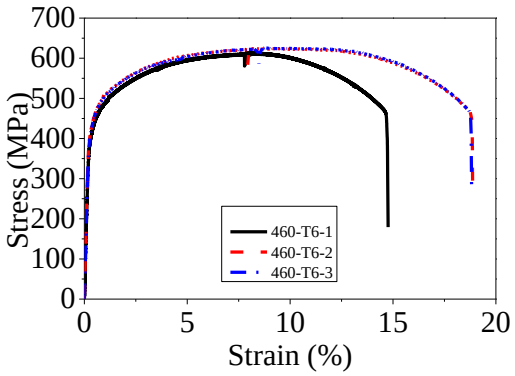

(a) Q460, thickness = 6 mm

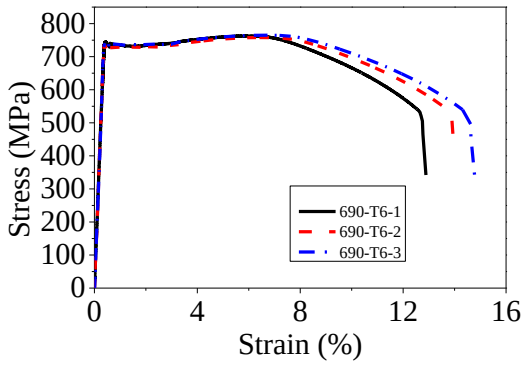

(b) Q690, thickness = 6 mm

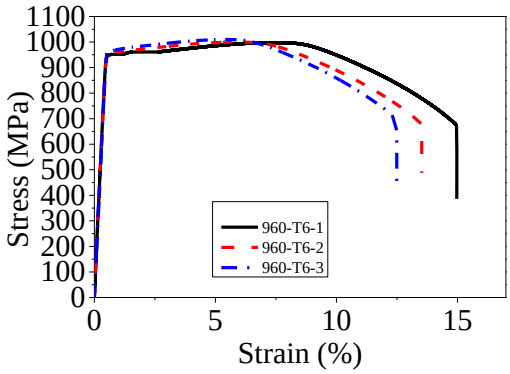

(c) Q960, thickness = 6 mm

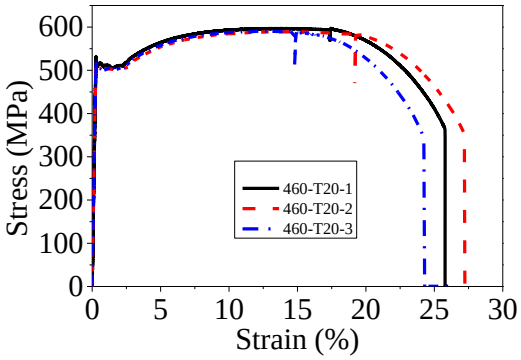

(d) Q460, thickness = 20 mm

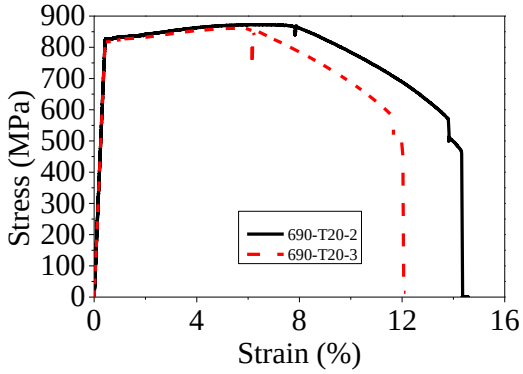

(e) Q690, thickness = 20 mm

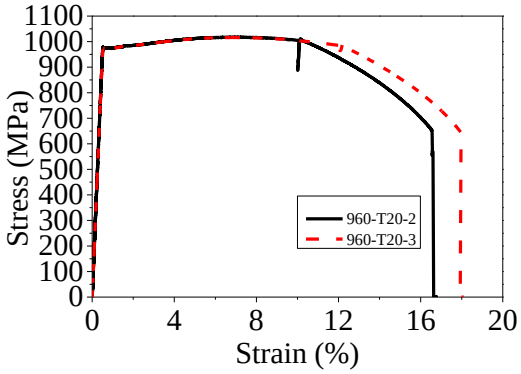

(f) Q960, thickness = 20 mm

Figure 4.2 Stress-strain curves of tensile coupons

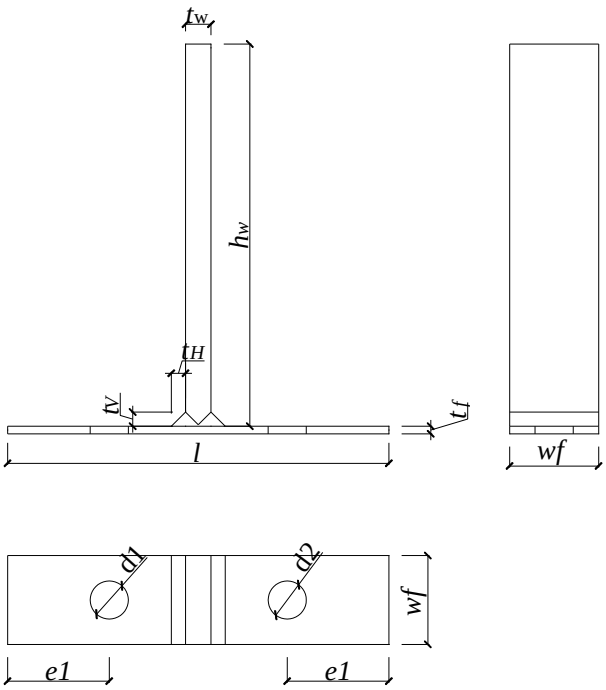

Figure 4.3 Single row T-stub joint geometry

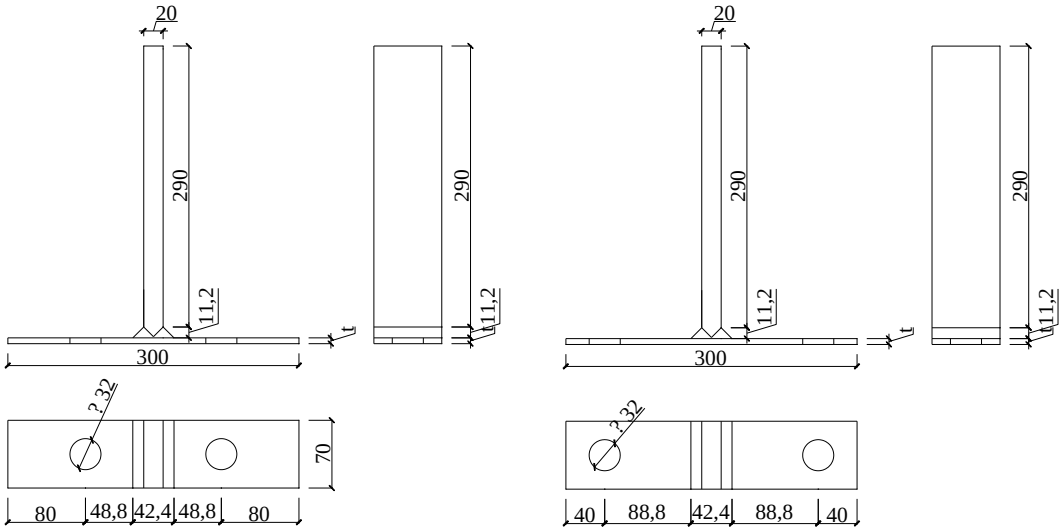

(a) e_1 = 80 mm (b) e_1=40 mm

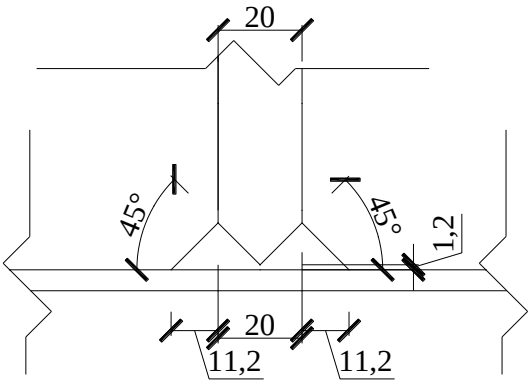

(c) Weld details

Figure 4.4 Geometric dimensions of single row T-stub joints (Unit: mm)

Figure 4.5 Prevention of welding distortion

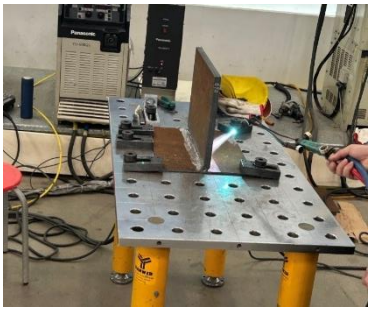

Figure 4.6 Preheating by torching gun

Figure 4.7 Interpass temperature measuring

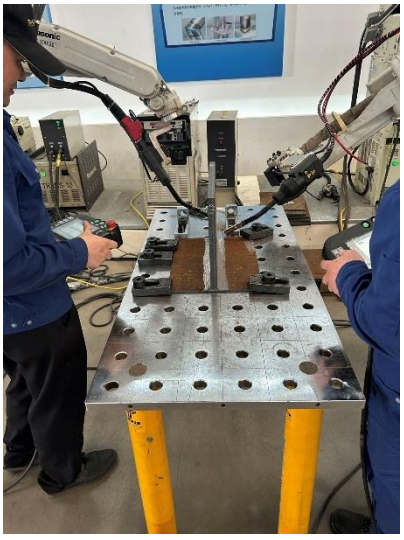

Figure 4.8 Two robots at two sides.

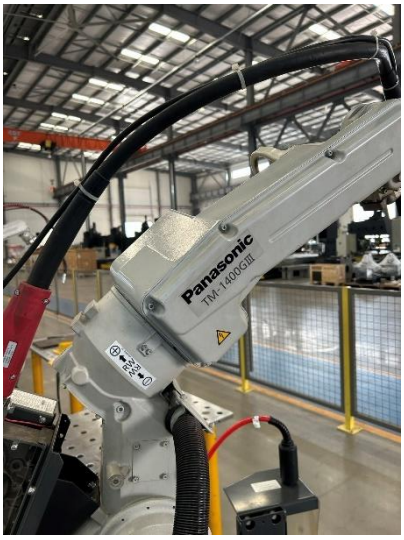

(a) welding robot at left side

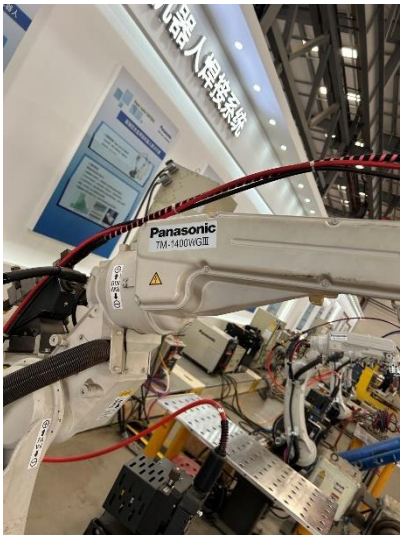

(b) welding robot at right side

Figure 4.9 Brand numbers for welding robots

Figure 4.10 Welding angle and placement of welding gun

Figure 4.11 Cutting short T-stub joint

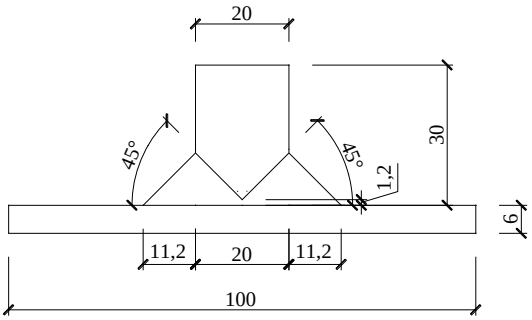

Figure 4.12 Dimensions of test block for hardness test (Unit: mm)

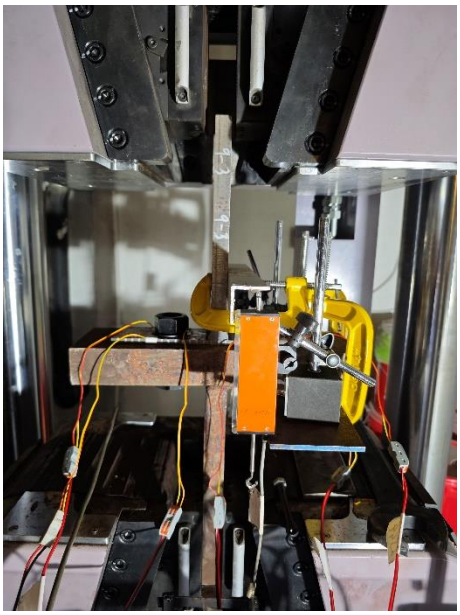

(a) Front view for rigid boundary

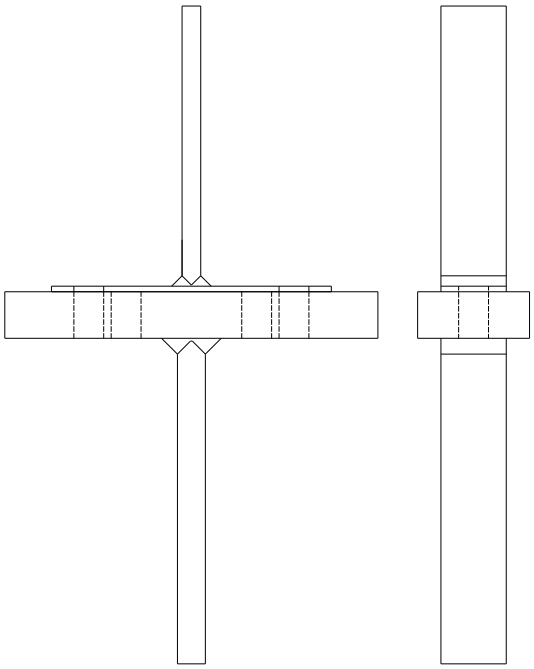

(b) Sketch for rigid boundary

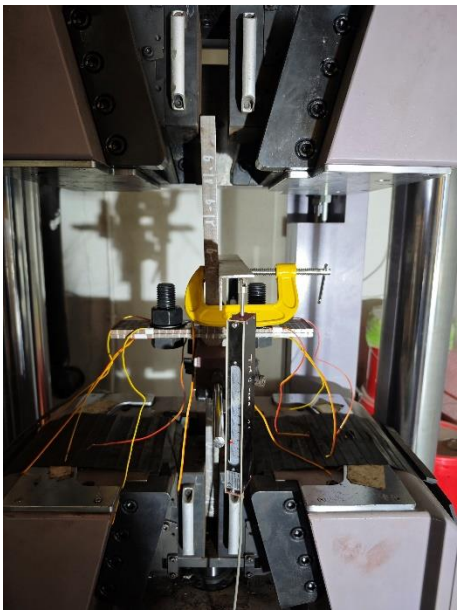

(c) Front view for flexible boundary

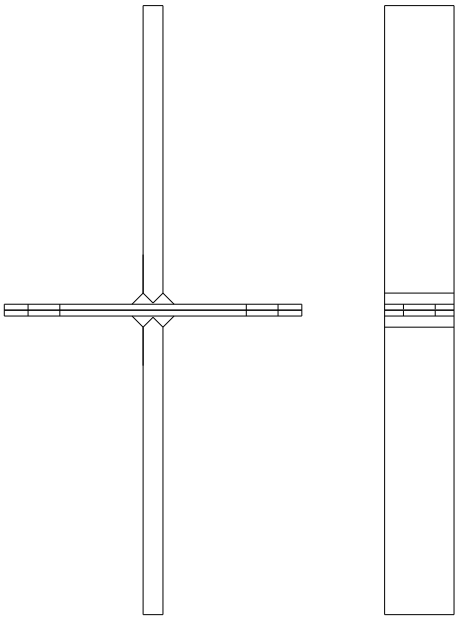

(d) Side view for flexible boundary

Figure 4.13 Test setup

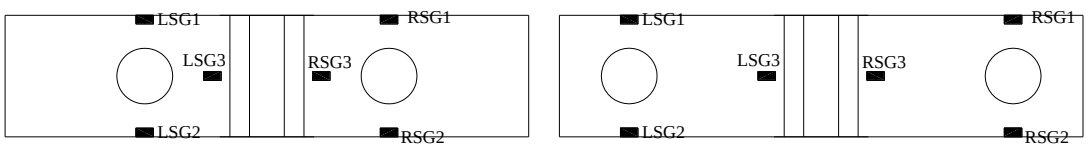

(a) end distance = 80 mm (b) end distance = 40 mm

Figure 4.14 Instrumentation

Figure 4.15 BUEHLER EcoMet 30

Figure 4.16 Polishing material MasterPolish

Figure 4.17 DURAMIN-40 A3

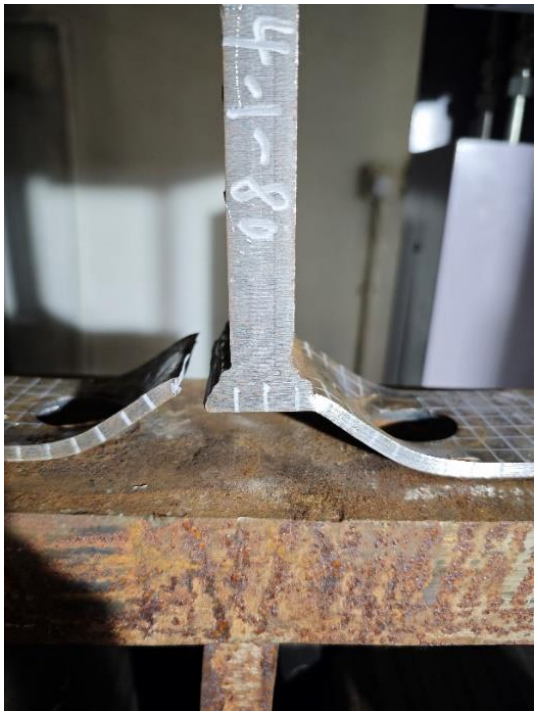

(a) Q460-H1-E80-Rig, flange punching shear failure

(b) Q460-H3-E40-Rig, bolt hole failure

(c) Q690-H3-E80-Rig, complete yielding of flange with stripping out of nut

(d) Q690-H1-E80-Rig, a combination of bolt hole failure and weld toe cracking

Figure 4.18 Typical failure modes at the ultimate state for the single row T-stub joints

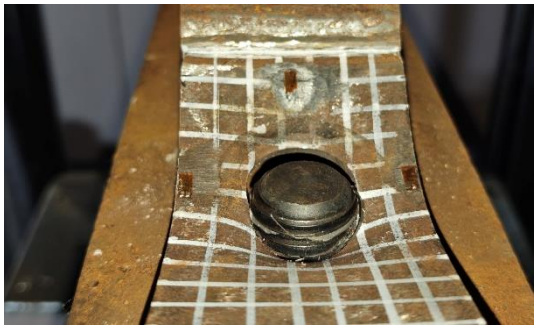

Figure 4.19 Thread failure on the bolt shank for Q690-H3-E80-Rig

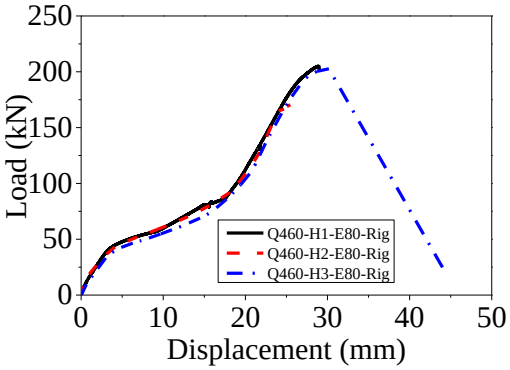

(a) Q460 single row T-stub joints with e_1 = 80

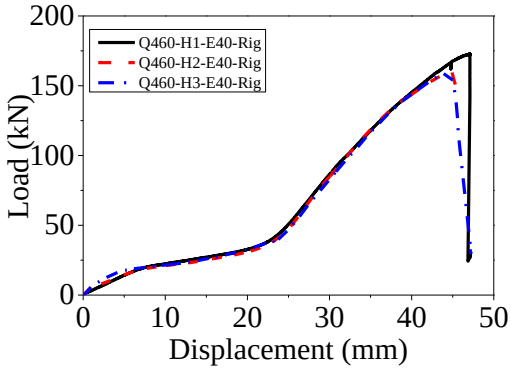

(b) Q460 single row T-stub joints with e_1 = 40

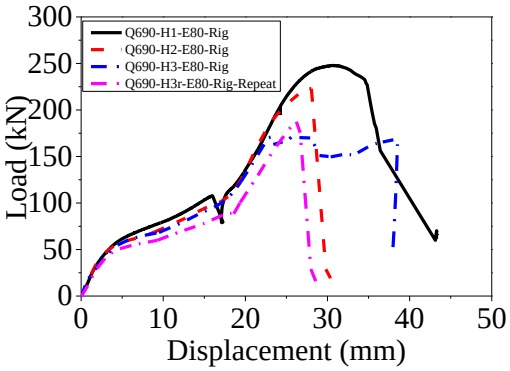

(c) Q690 single row T-stub joints with e_1 = 80

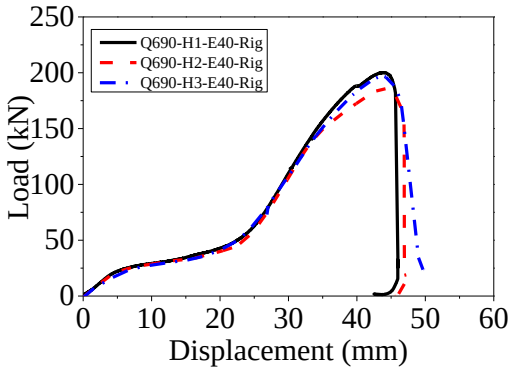

(d) Q690 single row T-stub joints with e_1 = 40

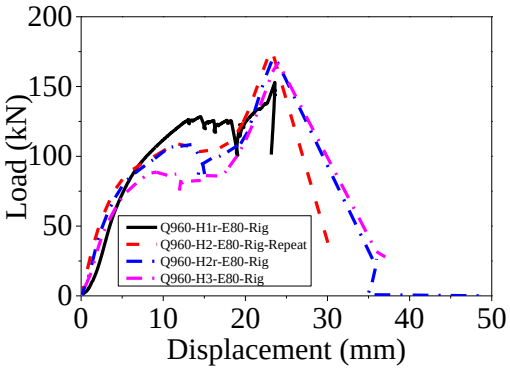

(e) Q960 single row T-stub joints with e_1 = 80

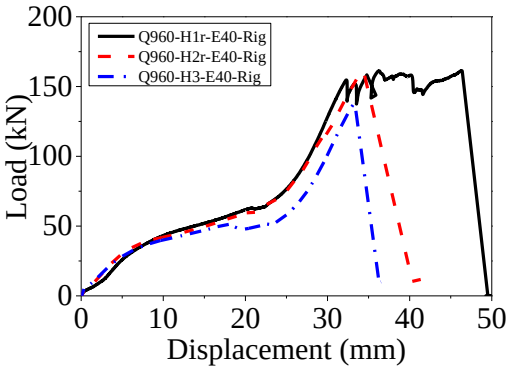

(f) Q960 single row T-stub joints with e_1 = 40

Figure 4.20 Load-displacement curves for single row T-stub joints with different heat inputs

(a) Q460-H1-E80-Rig, 0.531 kJ/mm

(b) Q460-H2-E80-Rig, 0.775 kJ/mm

(c) Q460-H3-E80-Rig, 1.267 kJ/mm

Figure 4.21 Heat input effect on flange cracking near weld toe for Q460 single row T-stub joint, e_1 = 80 mm

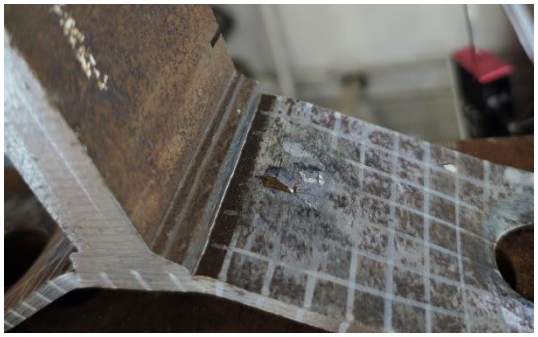

(a) Q460-H1-E40-Rig, 0.531 kJ/mm

(b) Q460-H2-E40-Rig, 0.775 kJ/mm

(c) Q460-H3-E40-Rig, 1.267 kJ.mm

Figure 4.22 Heat input effect on flange cracking near weld toe for Q460 single row T-stub joint, e_1 = 40 mm

(a) Q690-H1-E80-Rig, 0.548 kJ/mm

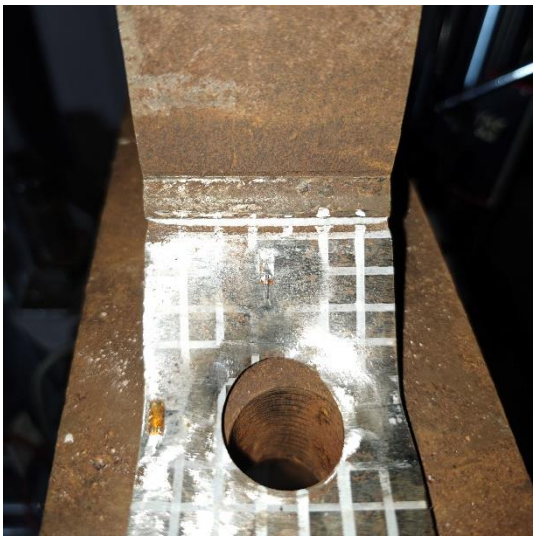

(b) Q690-H2-E80-Rig, 0.775 kJ/mm

(c) Q690-H3-E80-Rig, 1.126 kJ/mm

Figure 4.23 Heat input effect on flange cracking near weld toe for Q690 single row T-stub joint, e_1 = 80 mm

(a) Q690-H1-E40-Rig, 0.548 kJ/mm

(b) Q690-H2-E40-Rig, 0.775 kJ/mm

(c) Q690-H3-E40-Rig, 1.126 kJ/mm

Figure 4.24 Heat input effect on flange cracking near weld toe for Q690 single row T-stub joint, e_1 = 40 mm

(a) Q960-H1r-E80-Rig, 0.547 kJ/mm

(b) Q960-H2r-E80-Rig, 0.775 kJ/mm

(c) Q960-H3-E80-Rig, 1.267 kJ/mm

Figure 4.25 Heat input effect on flange cracking near weld toe for Q960 single row T-stub joint, e_1 = 80 mm

(a) Q960-H1r-E40-Rig, 0.547 kJ/mm

(b) Q960-H2r-E40-Rig, 0.775 kJ/mm

(c) Q960-H3-E40-Rig, 1.267 kJ/mm

Figure 4.26 Heat input effect on flange cracking near weld toe for Q960 single row T-stub joint, e_1 = 40 mm

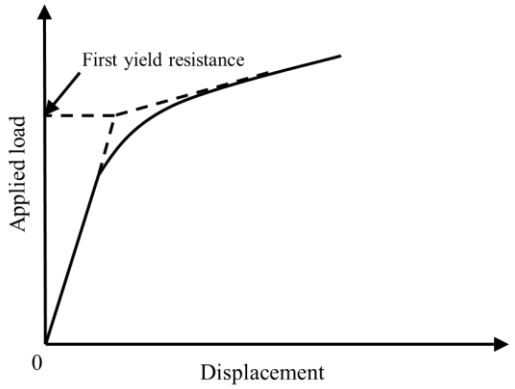

Figure 4.27 Plastic resistance definition

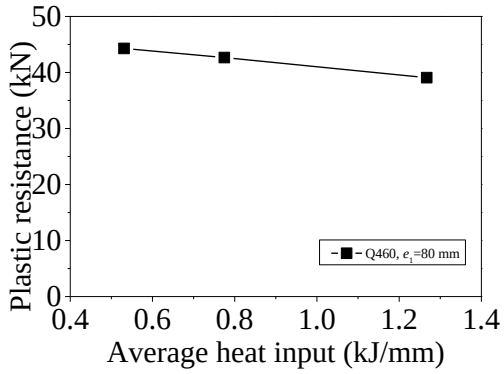

(a) Q460, e_1 = 80 mm

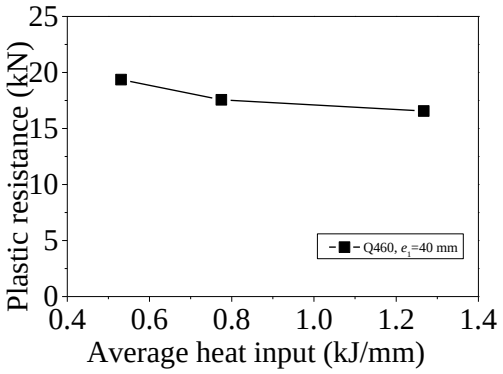

(b) Q460, e_1 = 40 mm

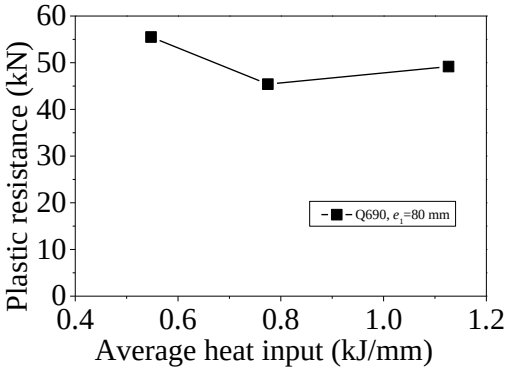

(c) Q690, e_1 = 80 mm

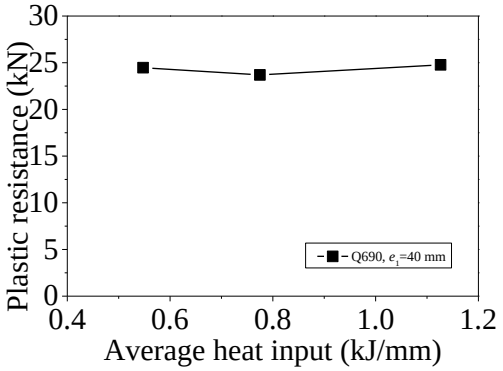

(d) Q690, e_1 = 40 mm

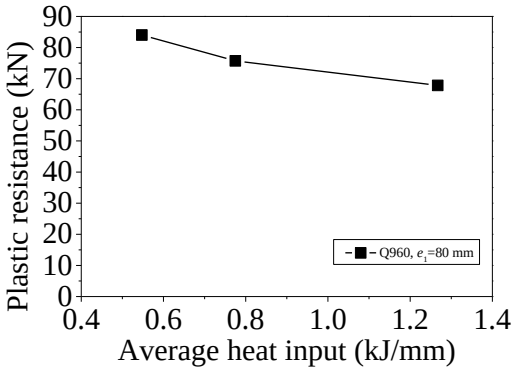

(e) Q960, e_1 = 80 mm

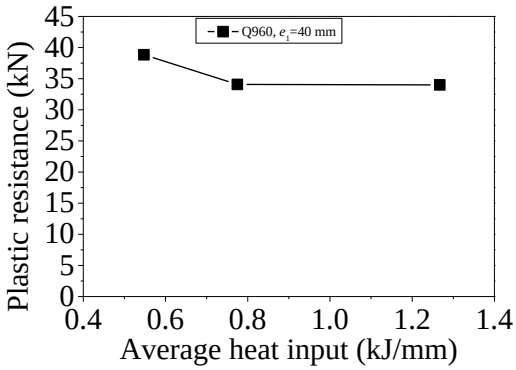

(f) Q960, e_1 = 40 mm

Figure 4.28 Influence of heat input on plastic resistance of single row T-stub joints

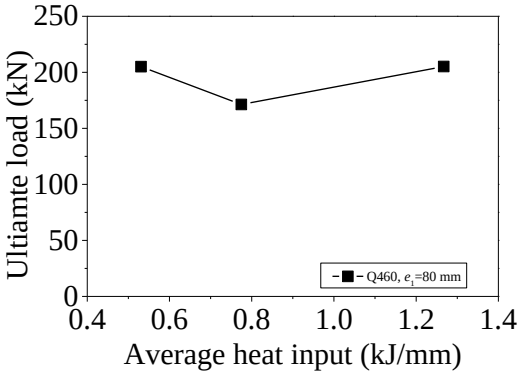

(a) Q460, e_1 = 80 mm

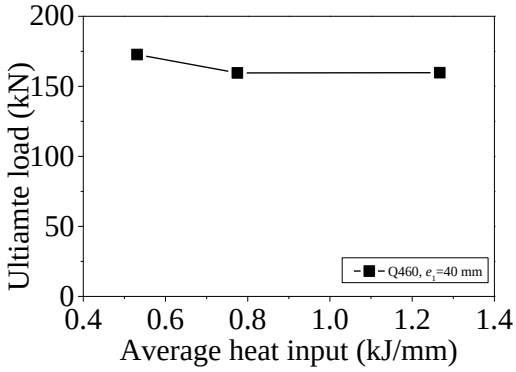

(b) Q460, e_1 = 40 mm

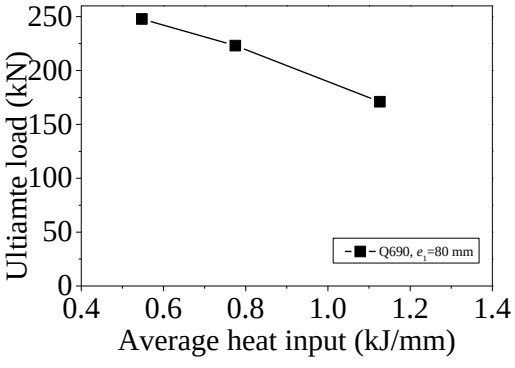

(c) Q690, e_1 = 80 mm

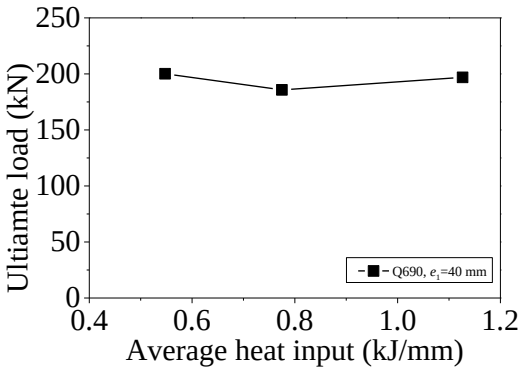

(d) Q690, e_1 = 40 mm

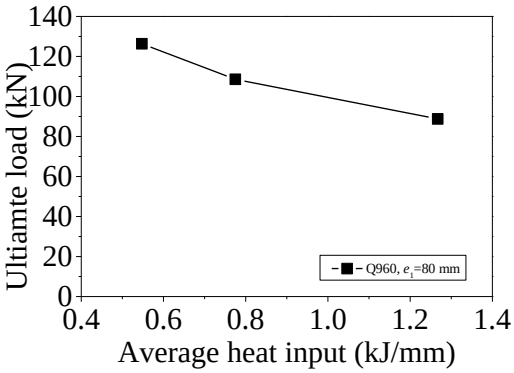

(e) Q960, e_1 = 80 mm

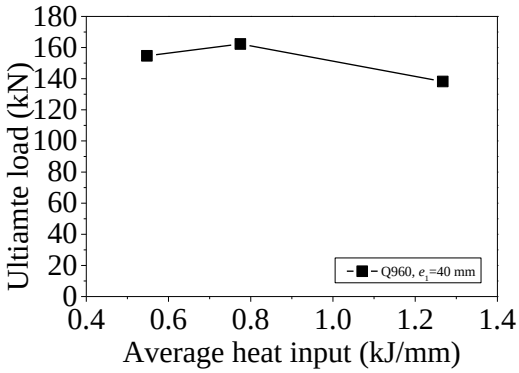

(f) Q960, e_1 = 40 mm

Figure 4.29 Influence of heat input on the ultimate load of single row T-stub joints

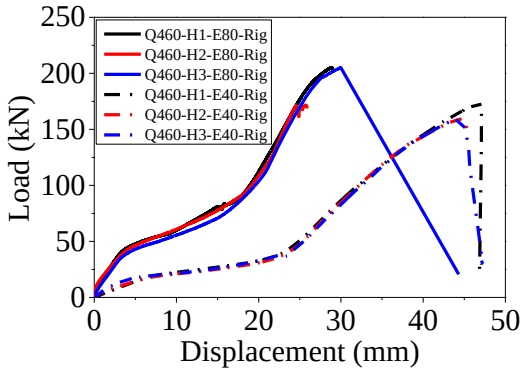

(a) Q460 single row T-stub joint with different end distances

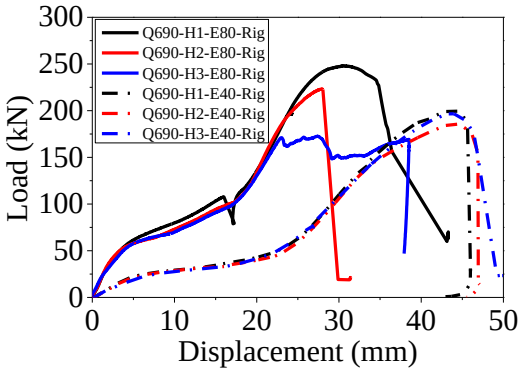

(b) Q690 single row T-stub joint with different end distances

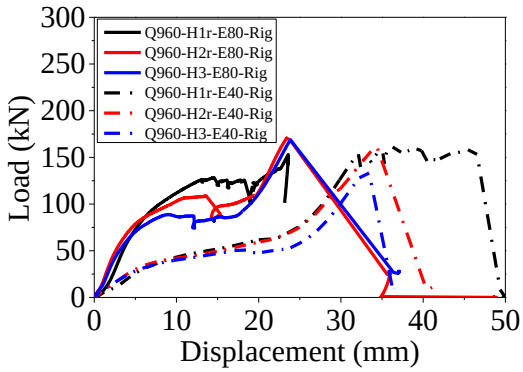

(c) Q960 single row T-stub joint with different end distances

Figure 4.30 Load-displacement curves for single row T-stub joints with different end distances

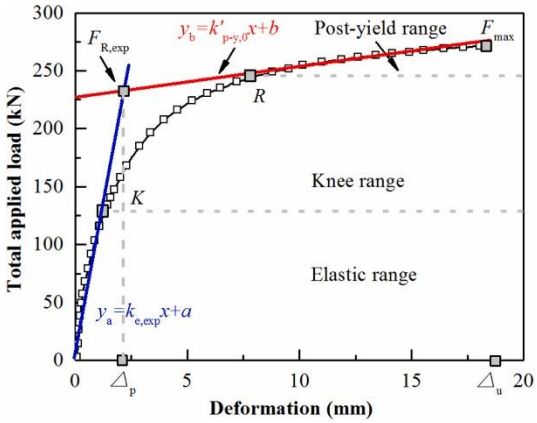

Figure 4.31 Displacement ductility coefficients definition (Liang et al., 2019)

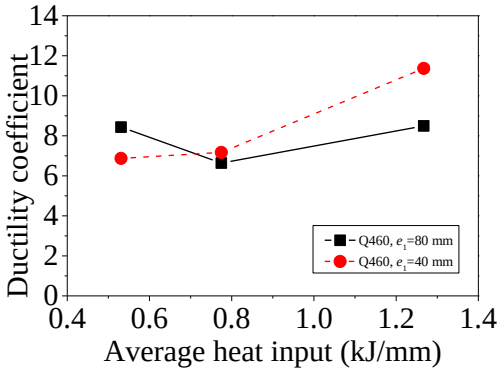

(a) Q460 single row T-stub joints

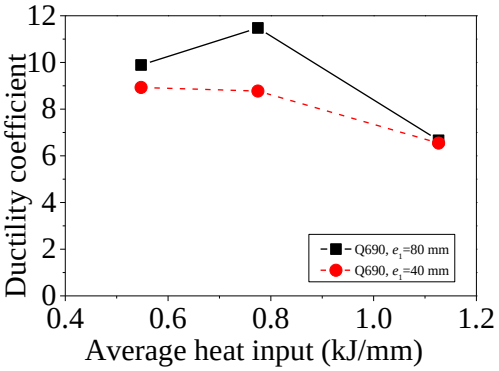

(b) Q690 single row T-stub joints

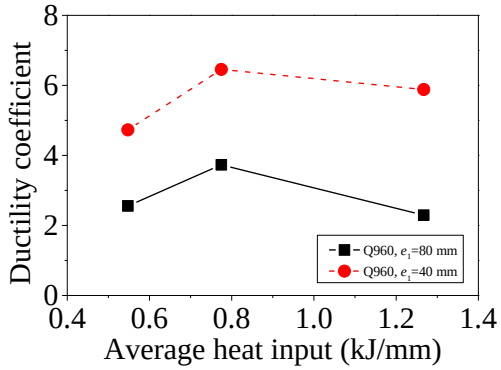

(c) Q960 single row T-stub joints

Figure 4.32 Displacement ductility coefficients vs. end distances

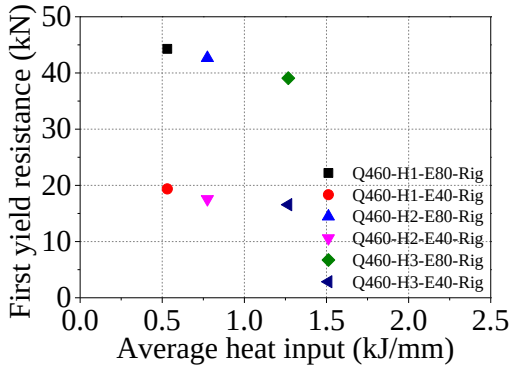

(a) Q460 single row T-stub joints

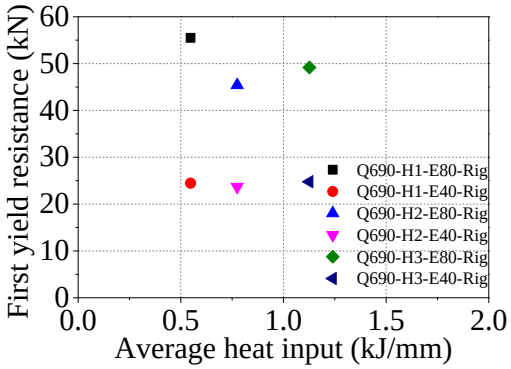

(b) Q690 single row T-stub joints

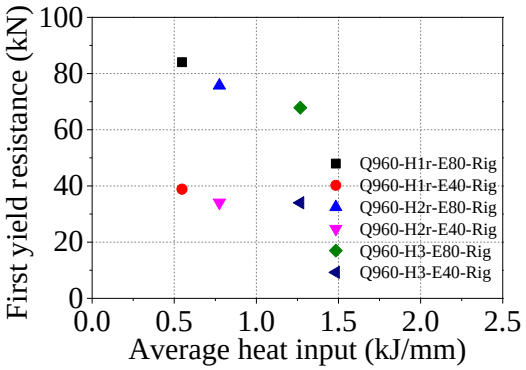

(c) Q960 single row T-stub joints

Figure 4.33 Influence of end distance on plastic resistance

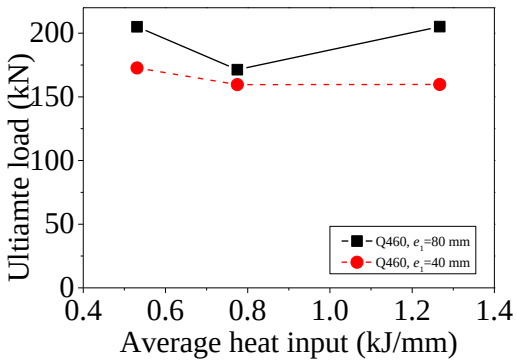

(a) Q460 single row T-stub joints

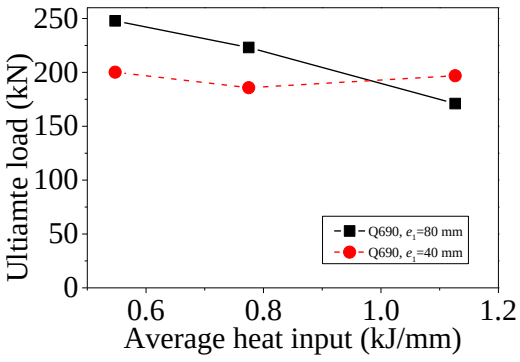

(b) Q690 single row T-stub joints

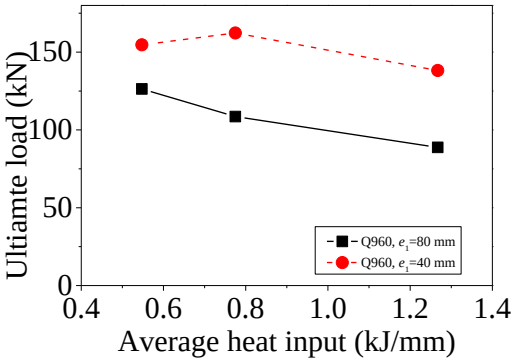

(c) Q960 single row T-stub joints

Figure 4.34 Influence of end distance on ultimate load

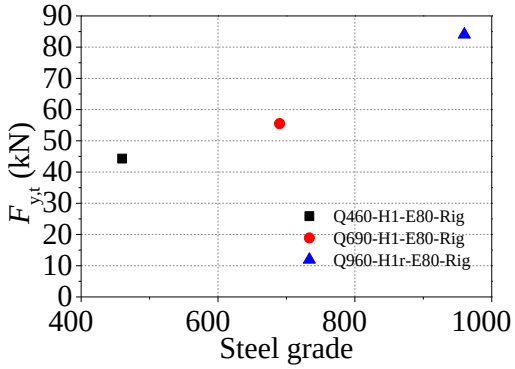

(a) Heat input 1, e_1 = 80 mm

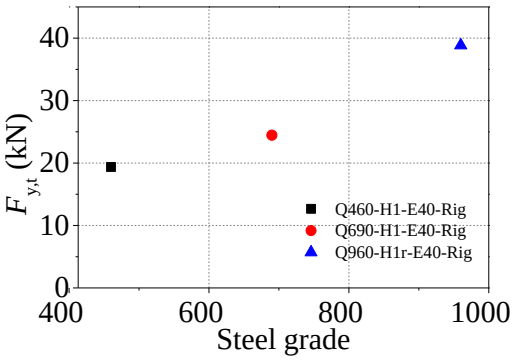

(b) Heat input 1, e_1 = 40 mm

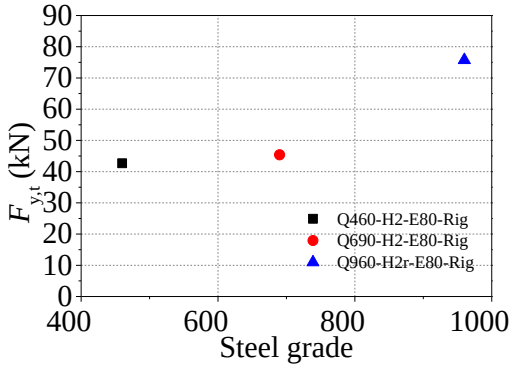

(c) Heat input 2, e_1 = 80 mm

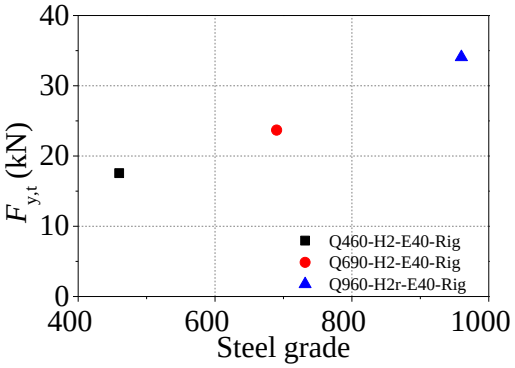

(d) Heat input 2, e_1 = 40 mm

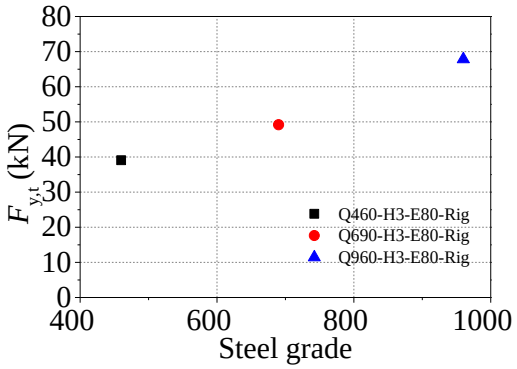

(e) Heat input 3, e_1 = 80 mm

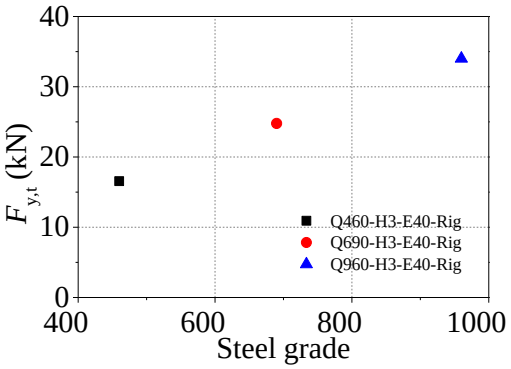

(f) Heat input 3, e_1 = 40 mm

Figure 4.35 Influence of steel grade on plastic resistance

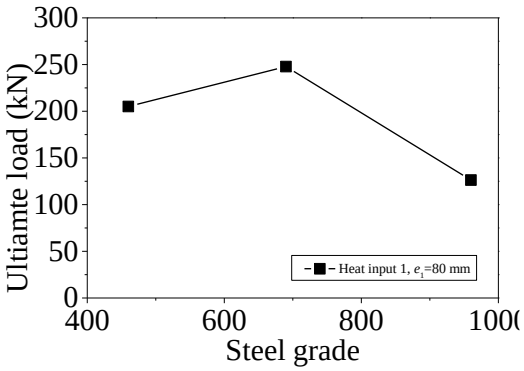

(a) Heat input 1, e_1 = 80 mm

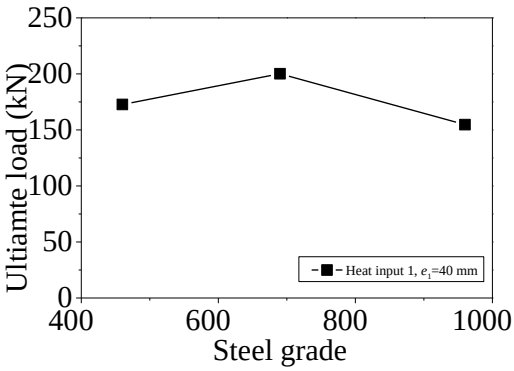

(b) Heat input 1, e_1 = 40 mm

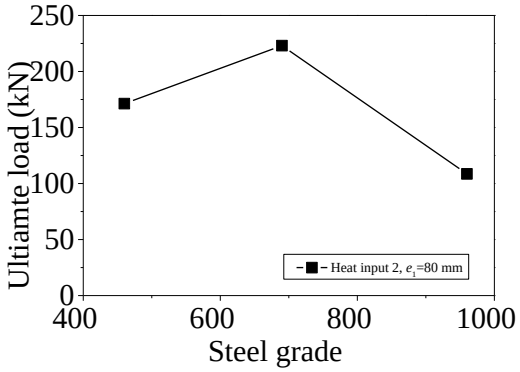

(c) Heat input 2, e_1 = 80 mm

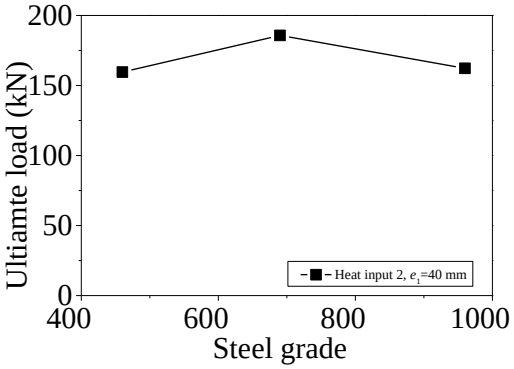

(d) Heat input 2, e_1 = 40 mm

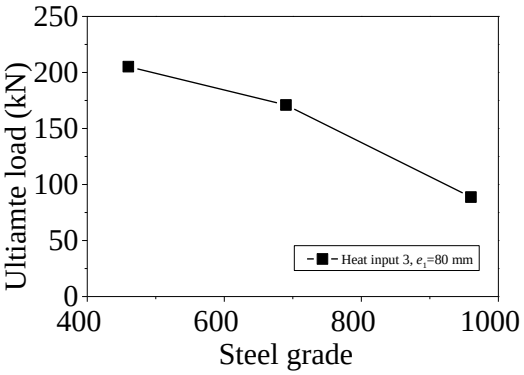

(e) Heat input 3, e_1 = 80 mm

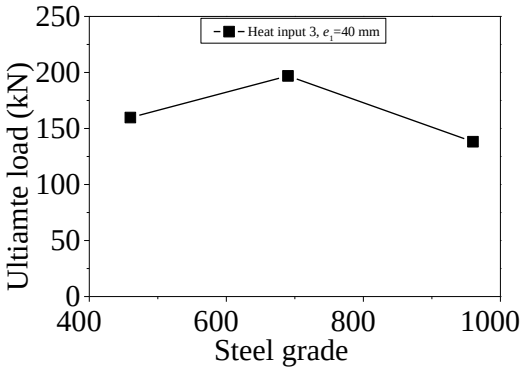

(f) Heat input 3, e_1 = 40 mm

Figure 4.36 Influence of steel grade on ultimate load

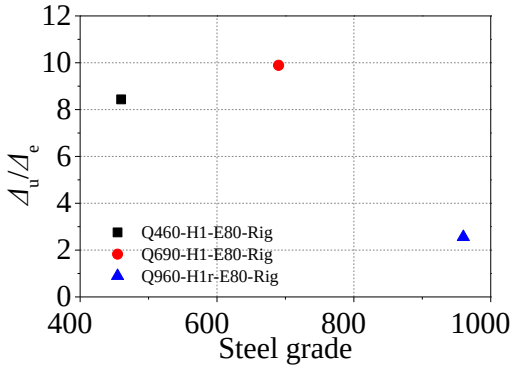

(a) Heat input 1, e_1 = 80 mm

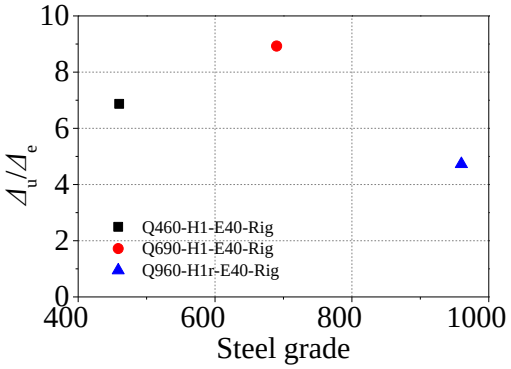

(b) Heat input 1, e_1 = 40 mm

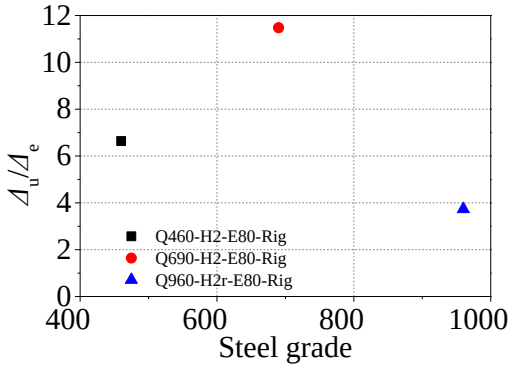

(c) Heat input 2, e_1 = 80 mm

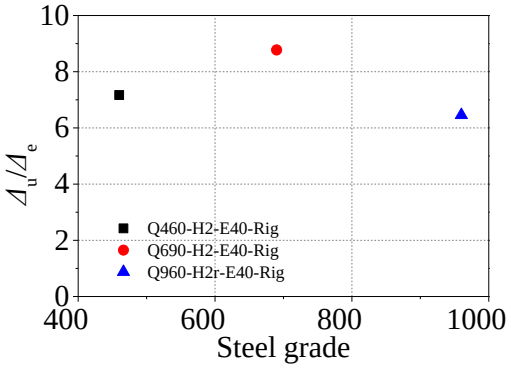

(d) Heat input 2, e_1 = 40 mm

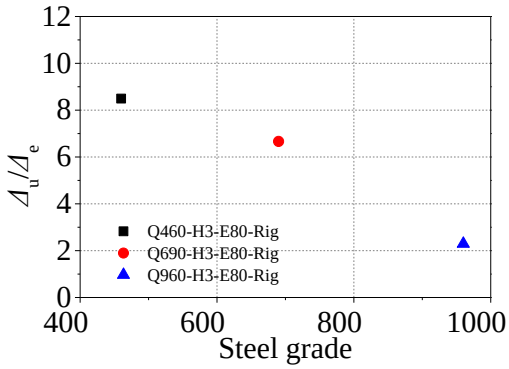

(e) Heat input 3, e_1 = 80 mm

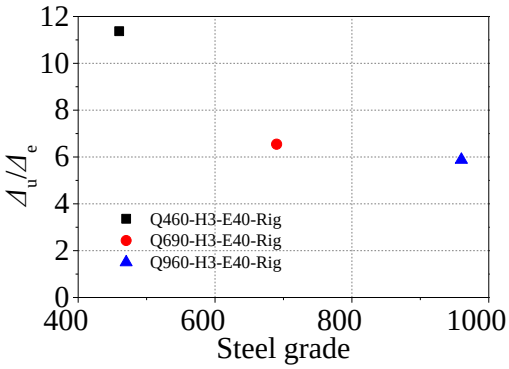

(f) Heat input 3, e_1 = 40 mm

Figure 4.37 Influence of steel grade on displacement ductility coefficient

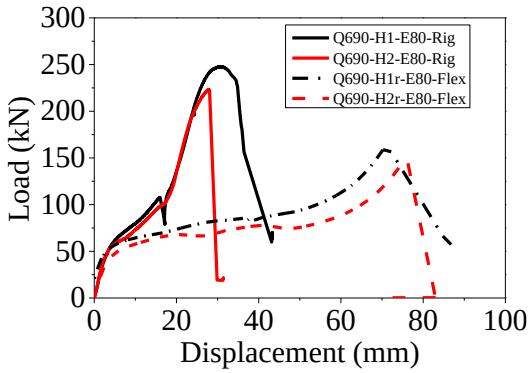

(a) Q690 single row T-stub joint with different boundary conditions

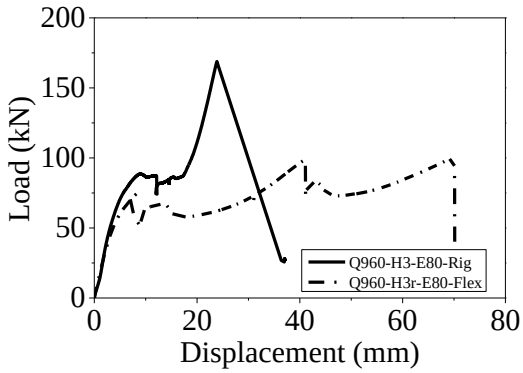

(b) Q960 single row T-stub joint with different boundary conditions

Figure 4.38 Load-displacement curves for single row T-stub joints with different boundary conditions

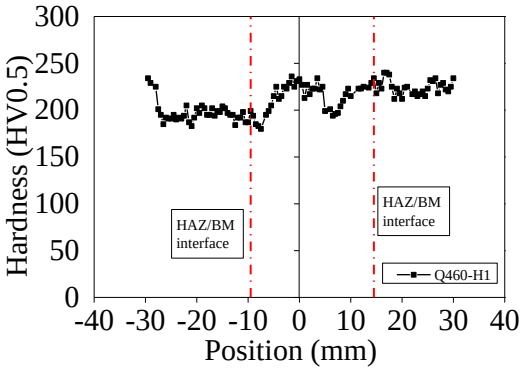

(a) Q460-H1

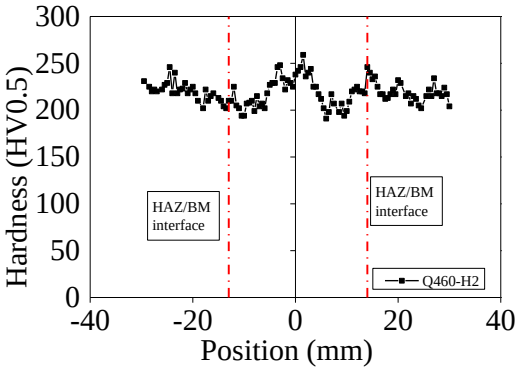

(b) Q460-H2

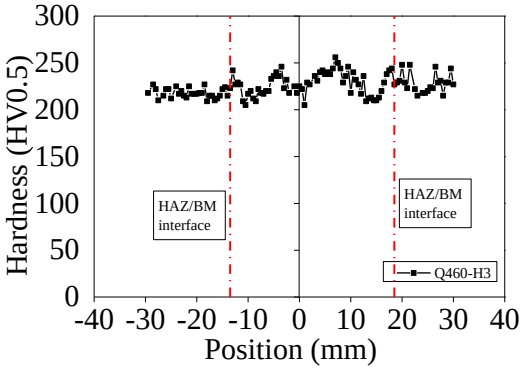

(c) Q460-H3

Figure 4.39 Hardness distributions of Q460 T-stub joints

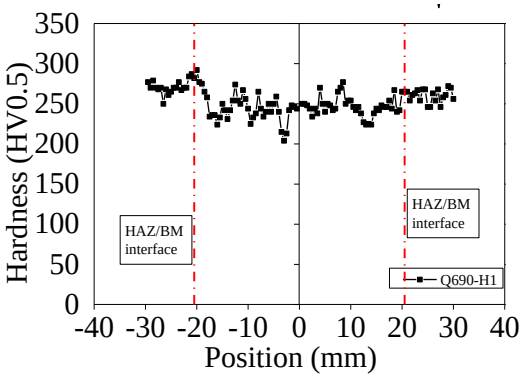

(a) Q690-H1

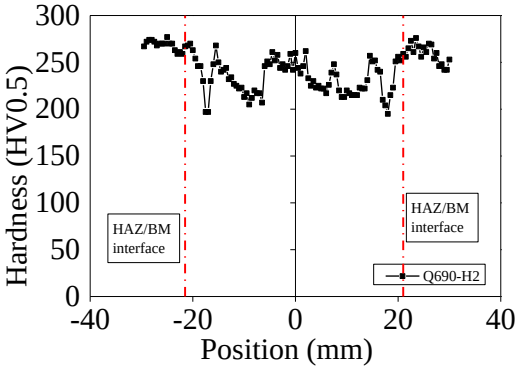

(b) Q690-H2

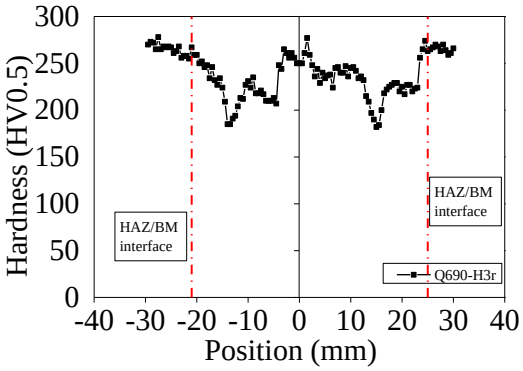

(c) Q690-H3r

Figure 4.40 Hardness distributions of Q690 T-stub joints

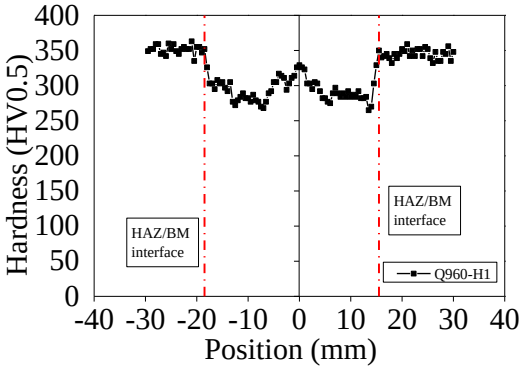

(a) Q960-H1

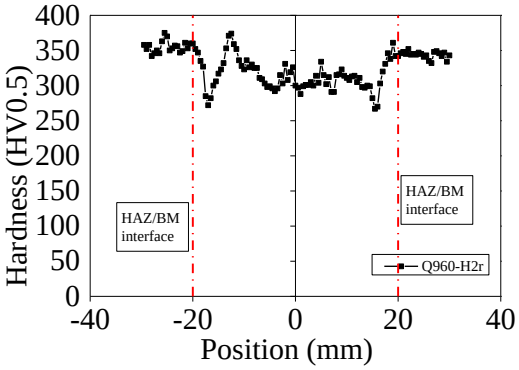

(b) Q960-H2r

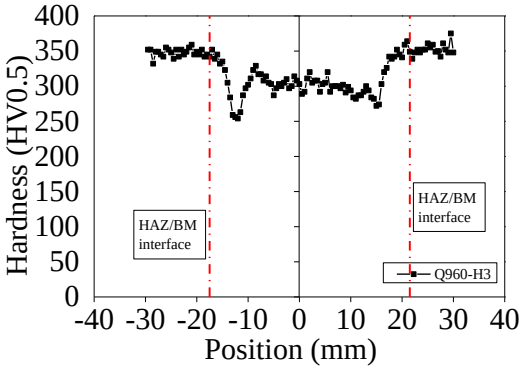

(c) Q960-H3

Figure 4.41 Hardness distributions of Q960 T-stub joints

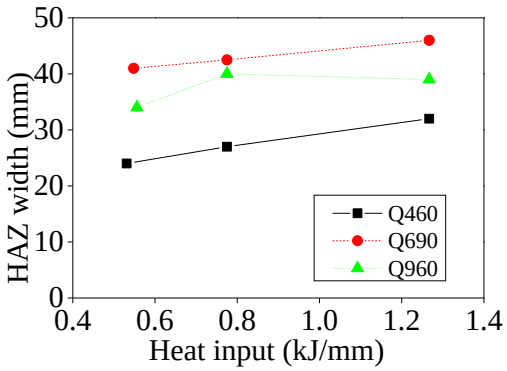

Figure 4.42 Relationship between HAZ width and heat input

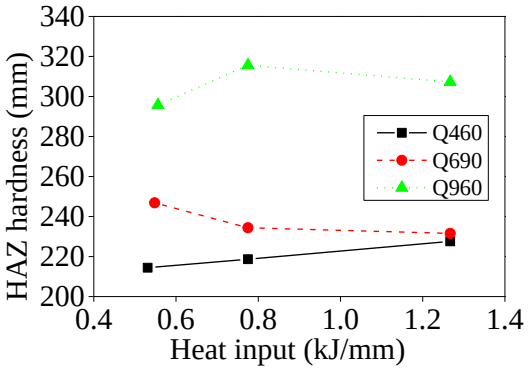

Figure 4.43 Relationship between HAZ average hardness and heat input

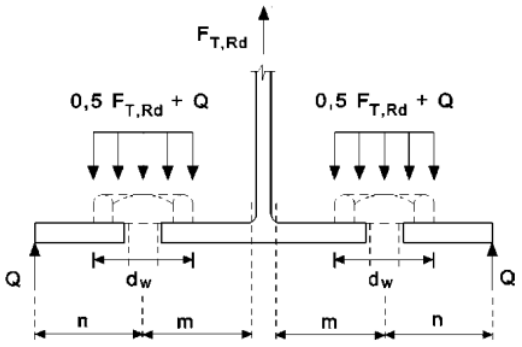

Figure 4.44 Illustrations of T-stub joint

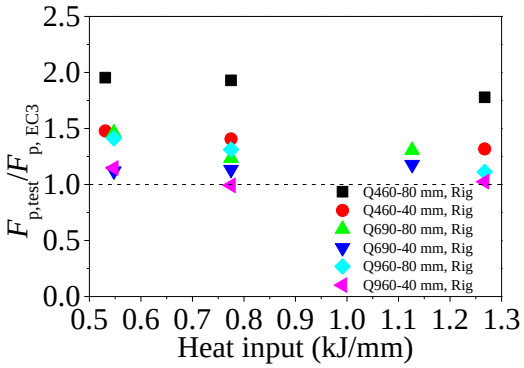

Figure 4.45 Influence of heat input and steel grade on $F_{y,t}$ / $F_{y,p}$

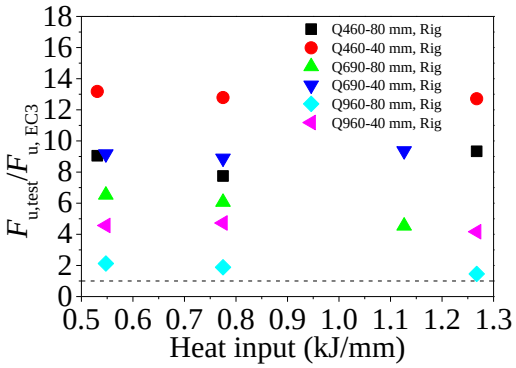

Figure 4.46 Influence of heat input and steel grade on $F_{u,t}$ / $F_{u,EC3}$

Chapter 5 Numerical modelling and parametric study for the HSS T-stub joints

5.1 Introduction

This chapter developed the numerical models for the tested HSS single row T-stub joints under axial tension. The numerical models were validated by the load-displacement curves and stress distributions. Then, a comprehensive parametric study was implemented. The geometric parameters included end distance and flange thickness. Particularly, the welding effect on the joint behaviour was incorporated by combining the modified Hollomon model and regression models considering different heat inputs in the parametric study. Three heat inputs were 0.5 kJ/mm, 1.4 kJ/mm and 2.3 kJ/mm.

5.2 Finite element analysis

5.2.1 Finite element model

The finite element software ABAQUS (2020) was used to implement the numerical analysis. The numerical model consisted of the single row T-stub joint, T-support, bolt, nut and washer. The actual dimensions of the single row T-stub joint were used to build the model. The HAZ width of the flange of the single row T-stub joint was in accordance with the hardness test results. The effective diameter of the bolt was calculated according to its net section area. For the T-support, only its part in contact with T-stub joint was built to reduce the number of elements, thus achieving high computation efficiency.

In the tests, Grade 12.9 bolt and nut and Grade 8.8 washer were used. For the T-support, Grade 70 steel based on Chinese standard was adapted. The elastic-perfectly plastic model was used for these components. Table 5.1 lists the material properties for above components, including density, elastic modulus, yield stress and Poisson's ratio. For the

flange and web, however, their material properties were obtained from the tested engineering stress-strain curves. Since matching welding was achieved and weld rupture did not happen in all the single row T-stub joints, the material properties of welds were assumed to be the same as its corresponding specimen's web. The HAZ of flange was treated as a homogeneous material, whose width was determined according to the hardness test results in Chapter 4. It should be emphasised that the true stress-strain curve of HAZ up to the engineering ultimate strength were calculated based on the modified Hollomon model in combination with the polynomial regression models. Furthermore, the true stress-true plastic strain curves can be obtained, as shown in Figure 5.1. It can be observed that for Q460, welding could even improve its strength. While for Q690 and Q960, welding impaired their strengths.

The Dynamic Explicit solver was used to analyse the numerical models. The mass scaling technique was adapted to save computation time. Target time increment type of mass scaling was set as $1e^{-6}$. The reaction force and displacement at positions which were corresponding to their physical counterparts in the tests were extracted from the models at a time interval of 0.002s (with the total time 1s).

The constraints between web, weld and flange were "Tie" to simulate the complete penetration welds. A controlling point was coupled with the upper surface of web to apply axial tensive displacement. There were three groups of contacts: flange related contacts, bolt shank related contacts and contacts related to nut and washer surfaces. For the flange related contacts, general contact in ABAQUS was adapted to avoid the ratio of deformation speed to wave speed exceeding 1.0. As for other contacts, surface to surface contact was utilised. Hard contact was adapted in the normal direction for all the contacts. For the tangential contact, however, a friction coefficient of 0.2 was adapted for the flange related contacts (Fernandez-Ceniceros et al., 2015). For the other contacts, frictionless contact was used for the tangential direction.

The developed numerical model was shown in Figure 5.2. Due to the symmetry of the single row T-stub joint, 1/4 model was used to improve computation efficiency. For the boundaries on the Y-Z plane, the displacement at X direction and rotations around the Y and Z axises were set to be zero. Similarly, for the boundaries on the X-Y plane, the displacement at Z direction and rotations around the X and Y axises were set to be zero. For the boundary conditions, the bottom surface of the T-support was fixed in all directions, and the T-stub joint was installed onto it by bolts. Element type C3D8R was adapted for all the components. For the mesh of the model, a mesh convergency sensitivity study was conducted to determine the mesh size. To avoid element penetration, the mesh size of the components around the flange bolt hole should match with each other by local seeds. The flange region between bolt holes had a refined mesh size of 1 mm, while other regions of flange had a mesh size of 3 mm. To avoid hour-glassing problem, at least 4 layers of element existed at the flange through thickness direction. The T-stub joint was properly partitioned, thus structural meshing technique could be adapted. Besides, for bolts and nuts, the medial axis algorithm was adapted for meshing. The meshed model was shown in Figure 5.3.

Figure 5.4 provides the load-displacement curves of all the tested single row T-stub joints and corresponding numerical counterparts with and without the HAZ. It was found that HAZ had almost no influence on the elastic and plastic stages of the load-displacement curves in Figure 5.4. The constraint effect is defined as the local disturbance of the stress state generated by adjacent zones for the HAZ (Neuvonen et al., 2021, Yan et al., 2022, Rodrigues et al., 2004, Sun et al., 2018a). The hardness test revealed that the HAZ located between BM had smaller average hardness value. It is likely that the constraint effect experienced by the HAZ of T-stub joint led to the neglectable HAZ effect on the load-displacement curves. Figure 5.5 provides the equivalent plastic strain distribution at the transition between elastic stage and plastic

stage for Q460-H1-E80-Rig. The plastic deformation initiated at the flange near the weld toe. As the equivalent plastic strain developed along the weld toe, the load-displacement curves gradually transmitted from the elastic stage to plastic stage. In Figure 5.6, it demonstrates the contact between the bolt shank and the bolt hole at the onset of second hardening stage for Q460-H1-E80-Rig. It can be found that the second hardening stage was triggered once the bolt shank was in contact with the support bolt hole during loading, as the stress concentration happened at the contact region between the bolt and the support.

In Figure 5.4, the transition zones between stage 2 (plastic stage) and stage 3 (second hardening stage) of numerical results occurred later than that of test results. The phenomenon was because the bolt effective diameter in the numerical model was smaller than the actual bolt diameter in the experiments, thus the contact between the bolt shank and the support hole in the numerical models was postponed compared to their experimental counterparts. For each single row T-stub joint, it had two numerical models: one neglected the HAZ material deterioration while the other took it into account. Corresponding numerical load-displacement curves for the same single row T-stub joint almost overlapped with each other, though the loads of the model considering HAZ was slightly lower. It then can be concluded that the HAZ material deterioration had minor effect on the joint behaviour. For Q460 and Q690 T-stub joints, the peak load of numerical simulations was greater than the peak load of test results. In the FE modelling, the fracture initiation and damage evolution were neglected. Hence, the flange cracks along the weld toe which could make the flange thinner was not reflected by the numerical models. At the peak load point, the numerical models had thicker flange thickness than experimental specimens. Therefore, the peak loads of the numerical models were greater than that of the experiments. For Q960 T-stub joints with the end distance equal to 80 mm, the numerical results deviated from the test results. It is because for this kind of joint the severe cracking developed in the plastic

stage during testing. However, the numerical models did not consider the fracture initiation and damage evolution. Therefore, their load-displacement curves behaved differently. For Q960 T-stub joints with the end distance equal to 40 mm, severe cracking happened during second hardening stage rather than plastic stage. Therefore, the FE and test agreed well before second hardening stage.

Figure 5.7 depicts the von Mises stress distribution at the second hardening stage for Q460-H1-E80-Rig. It was found that significant stress developed on the upper surface of the flange between the web and bolt hole. The material strain hardening in this region, which was named as the membrane action, was the mechanism for the second hardening of single row T-stub joint.

Figure 5.8 provides the deformation of Q460-H1-E80-Rig at the peak load point from experiments and simulations. The numerical model reflected the deformation characteristics of the experiments. Furthermore, the equivalent plastic strain along the weld toe developed significantly in the numerical models, which was in accordance with the flange cracks developing along the weld toe in the tests. In summary, the developed numerical models could capture the mechanical behaviours of the single row T-stub joints.

5.3 Parametric study

5.3.1 Specifications for parametric study

A comprehensive parametric study was conducted to reveal the effect of geometric dimensions (end distance and flange thickness) and welding heat inputs on the load-displacement curves for the HSS single row T-stub joints under tension. Table 5.2 provides the concerned range of parameters. Three steel grades, Q460, Q690 and Q960, were included in the parametric study. There were three kinds of end distances,

including 80 mm, 60 mm and 40 mm. For the flange thickness t_f, 6 mm, 12 mm and 18 mm were incorporated to find out their influence on the joint behaviour. For the heat inputs, three heat inputs from low to high were adapted in the study, namely 0.5 kJ/mm, 1.4 kJ/mm and 2.3 kJ/mm. These heat inputs were used to generate the true stress-strain curves for the HAZ. The hardness results in Chapter 4 showed that the HAZ outer boundary of the flange was close to the weld toe along the flange. Therefore, the HAZ width in the parametric study were assumed to be $w + t_w + w$, where w is the weld leg size and t_w is the web thickness. For the other geometric dimensions, for example, flange width, flange length, bolt diameter and web height, they were kept the same as the nominal dimensions of the test specimens. Particularly, the weld leg size was assumed to be 10 mm for all the numerical models in the parametric study. The nomenclature of numerical model was illustrated by taking "4C-e60-tf12-Q0_5" as an example: "4C" denoted the steel grade was Q460; "e60" denoted the end distance was 60 mm; "tf12" denoted the flange thickness was 12 mm; "Q0_5" denoted the heat input was 0.5 kJ/mm. The validated numerical simulation techniques in Section 5.2 were utilised in the parametric study.

5.3.2 Results and discussions

There were in total 81 numerical models for the HSS single row T-stub joints under tension in the parametric study. The load-deformation curves were demonstrated in Figure 5.9 to Figure 5.14. Since the numerical models did not incorporate fracture initiation and damage evolution, the load-displacement curves presented here only consisted of elastic and plastic stages.

Figure 5.9 to Figure 5.11 show the load-displacement curves of Q460, Q690 and Q960 single row T-stub joints considering the effect of heat input Q with constant end distances. It can be observed that for Q460 single row T-stub joints, the load-displacement curves were not significantly affected by varying heat inputs under the

same end distance and flange thickness. For Q690 and Q960 single row T-stub joints, however, increasing heat inputs could decrease the plastic stage, as the plastic stage initiated when the flange near weld toe yielded where the HAZ existed. Furthermore, as the end distances increased, the degree of plastic stage degradation were reduced. Besides, the initial stiffness and plastic resistance of the T-stub joint were significantly improved if the flange thickness was enlarged. Figure 5.12 to Figure 5.14 show the load-displacement curves of Q460, Q690 and Q960 single row T-stub joints considering the effect of end distance with constant heat inputs and flange thicknesses. It was quite clear that increasing end distance could significantly improve the initial stiffness and plastic resistance.

5.4 Summary

In this chapter, the numerical models for the tested HSS single row T-stub joints under axial tension were developed and validated. The geometric dimensions were in accordance with the test specimens. The material properties were determined as follows: for the bolt, nut, washer, and T-support, the elastic-perfectly plastic model was used for these components; for the flange and web of the T-stub joint, the tested engineering stress-strain curves were allocated. Particularly, the true stress-strain curves of the HAZ were obtained by combining the modified Hollomon model and polynomial regression models. The numerical models were validated through three aspects: load-displacement curve, stress distribution and crack initiation. It was proved that the developed numerical models could predict the single row T-stub joint with satisfactory accuracy.

A parametric study was conducted to reveal the effect of geometric dimensions (end distance and flange thickness) and welding heat inputs on the load-displacement curves for the HSS single row T-stub joints. It was found that for Q460 single row T-stub joints, the load-displacement curves were not significantly affected by varying heat inputs under the same end distance and flange thickness. For Q690 and Q960 single row T-

stub joints, however, increasing heat inputs could decrease the plastic stage, as the plastic stage initiated when the flange near weld toe yielded where the HAZ existed. Furthermore, as the end distances increased, the degree of plastic stage degradation were reduced.

Table 5.1 Material properties for numerical models for bolt, nut, washer and T-support

Component	Density (ton/mm^3)	E (MPa)	f_y (MPa)	μ
Bolt	7.85e^{-9}	210000	1080	0.3
Nut	7.85e^{-9}	210000	1080	0.3
T-support	7.85e^{-9}	210000	420	0.3
Washer	7.85e^{-9}	210000	640	0.3

Table 5.2 Range of parameters for the parametric study of Q460, Q690 and Q960 single row T-stub joints

end distance (mm)	80	60	40
t_f (mm)	6	12	18
heat input (kJ/mm)	0.5	1.4	2.3

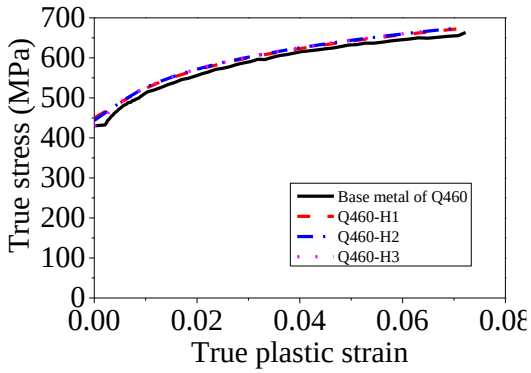

(a) HAZ of Q460 under various heat input

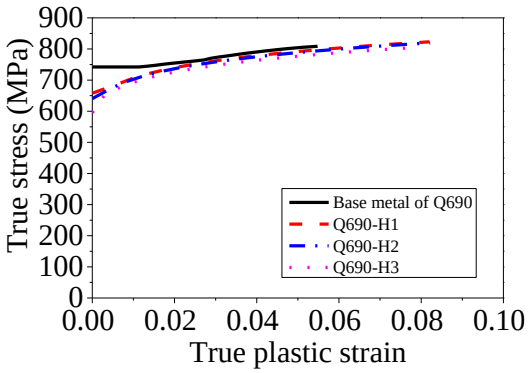

(b) HAZ of Q690 under various heat input

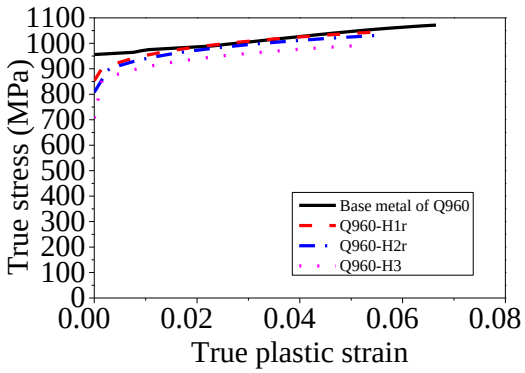

(c) HAZ of Q960 under various heat input

Figure 5.1 True stress-plastic strain curves for HAZ of Q460, Q690 and Q960 under different heat inputs

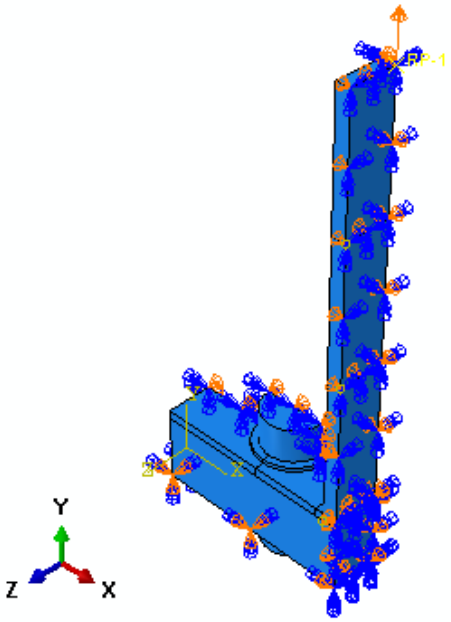

Figure 5.2 1/4 model for single row T-stub joint

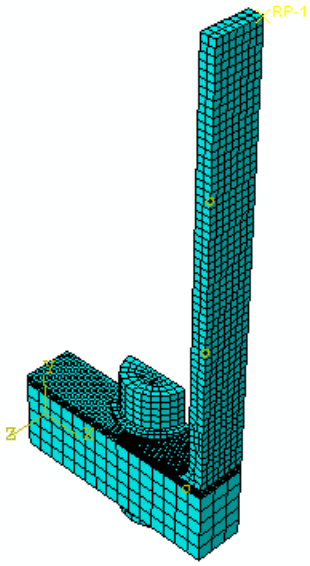

Figure 5.3 Numerical model of single row T-stub joint after meshing

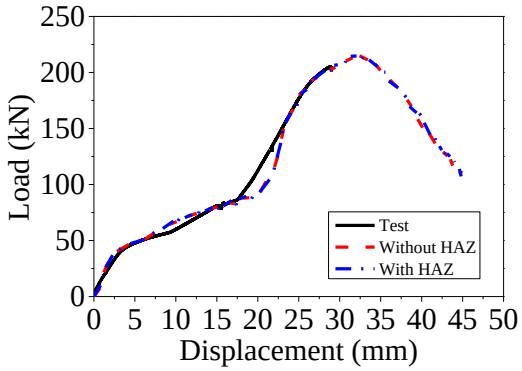

(a) Q460-H1-E80-Rig

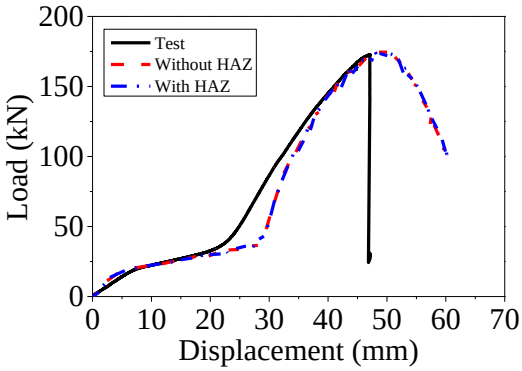

(b) Q460-H1-E40-Rig

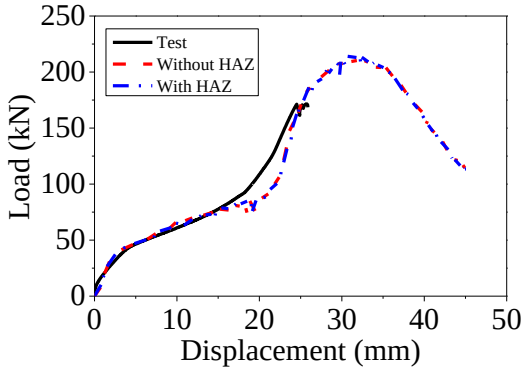

(c) Q460-H2-E80-Rig

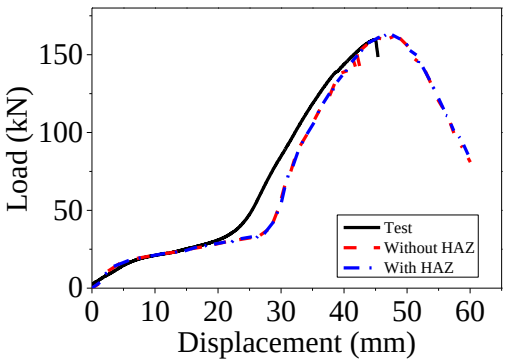

(d) Q460-H2-E40-Rig

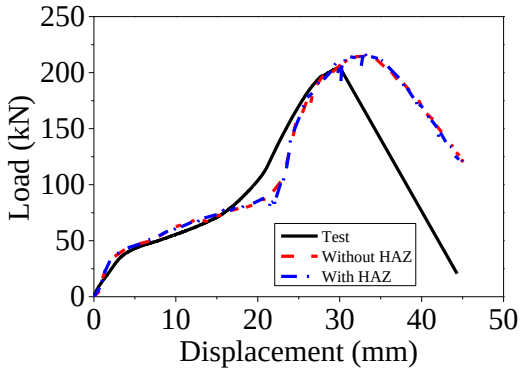

(e) Q460-H3-E80-Rig

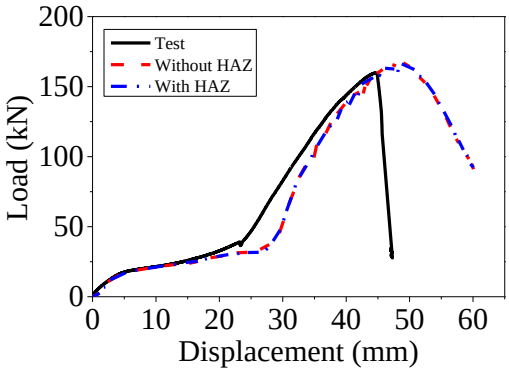

(f) Q460-H3-E40-Rig

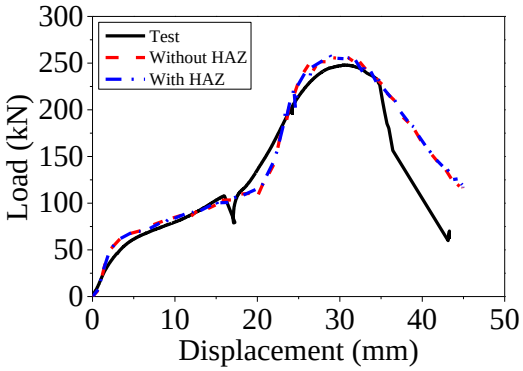

(g) Q690-H1-E80-Rig

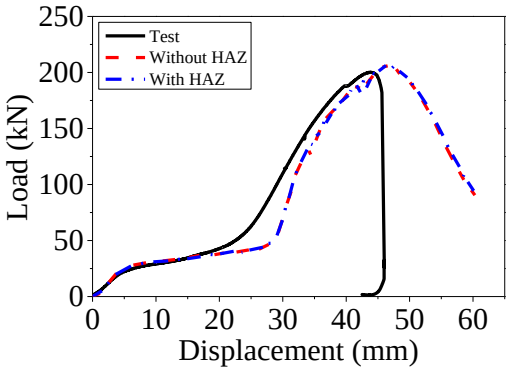

(h) Q690-H1-E40-Rig

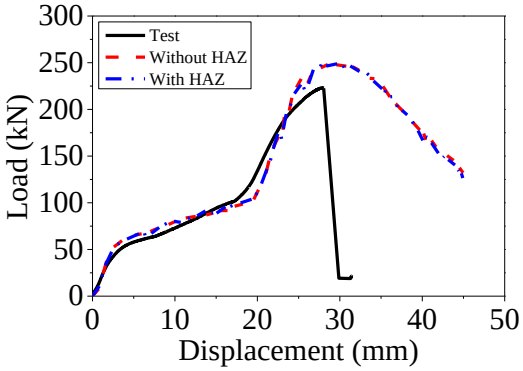

(i) Q690-H2-E80-Rig

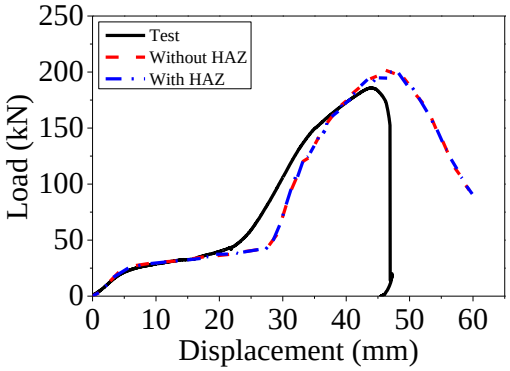

(j) Q690-H2-E40-Rig

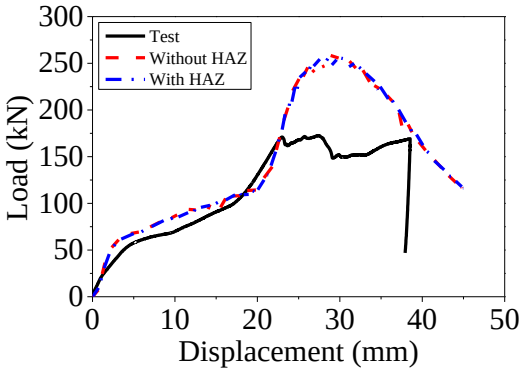

(k) Q690-H3-E80-Rig

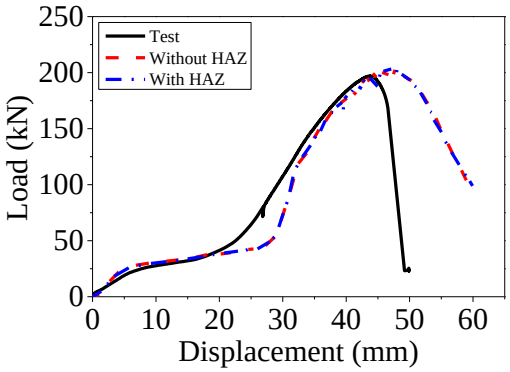

(l) Q690-H3-E40-Rig

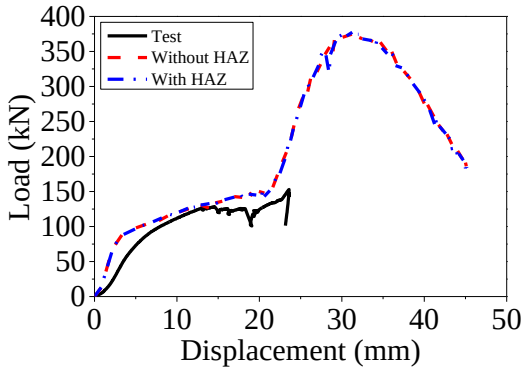

(m) Q960-H1r-E80-Rig

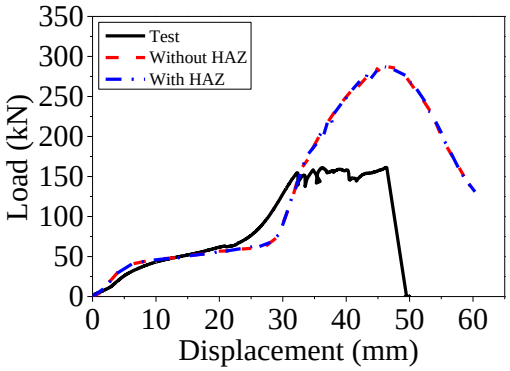

(n) Q960-H1r-E40-Rig

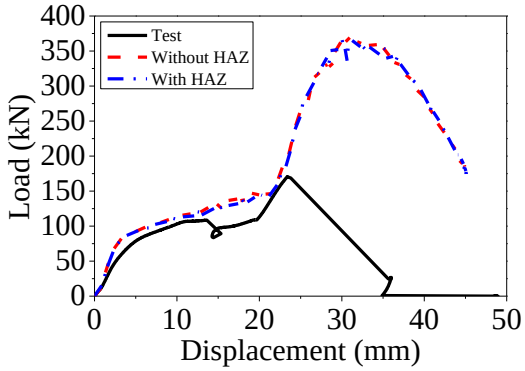

(o) Q960-H2r-E80-Rig

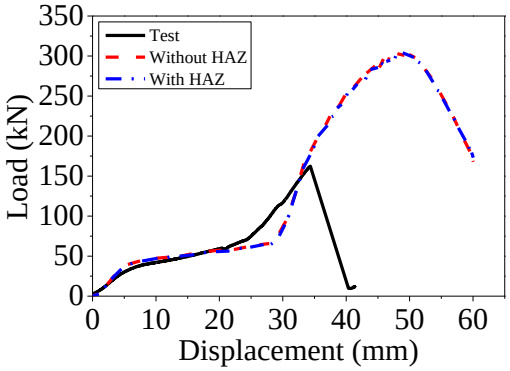

(p) Q960-H2r-E40-Rig

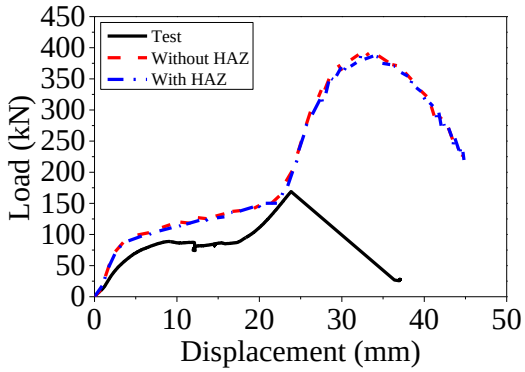

(q) Q960-H3-E80-Rig

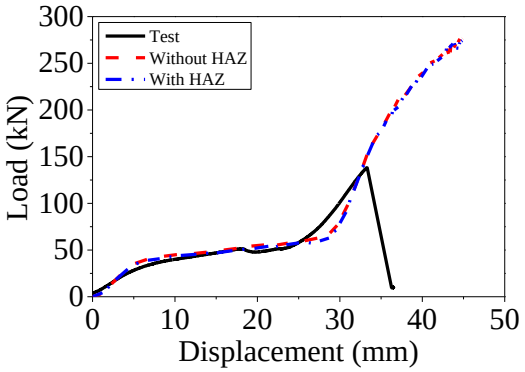

(r) Q960-H3-E40-Rig

Figure 5.4 Comparison between experimental and numerical load-displacement curves for single row T-stub joints

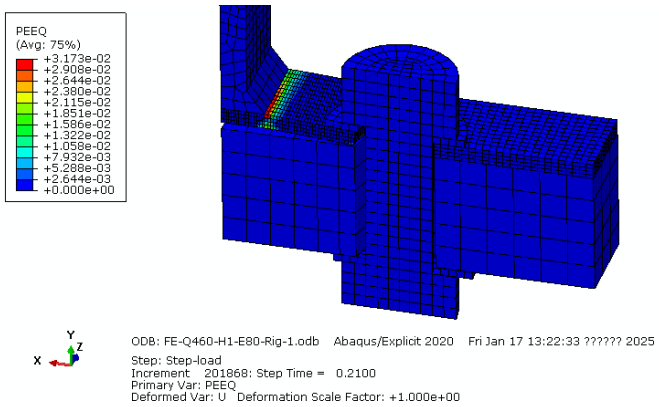

Figure 5.5 Equivalent plastic strain distribution at the transition zone between elastic stage and plastic stage for Q460-H1-E80-Rig

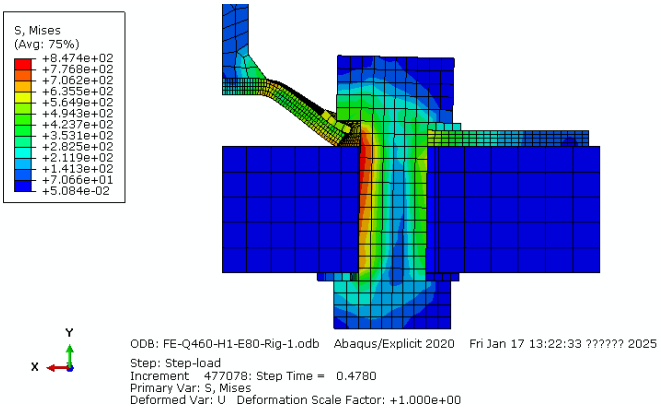

Figure 5.6 Stress state at the transition zone between plastic stage and second hardening stage for Q460-H1-E80-Rig

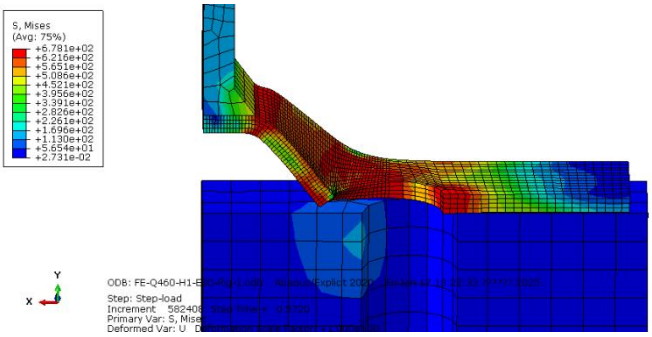

Figure 5.7 Membrane action developed in Q460-H1-E80-Rig

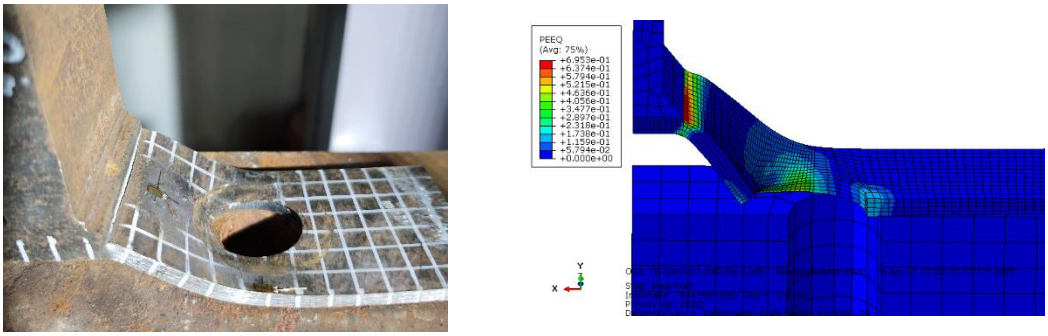

(a) Experiment (b) Numerical simulation

Figure 5.8 Deformation of Q460-H1-E80-Rig at peak load point

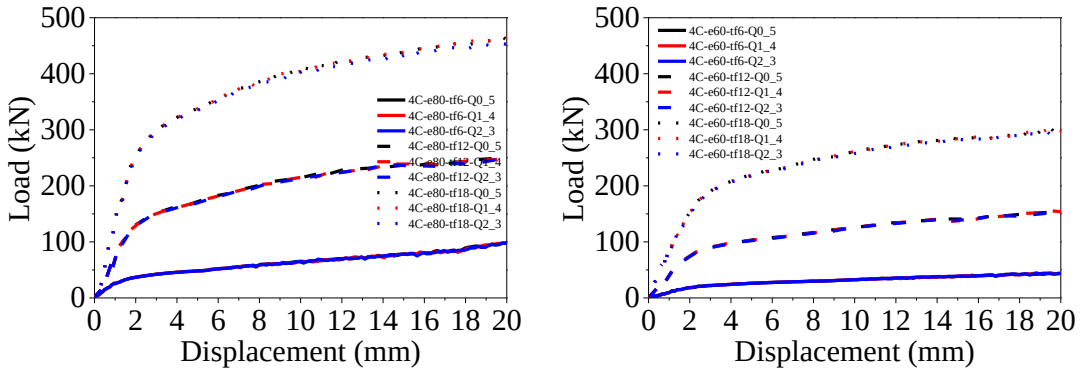

(a) Effect of Q with e_1 = 80 mm (b) Effect of Q with e_1 = 60 mm

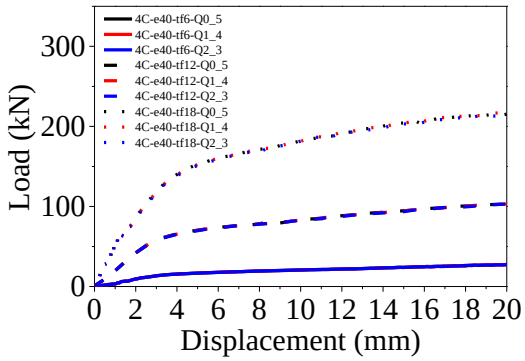

(c) Effect of Q with e_1 = 40 mm

Figure 5.9 Influence of welding heat input on the load-displacement curves for Q460 single row T-stub joints with different end distances

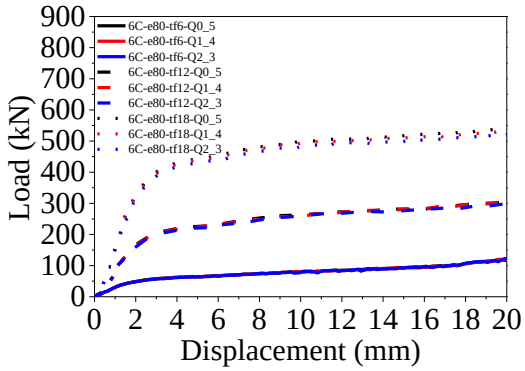

(a) Effect of Q with e_1 = 80 mm

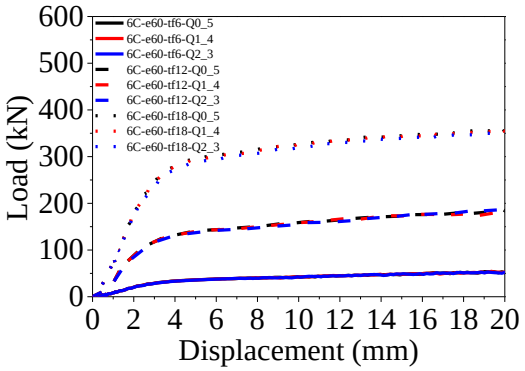

(b) Effect of Q with e_1 = 60 mm

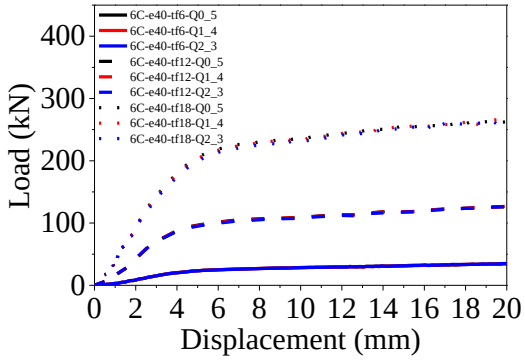

(c) Effect of Q with e_1 = 40 mm

Figure 5.10 Influence of welding heat input on the load-displacement curves for Q690 single row T-stub joints with different end distances

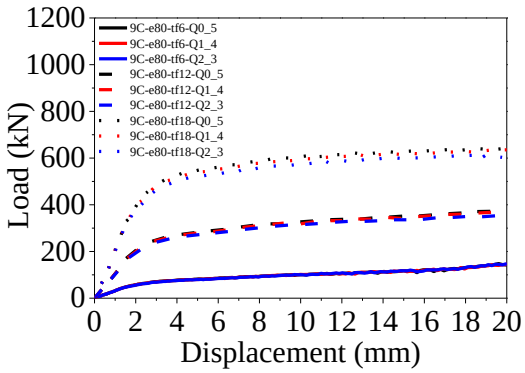

(a) Effect of Q with e_1 = 80 mm

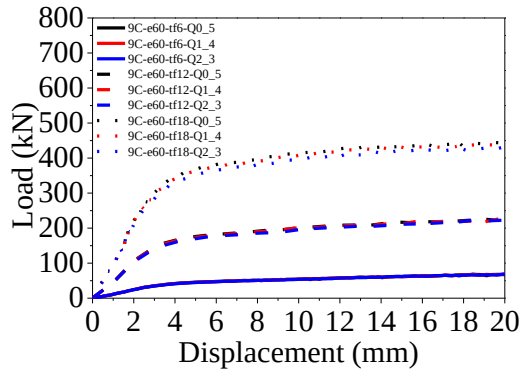

(b) Effect of Q with e_1 = 60 mm

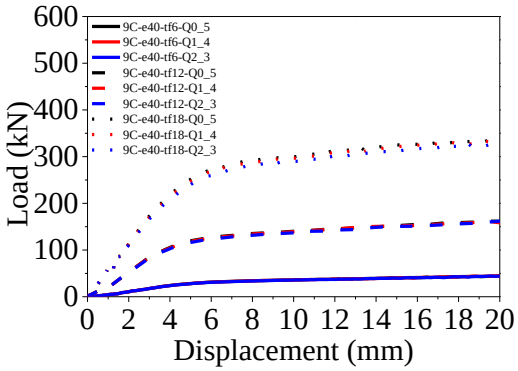

(c) Effect of Q with e_1 = 40 mm

Figure 5.11 Influence of welding heat input on the load-displacement curves for Q960 single row T-stub joints with different end distances

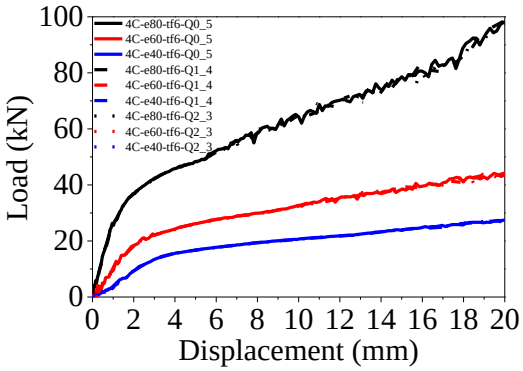

(a) Effect of e_1 with t_f = 6 mm

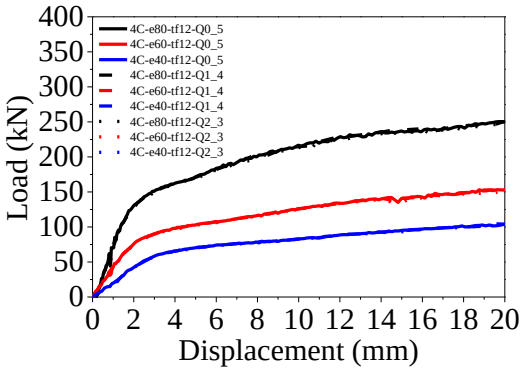

(b) Effect of e_1 with t_f = 12 mm

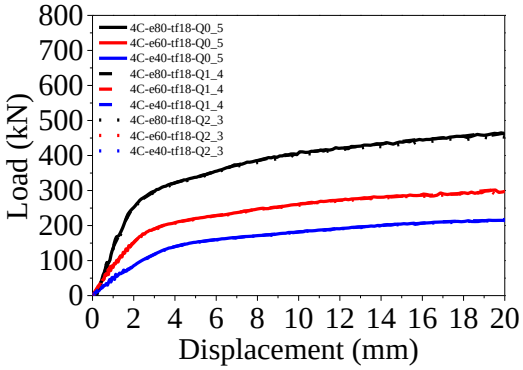

(c) Effect of e_1 with t_f = 18 mm

Figure 5.12 Influence of end distance on the load-displacement curves for Q460

single row T-stub joints with different flange thicknesses

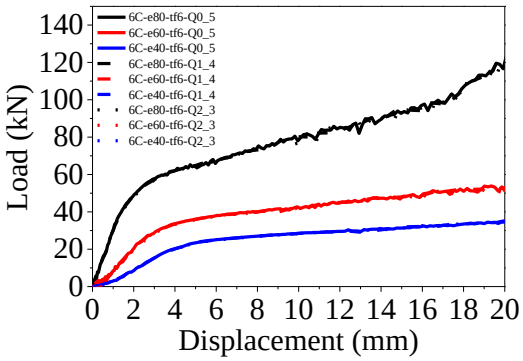

(a) Effect of e_1 with t_f = 6 mm

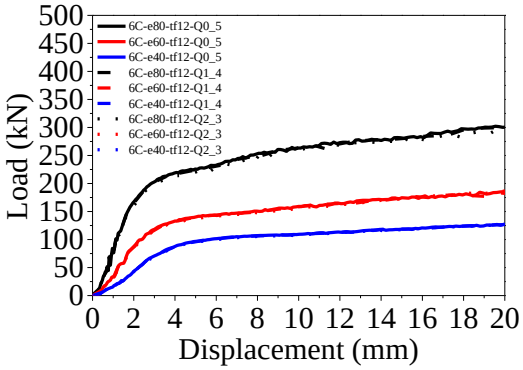

(b) Effect of e_1 with t_f = 12 mm

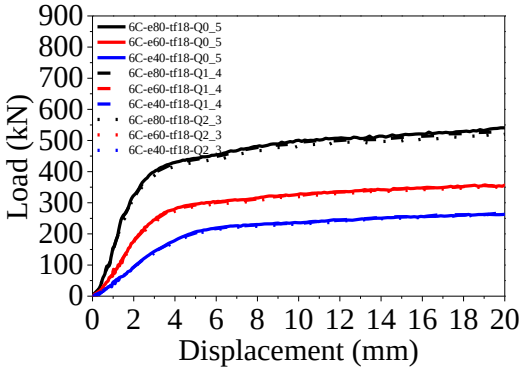

(c) Effect of e_1 with t_f = 18 mm

Figure 5.13 Influence of end distance on the load-displacement curves for Q690 single row T-stub joints with different flange thicknesses

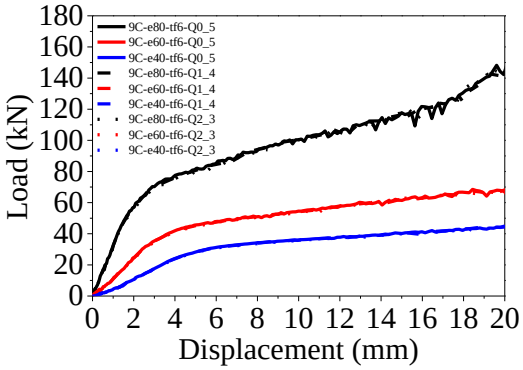

(a) Effect of e_1 with t_f = 6 mm

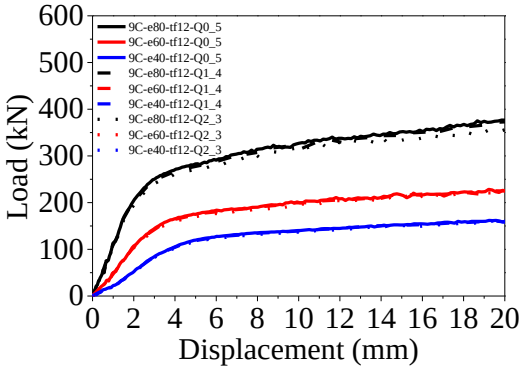

(b) Effect of e_1 with t_f = 12 mm

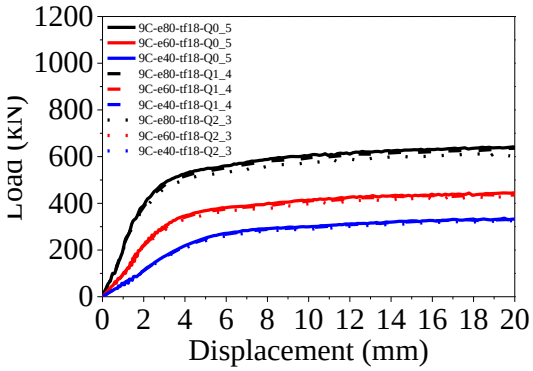

(c) Effect of e_1 with t_f = 18 mm

Figure 5.14 Influence of end distance on the load-displacement curves for Q960 single row T-stub joints with different flange thicknesses

Chapter 6 Experimental investigations of the HSS gusset plate to CHS X-joints under tension

6.1 Introduction

This chapter described the experimental investigations of the HSS gusset plate to circular hollow section (CHS) X-joints under tension. Similar to the butt-welded joints and single row T-stub joints, three kinds of steel grades, namely Q460, Q690 and Q960, were adapted to fabricate the gusset plate to CHS X-joints. The gusset plates were welded onto the CHS by gas metal arc welding (GMAW) operated by a skilled worker. The parameters concerned in the experiments included the ratio of brace width to chord diameter (β for the transverse plate and η for the longitudinal plate), the ratio of chord diameter to chord thickness (2γ), the steel grade, and the heat inputs of welding. Two heat inputs, one was around 1 kJ/mm, the other was around 2.4 kJ/mm, were adapted in the fabrication. A universal testing machine was utilised to exert axial tension to all 18 specimens. Based on the test results, the failure modes, load-deformation curves, joint strengths and deformation characteristics were comprehensively discussed. Besides, current design recommendations for tubular joints, such as ISO 14346 (ISO, 2013a), prEN 1993-1-8 (CEN, 2024a), and equations proposed by Voth (Voth, 2010), were evaluated according to test results.

6.2 Experimental programme

6.2.1 Base material properties

Three kinds of high strength steel (HSS), including Q460, Q960 and Q690, were used for both circular hollow sections (CHS) and gusset plates in this research. It should be pointed out that for each steel grade of gusset plate and CHS, the product batch was different. For the gusset plate with nominal thickness equal to 20 mm, the nominal chemical compositions and tensile coupon test results were already shown in Chapter

4. For the CHSs, the nominal chemical compositions were shown in Table 6.1. The tensile coupon test results were provided in Table 6.2.

6.2.2 Specimens

6.2.2.1 Specimen information

HSS transverse and longitudinal plate to CHS X-joints were fabricated and tested. Figure 6.1 demonstrates the definitions of symbols of the specimens. b_1 or h_1 represents the gusset plate width. L_1 represents the gusset plate length from the crown point. t_1 represents the gusset plate thickness. d_0 represents the chord diameter. L_0 represents the chord length. t_0 represents the chord wall thickness. Figure 6.2 shows the weld details. It contained bevels and was a combination of complete penetration weld and fillet weld. t_w represents the throat thickness.

Several parameters were considered in this test, including the ratio of brace width to chord diameter (β for the transverse plate and η for the longitudinal plate), the ratio of chord diameter to chord thickness (2γ), the steel grade, and the heat input of welding. Table 6.3 shows the specimen information and measured dimensions for the gusset plate to CHS X-joints in this research. All the joints were X type, and the load condition was tension. Besides, the angle between the plate and chord centreline was 90°. The nomenclature of the specimens demonstrated the specimen information straightforward. For example, "4C200x6-XT-B-Tran-0_7-M" was illustrated as follows:

1) "4C200x6" denoted that the steel grade was Q460, and the nominal chord diameter and chord wall thickness were 200 mm and 6 mm, respectively.
2) "XT" denoted that the joint was X type, and the load condition was tension.
3) "B" indicated that the gusset plate was branch.
4) "Tran" or "Long" demonstrated that the gusset plate direction were transverse and longitudinal to the chord centreline, respectively.

5) “0_7” denoted that β or η was 0.7.
6) “M” or “H1” denoted that the heat input was medium or high, respectively.
7) The specimen with “*” represented that it was a repeated test.

The 18 specimens were classified into 5 groups. Group 1 included No. 1 – 4, in which the influence of steel grade on the transverse plate to CHS X-joint was concerned. Group 2 contained No. 5 – 7 which had identical steel grades and geometric dimensions with Group 1 but higher heat inputs. No. 8 -9 in Group 3 were designed to investigate the influence of β on the transverse plate to CHS X-joints. In Group 4, the influence of steel grades and η were studied for the longitudinal plate to CHS X-joints by No. 10 - 15. Group 5 had identical steel grades and geometric dimensions with Group 4 but higher heat inputs. In addition, the measured dimensions were also given by Table 6.3.

6.2.2.2 Specimen fabrication

Figure 6.3 shows the components for the joints. To fabricate CHSs, the steel plates were cold formed first, and then they were welded along the chord length direction to form circular shapes. The gusset plates were laser-cut from the base metal plates. Then the flame-cutting was conducted to generate bevels with 45° angle by referring to the plate centreline. The area near bevels was carefully grinded to eliminate the rust.

For each steel grade, the corresponding filler electrode was adapted, as shown in Table 6.4. Since the gusset plate to CHS X-joint had two plates and each plate had two sides, four sides needed welding for one joint. The fabrication of the gusset plate to CHS X-joint was shown in Figure 6.4. Gas metal arc welding (GMAW) was adapted in this research. The shielding gas consisted of 80% CO_2 and 20% Ar. The gusset plate was spot-welded on the CHS after carful positioning which kept the plate vertical and centred. The welding area was preheated before welding to remove water on the surface. The specimens were classified by two kinds of average heat inputs in the welding, one

was around 1.1 kJ/mm, the other was around 2.3 kJ/mm. The horizontal position was used for the joint with its heat input equal to 1.1 kJ/mm, while the vertical position was used for the joint with its heat input equal to 2.5 kJ/mm. The first welding pass for one bevel side was manually welded by an experienced welder to fill the gaps between the plate and the CHS surface, otherwise the complete penetration cannot be achieved. Besides, the welding speed of the first welding pass for the joint with 2.3 kJ/mm heat input should be slower to avoid drawbacks like porosity. Robotic welding was adapted for the left welding passes. The experienced welder could adjust the welding gun travel angle, welding gun work angle and wire stick out length for each welding pass, which were crucial for acquiring satisfactory welds. The interpass temperature was between 100 ~ 120 ℃ for the Q690 and Q960 joints. After welding, the welding area was grinded, and the ultrasonic examination demonstrated that no drawbacks existed in the welds. Figure 6.5 shows the completed gusset plate to CHS X-joints. The number of welding passes for every specimen were provided in Table 6.5. X-joints had two gusset plates for both sides. Each plate had two sides to be welded, namely left and right side. For every side, the first welding pass were fabricated by manual welding to complete full penetration. For the other welding passes, robotic arc welding was adapted. The heat inputs for each specimen were shown in Table 6.6.

6.2.3 Test setup and procedure

A servo-hydraulic universal testing machine with a capacity of 2000 kN was used to apply the brace tension for the gusset plate to CHS X-joints. The joint was gripped at the center of the upper and lower clamps of the testing machine, as shown in Figure 6.6. A preload about 5 kN was applied to eliminate any possible gaps between the gusset plate and the clamps. Then, the load was applied to the specimen by the displacement control at a rate of 1 mm/min.

Figure 6.7 illustrates the instrumentation for both transverse and longitudinal plate to

CHS X-joints. Six calibrated linear variable displacement transducers (LVDTs) were used to measure the local deformations of the gusset plate to CHS X-joint. All the bases of the LVDTs were fixed to the universal testing machine and would not move during displacement loading. Figure 6.8 shows the measurement of the chord face deformation. For the joints whose nominal chord diameter was 200 mm, chord face deformation was obtained by 4 LVDTs placed at a distance of 35 mm from the brace face at the chord crown. Similarly, for the joints whose nominal chord diameter was 150 mm, chord face deformation was also obtained by 4 LVDTs placed at a distance of 20 mm from the brace face at the chord crown. Particularly, the extension arms were attached to the tips of these 4 LVDTs, as shown in Figure 6.9. The chord face deformation can be calculated as follows:

$$\frac{1}{2} \times \left(\frac{LVDT1 + LVDT2}{2} - \frac{LVDT3 + LVDT4}{2}\right)$$

LVDT1, 2, 3, 4 represented the absolute displacement value measured by the corresponding LVDT, respectively.

Figure 6.10 shows the measurement of the chord sidewall deformation. 2 LVDTs were placed horizontally and contacted with the chord sidewall. The poly methyl methacrylate (PMMA) plates were attached to the tips of these 2 LVDTs (Figure 6.11), thus the maximum chord sidewall deformation could be continuously captured, though the vertical displacement of the joint existed during testing. The chord sidewall deformation can be calculated as follows:

$$\frac{LVDT5 + LVDT6}{2}$$

LVDT5 and 6 represented the absolute displacement value by the corresponding LVDT. Five strain gauges were evenly installed on the plate surface and 35 mm above the chord crown, as shown in Figure 6.12. They were used to measure the plate strain distribution.

6.3 Experimental results of gusset plate to CHS X-joints

6.3.1 Failure modes

The joint strengths were determined as either the peak load or the load at 3% d_0 deformation limit, whichever occurred first. The typical failure modes for the gusset plate to CHS X-joints included the chord face failure and punching shear failure. The specimen failed in the chord face failure if the chord face deformation exceeded 3% d_0. The specimen failed in the chord punching shear failure if the peak load appeared before 3% d_0. For the joints who failed in chord face failure, if they were continuously loaded after 3% d_0, the chord punching shear would be finally triggered. Table 6.7 gives the failure mode for each specimen. Most specimens failed in chord face failure. However, 6C200x6-XT-B-Tran-0_7-M, 9C200x5-XT-B-Tran-0_7-M, 6C200x6-XT-B-Tran-0_7-H1 and 9C200x5-XT-B-Tran-0_7-H1 failed before reaching to 3% d_0 deformation. Therefore, they failed in chord punching shear. This fact indicated that for HSS gusset plate to CHS X-joint under brace tension, the failure mode may change from the deformation control (chord face failure) to the strength control (chord punching shear failure). The reasons could be explained by load versus deformation curves. Figure 6.13 to Figure 6.15 demonstrated the typical experimental failure modes for the gusset plate to CHS X-joints. The transverse plate to CHS X-joint ruptured at the chord saddle, as shown in Figure 6.13. The ovalisation was obvious in the core region of the joint. The longitudinal plate to CHS X-joint also ruptured along the plate length direction. And the significant ovalisation occurred along the overall chord length (see Figure 6.14). Besides, 9C150x5-XT-B-Long-0_5-H1 ruptured along the weld of the chord (see Figure 6.15). No ovalisation was exhibited along the chord length. Therefore, it may be caused by unsatisfactory welding of CHS.

6.3.2 Load versus deformation curves and joint strengths

The load versus deformation curves are illustrated in Figure 6.16 to Figure 6.20. Several

factors that may influence the load-deformation behaviour were investigated, including the steel grade, heat input, β, γ, η and plate direction. It was noted that the load-chord face deformation curves of 6C200x6-XT-B-Tran-0_7-M, 9C200x5-XT-B-Tran-0_7-M and 4C150x6-XT-B-Long-0_5-M were not as smooth as those of other specimens. It was because the chord face area which was contacted with the extension of LVDTs was not completely grinded to remove all the rust. The load-deformation curves of repeated specimens, including 4C200x6*-XT-B-Tran-0_7-M and 6C150x6*-XT-B-Long-0_5-M, overlapped with corresponding specimens, indicating that the test results were reliable.

The load-deformation curves of the gusset plate to CHS X-joints consisted of different stages. All the specimens had elastic stages. The plastic stage was subsequent to the elastic stage. However, 6C200x6-XT-B-Tran-0_7-M, 9C200x5-XT-B-Tran-0_7-M, 6C200x6-XT-B-Tran-0_7-H1, and 9C200x5-XT-B-Tran-0_7-H1 had little or even no plastic stage, thus showing low ductility. And the plate direction of them were all transverse. Limited specimens, like 4C150x6-XT-B-Long-0_5-M, 4C150x6-XT-B-Long-0_5-H1, and 6C150x6-XT-B-Long-0_8-M, had a significant second hardening stage after the plastic stage, thus showing high ductility. The plate direction of them were all longitudinal. This implied that the gusset plate to CHS X-joint with the longitudinal plate had better ductility compared to the transverse plate.

Figure 6.16 and Figure 6.17 show the load-chord face and load-chord sidewall deformation curves for the transverse plate to CHS X-joints, respectively. Figure 6.16(a)(b) show that the peak load of the Q690 joint was smaller than that of the Q460 joints, as higher steel grade may encounter more severe material deterioration under the welding influence. However, the joint strengths corresponding to 3%d_0 deformation limit increased with higher steel grades. In addition, the initial stiffness of the Q690 joint was larger than that of the Q460 joints. Figure 6.16(c)-(e) exhibit the influence of

heat inputs on the transverse plate to CHS X-joints made of different steel grades. There was no obvious tendency for the peak load of the Q460 and Q690 joints as heat input increased. While for the Q960 joints, the peak load was reduced with the increase of heat input. Besides, the initial stiffness of all the steel grades degraded as heat input increased. In Figure 6.16(f), the initial stiffness, peak load and joint strength corresponding to 3%d_0 deformation limit rose as β increased from 0.5 to 0.7 for the transverse plate to CHS X-joints. In Figure 6.16(g), the peak load varied insignificant, but the initial stiffness and joint strength corresponding to 3%d_0 deformation limit increased as γ decreased for the Q460 joints with the same heat input.

Figure 6.18 and Figure 6.19 show the load-chord face and load-chord sidewall deformation curves for the longitudinal plate to CHS X-joints, respectively. Figure 6.18(a)(b) demonstrate that the Q460 longitudinal plate to CHS X-joints exhibited the second hardening stages caused by the membrane effect during brace axial tension loading under both heat inputs. The Q690 steel usually had enhanced strength but reduced ductility, and welding usually had a more severe effect on the higher steel grade. Therefore, there was no second hardening effect for the Q690 joints. The load-chord face deformation curves of the Q690 joints had longer elastic stages and thus larger joint strengths corresponding to 3% d_0 deformation limit compared to the Q460 joints, indicating the advantage of the higher strength steel. However, the peak load of the Q460 joints was significantly larger than that of the Q690 joints, which was caused by the second hardening effect. Figure 6.18(c)-(e) give the influence of heat inputs on the longitudinal plate to CHS X-joints made of different steel grades. For the Q460 and Q690 joints, there was no obvious effect of heat inputs on the load-chord face deformation curves. But for the Q960 joints, increasing heat input could decrease the initial stiffness and the peak load significantly. This revealed that welding had a more evident effect on the Q960 joints. Figure 6.18(f)(g) indicate that increasing η could enlarge the peak load for both the Q690 and Q960 joints but have little influence on the

initial stiffness. However, the joint strengths corresponding to 3% d_0 deformation limit did not vary with η. Furthermore, 6C150x6-XT-B-Long-0_8-M had the second hardening effect compared to 6C150x6-XT-B-Long-0_5-M.

Figure 6.20 shows the plate skew angle influence on the gusset plate to CHS X-joint made of Q460. It can be observed that the transverse plate to CHS X-joint had longer elastic stage and larger initial stiffness but reduced ductility. The joint strength corresponding to 3% d_0 deformation limit of the transverse joint was significantly larger than that of the longitudinal joint. However, since the longitudinal joint exhibited the second hardening effect, the peak loads of both specimens were approximate.

The joint strengths corresponding to 3% d_0 deformation limit and the peak loads of the gusset plate to CHS X-joints were obtained from the load-chord deformation curves, as listed in Table 6.7.

Figure 6.21 to Figure 6.24 exhibited the influence of several factors on the joint strengths corresponding to 3% d_0 deformation limit and the peak loads for the transverse plate to CHS X-joints. For the Q460 joints, increasing the heat input or γ had little effect on not only the joint strengths corresponding to 3% d_0 deformation limit but also the peak load. In contrast, both the joint strengths corresponding to 3% d_0 deformation limit and peak load increased significantly as β increased for the Q460 joints. It can be noted that the peak load did not absolutely amplify by increasing the steel grade from Q460 to Q690 (see Figure 6.22), as the HAZ of Q690 was more degraded than that of Q460, which led to the premature of the Q690 joints under tension. Furthermore, the peak load of the Q960 joints was reduced with the increase of the heat input, which indicated the material degradation of Q960 got severer.

Figure 6.25 to Figure 6.30 demonstrated the influence of several factors on the joint

strengths corresponding to 3% d_0 deformation limit and the peak loads for the longitudinal plate to CHS X-joints. Under both heat inputs, the joint strengths corresponding to 3% d_0 deformation limit increased as the steel grades increased. However, the peak loads corresponding to the moment chord punching shear happened decreased significantly with the increase of the steel grades, because severer material deterioration existed for higher steel grades. The influence of the heat inputs on the joint strengths at 3% d_0 deformation limit and the peak load was neglectable for both Q460 and Q690 longitudinal plate to CHS X-joints. But for the Q960 joints, both the joint strengths and peak loads degraded with the increase of the heat inputs. The increase of the geometric parameter η could only increase the peak loads for both Q690 and Q960 joints but not the joint strengths at 3% d_0 deformation limit.

Figure 6.31 illustrates the influence of plate skew angle on Q460 gusset plate to CHS X-joints. It can be noted that the plate skew angle could increase the joint strengths at 3% d_0 deformation but the peak loads remained almost identical.

6.3.3 Deformation characteristics

6.3.3.1 Joint ductility

A modified bi-linear model proposed by Yan (2023) was adapted here to represent the overall joint behaviour. In this model, the elastic behaviour of the joint was described by a straight line whose slope was the initial stiffness, as shown in Figure 6.32. The equal energy criterion was applied to determine the post-yielding stiffness for the plastic behaviour. A straight line ending at the ultimate state point was adjusted to make the blue regions in Figure 6.32 had the same areas. The load corresponding to the intersection point of the elastic and plastic lines was defined as the yield resistance (R_y). And the ratio of the ultimate deformation (D_2) and the deformation corresponding to the intersection point of the plastic line and load-displacement curve (D_1) was determined to evaluate the joint ductility.

Table 6.8 presents the ductility results for the tested gusset plate to CHS X-joints. Figure 6.33 to Figure 6.35 show the ductility of transverse plate to CHS X-joints varied with different parameters. It was clear that the ductility declined as the steel grade increased. However, the influence of heat input on the ductility was obscure: for the Q460 and Q960 joints, the ductility was reduced by enlarging the heat input; while for the Q690 joints, the ductility was enhanced as the heat input increased. Besides, increasing β could reduce the joint ductility while enhancing γ could enhance it.

Figure 6.36 to Figure 6.38 demonstrated the ductility variation of longitudinal plate to CHS X-joints. Similar to the transverse plate joints, with the steel grades increased from Q460 to Q690, the longitudinal joint ductility significantly lowered no matter the heat input was. The influence of heat input was also indistinct for HSS longitudinal plate to CHS X-joint because the Q690 joints had different tendency compared to the Q460 and Q960 joints. In contrast, increasing η could significantly improve the longitudinal plate joint ductility. But the degree of improvement decreased if the steel grade increased from Q690 to Q960.

Figure 6.39 illustrates the influence of plate skew angle on the joint ductility. It can be observed that the influence was quite mild as the skew angle increased from 0° to 90°, the D_2/D_1 ratio only reduced from 3.886 to 3.639.

6.3.3.2 Plate surface stress distribution

Figure 6.40 and Figure 6.41 demonstrate the plate surface stress distributions of the transverse and longitudinal plate to CHS X-joints under ten different load levels, respectively. It is noted that the SG5 of 4C200x6-XT-B-Tran-0_7-H1 was broken under high loading levels. In general, the transverse joints exhibited more uneven plate surface stress distributions than the longitudinal joints. It was because the stiffness around the chord perimeter was more non-uniform while that along the chord length. The plate

stress distributions of both joints got elevated stress levels at the outer regions of the plate as load levels increased. The plate stresses near the brace edge were usually much larger than those in the brace centre, which explained the reason why the chord punching shear initiated at the chord saddle for the transverse joints and at the chord crown for the longitudinal joints due to the stress concentration.

Particularly, regardless of the heat inputs, compressive stresses increased in the plate centre area for the transverse plate to CHS X-joints with 200 mm chord made of Q690 and Q960 with the increase of load level, as shown in Figure 6.40(b)(c)(e)(f). In comparison, only tensile stresses existed along the plate width for the counterpart made of Q460. It was likely that the heat affected zone (HAZ) near the weld toe changed the chord stress distribution since Q690 and Q960 were more susceptible to the welding effect, thus leading to the stress redistribution. Significant non-uniform plate stress distributions could be generated if β increased for the transverse plate to CHS X-joints, as shown in Figure 6.40(g)(h).

Figure 6.41(a)(b)(d) and (f)(g)(h) show that under large load levels, the longitudinal joint made of Q460 had a more uneven plate surface stress distribution than the joints made of Q690 and Q960 regardless of the heat inputs, since the Q460 joint entered the second hardening stage. Furthermore, as η increased, the stresses at the outer regions of the plate got obviously larger than those at the brace centre area, as shown in Figure 6.41(b)(c) and (d)(e).

6.4 Evaluation of current design codes

6.4.1 Current design recommendations

6.4.1.1 ISO 14346

ISO 14346 regulates the design methods for the gusset plate to CHS X-joints under

brace axial loads. In this code, the nominal yield strength of the steel should be within 460 MPa. Besides, the yield stress f_y of the steel should not exceed 0.8 of the ultimate stress f_u, otherwise the design yield strength should be 0.8 f_u. Design equations for the joints failed in chord plastification and chord punching shear under brace axial force are suggested in ISO 14346, shown as follows:

Chord plastification:

$$N_{CF,ISO} = Q_u Q_f \frac{f_{y0} t_0^2}{sin\theta} \quad \text{Eq. 6.1}$$

in which, Q_u is the partial design strength function, Q_f is the chord preload function, f_{y0} is the design yield stress, t_0 is the chord wall thickness, θ is the angle between the gusset plate and chord member. In addition, the partial design strength function Q_u can be calculated according to Eq. 6.2 and Eq. 6.3. The chord preload function can be obtained according to Eq. 6.4.

For transverse plate:

$$Q_u = 2.2\left(\frac{1+\beta}{1-0.7\beta}\right)\gamma^{0.15} \quad \text{Eq. 6.2}$$

For longitudinal plate:

$$Q_u = 5\ （1+0.4\eta） \quad \text{Eq. 6.3}$$

The chord preload function:

$$Q_f = (1-|n|)^{C_1} \quad \text{Eq. 6.4}$$

in which, n is the factor to account for chord stress, C_1 is the coefficient used in the chord preload function.

Chord punching shear:

$$N_{PS,ISO} \leq 1.16 f_{y0} b_1 t_0 \quad \text{Eq. 6.5}$$

in which, b_1 is the gusset plate width.

The partial safety factors have been implicitly incorporated into these design equations. Besides, a reduction factor of 0.9 should be applied to the above calculated joint resistances if f_y was larger than 355 MPa. It should be noted that for both transverse and longitudinal plate to CHS X-joints, there are ranges of validity for these equations, as listed in Table 6.9. For the joints which satisfy to the range of validity, the design resistance is taken as the minimum for chord plastification and chord punching shear, which also determines the predicted failure mode. But for the joints which do not comply with the range of validity, all possible failure modes of the joints should be considered to obtain the design resistance.

6.4.1.2 prEN 1993-1-8

The prEN 1993-1-8 (CEN, 2024b) proposes the design equations for the gusset plate to CHS X-joints under brace axial loads. Compared to previous version of EN 1993-1-8 (CEN, 2005a), the latest version is applicable to the steel with the nominal yield stress up to 700 MPa. The yield ratio f_y/f_u should be restricted to 0.8 for the joints failed by chord punching shear. The design equations are demonstrated as follows:

Chord plastification:

$$N_{CF,EC3} = \frac{C_f Q_u Q_f \frac{f_{y0} t_0^2}{sin\,\theta}}{\gamma_{M5}} \quad \text{Eq. 6.6}$$

in which, Q_u, Q_f, f_{y0}, t_0, θ have identical meanings as previous discussion. C_f is the material reduction factor, as illustrated in Table 6.10.

The partial safety factor is explicitly considered by γ_{M5}, which is taken as 1.0. The partial design strength function Q_u can be determined by Eq. 6.7 and Eq. 6.8. The chord preload function can also be obtained according to Eq. 6.4.

For transverse plate:

$$Q_u = 2.1(1 + 3\beta^2)\gamma^{0.25} \quad \text{Eq. 6.7}$$

For longitudinal plate:

$$Q_u = 4.4(1 + 0.4\eta) \quad \text{Eq. 6.8}$$

Chord punching shear:

$$N_{\mathrm{PS,EC3}} = 1.16 C_f \frac{f_{y0} t_0 b_1}{\gamma_{\mathrm{M5}}} \quad \text{Eq. 6.9}$$

The meanings of the symbols in Eq. 6.9 are identical to those for chord plastification failure. It is suggested that there are ranges of validity for both transverse and longitudinal plate to CHS X-joints in the prEN 1993-1-8 (CEN, 2024b), as shown in Table 6.11. The design resistance is determined as the smaller value of the chord plastification and the chord punching shear if the joint complies with Table 6.11. Otherwise, all possible failure modes should be taken into account to calculate the design resistance.

6.4.1.3 Design equations proposed by Voth

The design equations in ISO 14346 and EN 1993-1-8 do not include the effect of plate thickness on the joint resistance. Besides, the joint subjected to brace tension and compression adapted the same design recommendations. However, the investigations implemented by Voth (Voth, 2010) proved that not only the effect of plate thickness should be included but also different equations for different loading cases were proposed for the gusset plate to CHS X-joint. The design equations are illustrated as follows:

Chord plastification:

$$N_{CF,Voth} = Q_u Q_f \frac{f_{y0} t_0^2}{sin\theta} \quad \text{Eq. 6.10}$$

in which, Q_u, Q_f, f_{y0}, t_0, θ have identical meanings as Section 3.1.1 and 3.1.2. The chord preload functions are provided in Eq. 6.4.

For transverse plate under tension:

$$Q_u = 1.8\zeta(\frac{1+\beta}{1-0.6\beta})(1+\eta)\gamma^{0.4} \quad \text{Eq. 6.11}$$

For longitudinal plate under tension:

$$Q_u = 4.3\zeta(\frac{1+\beta}{1-0.6\beta})(1+0.5\eta)\gamma^{0.1} \quad \text{Eq. 6.12}$$

in which, ζ is the reduction factor which can compensate the differences between the parametric FE data and the international database. For the gusset plate to CHS X-joint, ζ is 0.85.

6.4.2 Comparison of test results and design code predictions

Table 6.12 provides the test strengths and the design resistances for the gusset plate to CHS X-joints. The load at 3% d_0 deformation and peak load were obtained from the load-displacement curves, denoted by $N_{3\%}$ and N_{max}. ISO 14346, prEN 1993-1-8 and design methods proposed by Voth were applied to calculate the predicted joint strengths. The relevant equations were introduced in Section 3.1. The $N_{CF, ISO}$ and $N^*_{CF, ISO}$ denoted the predicted load at 3% d_0 deformation (chord face failure) without and with reduction factors by ISO 14346, respectively. Similarly, the $N_{CF, prEC3}$ and $N^*_{CF, prEC3}$ represented the predicted load at 3% d_0 deformation (chord face failure) without and with reduction factors by prEN 1993-1-8, respectively. The predicted loads at 3% deformation without and with reduction factors obtained from the design equations proposed by Voth were $N_{CF, Voth}$ and $N^*_{CF, Voth}$. As for the peak loads corresponding to chord punching shear failure, $N_{PS, ISO}$ and $N^*_{PS, ISO}$ were calculated based on ISO 14346 without and with reduction factors, respectively. $N_{PS, prEC3}$ and $N^*_{PS, prEC3,}$ similarly, denoted the peak loads corresponding to chord punching shear failure respectively. It should be noted that for 9C150x5-XT-B-Long-0_5-H1, it fractured at the chord seam when reaching its peak load. For other specimens, in contrast, the chord punching shear happened when the peak load was achieved.

Figure 6.42 and Figure 6.43 plot the data of test strengths and corresponding predicted

joint strengths without and with reduction factors. It can be concluded that current design methods generally overestimated the load at 3% d_0 deformation for the gusset plate to CHS X-joints, as shown in Figure 6.42. In contrast, Figure 6.43 shows a more scattered plot, which meant the design methods were not accurate and consistent when prediction the load corresponding to chord punching shear. Some datasets were below $y=x$ curve in Figure 6.43, indicating that for some joints the load corresponding to the chord punching shear failure were underestimated.

Table 6.13 to Table 6.16 illustrate the comparisons between the test strengths and the design resistances. The ratios of the test strengths and the design resistances were demonstrated in Table 6.13. If the ratio was greater than unity, the corresponding design method was conservative. Otherwise, the design method was unsafe. Table 6.14 shows the statistical results of the design method evaluations. The mean ratios of $N_{3\%}$ and the predicted load at 3% d_0 deformation by above mentioned design methods were all much greater than unity without and with the reduction factors, indicating that the reduction factor was not necessary, and these design methods were all applicable. No matter whether incorporating the reduction factor, the mean values of the ratios between $N_{3\%}$ and the predicted load by the Voth's method were closest to unity and had small coefficient of variation (COV), which proved that incorporating the effect of plate thickness could improve the joint strength predictions. While the mean values of the ratios between $N_{3\%}$ and the predicted load by ISO 14346 and prEN 1993-1-8 were greater than 1.5, representing the over-conservativeness of these design codes. The mean ratios of N_{max} and the predicted load corresponding to chord punching shear by ISO 14346 and prEN1994-1-8 were close to unity. However, the COVs of N_{max} and the predicted load corresponding to chord punching shear were all above 0.3, which were much greater than the counterpart of $N_{3\%}$ and the predicted load at 3% d_0 deformation. This meant that the design methods for chord punching shear failure were unsafe as it may underestimate the peak load, as revealed in Figure 6.43. Table 6.15 and Table

6.16 compare the test strengths with design resistances for the gusset plate to CHS XZ joints under different heat inputs. It can be observed that the COVs of the joints under higher heat input were greater that the counterpart under lower heat input. This implied that to improve the consistency of the design methods, the effect of the heat inputs should also be incorporated.

6.5 Summary

In this investigation, a total of 18 HSS gusset plate to CHS X-joints were fabricated by various steel grades including Q460, Q690 and Q960. During welding, two different heat inputs were adapted. The influences of geometric parameters, like β, η, γ and plate skew angle, on the mechanical behaviours of the joints were covered in the test programme. All the specimens were subjected to brace axial tension by displacement control. The failure modes, chord face deformation, chord sidewall deformation, and deformation characteristics were recorded and analysed. The joint strengths obtained from the experiments were used to evaluate the applicability of current design methods on HSS tubular joints, including ISO 14346, prEN 1993-1-8 and Voth's method. Following conclusions can be drawn:

1. According to the 3% d_0 deformation limit, most specimens failed by chord face failure. However, 6C200x6-XT-B-Tran-0_7-M, 9C200x5-XT-B-Tran-0_7-M, 6C200x6-XT-B-Tran-0_7-H1 and 9C200x5-XT-B-Tran-0_7-H1 failed before reaching to 3% d_0 deformation, known as chord punching shear failure. This fact proved that for HSS transverse plate to CHS X-joint under tension, the strength control could also determine the joint strength.

2. For the HSS gusset plate to CHS X-joints, the steel grades, heat inputs and geometric parameters can affect the joint strengths. The loads at 3% d_0 deformation enhanced with the increase of the steel grade since the higher steel grade could exhibit the longer elastic

stage. In contrast, the peak loads corresponding to chord punching shear did not linearly increase as the steel grades increased, as the peak loads of the Q460 gusset plate to CHS joints were greater than that of the Q690 joints with the same configurations. On the one hand, the Q460 steel experienced less HAZ deterioration than the Q690 steel. On the other hand, the Q460 joints could have the second hardening stage which improved the peak loads. Besides, the effect of heat inputs on the peak loads became significant when the steel grade increased to Q960, as a result of severe HAZ material deterioration caused by welding. As for the geometric parameters, β, η and γ all had effects on the joint strengths. Particularly, the Q460 transverse plate to CHS X-joint had longer elastic stage, larger stiffness, higher load at 3% d_0 deformation but reduced ductility compared to the Q460 longitudinal counterpart. However, the peak loads of both joints were approximate.

3. The ductility of the HSS gusset plate to CHS X-joints was influenced by the steel grade, heat input and geometric parameters. The ductility was represented by D_2/D_1 according to a bi-linear model. The larger the value was the better the ductility was. The ductility declined as the steel grades increased for both transverse and longitudinal joints. The influence of heat input, however, was obscure regardless of the plate skew angle: for the Q460 and Q960 joints, the ductility was reduced by enlarging the heat input; while for the Q690 joints, the ductility was enhanced as the heat input increased. As for the geometric parameters, β, γ, and η could all affect the joint ductility. Specially, the influence of the plate skew angle was quite mild as the skew angle increased from 0° to 90°, the D_2/D_1 of Q460 plate to CHS X-joints only reduced slightly from 3.886 to 3.639.

4. The plate surface stress distributions could indicate the position where the chord punching shear initiated. The plate surface stresses near the brace plate edge were usually higher than those in the plate centre under large load levels, therefore inducing

the crack initiation at the chord saddle for the transverse joints and at the chord crown for the longitudinal joints due to the stress concentration.

5. The test strengths were compared with the design methods recommended by ISO 14346, prEN 1993-1-8 and Voth. These design methods usually underestimated the load at 3% d_0 deformation for the HSS gusset plate to CHS X-joints without and with reduction factors. Therefore, incorporating the reduction factor was not necessary when calculating $N_{3\%}$. The mean values of the ratios between $N_{3\%}$ and the predicted load by the Voth's method were closest to unity and had small coefficient of variation (COV), which proved that considering the effect of plate thickness could improve the joint strength predictions. Besides, the design methods were not accurate and reliable when predicting the load corresponding to chord punching shear, because for some transverse joints failed by punching shear, the loads could be overestimated up to 30%. Finally, the COVs of the joints under higher heat input were greater that the counterpart under lower heat input. Therefore, the effect of the heat inputs should also be incorporated when designing the HSS gusset plate to CHS X-joints subjected to tension.

Table 6.1 Nominal chemical compositions of CHSs

Steel	Thickness	C	Si	Mn	P	S	Cr	V	Mo	Cu	Ni	Ti	B	CEV
Q460	6 mm	0.08	0.15	1.43	0.013	0.003	-	0.002	-	-	0.023	0.011	-	0.32
Q690	6 mm	0.14	0.27	1.4	0.019	0.001	0.26	-	0.14	-	0.0024	0.013	0.0015	0.45
Q960	5 mm	0.17	0.26	1.19	0.007	0.001	0.43	-	0.57	0.02	-	-	0.0016	0.57

Table 6.2 Material properties of base material for CHS

Steel	Coupon	E_s (GPa)	v -	f_y / $f_{0.2}$ (MPa)	f_u (MPa)	ε_u (%)
Q460-6 mm	1	214.3	0.28	581.7	668.4	10.6
	2	212.0	0.29	581.3	663.7	10.0
	3	213.5	0.27	579.1	666.2	9.8
	Avg	213.3	0.28	580.7	666.1	10.1
Q690-6 mm	1	207.6	0.28	754.3	789.3	5.6
	2	208.5	0.29	753.5	787.9	5.4
	3	209.9	0.28	761.0	795.5	5.6
	Avg	208.7	0.28	756.3	790.9	5.6
Q960-5 mm	1	207.2	0.29	972.6	1022.8	4.7
	2	208.2	0.29	973.5	1022.6	5.3
	3	204.4	0.29	973.8	1024.3	4.7
	Avg	206.6	0.29	973.3	1023.2	4.9

Table 6.3 Measured dimensions and specimen information for gusset plate to CHS X-joint

No.	Specimen	Steel grade	Joint type	Loading case	Direction of gusset plate	d_0 (mm)	t_0 (mm)	L_0 (mm)	t_1 (mm)	b_1 (mm)	h_1 (mm)	t_w (mm)	$\beta=b_1/d_0$	$\eta=h_1/d_0$	$\gamma=d_0/(2t_0)$
1	4C200x6-XT-B-Tran-0_7-M	Q460	X	tension	transverse	200.6	5.94	599.0	20.93	139.3	-	12.6	0.694	-	16.883
2	4C200x6*-XT-B-Tran-0_7-M	Q460	X	tension	transverse	201.0	5.94	595.2	21.04	139.1	-	11.4	0.692	-	16.916
3	6C200x6-XT-B-Tran-0_7-M	Q690	X	tension	transverse	200.9	6.20	598.1	20.61	139.7	-	11.4	0.695	-	16.199
4	9C200x5-XT-B-Tran-0_7-M	Q960	X	tension	transverse	199.6	5.05	598.1	22.13	139.2	-	12.3	0.697	-	19.762

5	4C200x6-XT-B-Tran-0_7-H1	Q460	X	tension	transverse	200.7	5.90	598.1	20.90	138.9	-	12.0	0.692	-	17.006
6	6C200x6-XT-B-Tran-0_7-H1	Q690	X	tension	transverse	202.1	6.15	597.5	20.48	139.1	-	10.3	0.688	-	16.425
7	9C200x5-XT-B-Tran-0_7-H1	Q960	X	tension	transverse	200.3	5.07	598.1	22.22	138.9	-	11.5	0.694	-	19.753
8	4C150x6-XT-B-Tran-0_7-M	Q460	X	tension	transverse	150.3	5.96	449.9	20.94	103.9	-	10.9	0.691	-	12.599
9	4C150x6-XT-B-Tran-0_5-M	Q460	X	tension	transverse	151.1	5.94	447.9	20.99	74.0	-	10.2	0.490	-	12.726
10	4C150x6-XT-B-Long-0_5-M	Q460	X	tension	longitudinal	148.8	5.94	444.6	21.03	-	74.1	8.8	-	0.498	12.521
11	6C150x6-XT-B-Long-0_5-M	Q690	X	tension	longitudinal	151.9	6.11	449.2	20.76	-	74.1	11.0	-	0.488	12.426
12	6C150x6*-XT-B-Long-0_5-M	Q690	X	tension	longitudinal	153.0	6.13	447.7	20.63	-	73.9	8.5	-	0.483	12.473
13	6C150x6-XT-B-Long-0_8-M	Q690	X	tension	longitudinal	152.2	6.12	448.4	20.63	-	119.5	9.7	-	0.785	12.425
14	9C150x5-XT-B-Long-0_5-M	Q960	X	tension	longitudinal	150.2	5.05	446.7	22.23	-	74.1	10.5	-	0.494	14.871
15	9C150x5-XT-B-Long-0_8-M	Q960	X	tension	longitudinal	151.1	5.14	447.8	22.20	-	118.6	10.4	-	0.785	14.698
16	4C150x6-XT-B-Long-0_5-H1	Q460	X	tension	longitudinal	150.2	5.95	446.1	20.95	-	74.2	10.0	-	0.494	12.615
17	6C150x6-XT-B-Long-0_5-H1	Q690	X	tension	longitudinal	151.5	6.14	446.8	20.59	-	74.3	9.6	-	0.491	12.337

18	9C150x5-XT-B-Long-0_5-H1	Q960	X	tension	longitudinal	149.8	5.00	449.8	22.21	-	74.2	9.7	-	0.495	14.983

Table 6.4 Filler electrodes used in welding

Steel grade	Filler electrode	Ultimate strength (MPa)
Q460	AWS A5.28 ER 80S-G	550
Q690	AWS A5.28 ER 110S-G	760
Q960	AWS A5.28 ER 130S-G	900

Table 6.5 Number of welding passes for gusset plate to CHS X-joints

	Number of welding passes for plate 1		Number of welding passes for plate 2	
Specimen	Left	Right	Left	Right
4C200x6-XT-B-Tran-0_7-M	10	6	8	6
4C200x6*-XT-B-Tran-0_7-M	6	6	6	7
6C200x6-XT-B-Tran-0_7-M	5	6	6	5
9C200x5-XT-B-Tran-0_7-M	6	5	6	6
4C200x6-XT-B-Tran-0_7-H1	5	4	4	5
6C200x6-XT-B-Tran-0_7-H1	4	4	4	4
9C200x5-XT-B-Tran-0_7-H1	4	4	4	4
4C150x6-XT-B-Tran-0_7-M	6	6	6	6
4C150x6-XT-B-Tran-0_5-M	6	6	6	6
4C150x6-XT-B-Long-0_5-M	7	6	6	6
6C150x6-XT-B-Long-0_5-M	6	6	6	6
6C150x6*-XT-B-Long-0_5-M	6	6	6	6

6C150x6-XT-B-Long-0_8-M	7	7	6	6
9C150x5-XT-B-Long-0_5-M	6	6	6	6
9C150x5-XT-B-Long-0_8-M	6	6	6	6
4C150x6-XT-B-Long-0_5-H1	3	3	3	3
6C150x6-XT-B-Long-0_5-H1	3	3	4	4
9C150x5-XT-B-Long-0_5-H1	3	3	3	3

Table 6.6 Heat inputs for the specimens

No.	Specimen	Average heat input for plate 1 (kJ/mm)	Average heat input for plate 2 (kJ/mm)	Average heat input (kJ/mm)
1	4C200x6-XT-B-Tran-0_7-M	1.154	1.090	1.122
2	4C200x6*-XT-B-Tran-0_7-M	1.061	1.062	1.062
3	6C200x6-XT-B-Tran-0_7-M	1.000	1.010	1.005
4	9C200x5-XT-B-Tran-0_7-M	1.042	0.986	1.014
5	4C200x6-XT-B-Tran-0_7-H1	2.332	2.450	2.391
6	6C200x6-XT-B-Tran-0_7-H1	2.022	1.858	1.940
7	9C200x5-XT-B-Tran-0_7-H1	1.771	1.786	1.778
8	4C150x6-XT-B-Tran-0_7-M	1.045	0.984	1.014
9	4C150x6-XT-B-Tran-0_5-M	1.108	1.036	1.072
10	4C150x6-XT-B-Long-0_5-M	1.027	1.037	1.032
11	6C150x6-XT-B-Long-0_5-M	1.065	1.013	1.039
12	6C150x6*-XT-B-Long-0_5-M	1.037	1.041	1.039
13	6C150x6-XT-B-Long-0_8-M	1.041	1.065	1.053

14	9C150x5-XT-B-Long-0_5-M	1.073	1.065	1.069
15	9C150x5-XT-B-Long-0_8-M	1.060	1.087	1.074
16	4C150x6-XT-B-Long-0_5-H1	2.466	2.316	2.391
17	6C150x6-XT-B-Long-0_5-H1	2.554	2.233	2.393
18	9C150x5-XT-B-Long-0_5-H1	2.323	2.342	2.332

Table 6.7 Tested failure modes for the gusset plate to CHS X-joints

No.	Specimen	Load at 3% deformation	peak load (kN)	Tested failure mode
1	4C200x6-XT-B-Tran-0_7-M	447.245	568.707	chord face failure
2	4C200x6*-XT-B-Tran-0_7-M	479.672	587.932	chord face failure
3	6C200x6-XT-B-Tran-0_7-M	N/A	450.212	chord punching shear
4	9C200x5-XT-B-Tran-0_7-M	N/A	413.053	chord punching shear
5	4C200x6-XT-B-Tran-0_7-H1	457.797	553.108	chord face failure
6	6C200x6-XT-B-Tran-0_7-H1	N/A	511.018	chord punching shear
7	9C200x5-XT-B-Tran-0_7-H1	N/A	348.153	chord punching shear
8	4C150x6-XT-B-Tran-0_7-M	447.543	552.424	chord face failure
9	4C150x6-XT-B-Tran-0_5-M	304.433	414.354	chord face failure
10	4C150x6-XT-B-Long-0_5-M	188.530	444.024	chord face failure
11	6C150x6-XT-B-Long-0_5-M	229.992	358.738	chord face failure
12	6C150x6*-XT-B-Long-0_5-M	225.398	362.315	chord face failure
13	6C150x6-XT-B-Long-0_8-M	235.666	499.652	chord face failure

14	9C150x5-XT-B-Long-0_5-M	196.747	305.414	chord face failure
15	9C150x5-XT-B-Long-0_8-M	208.799	425.611	chord face failure
16	4C150x6-XT-B-Long-0_5-H1	181.157	471.500	chord face failure
17	6C150x6-XT-B-Long-0_5-H1	231.107	348.717	chord face failure
18	9C150x5-XT-B-Long-0_5-H1	167.148	258.129	chord fracture along the weld

Table 6.8 Ductility of gusset plate to CHS X-joints

No.	Specimen	D_1 (mm)	D_2 (mm)	D_2/D_1
1	4C200x6-XT-B-Tran-0_7-M	2.485	9.143	3.679
2	4C200x6*-XT-B-Tran-0_7-M	3.043	8.522	2.801
3	6C200x6-XT-B-Tran-0_7-M	2.027	2.928	1.444
4	9C200x5-XT-B-Tran-0_7-M	2.165	3.193	1.475
5	4C200x6-XT-B-Tran-0_7-H1	2.595	7.930	3.056
6	6C200x6-XT-B-Tran-0_7-H1	2.208	4.123	1.867
7	9C200x5-XT-B-Tran-0_7-H1	2.103	3.080	1.465
8	4C150x6-XT-B-Tran-0_7-M	2.105	7.035	3.342
9	4C150x6-XT-B-Tran-0_5-M	2.768	10.073	3.639
10	4C150x6-XT-B-Long-0_5-M	4.583	17.810	3.886
11	6C150x6-XT-B-Long-0_5-M	5.940	13.500	2.273
12	6C150x6*-XT-B-Long-0_5-M	6.758	15.888	2.351
13	6C150x6-XT-B-Long-0_8-M	4.423	18.085	4.089
14	9C150x5-XT-B-Long-0_5-M	5.193	10.713	2.063

15	9C150x5-XT-B-Long-0_8-M	5.378	14.673	2.728
16	4C150x6-XT-B-Long-0_5-H1	5.133	18.554	3.615
17	6C150x6-XT-B-Long-0_5-H1	5.625	14.353	2.552
18	9C150x5-XT-B-Long-0_5-H1	5.620	10.988	1.955

Table 6.9 Range of validity for gusset plate to CHS X-joints under tension in ISO 14346

Joint type	Range of validity
Transverse plate to CHS X-joint	$d_0/t_0 \leq 50$, and $b_1/d_0 \leq 0.4$
Longitudinal plate to CHS X-joint	$d_0/t_0 \leq 50$, and $1 \leq h_1/d_0 \leq 4$

Table 6.10 Material reduction factors in EN 1993-1-8 (CEN, 2024b)

$f_y \leq 355$ MPa	$C_f = 1.00$
355 MPa $< f_y \leq 460$ MPa	$C_f = 0.90$
460 MPa $< f_y \leq 550$ MPa	$C_f = 0.86$
550 MPa $< f_y \leq 700$ MPa	$C_f = 0.80$

Table 6.11 Range of validity for gusset plate to CHS X-joints under tension in prEN 1993-1-8

Joint type	Range of validity
Transverse plate to CHS X-joint	$d_0/t_0 \leq 40$, and $b_1/d_0 \geq 0.25$
Longitudinal plate to CHS X-joint	$d_0/t_0 \leq 40$, and $0.6 \leq h_1/d_0 \leq 4$

Table 6.12 Test strengths and design resistances for gusset plate to CHS X-joints

No.	Specimen	Test strengths (kN)		Design resistances without reduction factors (kN)					Design resistances with reduction factors (kN)				
		$N_{3\%}$	N_u	$N_{CF,\ ISO}$	$N_{CF,\ prEC3}$	$N_{CF,\ Voth}$	$N_{PS,\ ISO}$	$N_{PS,\ prEC3}$	$N^*_{CF,\ ISO}$	$N^*_{CF,\ prEC3}$	$N^*_{CF,\ Voth}$	$N^*_{PS,\ ISO}$	$N^*_{PS,\ prEC3}$
1	4C200x6-XT-B-Tran-0_7-M	447.245	568.707	218.504	231.597	352.568	536.226	536.226	196.654	208.437	299.683	482.604	482.604
2	4C200x6*-XT-B-Tran-0_7-M	479.672	587.932	217.629	230.841	351.702	535.584	535.584	195.866	207.757	298.947	482.026	482.026
3	6C200x6-XT-B-Tran-0_7-M	N/A	450.212	274.177	300.922	437.010	649.298	649.298	246.759	240.738	371.459	584.368	519.438
4	9C200x5-XT-B-Tran-0_7-M	N/A	413.053	242.233	267.795	408.553	678.604	678.604	218.010	214.236	347.270	610.744	542.884
5	4C200x6-XT-B-Tran-0_7-H1	457.797	553.108	214.963	228.122	347.657	531.340	531.340	193.466	205.310	295.508	478.206	478.206
6	6C200x6-XT-B-Tran-0_7-H1	N/A	511.018	266.792	293.747	427.257	641.642	641.642	240.113	234.997	363.169	577.478	513.314
7	9C200x5-XT-B-Tran-0_7-H1	N/A	348.153	242.427	268.240	409.350	680.150	680.150	218.185	214.592	347.947	612.135	544.120
8	4C150x6-XT-B-Tran-0_7-M	447.543	552.424	208.456	213.680	322.845	399.496	399.496	187.610	192.312	274.418	359.546	359.546
9	4C150x6-XT-B-Tran-0_5-M	304.433	414.354	143.083	149.970	234.366	283.258	283.258	128.775	134.973	199.211	254.932	254.932
10	4C150x6-XT-B-Long-0_5-M	188.530	444.024	117.730	116.288	169.315	284.087	284.087	105.957	104.659	143.918	255.678	255.678

11	6C150x6-XT-B-Long-0_5-M	229.992	358.738	144.460	150.358	205.973	339.921	339.921	130.014	120.286	175.077	305.929	271.937
12	6C150x6*-XT-B-Long-0_5-M	225.398	362.315	145.189	151.116	206.468	340.266	340.266	130.670	120.893	175.498	306.239	272.213
13	6C150x6-XT-B-Long-0_8-M	235.666	499.652	159.360	165.865	230.987	548.929	548.929	143.424	132.692	196.339	494.036	439.143
14	9C150x5-XT-B-Long-0_5-M	196.747	305.414	127.671	128.855	188.661	363.122	363.122	114.903	103.084	160.362	326.810	290.497
15	9C150x5-XT-B-Long-0_8-M	208.799	425.611	145.124	146.471	217.663	591.117	591.117	130.612	117.177	185.014	532.005	472.893
16	4C150x6-XT-B-Long-0_5-H1	181.157	471.500	117.956	116.512	169.241	284.693	284.693	106.161	104.860	143.855	256.224	256.224
17	6C150x6-XT-B-Long-0_5-H1	231.107	348.717	145.867	151.821	207.636	342.479	342.479	131.280	121.457	176.491	308.231	273.983
18	9C150x5-XT-B-Long-0_5-H1	167.1476667	258.129	125.233	126.396	185.286	360.011	360.011	112.710	101.116	157.493	324.010	288.009

Table 6.13 Comparison of test strengths with design resistances for gusset plate to CHS X-joints

No.	Specimen	chord face failure, without reduction factor			chord face failure, with reduction factor			chord punching shear, without reduction factor		chord punching shear, with reduction factor	
		$N_{3\%}/N_{C}$	$N_{3\%}/N_{CF,}$	$N_{3\%}/N_{CF,}$	$N_{3\%}/N^{*}_{CF,}$	$N_{3\%}/N^{*}_{CF,}$	$N_{3\%}/N^{*}_{CF,}$	$N_{max}/N_{PS, ISO}$	$N_{max}/N_{PS, prEC3}$	$N_{max}/N^{*}_{PS, ISO}$	$N_{max}/N^{*}_{PS, prEC3}$
		F, ISO	prEC3	Voth	ISO	prEC3	Voth				
1	4C200x6-XT-B-Tran-0_7-M	2.047	1.931	1.269	2.274	2.146	1.492	1.061	1.061	1.178	1.178
2	4C200x6*-XT-B-Tran-0_7-M	2.204	2.078	1.364	2.449	2.309	1.605	1.098	1.098	1.220	1.220
3	6C200x6-XT-B-Tran-0_7-M	N/A	N/A	N/A	N/A	N/A	N/A	0.693	0.693	0.770	0.867
4	9C200x5-XT-B-Tran-0_7-M	N/A	N/A	N/A	N/A	N/A	N/A	0.609	0.609	0.676	0.761
5	4C200x6-XT-B-Tran-0_7-H1	2.130	2.007	1.317	2.366	2.230	1.549	1.041	1.041	1.157	1.157
6	6C200x6-XT-B-Tran-0_7-H1	N/A	N/A	N/A	N/A	N/A	N/A	0.796	0.796	0.885	0.996
7	9C200x5-XT-B-Tran-0_7-H1	N/A	N/A	N/A	N/A	N/A	N/A	0.512	0.512	0.569	0.640
8	4C150x6-XT-B-Tran-0_7-M	2.147	2.094	1.386	2.385	2.327	1.631	1.383	1.383	1.536	1.536
9	4C150x6-XT-B-Tran-0_5-M	2.128	2.030	1.299	2.364	2.256	1.528	1.463	1.463	1.625	1.625

10	4C150x6-XT-B-Long-0_5-M	1.601	1.621	1.113	1.779	1.801	1.310	1.563	1.563	1.737	1.737
11	6C150x6-XT-B-Long-0_5-M	1.592	1.530	1.117	1.769	1.912	1.314	1.055	1.055	1.173	1.319
12	6C150x6*-XT-B-Long-0_5-M	1.552	1.492	1.092	1.725	1.864	1.284	1.065	1.065	1.183	1.331
13	6C150x6-XT-B-Long-0_8-M	1.479	1.421	1.020	1.643	1.776	1.200	0.910	0.910	1.011	1.138
14	9C150x5-XT-B-Long-0_5-M	1.541	1.527	1.043	1.712	1.909	1.227	0.841	0.841	0.935	1.051
15	9C150x5-XT-B-Long-0_8-M	1.439	1.426	0.959	1.599	1.782	1.129	0.720	0.720	0.800	0.900
16	4C150x6-XT-B-Long-0_5-H1	1.536	1.555	1.070	1.706	1.728	1.259	1.656	1.656	1.840	1.840
17	6C150x6-XT-B-Long-0_5-H1	1.584	1.522	1.113	1.760	1.903	1.309	1.018	1.018	1.131	1.273
18	9C150x5-XT-B-Long-0_5-H1	1.335	1.322	0.902	1.483	1.653	1.061	N/A	N/A	N/A	N/A

Table 6.14 Summarised comparison of test strengths with design resistances for gusset plate to CHS X-joints

Joint resistance	Load at 3% deformation						Load corresponding to chord punching shear			
Ratio	$N_{3\%}/N_{CF,\ ISO}$	$N_{3\%}/N_{CF,\ prEC3}$	$N_{3\%}/N_{CF,\ Voth}$	$N_{3\%}/N^*_{CF,\ ISO}$	$N_{3\%}/N^*_{CF,\ prEC3}$	$N_{3\%}/N^*_{CF,\ Voth}$	$N_{max}/N_{PS,\ ISO}$	$N_{max}/N_{PS,\ prEC3}$	$N_{max}/N^*_{PS,\ ISO}$	$N_{max}/N^*_{PS,\ prEC3}$
No of Specimens	14	14	14	14	14	14	17	17	17	17
Mean	1.737	1.683	1.147	1.930	1.971	1.350	1.028	1.028	1.143	1.210
COV	0.174	0.159	0.129	0.174	0.114	0.129	0.312	0.312	0.312	0.269

Table 6.15 Summarised comparison of test strengths with design resistances for gusset plate to CHS X-joints under heat input M

Joint resistance	Load at 3% deformation						Load corresponding to chord punching shear			
Ratio	$N_{3\%}/N_{CF,\ ISO}$	$N_{3\%}/N_{CF,\ prEC3}$	$N_{3\%}/N_{CF,\ Voth}$	$N_{3\%}/N^*_{CF,\ ISO}$	$N_{3\%}/N^*_{CF,\ prEC3}$	$N_{3\%}/N^*_{CF,\ Voth}$	$N_{max}/N_{PS,\ ISO}$	$N_{max}/N_{PS,\ prEC3}$	$N_{max}/N^*_{PS,\ ISO}$	$N_{max}/N^*_{PS,\ prEC3}$
No of Specimens	12	12	12	12	12	12	12	12	12	12
Mean	1.773	1.715	1.166	1.970	2.008	1.372	1.038	1.038	1.154	1.222
COV	0.168	0.157	0.123	0.168	0.107	0.123	0.283	0.283	0.283	0.240

Table 6.16 Summarised comparison of test strengths with design resistances for gusset plate to CHS X-joints under heat input H1

Joint resistance	Load at 3% deformation						Load corresponding to chord punching shear			
Ratio	$N_{3\%}/N_{CF,\ ISO}$	$N_{3\%}/N_{CF,\ prEC3}$	$N_{3\%}/N_{CF,\ Voth}$	$N_{3\%}/N^*_{CF,\ ISO}$	$N_{3\%}/N^*_{CF,\ prEC3}$	$N_{3\%}/N^*_{CF,\ Voth}$	$N_{max}/N_{PS,\ ISO}$	$N_{max}/N_{PS,\ prEC3}$	$N_{max}/N^*_{PS,\ ISO}$	$N_{max}/N^*_{PS,\ prEC3}$
No of Specimens	6	6	6	6	6	6	5	5	5	5
Mean	1.646	1.602	1.101	1.829	1.878	1.295	1.005	1.005	1.116	1.181
COV	0.179	0.156	0.134	0.179	0.118	0.134	0.376	0.376	0.376	0.332

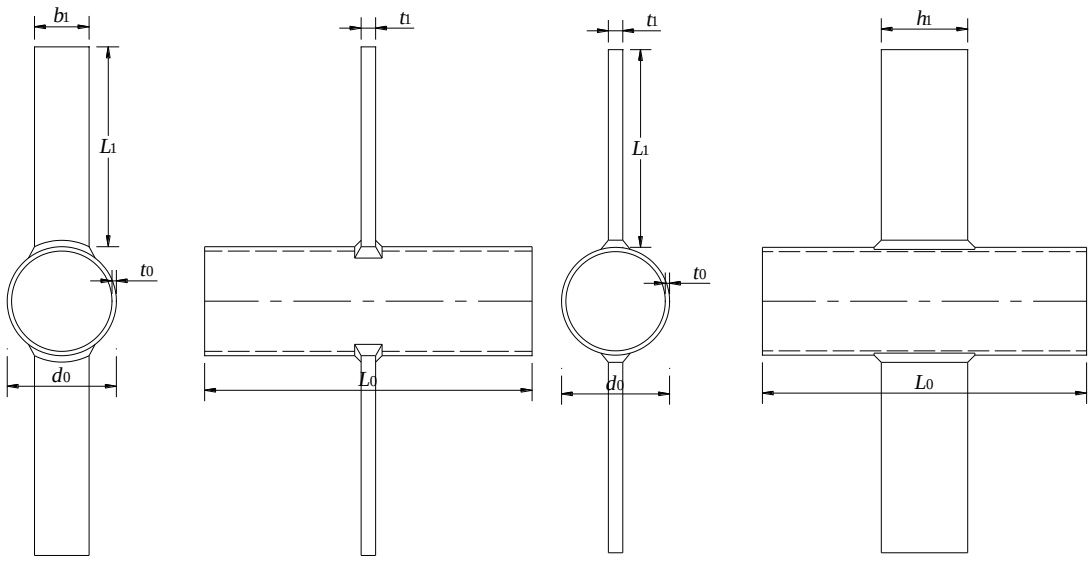

(a) Transverse plate to CHS X-joint (b) Longitudinal plate to CHS X-joint

Figure 6.1 Definition of symbols

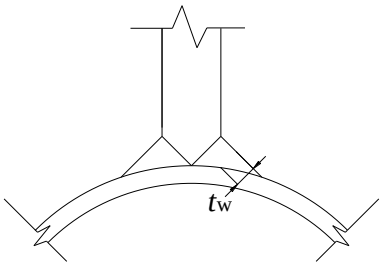

Figure 6.2 Weld details

(a) CHSs (b) Gusset plates

Figure 6.3 Components for joint fabrication

(a) Positioning

(b) Preheating

(c) Robotic welding

(d) Interpass temperature control

(e) Grinding after welding

(f) Ultrasonic examination

Figure 6.4 Fabrication of gusset plate to CHS X-joint

Figure 6.5 The completed gusset plate to CHS X-joints

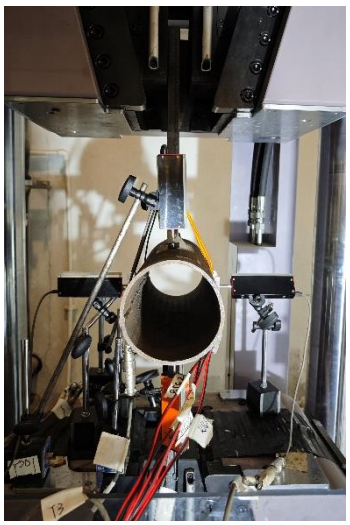

Figure 6.6 The longitudinal plate to CHS X-joint gripped by clamps

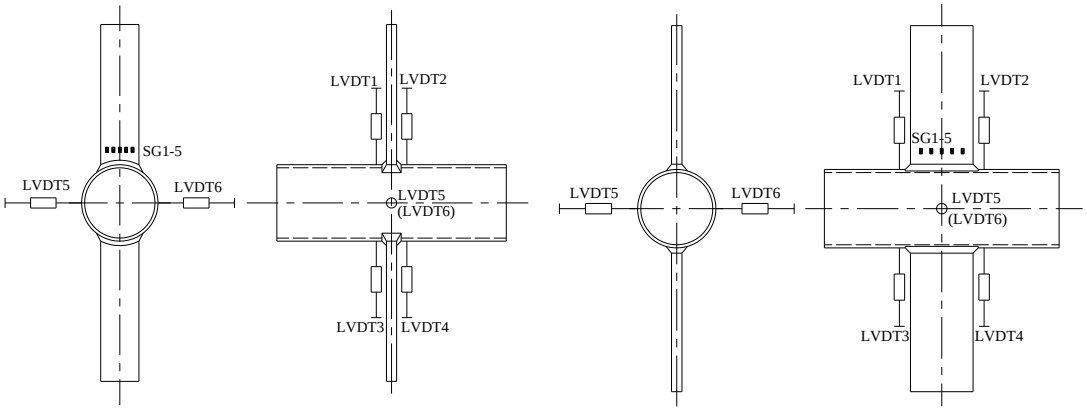

(a) Transverse plate to CHS X-joint (b) Longitudinal plate to CHS X-joint

Figure 6.7 Instrumentation for the specimens

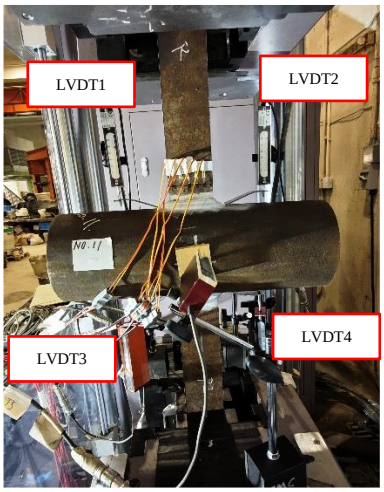

Figure 6.8 Chord face deformation measurement

Figure 6.9 The extension arm at the tips of LVDTs

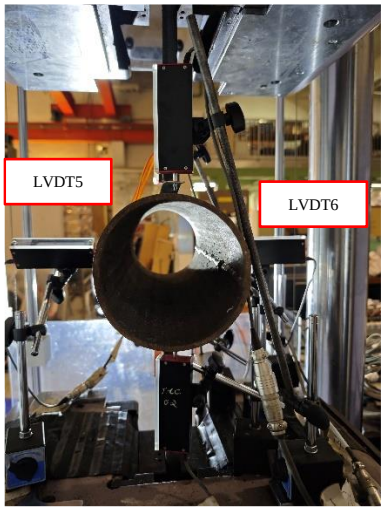

Figure 6.10 Chord sidewall deformation

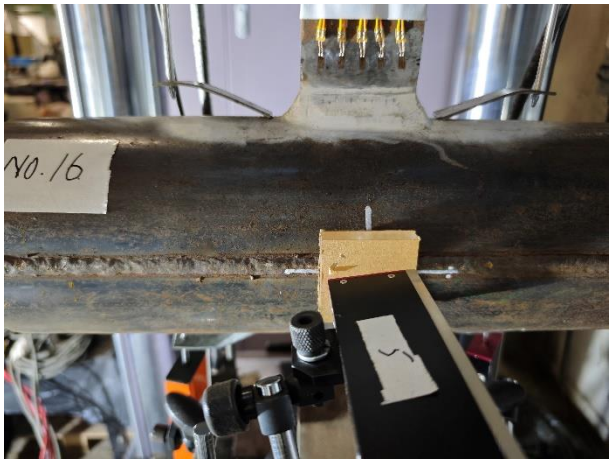

Figure 6.11 The PMMA at the tips of LVDTs

Figure 6.12 Strain gauges on the plate

Figure 6.13 Experimental failure mode of No.2-4C200x6*-XT-B-Tran-0_7-M

Figure 6.14 Experimental failure mode of No. 13-6C150x6-XT-B-Long-0_8-M

Figure 6.15 Experimental failure mode of No. 18-9C150x5-XT-B-Long-0_5-H1

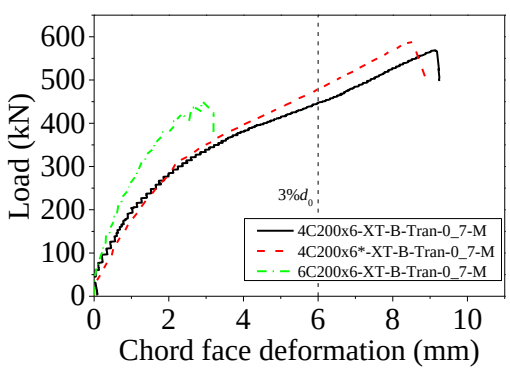

(a) Steel grade influence under heat input M

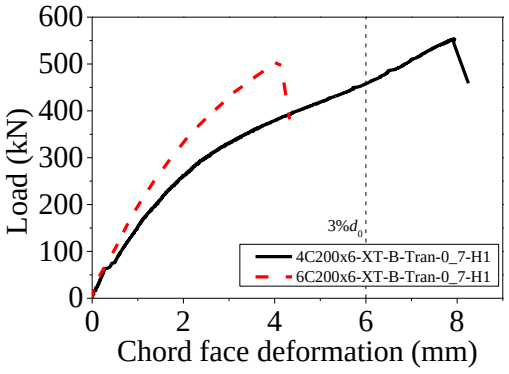

(b) Steel grade influence under heat input H1

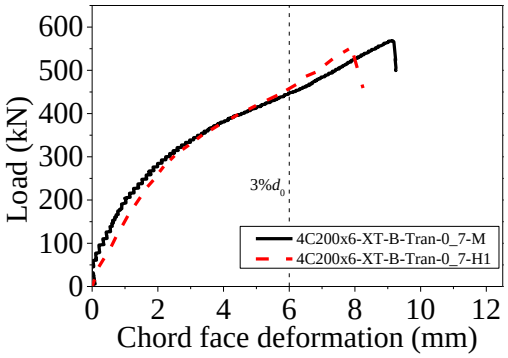

(c) Heat input influence on Q460 joints

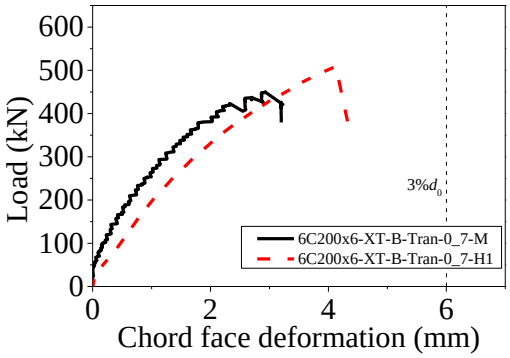

(d) Heat input influence on Q690 joints

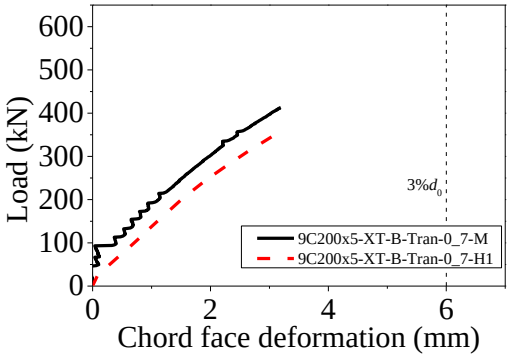

(e) Heat input influence on Q960 joints

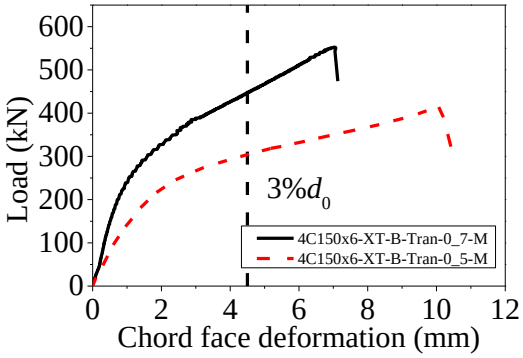

(f) β influence on Q460 joints

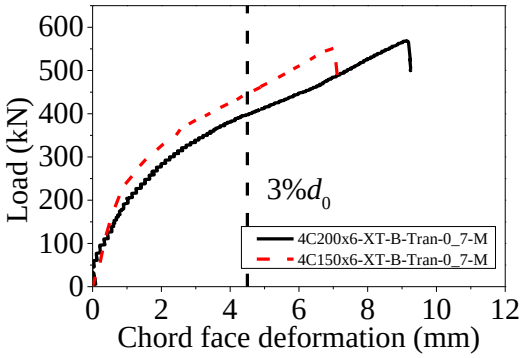

(g) γ influence on Q460 joints

Figure 6.16 Load versus chord face deformation curves for transverse plate to CHS X-joints

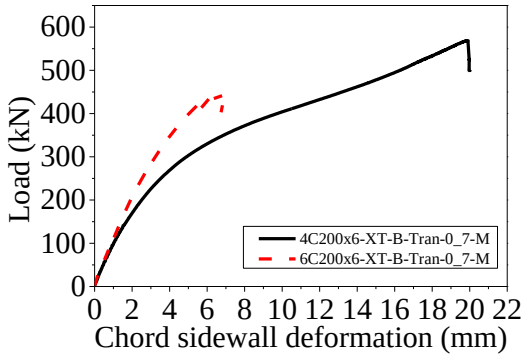

(a) Steel grade influence under heat input M

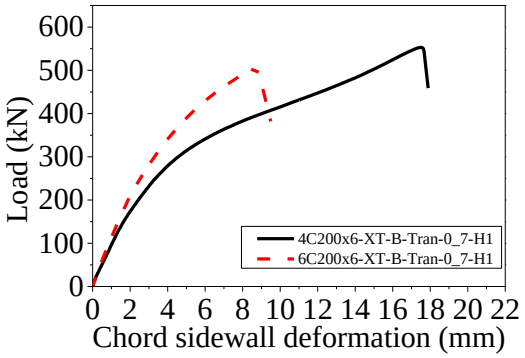

(b) Steel grade influence under heat input H1

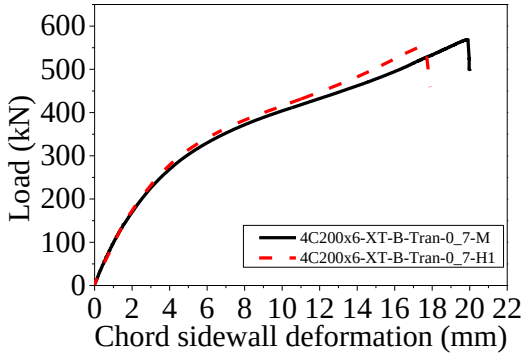

(c) Heat input influence on Q460 joints

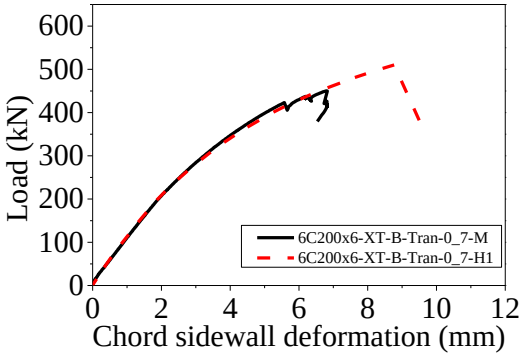

(d) Heat input influence on Q690 joints

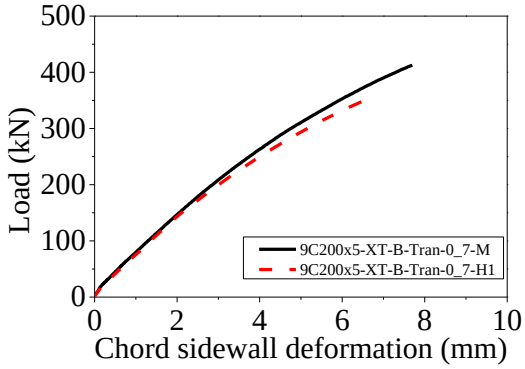

(e) Heat input influence on Q960 joints

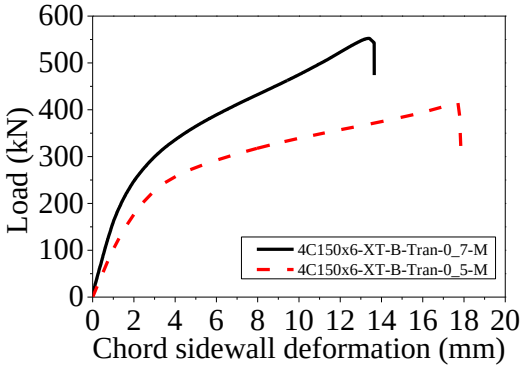

(f) β influence on Q460 joints

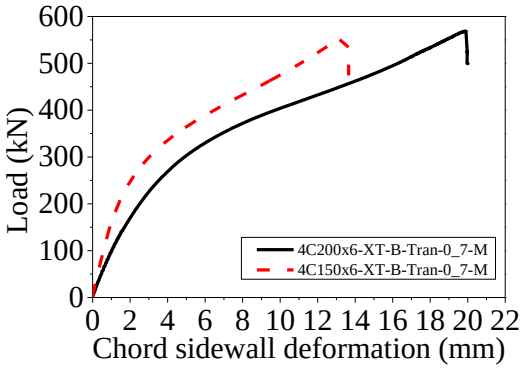

(g) γ influence on Q460 joints

Figure 6.17 Load versus chord sidewall deformation curves for transverse plate to CHS X-joints

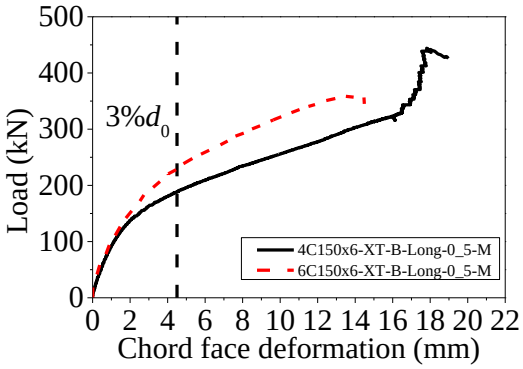

(a) Steel grade influence under heat input M

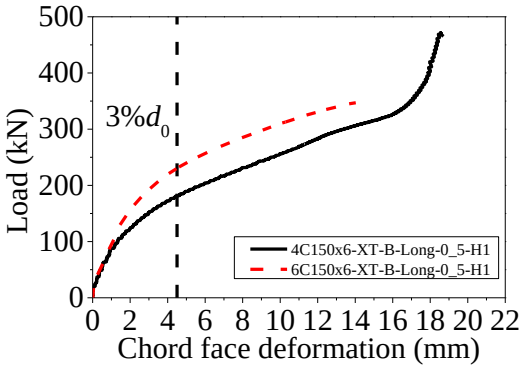

(b) Steel grade influence under heat input H1

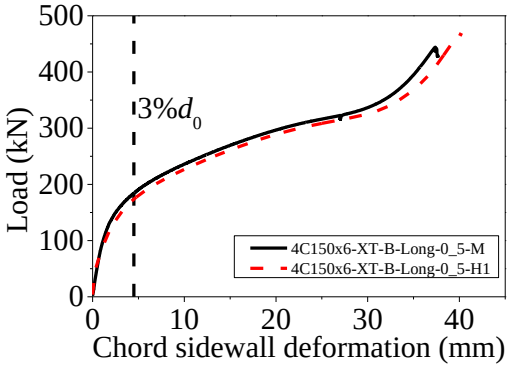

(c) Heat input influence on Q460 joints

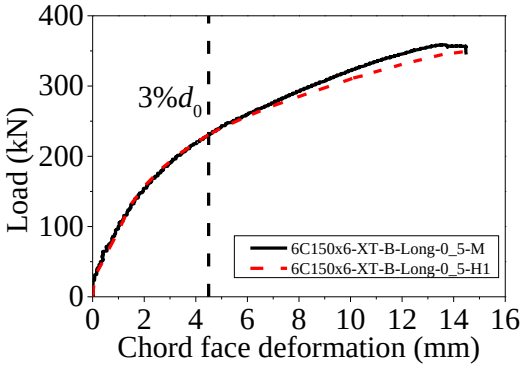

(d) Heat input influence on Q690 joints

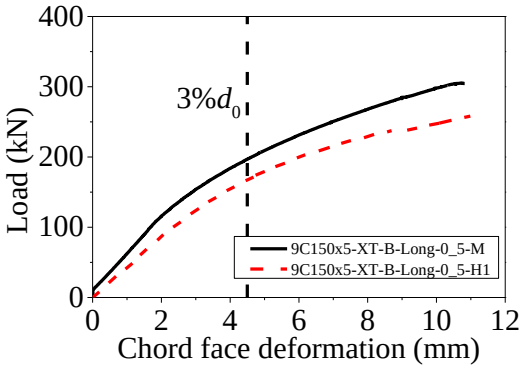

(e) Heat input influence on Q960 joints

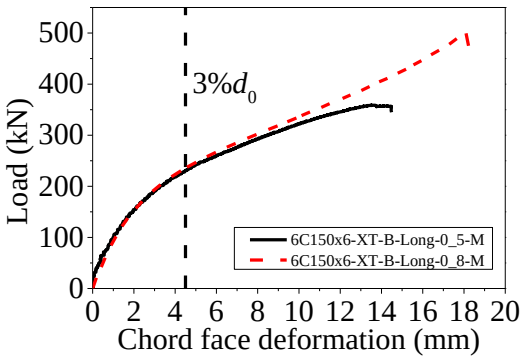

(f) η influence on Q690 joints

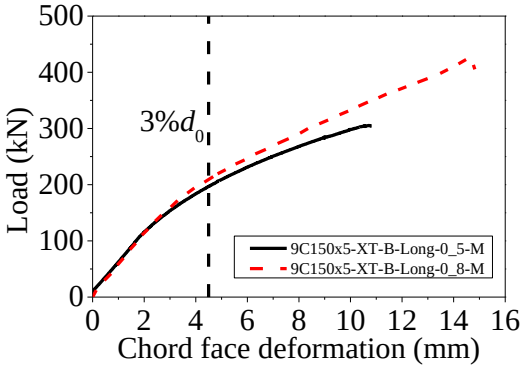

(g) η influence on Q960 joints

Figure 6.18 Load versus chord face deformation curves for longitudinal plate to CHS X-joints

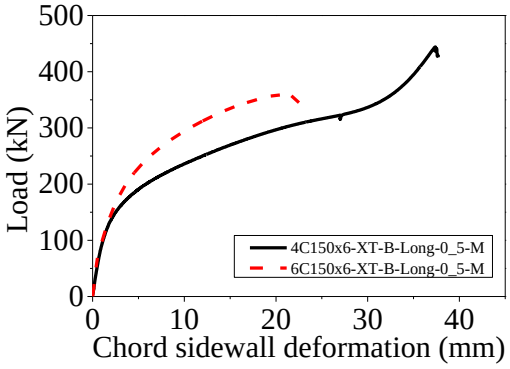

(a) Steel grade influence under heat input M

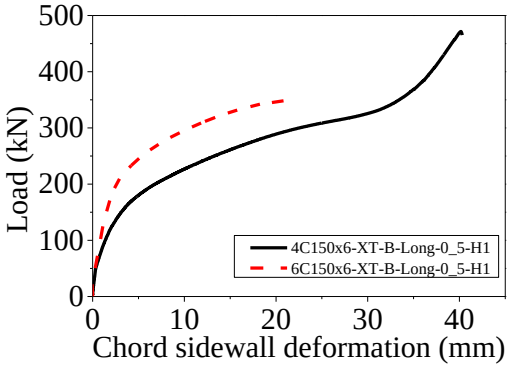

(b) Steel grade influence under heat input H1

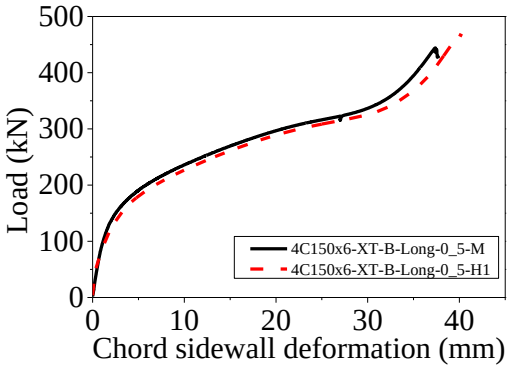

(c) Heat input influence on Q460 joints

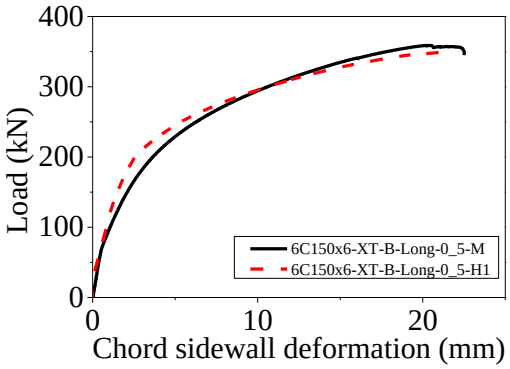

(d) Heat input influence on Q690 joints

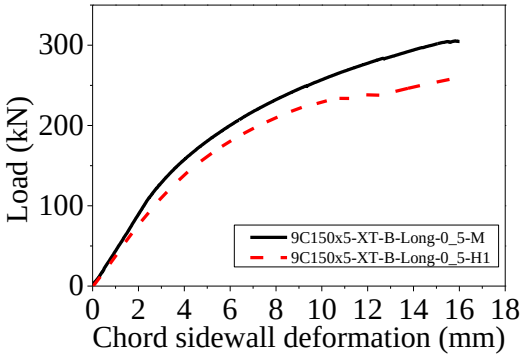

(e) Heat input influence on Q960 joints

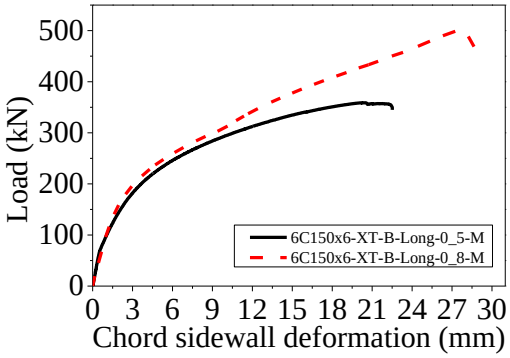

(f) η influence on Q690 joints

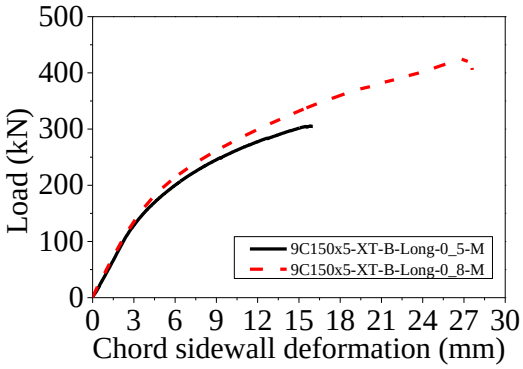

(g) η influence on Q960 joints

Figure 6.19 Load versus chord sidewall deformation curves for longitudinal plate to CHS X-joints

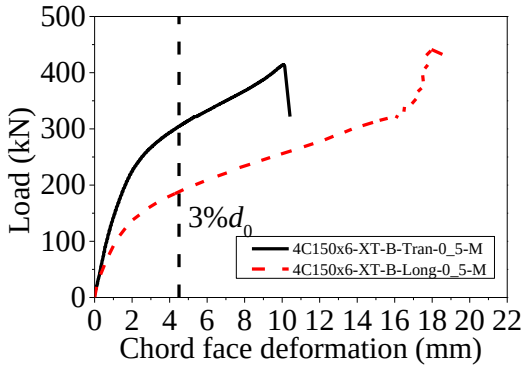

(a) Load-chord face deformation curve

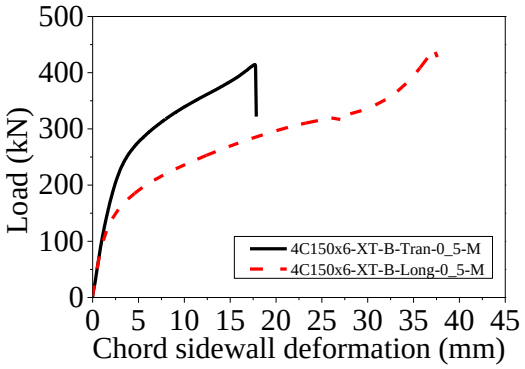

(b) Load-chord sidewall deformation curve

Figure 6.20 Plate skew angle influence on gusset plate to CHS X-joint

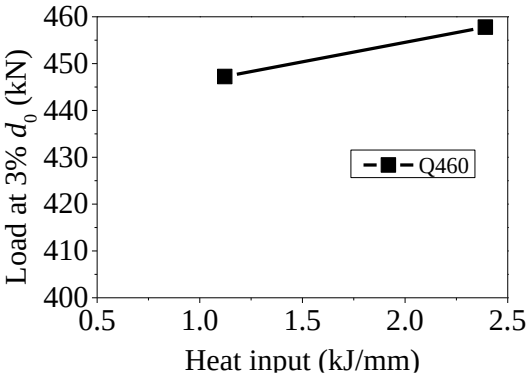

(a) Heat input influence on Q460 joints

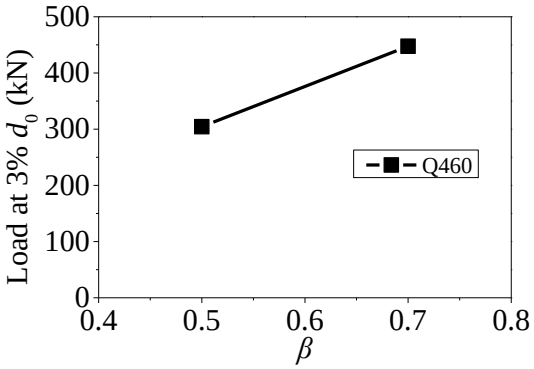

(b) β influence on Q460 joints

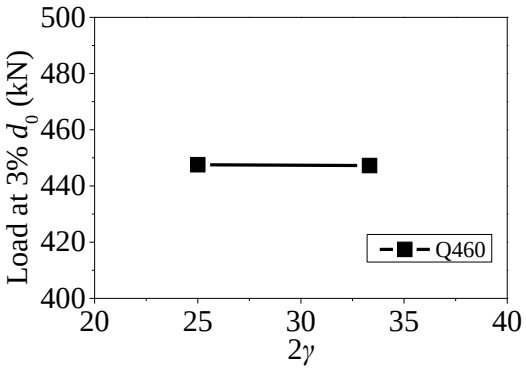

(c) γ influence on Q460 joints

Figure 6.21 Load at 3% d_0 deformation of Q460 transverse plate to CHS X-joints

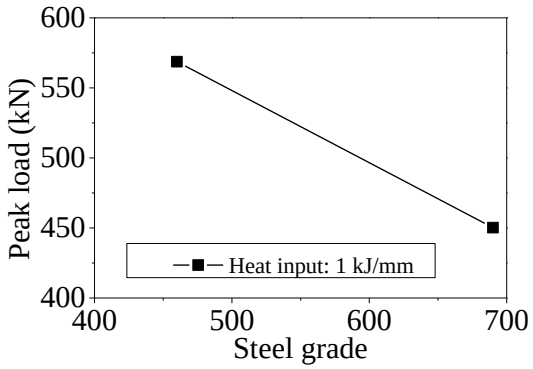

(a) Steel grade influence under heat input M

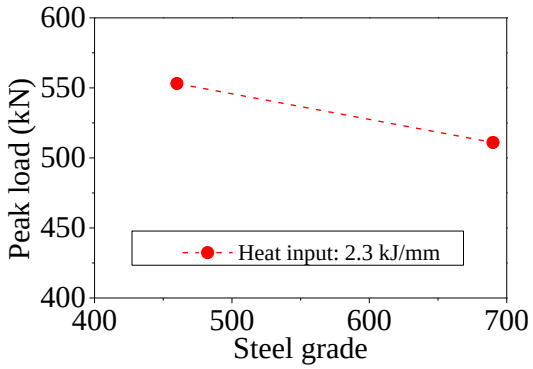

(b) Steel grade influence under heat input H1

Figure 6.22 Influence of steel grade on peak load of transverse plate to CHS X-joints

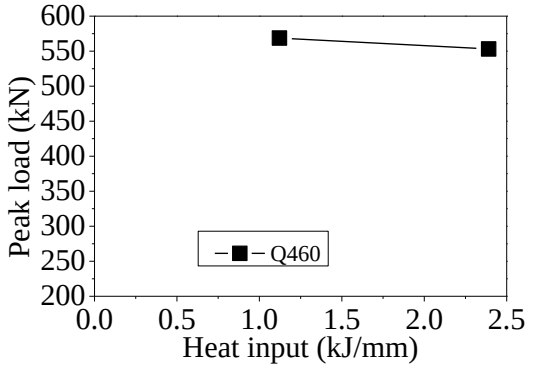

(a) Heat input influence on Q460 joints

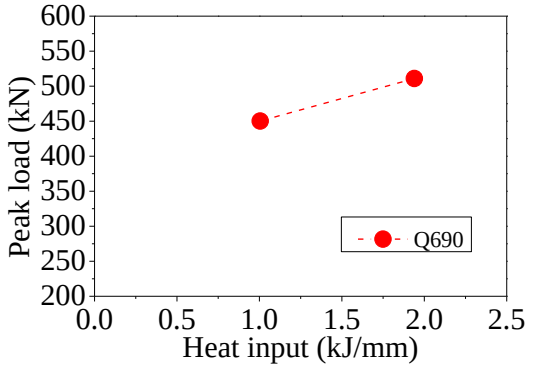

(b) Heat input influence on Q690 joints

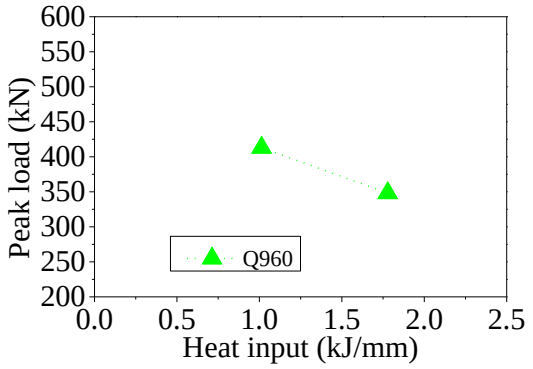

(c) Heat input influence on Q960 joints

Figure 6.23 Influence of heat input on peak load of transverse plate to CHS X-joints

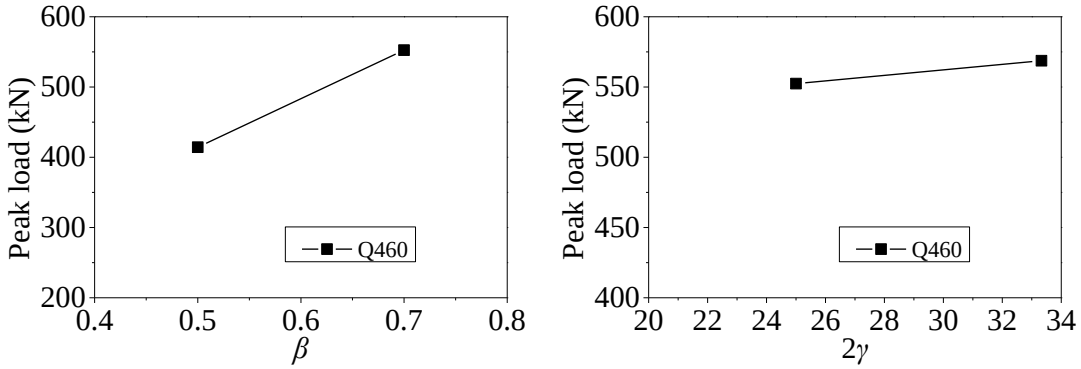

(a) β influence on Q460 joints (b) γ influence on Q460 joints

Figure 6.24 Influence of geometric parameters on peak load of transverse plate to CHS X-joints

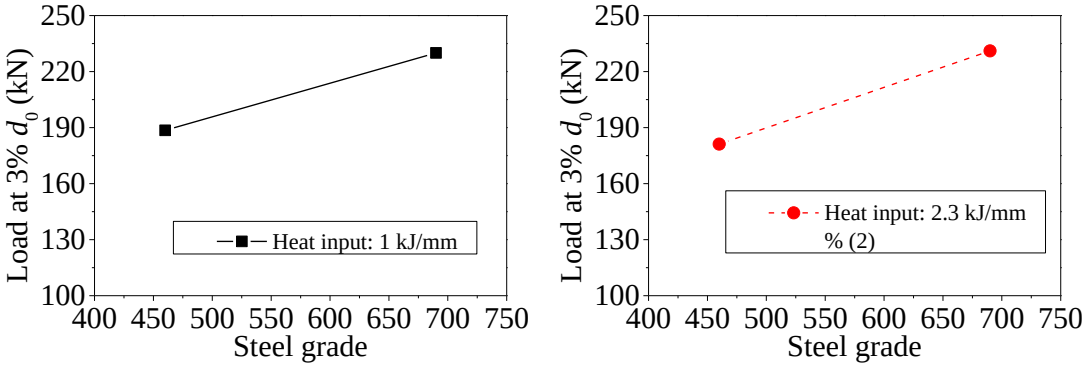

(a) Steel grade influence under heat input M

(b) Steel grade influence under heat input H1

Figure 6.25 Influence of steel grade on load at 3% d_0 deformation of longitudinal plate to CHS X-joints

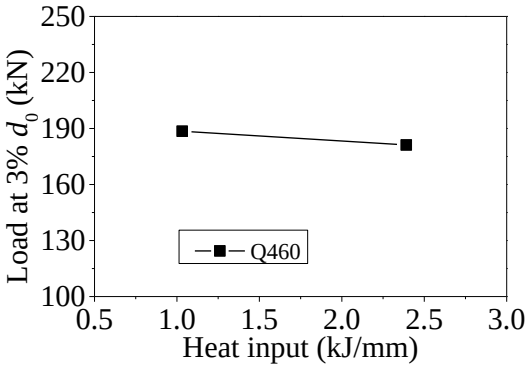

(a) Heat input influence on Q460 joints

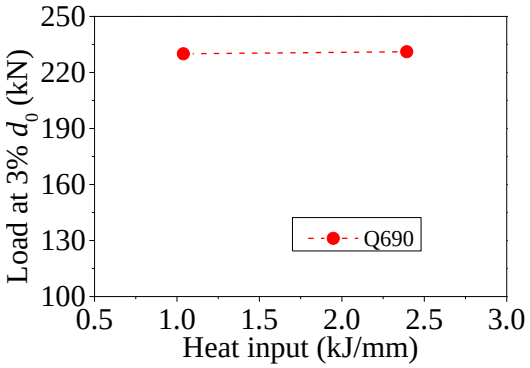

(b) Heat input influence on Q690 joints

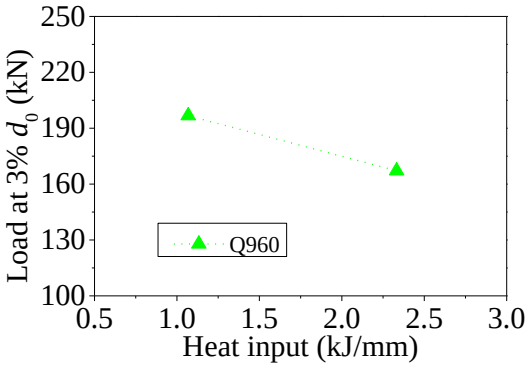

(c) Heat input influence on Q960 joints

Figure 6.26 Influence of heat input on load at 3% d_0 deformation of longitudinal plate to CHS X-joints

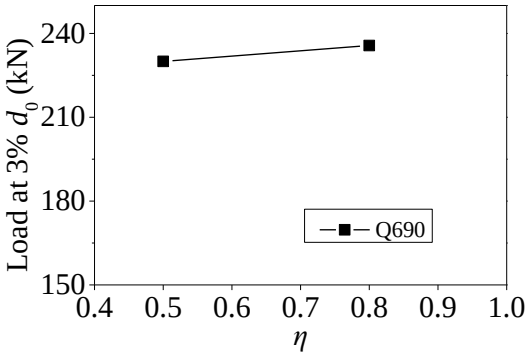

(a) η influence on Q690 joints

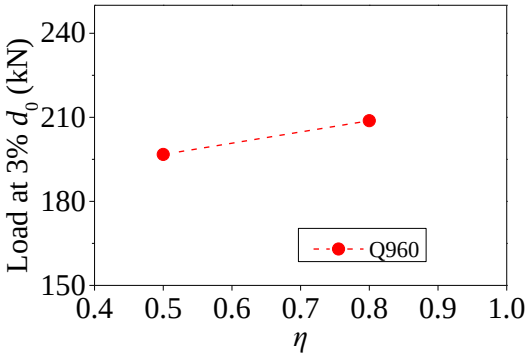

(b) η influence on Q960 joints

Figure 6.27 Influence of η on load at 3% d_0 deformation of longitudinal plate to CHS X-joints

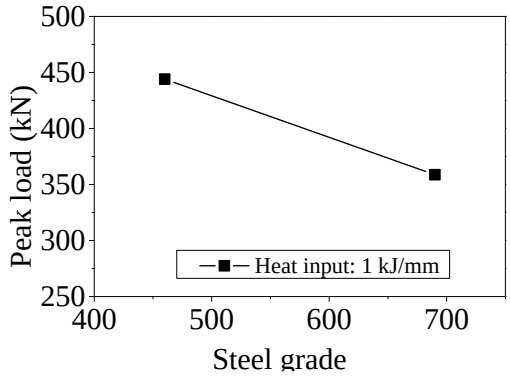

(a) Steel grade influence under heat input M

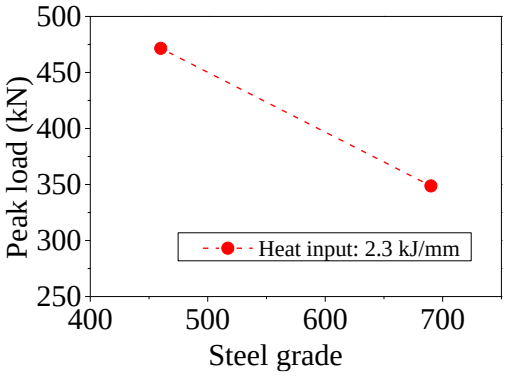

(b) Steel grade influence under heat input H1

Figure 6.28 Influence of steel grade on peak load of longitudinal plate to CHS X-joints

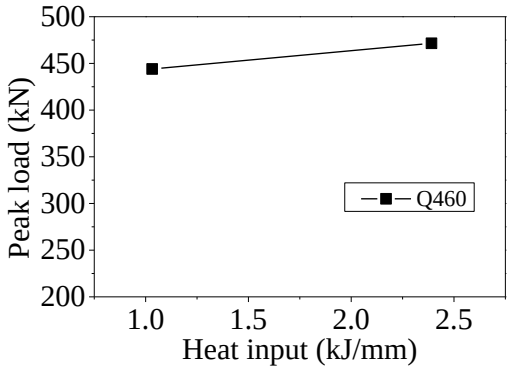

(a) Heat input influence on Q460 joints

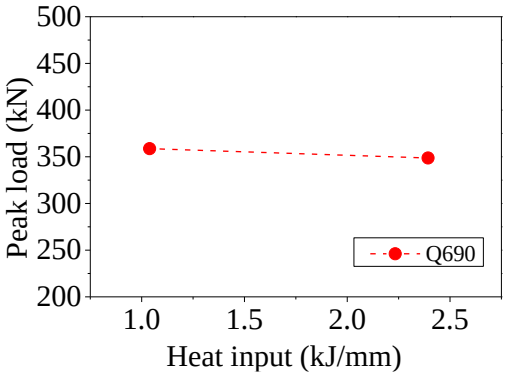

(b) Heat input influence on Q690 joints

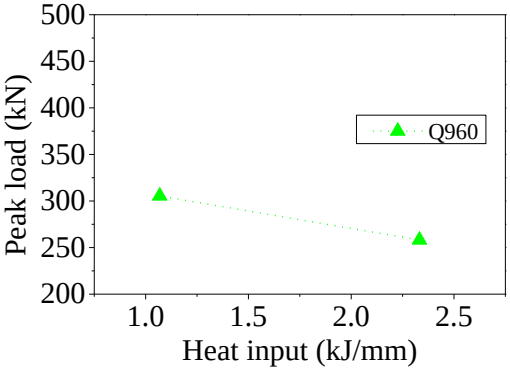

(c) Heat input influence on Q960 joints

Figure 6.29 Influence of heat input on peak load of longitudinal plate to CHS X-joints

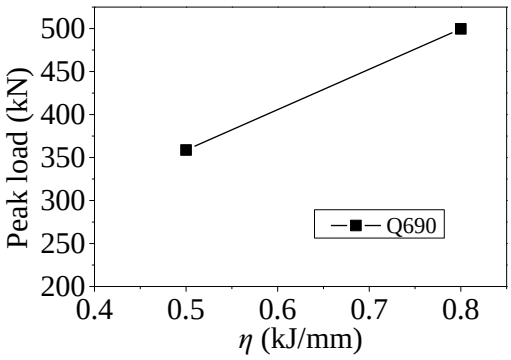

(a) η influence on Q690 joints

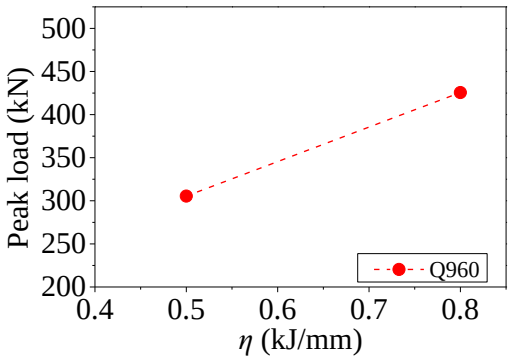

(b) η influence on Q960 joints

Figure 6.30 Influence of η on peak load of longitudinal plate to CHS X-joints

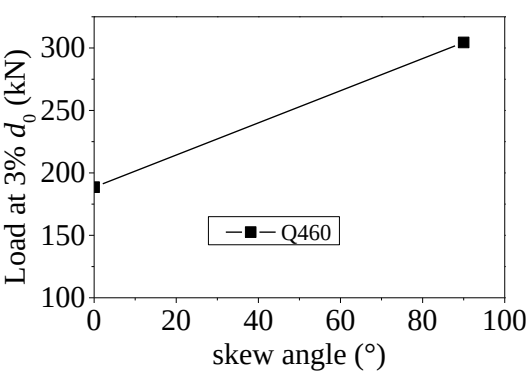

(a) Load at 3% d_0 deformation

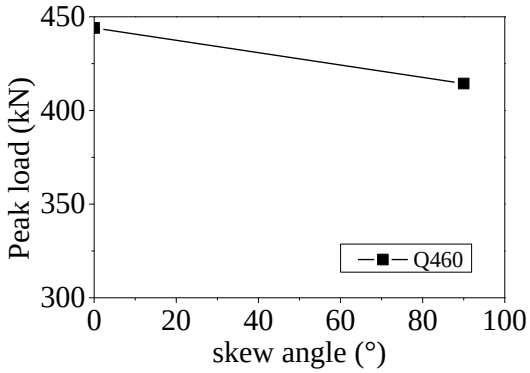

(b) Peak load

Figure 6.31 Influence of plate skew angle on Q460 gusset plate to CHS X-joint

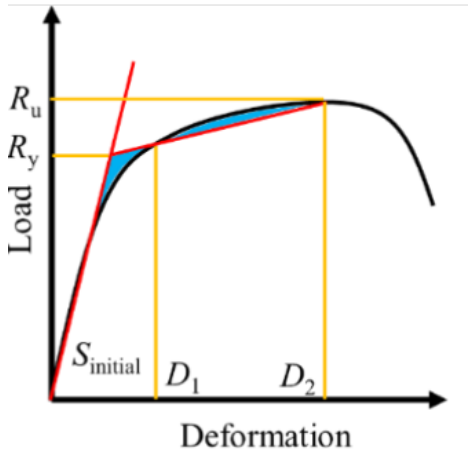

Figure 6.32 Modified bi-linear model (Yan, 2023)

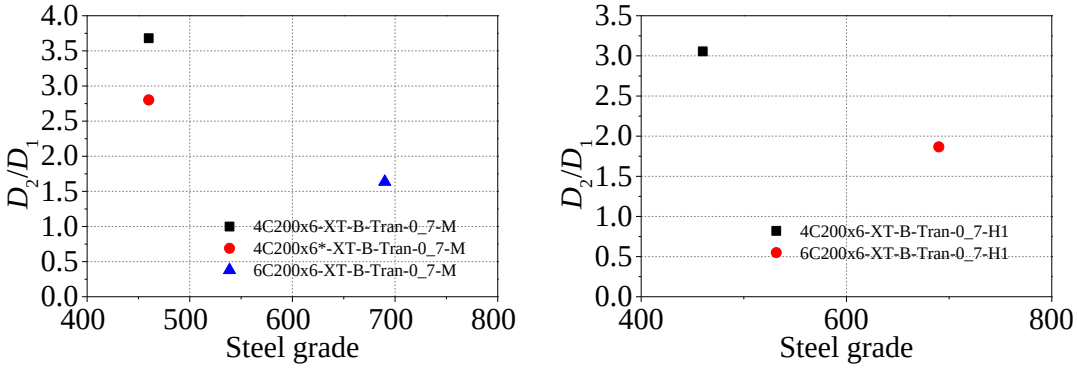

(a) Heat input M (b) Heat input H1

Figure 6.33 Influence of steel grade on ductility of transverse plate to CHS X-joints

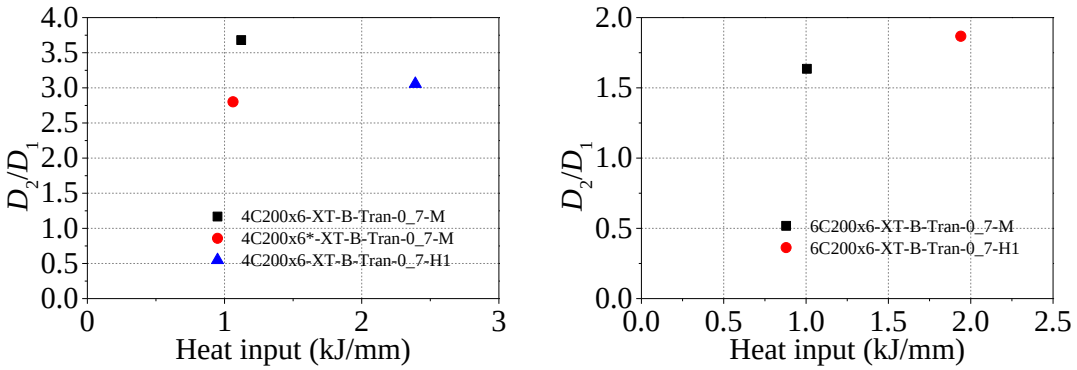

(a) Q460 (b) Q690

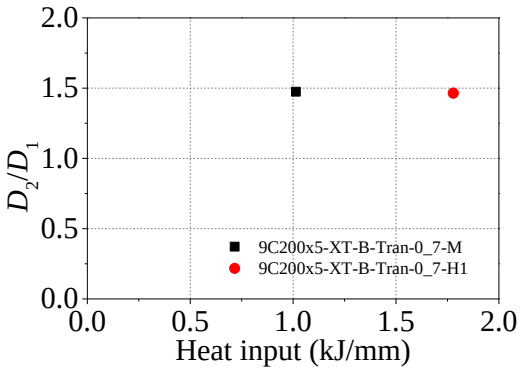

(c) Q960

Figure 6.34 Influence of heat input on ductility of transverse plate to CHS X-joints

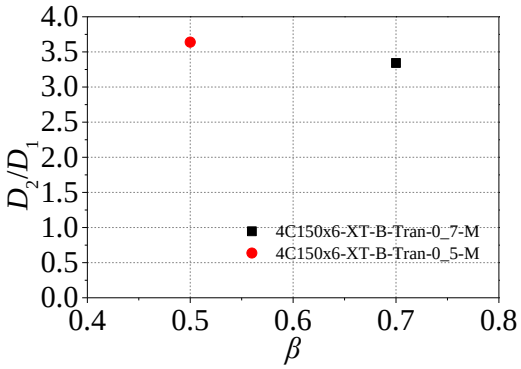

(a) β

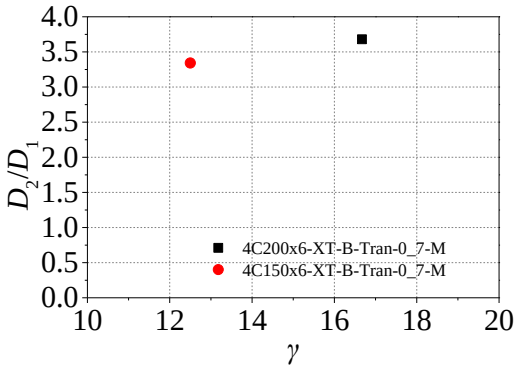

(b) γ

Figure 6.35 Influence of geometric parameters on ductility of transverse plate to CHS X-joints

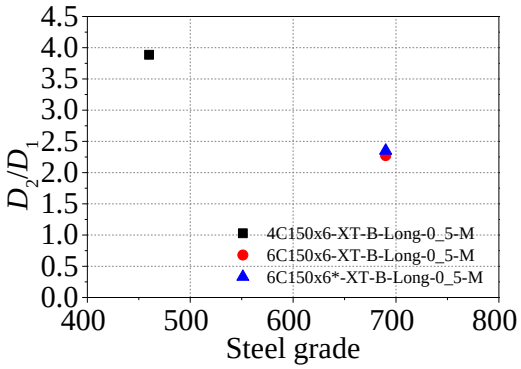

(a) Heat input M

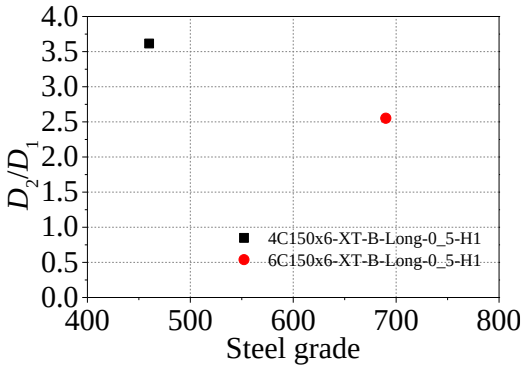

(b) Heat input H1

Figure 6.36 Influence of steel grade on ductility of longitudinal plate to CHS X-joints

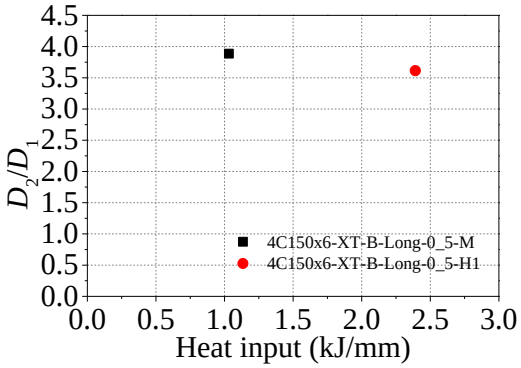

(a) Q460

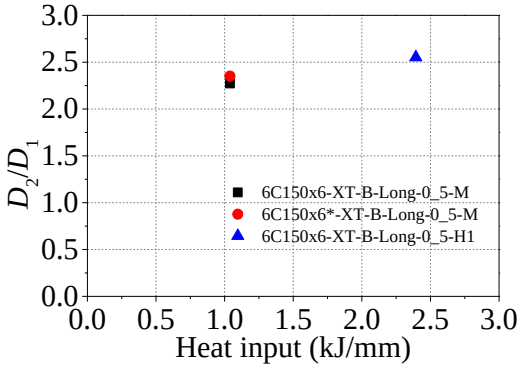

(b) Q690

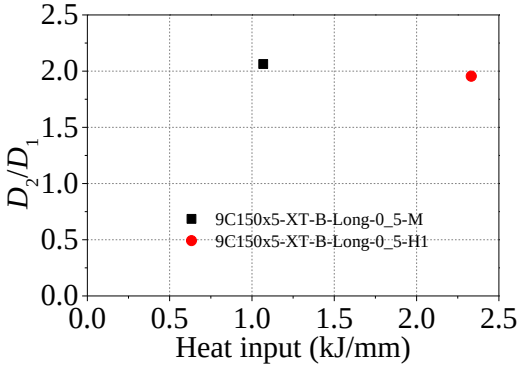

(c) Q960

Figure 6.37 Influence of heat input on ductility of longitudinal plate to CHS X-joints

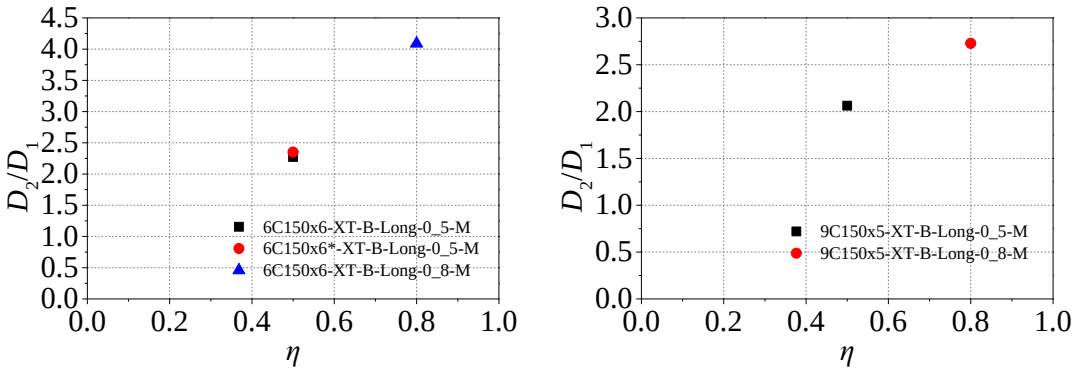

(a) Q690 (b) Q960

Figure 6.38 Influence of η on ductility of longitudinal plate to CHS X-joints

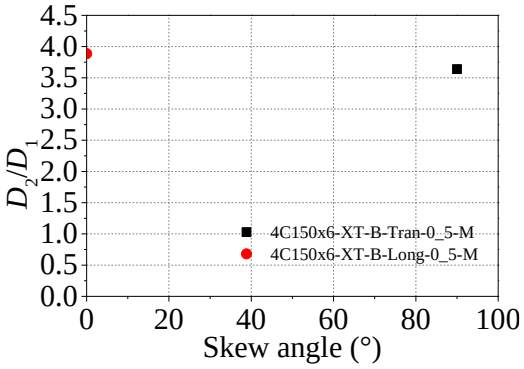

Figure 6.39 Influence of plate skew angle on ductility of longitudinal plate to CHS X-joints

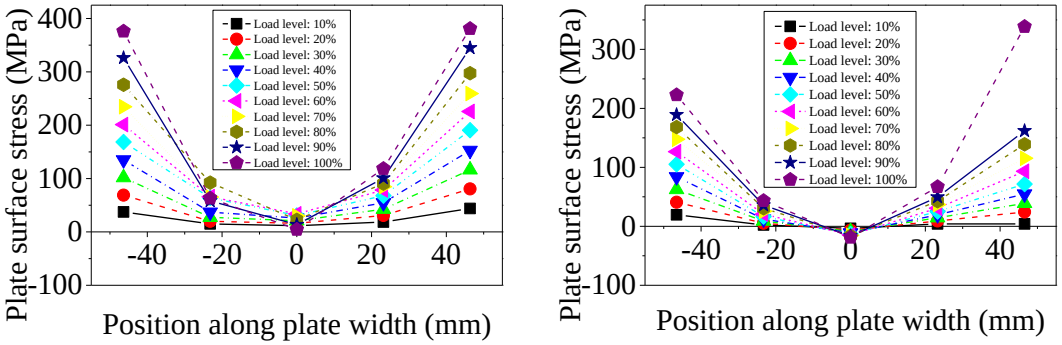

(a) 4C200x6*-XT-B-Tran-0_7-M

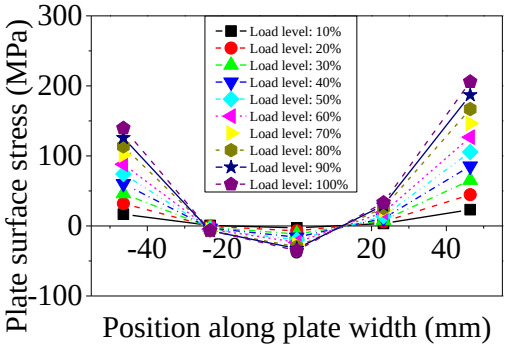

(b) 6C200x6-XT-B-Tran-0_7-M

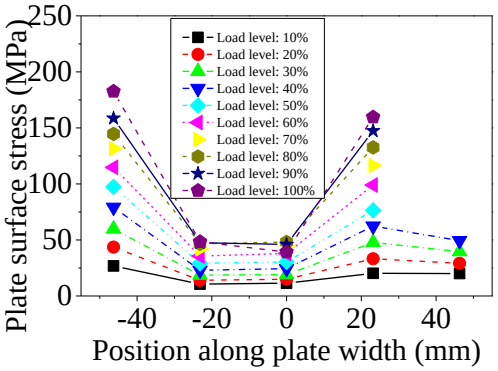

(c) 9C200x5-XT-B-Tran-0_7-M

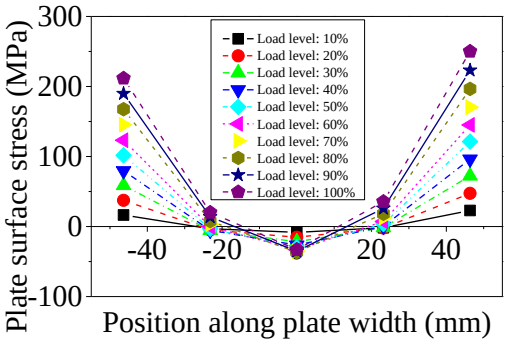

(d) 4C200x6-XT-B-Tran-0_7-H1

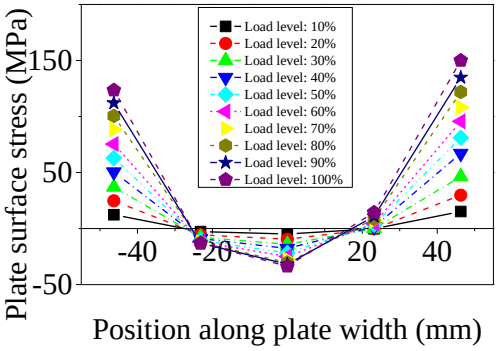

(e) 6C200x6-XT-B-Tran-0_7-H1

(f) 9C200x5-XT-B-Tran-0_7-H1

(g) 4C150x6-XT-B-Tran-0_7-M

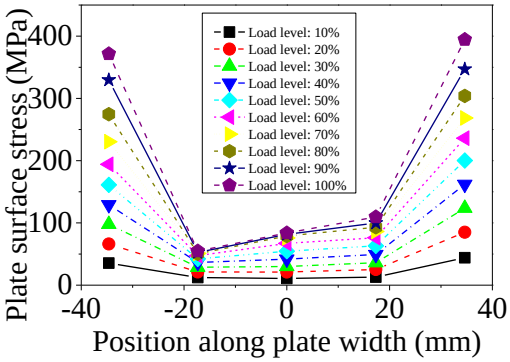

(h) 4C150x6-XT-B-Tran-0_5-M

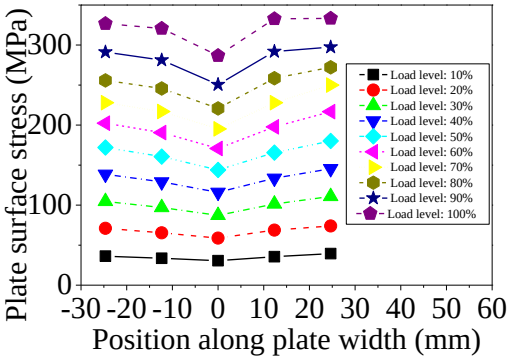

Figure 6.40 Plate surface stress distributions for transverse plate to CHS X-joints

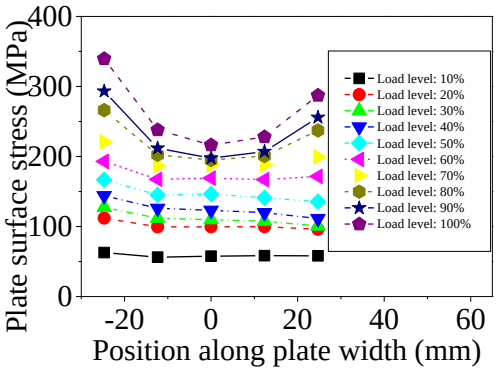

(a) 4C150x6-XT-B-Long-0_5-M

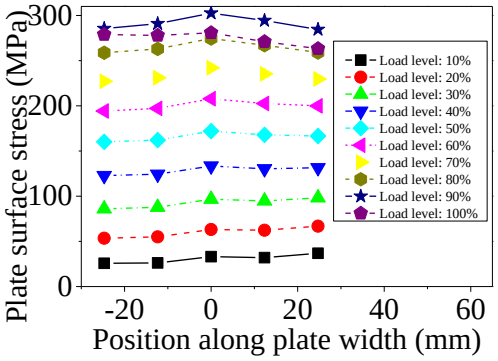

(b) 6C150x6-XT-B-Long-0_5-M

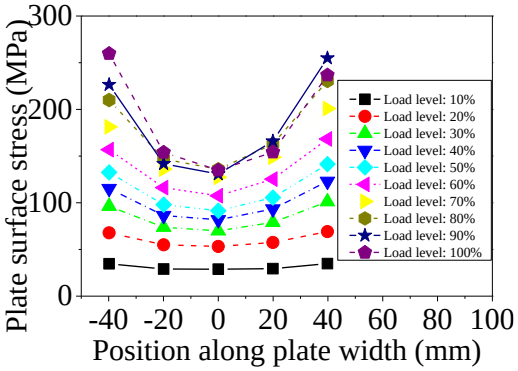

(c) 6C150x6-XT-B-Long-0_8-M

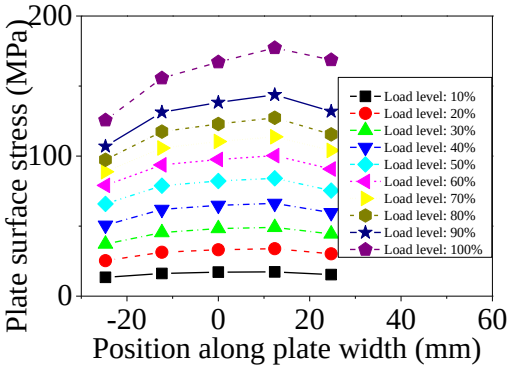

(d) 9C150x5-XT-B-Long-0_5-M

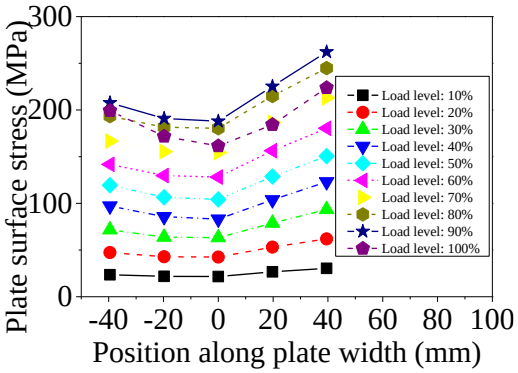

(e) 9C150x5-XT-B-Long-0_8-M

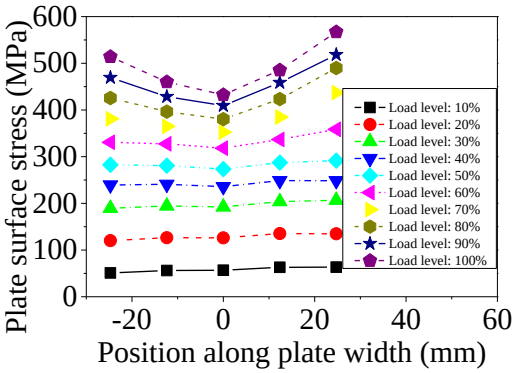

(f) 4C150x6-XT-B-Long-0_5-H1

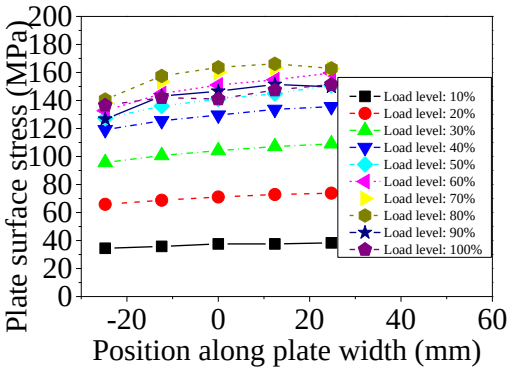

(g) 6C150x6-XT-B-Long-0_5-H1

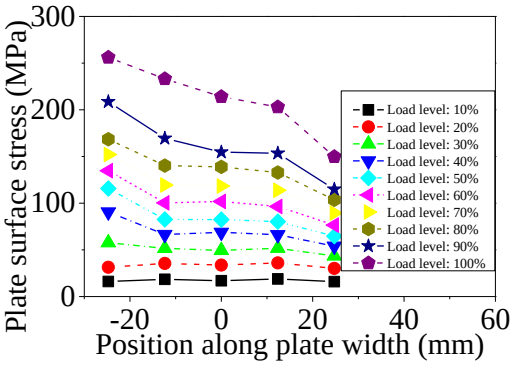

(h) 9C150x5-XT-B-Long-0_5-H1

Figure 6.41 Plate surface stress distributions for longitudinal plate to CHS X-joints

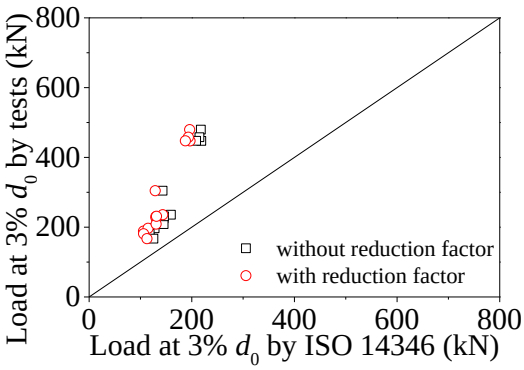

(a) ISO 14346

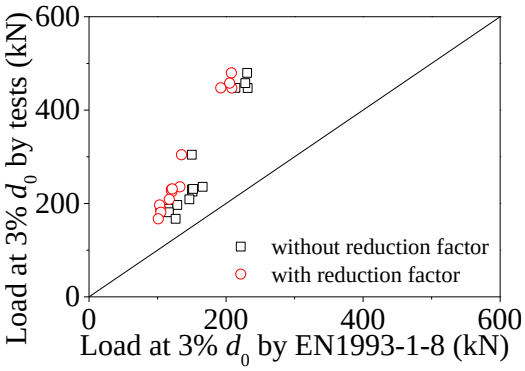

(b) prEN 1993-1-8

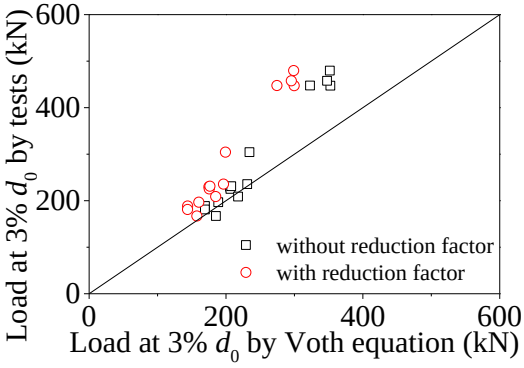

(c) Voth's method

Figure 6.42 Comparison between test strengths and predicted strengths on load at 3% d_0 deformation for gusset plate to CHS X-joints

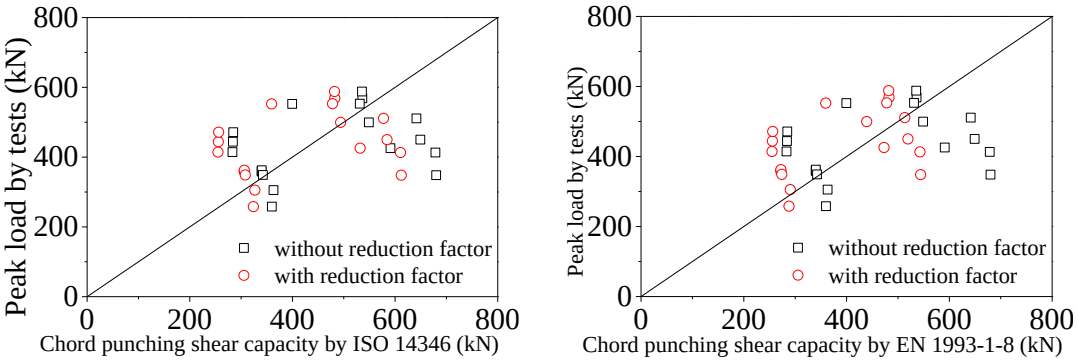

(a) ISO 14346 (b) prEN 1993-1-8

Figure 6.43 Comparison between test strengths and predicted strengths on load corresponding to chord punching shear for gusset plate to CHS X-joints

Chapter 7 Numerical modelling and parametric study for the HSS gusset plate to CHS X-joints under tension

7.1 Introduction

This chapter developed the numerical models for the tested HSS gusset plate to CHS X-joints under axial tension. The numerical models were validated by the load-deformation curves, stress distributions, and joint deformations. Then, the effect of HAZs on the joint behaviour was investigated by numerical analysis. A comprehensive parametric study was implemented for the longitudinal HSS gusset plate to CHS X-joints, whose joint strengths were deformation controlled and did not happen punching shear before 3 % d_0 deformation limit. The concerned parameters included steel grade, η, gusset plate thickness, weld leg size and heat input. Particularly, the welding effect on the joint behaviour was incorporated by combining the modified Hollomon model and regression models considering different heat inputs in the parametric study. Three heat inputs were 0.5 kJ/mm, 1.4 kJ/mm and 2.3 kJ/mm. By collating the numerical results, current design equations were evaluated.

7.2 Finite element model

7.2.1 Finite element model

The finite element (FE) software ABAQUS (2020) was used to implement numerical simulations for the gusset plate to circular hollow section joints under tension in this investigation. The measured geometric dimensions were used to develop the numerical models. The dimensions of heat affected zones (HAZ) were determined as follows: for the direction parallel to the chord length, the HAZ width was determined as Eq. 7.1 (Lan et al., 2018), where w_{HAZ} is the width of HAZ, t_1 is the width of gusset plate parallel the chord length, and w is the weld leg size; for the direction perpendicular to the chord length, the width of HAZ was determined as Eq. 7.2 and Eq. 7.3, where w_{gusset} is the

gusset plate width perpendicular to the chord length direction. The reason that the HAZ widths along two directions were different is that by adapting Eq. 7.2 and Eq. 7.3, the mesh control incompatibility could be avoided and geometrically regular mesh could be generated for the chord.

$$w_{HAZ} = t_1 + w + 12 \quad \text{Eq. 7.1}$$

For the transverse gusset plate to CHS joints:

$$w_{HAZ} = 12 + \frac{w_{gusset}}{2} \quad \text{Eq. 7.2}$$

For the longitudinal gusset plate to CHS joints:

$$w_{HAZ} = \frac{w_{gusset}}{2} + w + 12 \quad \text{Eq. 7.3}$$

The tested stress-strain curves of three steel grades, including Q460, Q690 and Q960 for the base metal of CHS tube and gusset plate were used for the FE models. The engineering stress-strain curves until ultimate strength were converted into true stress-strain curves. For the HAZ which was located on the chord, it was treated as a homogeneous region with different heat inputs for all steel grades, the modified Hollomon model in combination with the polynomial regression analysis was adapted to obtain the true stress-plastic strain curves, as shown in Figure 7.1. For all the materials the Poisson's ratio was taken as 0.3.

Both the upper and lower gusset plate were coupled to corresponding reference points. Fixed boundary condition was set for the lower reference point, and axial tensive displacement was applied to the upper reference point. The interactions between the weld, gusset plate and chord were simulated by "Tie" constraints to simulate the complete penetration welds.

The Dynamic Explicit solver was used to analyse the numerical models. The mass

scaling techniques were applied to achieve a balance between computation efficiency and accuracy. The overall numerical model was scaled by a factor of 1000. An 8-node solid element with reduced integration (C3D8R) was applied for the chord, gusset plate and weld. By proper partitioning, structural meshing techniques was used as the main mesh controls. For the region near the centre of the joint, both chord and gusset plate were meshed finer compared to other regions. After a mesh convergence study, the weld and fine regions of chord and gusset had a mesh size of 3 mm, while other regions had a mesh size of 6 mm. Four layers of elements were meshed through the chord wall thickness to avoid hour-glassing problem.

7.2.2 Results and discussions

7.2.2.1 Validation of numerical models

Figure 7.2 and Figure 7.3 provides the comparison of load-chord plastification curves and load-chord side wall deformation curves between the tests and simulations for the gusset plate to CHS joints except the repeated specimens. In the numerical simulations, fracture initiation and damage evolution were not defined. Therefore, the chord punching shear failure was not captured by the FE models. The load-deformation curves from the start of loading until the moment at which specimens fractured were extracted for each numerical model. It was found that for both chord plastification and chord side wall deformation, generally the experimental and numerical load-deformation curves agreed well.

Most specimens except 6C200x6-XT-B-Tran-0_7-M, 9C200x5-XT-B-Tran-0_7-M, 6C200x6-XT-B-Tran-0_7-H1 and 9C200x5-XT-B-Tran-0_7-H1 reached to the 3% d deformation limit, which meant the joint strengths were deformation controlled. Table 7.1 provides the comparison of joint strengths corresponding to 3% d deformation limit between experiments and simulations. $N_{3\%}$ denoted the joint strength obtained from the experimental load-chord plastification curves. $N_{3\%,\ \text{FE-noHAZ}}$ denoted the joint strength

obtained from the numerical models which did not take HAZ into account. $N_{3\%,\ \text{FE-HAZ}}$ denoted the joint strength obtained from the numerical models which considered the HAZ material deterioration. The mean value of $N_{3\%}/N_{3\%,\ \text{FE-noHAZ}}$ was 0.911 with its coefficient of variation (COV) of 0.069. Besides, the mean value of $N_{3\%}/N_{3\%,\ \text{FE-HAZ}}$ was 0.925 with its coefficient of variation (COV) of 0.066. It can then be concluded that the developed numerical models can properly simulate the mechanical behaviours of the HSS gusset plate to CHS joints under tension. The FE models can be adapted to conduct parametric studies.

Figure 7.4 to Figure 7.7 show the comparisons of 4 joints at the ultimate load between the experimental specimens and numerical models with HAZ. For Q690 and Q960 steel, both HSS transverse and longitudinal gusset plate to CHS joints under tension were presented. Figure 7.4 and Figure 7.6 compares the experimental and numerical results of 6C200x6-XT-B-Tran-0_7-H1 and 9C200x5-XT-B-Tran-0_7-H1 at ultimate load, respectively. It can be observed that regardless of the steel grade, the stress concentrated at the saddle point for the transverse joint in Figure 7.4(a) and Figure 7.6(a). Besides, the gusset plate tension was transferred to the chord side wall and finally resisted by the core region of the chord side wall. The equivalent plastic strain distributions (PEEQ) which described the accumulation of plastic deformation during the overall loading process for these transverse joints were provided in Figure 7.4(b) and Figure 7.6(b). It can be found that the plastic strain concentrated at the saddle points. This fact coincided with the observations in the test that the chord punching shear initiated at the saddle points, as shown in Figure 7.4(c) and Figure 7.6(c). Finally, the transverse joint deformations of experiments and simulations agreed well with each other.

Figure 7.5 and Figure 7.7 compares the experimental and numerical results of 6C150x6-XT-B-Long-0_5-H1 and 9C150x5-XT-B-Long-0_5-M at ultimate load, respectively. For both longitudinal joints with different steel grades, the stress concentrated along the weld leg size parallel to the chord length direction, as shown in Figure 7.5(a) and Figure

7.7(a). Like the transverse joint, the gusset plate tension of the longitudinal joint was also resisted by the chord side wall but spread to a wider region. The PEEQ distributed along the weld leg size in Figure 7.5(b) and Figure 7.7(b), which coincided with the experimental phenomenon that the chord punching shear developed along the weld leg size in Figure 7.5(c) and Figure 7.7(c). At last, the simulated joint deformation agreed well with its experimental counterpart.

The discussions about load-displacement curves, joint strengths, stress and strain distributions and joint deformations in this section led to the natural conclusion that the developed numerical models can reasonably predict the structural behaviour and static strength for the HSS gusset plate to CHS joints under tension.

7.2.2.2 Effect of heat affected zones

It is impossible to fabricate HSS gusset plate to CHS joint without HAZ by gas metal arc welding (GMAW). To investigate the effect of HAZ on joint behaviours, FE modelling can be a useful tool by including or not HAZ into numerical models. In Figure 7.2, the load-chord plastification curves of the tested specimens with and without HAZ were presented, respectively. For all the specimens, the joint initial stiffness was not affected by HAZ since the load-chord plastification curves with and without HAZ overlapped with each other. The reason behind this phenomenon was that the Young's modulus of HAZ remained unchanged compared to BM. Therefore, the joint initial stiffness was only affected by its geometric dimensions. For the HSS transverse gusset plate to CHS joints under tension, if the welding heat input was no more than 2.3 kJ/mm, the load-chord plastification curves for all three steel grades with and without HAZ almost overlapped with each other, indicating that the effect of HAZ was neglectable. The reason may be that the stress and plastic strain concentrated at the chord saddle points (as shown in Figure 7.4), where the yield HAZ developed limited. The adjacent zones near the HAZ imposed the constraint effect on the HAZ significantly. For the

HSS longitudinal gusset plate to CHS joints under tension, however, if the heat input was as high as 2.3 kJ/mm and high steel grades like Q690 and Q960 were adapted, the load-chord plastification curves with and without HAZ diverged obviously after elastic stage, as shown in Figure 7.2(n)(o). The degree of divergence was enlarged for the HSS longitudinal joints as the chord plastification increased. The reason could be that the stress and plastic strain concentrated along the weld length (as shown in Figure 7.5), thus the constraint effect for the yielded HAZ was not significant. Besides, as the chord plastification was enlarged, the plastic deformation accumulated more around the HAZ near the weld leg size. Therefore, under the same loading level, the longitudinal gusset plate to CHS joint with HAZ would experience larger deformation than its counterpart without HAZ.

Table 7.2 shows the comparisons of joint strengths corresponding to 3% d deformation between tests and numerical simulations. $N_{3\%}$ presented the joint strength for specimens obtained from load-chord plastification curves; $N_{3\%,\ \text{FE-noHAZ}}$ presented the joint strengths obtained from numerical load-chord plastification curves without HAZ; $N_{3\%,\ \text{FE-HAZ}}$ presented the joint strengths obtained from numerical load-chord plastification curves with HAZ. The differences between $N_{3\%}/N_{3\%,\ \text{HAZ}}$ - $N_{3\%}/N_{3\%,\ \text{noHAZ}}$ denoted the influence of HAZ on joint strengths. It can be found that for the tested HSS gusset plate to CHS joints under tension, the influence of HAZ was existent but not quite significant, as the differences of joint strengths by deformation control between the models with and without HAZ were within 5%. However, for joints with heat input equal to around 2.3 kJ/mm, this difference was rather larger than other joints, indicating that higher heat input could affect the mechanical behaviours of the joint more obviously. Besides, the mean value of $N_{3\%,\ \text{FE-noHAZ}}$ changed from 0.911 to 0.925, getting closer to unity and the coefficient of variation was slightly reduced from 0.069 to 0.066 when the HAZ was included into the numerical models. This demonstrated that by considering HAZ in numerical models, the overall performance of numerical simulations was improved.

From above discussions, it can be concluded that the effect caused by HAZ was not as significant as illustrated by other research. To explain these phenomena, the modified Hollomon model should be reviewed. The modified Hollomon model was based on the HSS butt-welded joint test. In these tests, the existence of HAZ significantly impaired the yield strength (up to 40% reduction for Q960) but not the tensile strength (only up to 17% reduction for Q960), as introduced in the chapter related to butt-welded joints. In contrast, in a similar study conducted by Pandey et al. (2021a), the joint strengths of HSS RHS-RHS T-joints made of S900 and S960 can be overestimated in the range of 12 to 34%. One possible reason was that in the HAZ strength predictions, Pandey et al. (2021a) obtained conservative reduction factors by trial and error. In their research, for HSS plate with 6 mm thickness, a reduction of 20% was applied for both yield strength and ultimate strength. Similarly, Sun et al. (2018c) adapted reduction factors of 0.47 and 0.93 to calculate the yield and ultimate strength of HAZ for Q690, respectively. The reduction of yield strength was far beyond the butt-welded joint tests in this study. The HAZ was considered in Q690 T-stub joints. The load-displacement curves exhibited that significant influences were exerted by the existence of HAZ. HAZ geometry influenced a lot by Sun. so in the parametric study, this was considered. Furthermore, as the numerical simulations in this study did not include the fracture initiation and damage evolution for HAZ under different heat inputs, the advance chord punching shear induced by increasing heat inputs in the experiments was not reflected by the numerical models.

7.3 Parametric study

7.3.1 Specifications for parametric FE models

A comprehensive parametric study was implemented to investigate the influence of geometric dimensions and welding heat inputs on the joint strengths defined by the 3% *d* deformation limit for the HSS longitudinal gusset plate to CHS X-joints under tension.

In the experiments, chord punching shear failure happened for the specimens including 6C200x6-XT-B-Tran-0_7-M, 9C200x5-XT-B-Tran-0_7-M, 6C200x6-XT-B-Tran-0_7-H1, and 9C200x5-XT-B-Tran-0_7-H1 before reaching to the 3% d deformation limit. As the fracture initiation and damage evolution were not incorporated into the numerical models, the HSS transverse gusset plate to CHS X-joints under tension were not simulated in parametric study. Table 7.3 and Table 7.4 demonstrated the range of parameters. Three steel grades, Q460, Q690 and Q960, were included in the parametric study. The chord diameter (d_0) was 150 mm. The chord length was set as $10d_0$ + plate width along the chord length direction, since Packer and Voth (2008) found that this chord length could exclude the chord end effect on the joint strengths of the longitudinal plate to HSS CHS X-joints. The chord wall thickness was set as 6 mm for all specimens, thus obtaining constant ratio of the chord diameter to the chord wall thickness (2γ) with a value of 25. The gusset plate thickness (t_1) was 20 mm and 30 mm. By the constant 2γ and plate thickness no thinner than 20 mm, the plate or weld failure could be avoided for the simulated HSS longitudinal gusset plate to CHS X-joints under tension. For the Q460 joints, only 20 mm thickness gusset plate was simulated. But for the Q690 and Q960 joints, not only 20 mm but also 30 mm gusset plate were incorporated. The experimental results indicated that increasing η could postpone the chord punching shear failure. Therefore, the ratios of the gusset plate width along the chord length direction to the chord diameter (η) were 0.5, 1.0, 1.5, 2.0, and 3.0. As for the weld leg size (w), it was set as 10 mm and 20 mm. Finally, three kinds of heat inputs (Q) were considered, including 0.5, 1.4 and 2.3 kJ/mm. Higher heat inputs were excluded to avoid premature chord punching shear before 3% d_0 deformation limit. The nomenclature of numerical model was illustrated by taking "4C-eta0p5-h0p5-wl10-p30" as an example: "4C" denoted the steel grade was Q460; "eta0p5" denoted the ratio η was 0.5; "h0p5" denoted the heat input was 0.5 kJ/mm; "wl10" denoted the weld leg size was 10 mm; "p30" denoted the gusset plate thickness was 30 mm.

Most numerical simulation techniques in the parametric study remained the same as previous section mentioned. However, two kinds of mass scaling techniques were applied to achieve a balance between computation efficiency and accuracy. The overall numerical model was scaled by a factor of 1000. For the weld, its elements were quite small and determined the time increment during calculating. Therefore, it was scaled by the target time increment with a value of 10^{-6} to improve the computation efficiency. The BM material properties were obtained by the tensile coupon test results. The HAZ material properties were determined by the modified Hollomon model.

7.3.2 Results and discussions

There were in total 87 numerical models for HSS gusset plate to CHS X-joints under tension in the parametric study. The effects of critical parameters were carefully investigated including η, w, t_1, and Q. Among these parameters, η, w, and t_1 were geometric parameters while Q was fabrication parameter. The load-chord plastification curves depicting the effect of these parameters were provided and discussed in this section, as shown in Figure 7.8 to Figure 7.10. Since the parameters were carefully chosen to avoid the chord punching shear failure before reaching to 3% d deformation limit, all the specimens in the parametric study were deformation controlled when determining the joint strengths.

Figure 7.8(a), Figure 7.9(a) and Figure 7.10(a) give the load-chord plastification curves of Q460, Q690 and Q960 respectively for η = 0.5, 1.0, 1.5, and 2.0 by keeping w = 10 mm, t_1 = 20 mm, and Q = 0.5 kJ/mm. It can be noticed that for all steel grades, increasing η improved the initial stiffness and joint strength corresponding to 3% d deformation. Figure 7.8(b), Figure 7.9(b) and Figure 7.10(b) present the variations of load-chord plastification curves of Q460, Q690 and Q960 respectively for w = 10 and 20 mm by keeping η = 2.0 and t_1 = 20 mm, and Q = 0.5 kJ/mm. Significant increase of initial stiffness and joint strength corresponding to 3% d deformation was observed by

enlarging w. Figure 7.9(c) and Figure 7.10(c) present the variations of load-chord plastification curves of Q690 and Q960 respectively for t_1 = 20 and 30 mm by keeping η = 2.0, w = 10 mm and Q = 0.5 kJ/mm. It was found that both initial stiffness and joint strengths corresponding to 3% d deformation enhanced with increasing t_1. With the increase of η w or t_1, the central region resisting the tension became wider, thus strengthening the initial stiffness and joint strength corresponding to 3% d deformation.

HSS experiences various thermal cycles at different steel plate positions during welding and undergoes phase transformations. Therefore, HAZ forms with impaired mechanical properties. Figure 7.11 demonstrated that the effect of welding heat input Q on the HSS gusset plate to CHS X-joints under tension regarding geometric parameters. The load-chord plastification curves of the Q460 gusset plate to CHS X-joints had almost no change by varying Q, as shown in Figure 7.11(a)(b). In Figure 7.11(c)(f), however, it was observed that as η increased, the load-chord plastification curves of Q690 and Q960 degraded. Furthermore, the higher Q was, the more degradation it was. Similar trend was observed if w and t_1 increased, which meant that the effect of HAZ on the load-chord plastification curves enhanced with increasing w and t_1.

7.4 Evaluation of design codes

In this section, the design methods for the longitudinal gusset plate to CHS X-joints under tension in different codes were applied to calculate the joint strengths corresponding to 3% d_0 deformation limit, including ISO 14346 (ISO, 2013a), prEN 1993-1-8 and design equations proposed by Voth (Voth, 2010). For all the three methods, reduction factors were applied but had different meanings. In ISO 14346 and prEN 1993-1-8, reduction factors were adapted to consider material effect for HSS. In the design equations proposed by Voth, however, reduction factors were utilised to compensate the differences between the parametric analysis FE results and the international database.

Figure 7.12 shows the comparison of the joint strengths at 3% d_0 deformation between the parametric results and the design equation predicting results without and with reduction factors. It can be observed that for all the design methods, the predicted joint strengths at 3% d_0 deformation were conservatively underestimated compared to the parametric counterparts with or without reduction factors.

Figure 7.13 to Figure 7.15 present the effect of critical parameters on the values of $N_{3\%,\ FE}/N_{CF,\ code}$ for the HSS gusset plate to CHS X-joints under tension, where $N_{3\%,\ FE}$ was the joint strength at 3% d_0 deformation obtained from the parametric study, and $N_{CF,\ code}$ was the nominal joint strength obtained from three codes without reduction factors. The critical parameters included η, w, t_1 and Q. Figure 7.13 demonstrated the variations of $N_{3\%,\ FE}/N_{CF,\ code}$ with respect to η for different values of w and Q when the steel grade was Q460. The tendencies in three codes were similar. It can be found that with w equal to 10 mm, $N_{3\%,\ FE}/N_{CF,\ code}$ firstly decreased then gradually increased with the increase of η. In contrast, if w was 20 mm, $N_{3\%,\ FE}/N_{CF,\ code}$ consistently increased as η increased. Besides, the influence of Q enlarged with larger w and η, as the value of $N_{3\%,\ FE}/N_{CF,\ code}$ decreased significantly with the increase of Q when w = 20 mm. In ISO 14346 and prEN 1993-1-8, the weld leg size was not included into the design equations, thus the conservativeness which represented by the value of $N_{3\%,\ FE}/N_{CF,\ code}$ increased when w increased. In the design equations proposed by Voth, since the weld leg size effect was incorporated, the conservativeness was less significant. Figure 7.14 and Figure 7.15 reveal similar tendencies for the values of $N_{3\%,\ FE}/N_{CF,\ code}$ with respect to η for different values of w and Q when the steel grades were Q690 and Q960 respectively. In addition, the values of $N_{3\%,\ FE}/N_{CF,\ code}$ significantly increased if the gusset plate thickness was increased from 20 mm to 30 mm. It can be observed from Figure 7.13 to Figure 7.15 that the influence of Q became more significant if the HAZ area enlarged by increasing η, w, or t_1, as under higher Q, $N_{3\%,\ FE}/N_{CF,\ code}$ diverged more obviously under the same geometric parameters, especially for larger η, w and t_1. The reason may be that

increasing η w and t_1 significantly amplified the HAZ area, thus the effect of HAZ material deterioration enhanced.

Figure 7.16 shows the values of $N_{3\%,\ FE}/N_{CF,\ code}$ by different codes with respect to η. It was evident that the design equations proposed by Voth which considered the weld effect and plate thickness effect performed best in three design codes. Figure 7.17 demonstrates the influence of Q for the HSS gusset plate to CHS X-joints under tension. It was observed that with the increase of Q, the value of $N_{3\%,\ FE}/N_{CF,\ code}$ tended to decrease regardless of the steel grades and design codes. It was because $N_{3\%,\ FE}$ was reduced when higher Q was adapted leading to more deterioration for the HAZ material properties.

7.6 Summary

In this chapter, numerical models for the tested HSS gusset plate to CHS X-joints under axial tension were developed. By comparing the load-deformation curves, stress distributions and joint deformations, the numerical models were validated and could be used to reproduce the joint behaviours of the test specimens. Then, a comprehensive parametric study was implemented for the longitudinal HSS gusset plate to CHS X-joints, since this kind of joint was deformation controlled, in other words, would not fracture along the gusset perimeter before reaching to 3% d_0 deformation limit. The concerned parameters included steel grade, η, gusset plate thickness, weld leg size and heat input. Current design equations for the gusset plate to CHS X-joints were evaluated based on the numerical data. Furthermore, design equations for the HSS longitudinal gusset plate to CHS X-joints were proposed. Following conclusions can be summarised:

1. For each simulated gusset plate to CHS X-joints under axial tension, both the load-chord plastification curve and load-chord side wall deformation curve agreed well with the test curves. Besides, the experimental and numerical results of 6C200x6-XT-B-

Tran-0_7-H1, 9C200x5-XT-B-Tran-0_7-H1, 6C150x6-XT-B-Long-0_5-H1 and 9C150x5-XT-B-Long-0_5-M at ultimate load were compared. The stress distribution, PEEQ distribution and joint deformation at the ultimate load all indicated that the numerical models could reproduce the joint behaviours of the test specimens. Therefore, the numerical models were validated and could be used for further parametric study.

2. The effect of HAZ on the tested gusset plate to CHS X-joints under tension was investigated by numerical simulations. It can be found that the joint initial stiffness was not affected by HAZ, because the Young's modulus of HAZ remained unchanged compared to BM. Therefore, the joint initial stiffness was only affected by its geometric dimensions. For the HSS transverse gusset plate to CHS X-joints under tension in this experimental programme, the effect of HAZ was neglectable. In contrast, if the heat input was as high as 2.3 kJ/mm and high steel grades like Q690 and Q960 were adapted for the HSS longitudinal gusset plate to CHS X-joints under tension, the load-chord plastification curves were obviously affected by HAZ. The influence of HAZ on the joint strengths corresponding to 3% d deformation was existent but not significant unless the heat input was increased to 2.3 kJ/mm.

3. A parametric investigation was implemented for the HSS longitudinal gusset plate to CHS X-joints under axial tension. For the HSS transverse gusset plate to CHS X-joints, the joint strength was sometimes controlled by chord punching shear rather than deformation. Since the fracture initiation and damage evolution were not considered in the numerical models, the HSS transverse joint was not included into the parametric study. The parametric analysis showed that for all steel grades, increasing η, w and t_1 could improve the initial stiffness and joint strength corresponding to 3% d deformation. The influence of Q was illustrated as follows: for the Q460 joints, varying Q almost had no effect on the load-chord deformation curves; in contrast, as η increased, the load-chord plastification curves of Q690 and Q960 degraded. Furthermore, the higher Q was,

the more degradation it was. Similarly, the effect of HAZ on the load-chord plastification curves enhanced with increasing w and t_1.

4. The design methods of the joint strengths corresponding to 3% d_0 were evaluated for the HSS longitudinal gusset plate to CHS X-joints under tension. These design methods included ISO 14346, prEN 1993-1-8 and design equations proposed by Voth. For all the design methods, the predicted joint strengths at 3% d_0 deformation were conservatively underestimated compared to the parametric counterparts with or without reduction factors. Besides, the effect of critical parameters on the values of $N_{3\%,\ FE}/N_{CF,\ code}$ was investigated. In ISO 14346 and prEN 1993-1-8, the weld leg size was not included into the design equations, thus the conservativeness which represented by the value of $N_{3\%,\ FE}/N_{CF,\ code}$ increased when w increased. In the design equations proposed by Voth, since the weld leg size effect was incorporated, the conservativeness was less significant.

Table 7.1 Comparison of joint strengths determined by 3% *d* deformation limit

No.	Specimen	$N_{3\%}$	$N_{3\%,\ \text{FE-noHAZ}}$	$N_{3\%,\ \text{FE-HAZ}}$	$N_{3\%}/N_{3\%,\ \text{FE-noHAZ}}$	$N_{3\%}/N_{3\%,\ \text{HAZ}}$
-	-	kN	kN	kN	-	-
1	4C200x6-XT-B-Tran-0_7-M	447.245	481.836	479.612	0.928	0.933
2	4C200x6*-XT-B-Tran-0_7-M	479.672	N/A	N/A	N/A	N/A
3	6C200x6-XT-B-Tran-0_7-M	N/A	N/A	N/A	N/A	N/A
4	9C200x5-XT-B-Tran-0_7-M	N/A	N/A	N/A	N/A	N/A
5	4C200x6-XT-B-Tran-0_7-H1	457.797	460.584	446.032	0.994	1.026
6	6C200x6-XT-B-Tran-0_7-H1	N/A	N/A	N/A	N/A	N/A
7	9C200x5-XT-B-Tran-0_7-H1	N/A	N/A	N/A	N/A	N/A
8	4C150x6-XT-B-Tran-0_7-M	447.543	445.920	442.444	1.004	1.012
9	4C150x6-XT-B-Tran-0_5-M	304.433	299.730	299.226	1.016	1.017
10	4C150x6-XT-B-Long-0_5-M	188.530	205.398	204.152	0.918	0.923
11	6C150x6-XT-B-Long-0_5-M	229.992	273.783	271.808	0.840	0.846
12	6C150x6*-XT-B-Long-0_5-M	225.398	N/A	N/A	N/A	N/A
13	6C150x6-XT-B-Long-0_8-M	235.666	280.521	277.734	0.840	0.849
14	9C150x5-XT-B-Long-0_5-M	196.747	210.881	208.771	0.933	0.942
15	9C150x5-XT-B-Long-0_8-M	208.799	235.104	231.913	0.888	0.900
16	4C150x6-XT-B-Long-0_5-H1	181.157	212.387	206.835	0.853	0.876
17	6C150x6-XT-B-Long-0_5-H1	231.107	261.482	254.732	0.884	0.907
18	9C150x5-XT-B-Long-0_5-H1	167.148	200.414	192.227	0.834	0.870
Mean					0.911	0.925
COV					0.069	0.066

Table 7.2 Comparisons of joint strengths corresponding to 3% *d* deformation between tests and numerical simulations

No.	Specimen	$N_{3\%}$	$N_{3\%,\ \text{FE-noHAZ}}$	$N_{3\%,\ \text{FE-HAZ}}$	$N_{3\%}/N_{3\%,\ \text{FE-noHAZ}}$	$N_{3\%}/N_{3\%,\ \text{HAZ}}$	Difference
-	-	kN	kN	kN	-	-	
1	4C200x6-XT-B-Tran-0_7-M	447.245	481.836	479.612	0.928	0.933	0.43%
2	4C200x6*-XT-B-Tran-0_7-M	479.672	N/A	N/A	N/A	N/A	N/A
3	6C200x6-XT-B-Tran-0_7-M	N/A	N/A	N/A	N/A	N/A	N/A
4	9C200x5-XT-B-Tran-0_7-M	N/A	N/A	N/A	N/A	N/A	N/A
5	4C200x6-XT-B-Tran-0_7-H1	457.797	460.584	446.032	0.994	1.026	3.24%
6	6C200x6-XT-B-Tran-0_7-H1	N/A	N/A	N/A	N/A	N/A	N/A
7	9C200x5-XT-B-Tran-0_7-H1	N/A	N/A	N/A	N/A	N/A	N/A
8	4C150x6-XT-B-Tran-0_7-M	447.543	445.920	442.444	1.004	1.012	0.79%
9	4C150x6-XT-B-Tran-0_5-M	304.433	299.730	299.226	1.016	1.017	0.17%

10	4C150x6-XT-B-Long-0_5-M	188.530	205.398	204.152	0.918	0.923	0.56%
11	6C150x6-XT-B-Long-0_5-M	229.992	273.783	271.808	0.840	0.846	0.61%
12	6C150x6*-XT-B-Long-0_5-M	225.398	N/A	N/A	N/A	N/A	N/A
13	6C150x6-XT-B-Long-0_8-M	235.666	280.521	277.734	0.840	0.849	0.84%
14	9C150x5-XT-B-Long-0_5-M	196.747	210.881	208.771	0.933	0.942	0.94%
15	9C150x5-XT-B-Long-0_8-M	208.799	235.104	231.913	0.888	0.900	1.22%
16	4C150x6-XT-B-Long-0_5-H1	181.157	212.387	206.835	0.853	0.876	2.29%
17	6C150x6-XT-B-Long-0_5-H1	231.107	261.482	254.732	0.884	0.907	2.34%
18	9C150x5-XT-B-Long-0_5-H1	167.148	200.414	192.227	0.834	0.870	3.55%
Mean					0.911	0.925	
Cov					0.069	0.066	

Table 7.3 Range of parameters for the parametric study of Q460 longitudinal gusset plate to CHS X-joints

Parameters	η				
	0.5	1.0	1.5	2.0	3.0
2γ	25	25	25	25	25
t_1 (mm)	20	20	20	20	20
w (mm)	10	10	10，20	10，20	10
Q (kJ/mm)	0.5，1.4，2.3	0.5，1.4，2.3	0.5，1.4，2.3	0.5，1.4，2.3	0.5，1.4，2.3

Table 7.4 Range of parameters for the parametric study of Q690/Q960 longitudinal gusset plate to CHS X-joints

Parameters	η				
	0.5	1.0	1.5	2.0	3.0
2γ	25	25	25	25	25
t_1 (mm)	20	20	20，30	20，30	20
w (mm)	10	10	10，20	10，20	10
Q (kJ/mm)	0.5，1.4，2.3	0.5，1.4，2.3	0.5，1.4，2.3	0.5，1.4，2.3	0.5，1.4，2.3

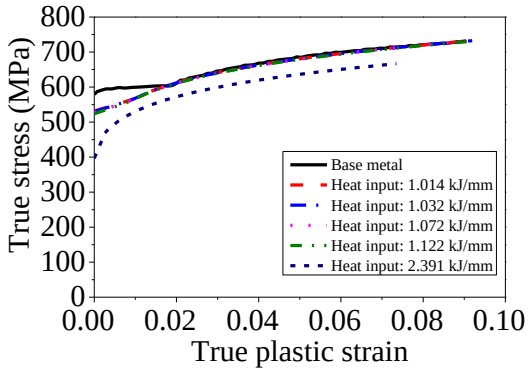

(a) HAZs for Q460 chord

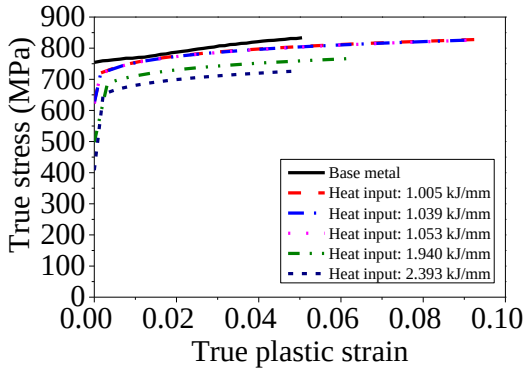

(b) HAZs for Q690 chord

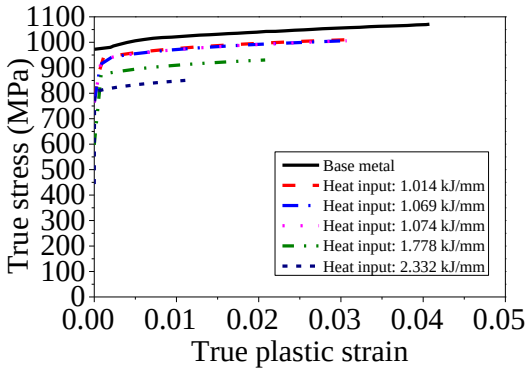

(c) HAZs for Q960 chord

Figure 7.1 True stress-plastic strain curves for chord HAZ under different heat inputs

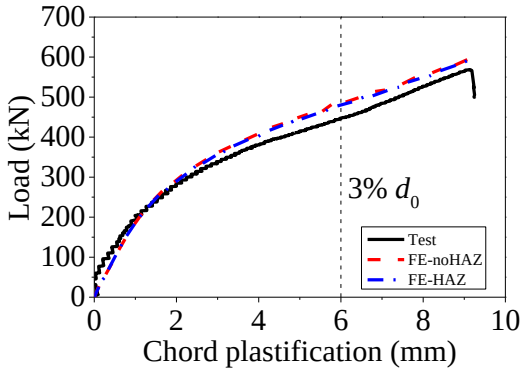

(a) 4C200x6-XT-B-Tran-0_7-M

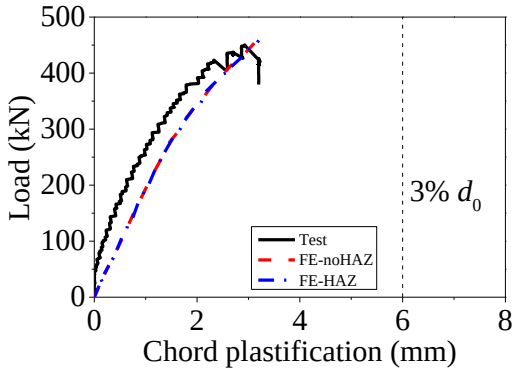

(b) 6C200x6-XT-B-Tran-0_7-M

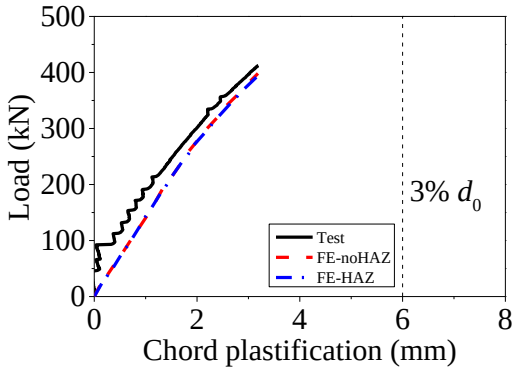

(c) 9C200x5-XT-B-Tran-0_7-M

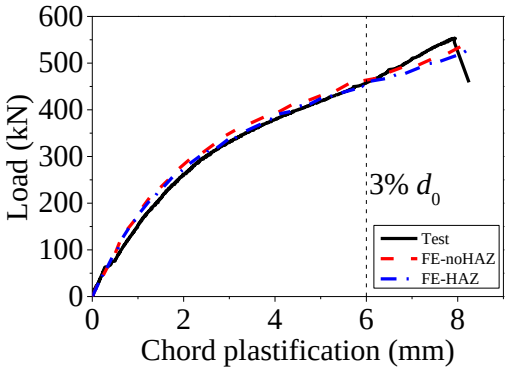

(d) 4C200x6-XT-B-Tran-0_7-H1

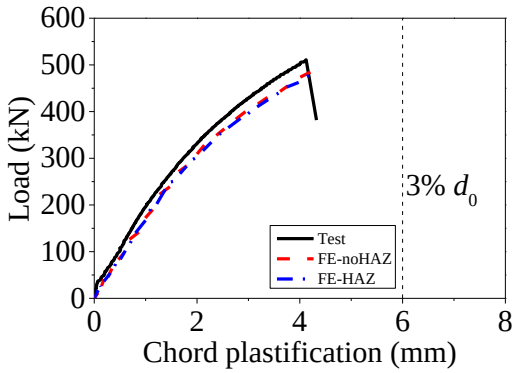

(e) 6C200x6-XT-B-Tran-0_7-H1

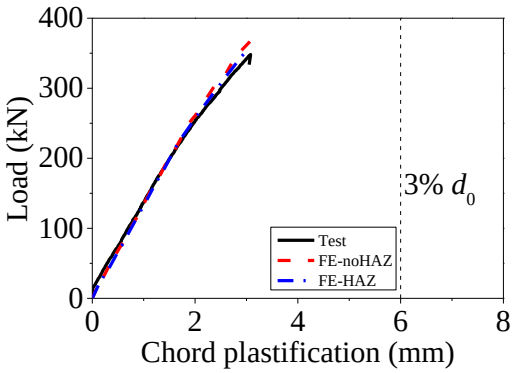

(f) 9C200x5-XT-B-Tran-0_7-H1

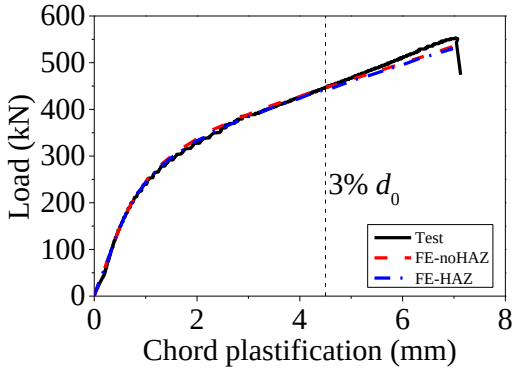

(g) 4C150x6-XT-B-Tran-0_7-M

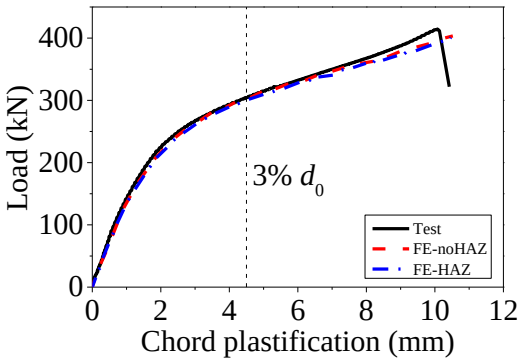

(h) 4C150x6-XT-B-Tran-0_5-M

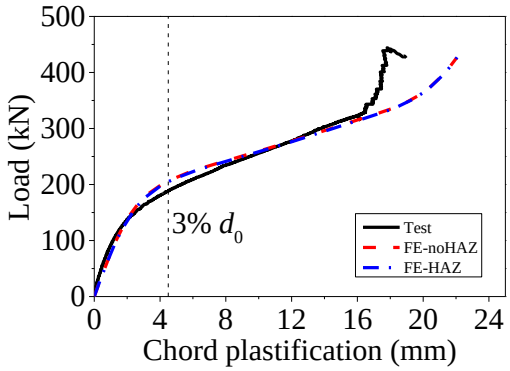

(i) 4C150x6-XT-B-Long-0_5-M

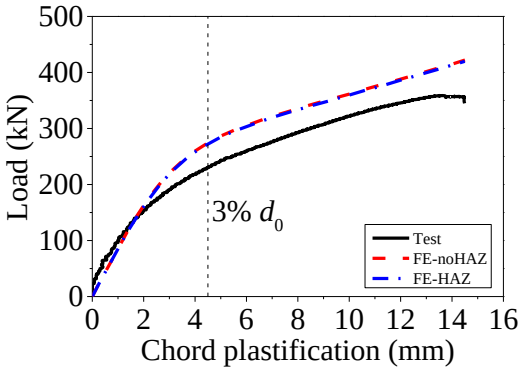

(j) 6C150x6-XT-B-Long-0_5-M

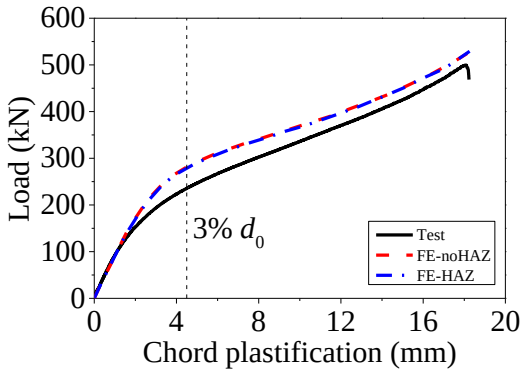

(j) 6C150x6-XT-B-Long-0_8-M

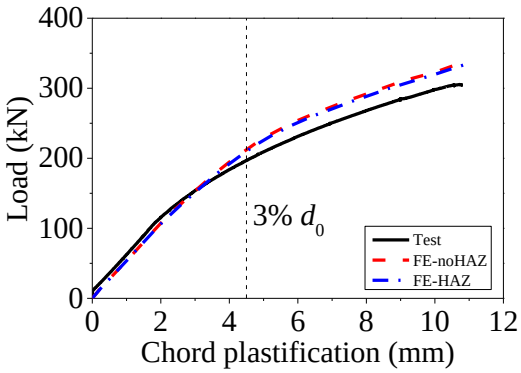

(k) 9C150x5-XT-B-Long-0_5-M

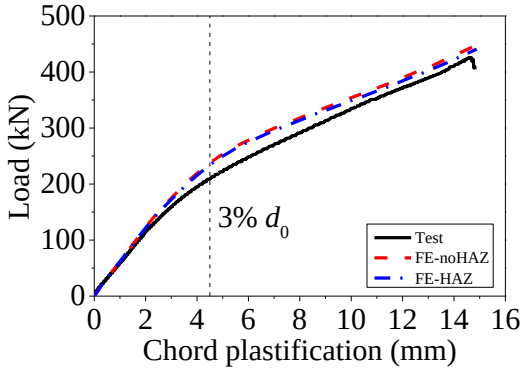

(l) 9C150x5-XT-B-Long-0_8-M

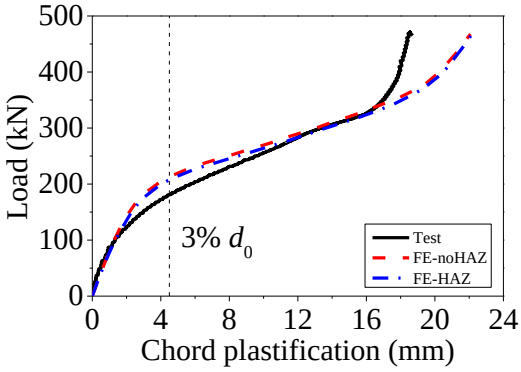

(m) 4C150x6-XT-B-Long-0_5-H1

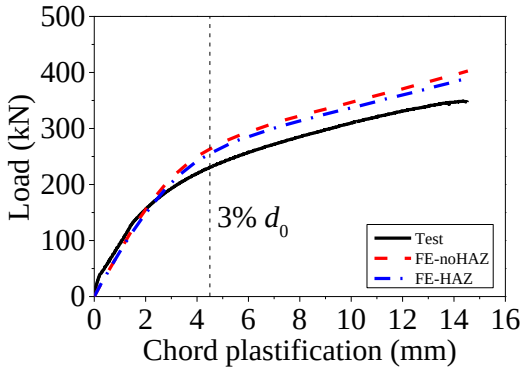

(n) 6C150x6-XT-B-Long-0_5-H1

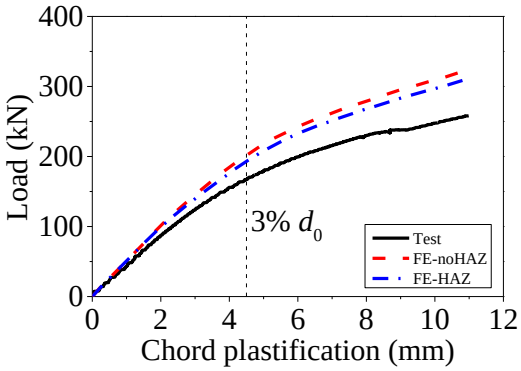

(o) 9C150x5-XT-B-Long-0_5-H1

Figure 7.2 Comparison of load-chord plastification curves between tests and simulations for all gusset plate to CHS joints

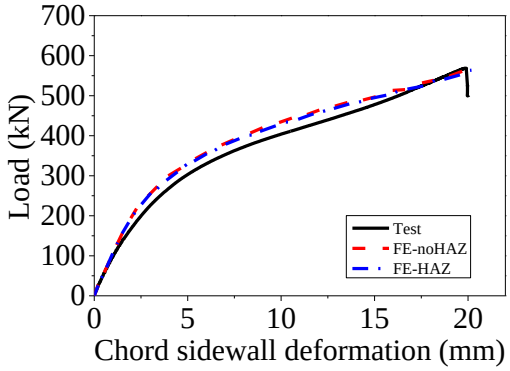

(a) 4C200x6-XT-B-Tran-0_7-M

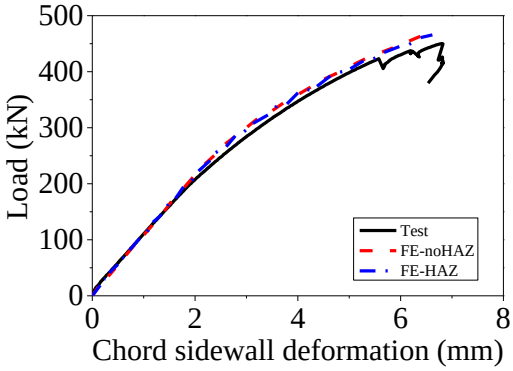

(b) 6C200x6-XT-B-Tran-0_7-M

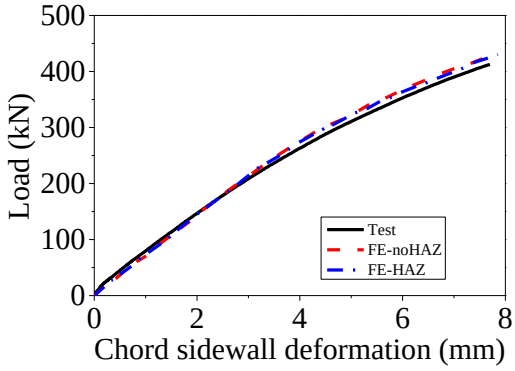

(c) 9C200x5-XT-B-Tran-0_7-M

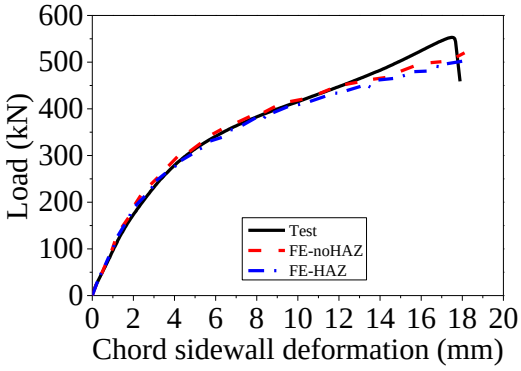

(d) 4C200x6-XT-B-Tran-0_7-H1

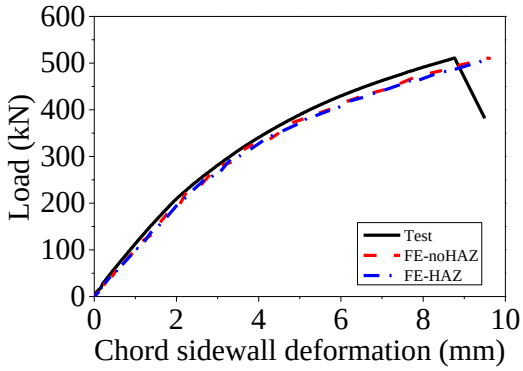

(e) 6C200x6-XT-B-Tran-0_7-H1

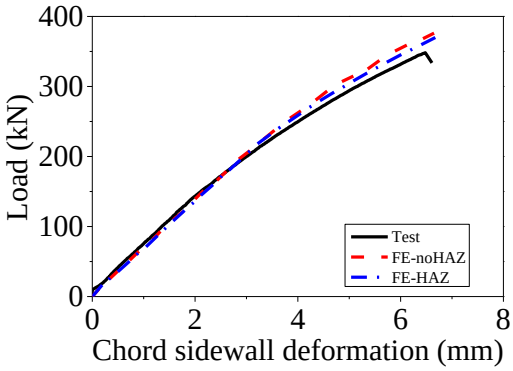

(f) 9C200x5-XT-B-Tran-0_7-H1

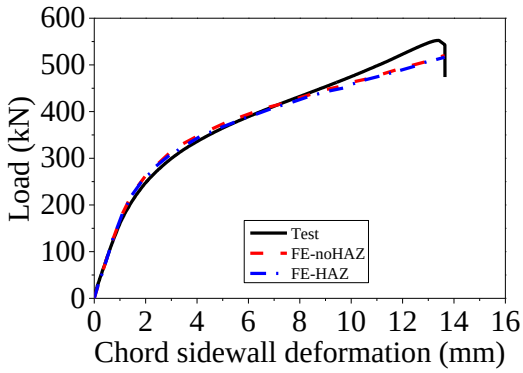

(g) 4C150x6-XT-B-Tran-0_7-M

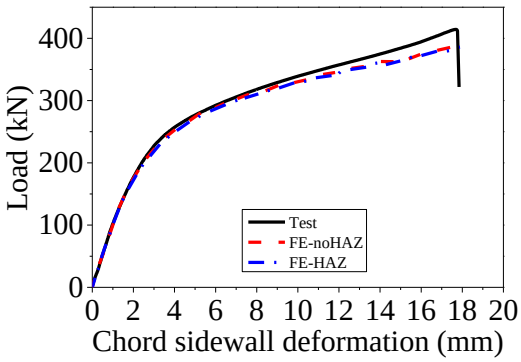

(h) 4C150x6-XT-B-Tran-0_5-M

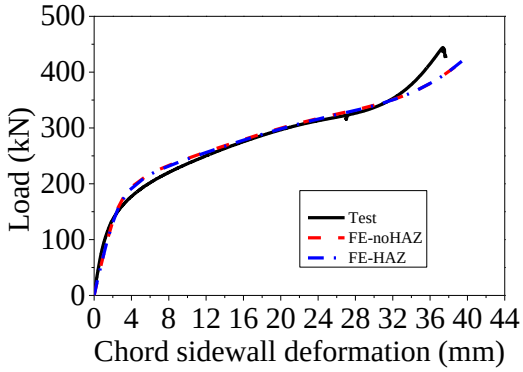

(i) 4C150x6-XT-B-Long-0_5-M

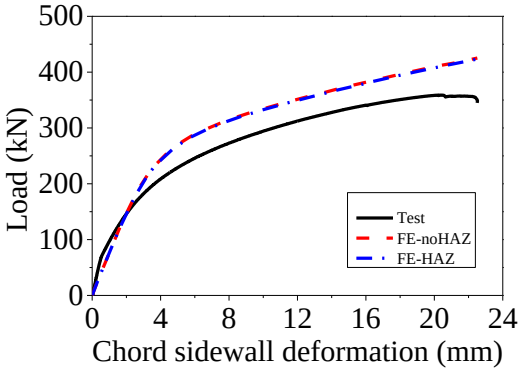

(j) 6C150x6-XT-B-Long-0_5-M

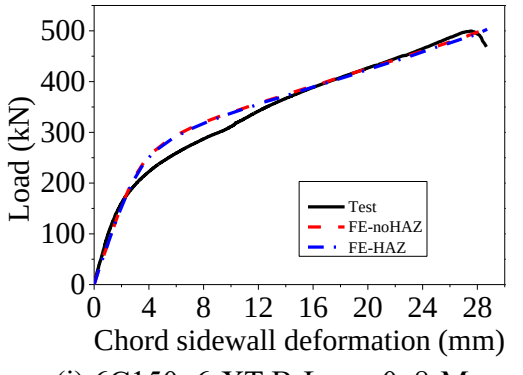

(j) 6C150x6-XT-B-Long-0_8-M

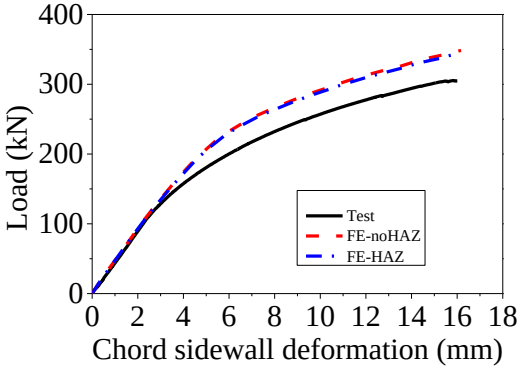

(k) 9C150x5-XT-B-Long-0_5-M

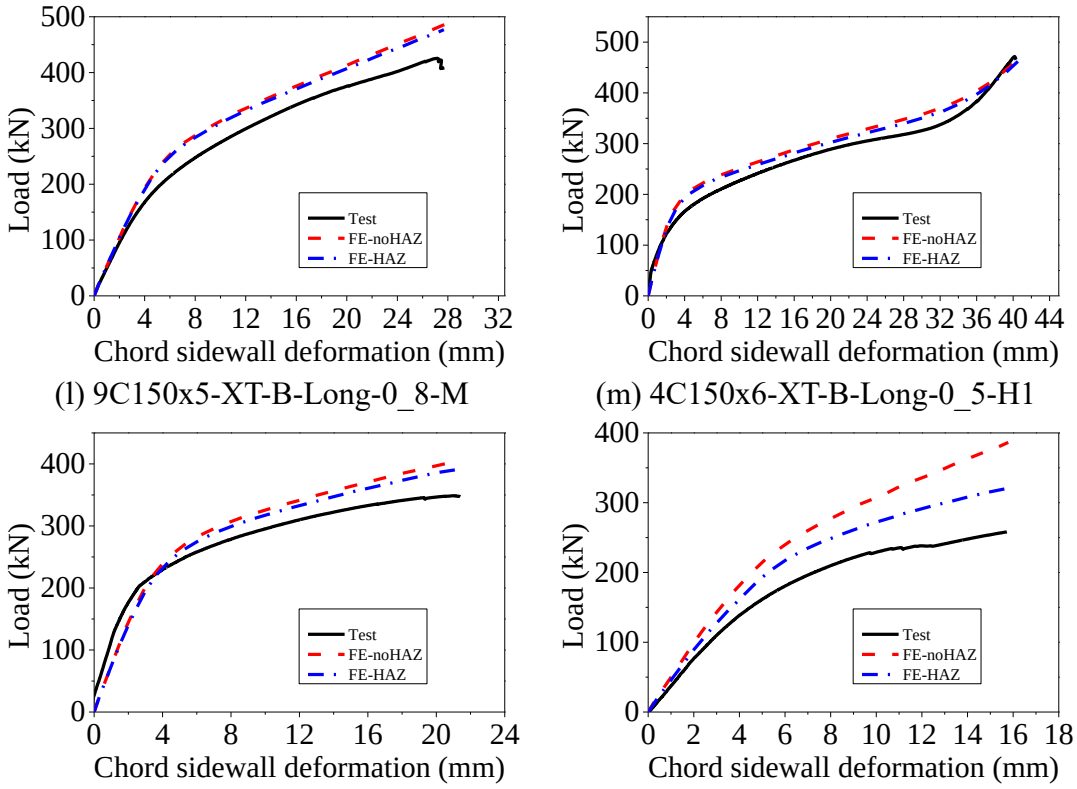

(l) 9C150x5-XT-B-Long-0_8-M (m) 4C150x6-XT-B-Long-0_5-H1

(n) 6C150x6-XT-B-Long-0_5-H1 (o) 9C150x5-XT-B-Long-0_5-H1

Figure 7.3 Comparison of load-chord sidewall deformation curves between tests and simulations for all gusset plate to CHS joints

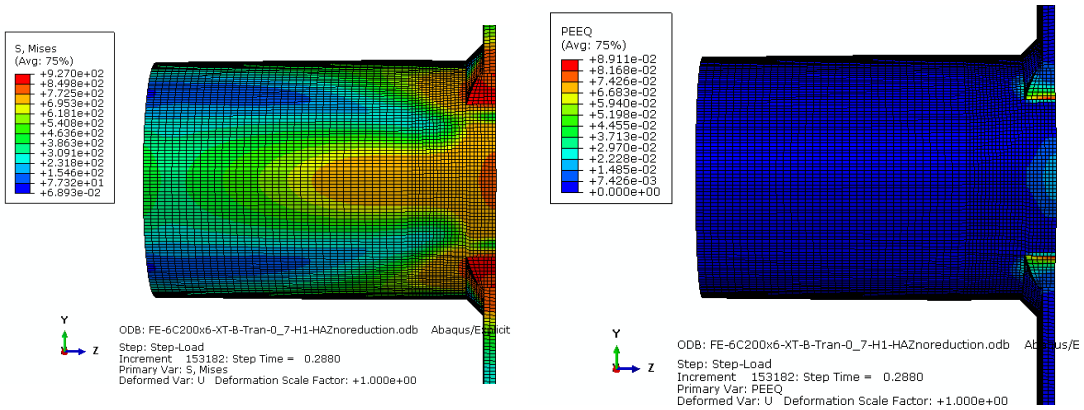

(a) Stress distribution of FE model (b) PEEQ distribution of FE model

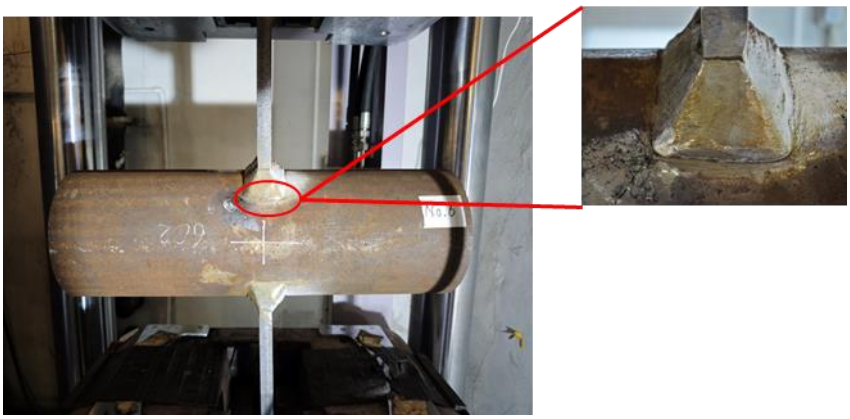

(c) Joint deformation at ultimate load

Figure 7.4 Comparison between experiments and numerical simulations for 6C200x6-XT-B-Tran-0_7-H1 at ultimate load

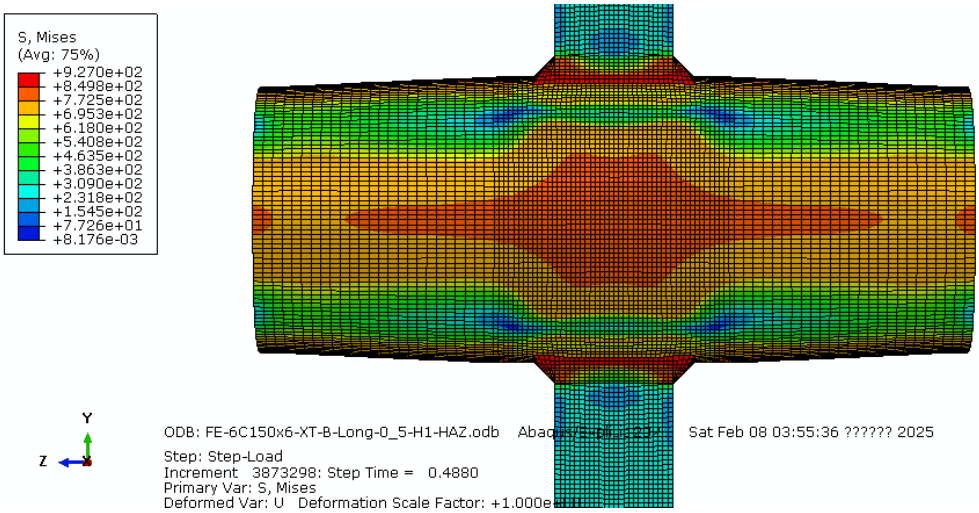

(a) Stress distribution of FE model

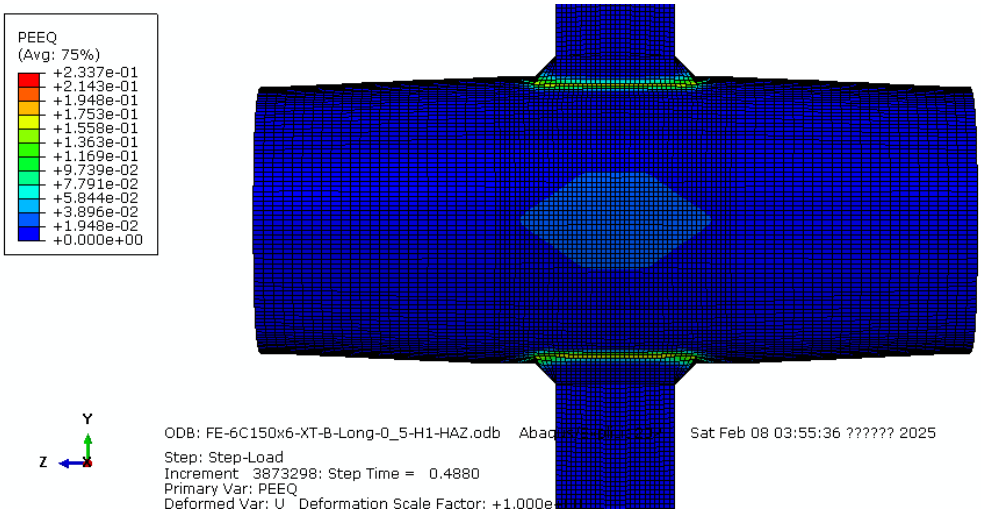

(b) PEEQ distribution of FE model

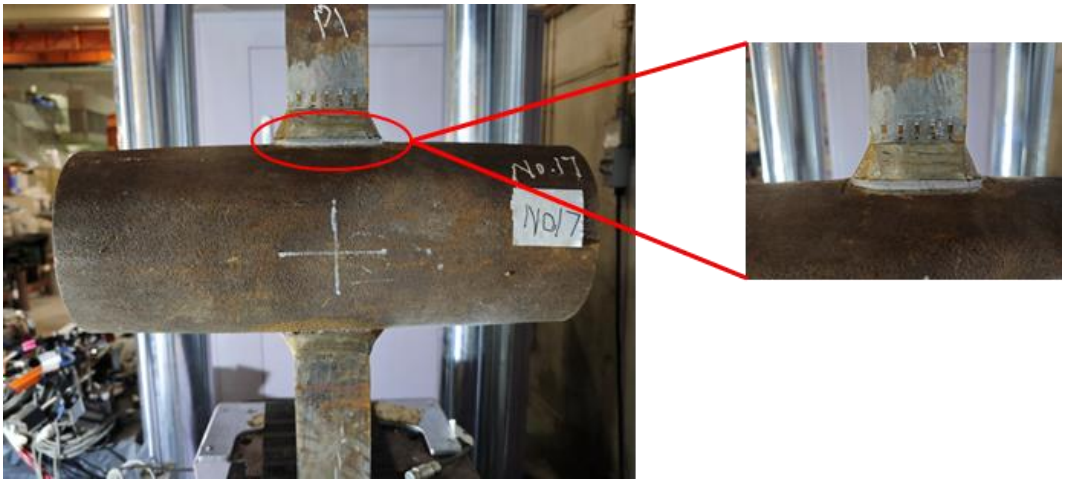

(c) Joint deformation at ultimate load

Figure 7.5 Comparison between experiments and numerical simulations for 6C150x6-XT-B-Long-0_5-H1 at ultimate load

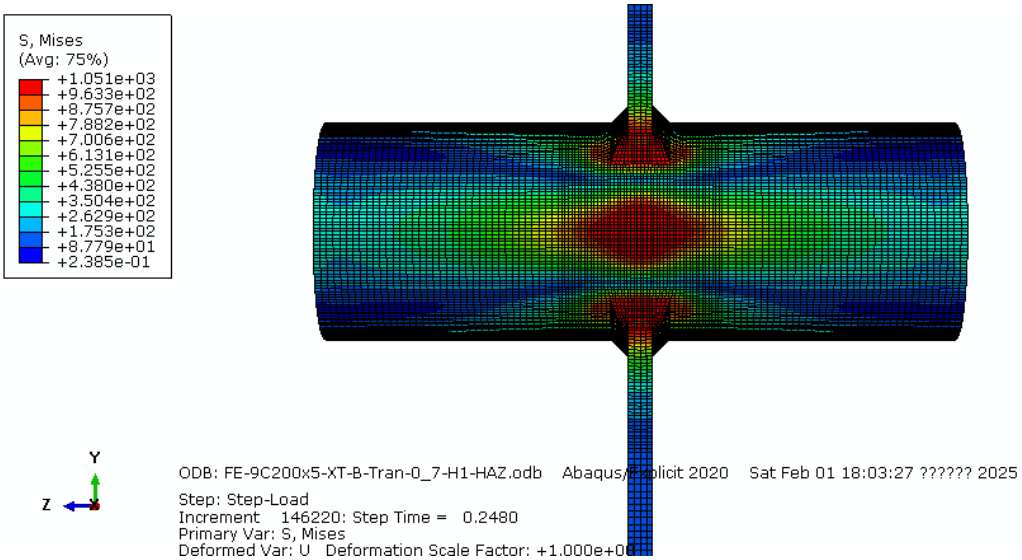

(a) Stress distribution of FE model

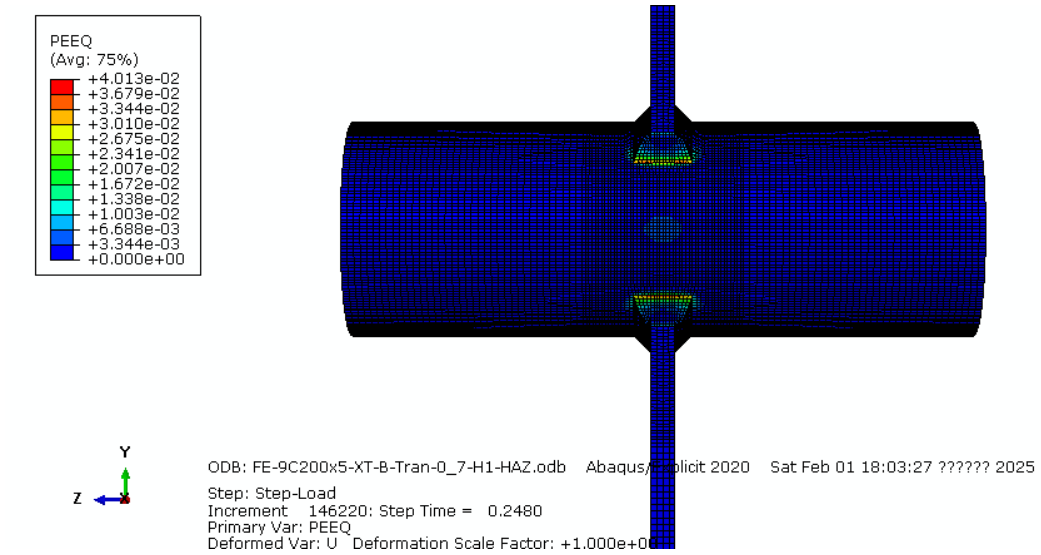

(b) PEEQ distribution of FE model

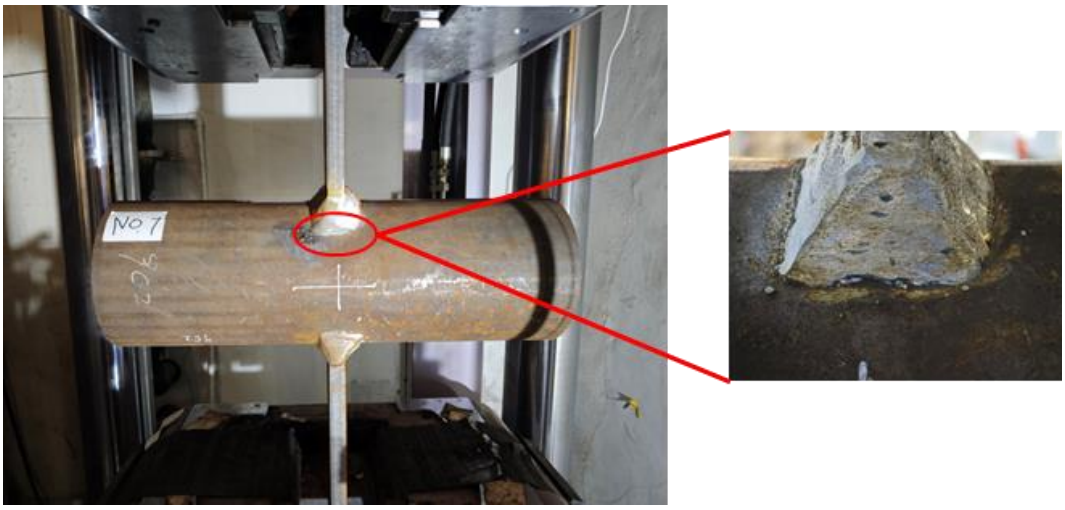

(c) Joint deformation at ultimate load

Figure 7.6 Comparison between experiments and numerical simulations for 9C200x5-XT-B-Tran-0_7-H1 at ultimate load

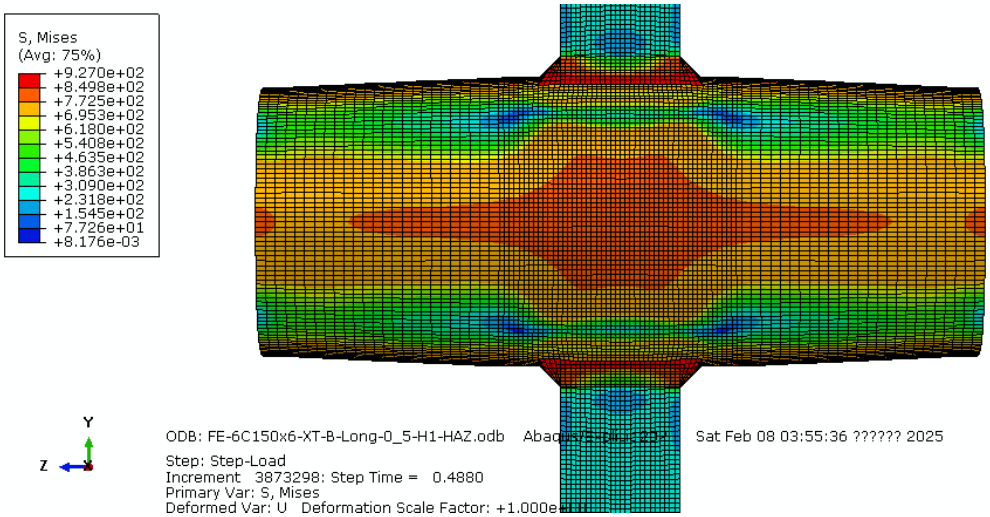

(a) Stress distribution of FE model

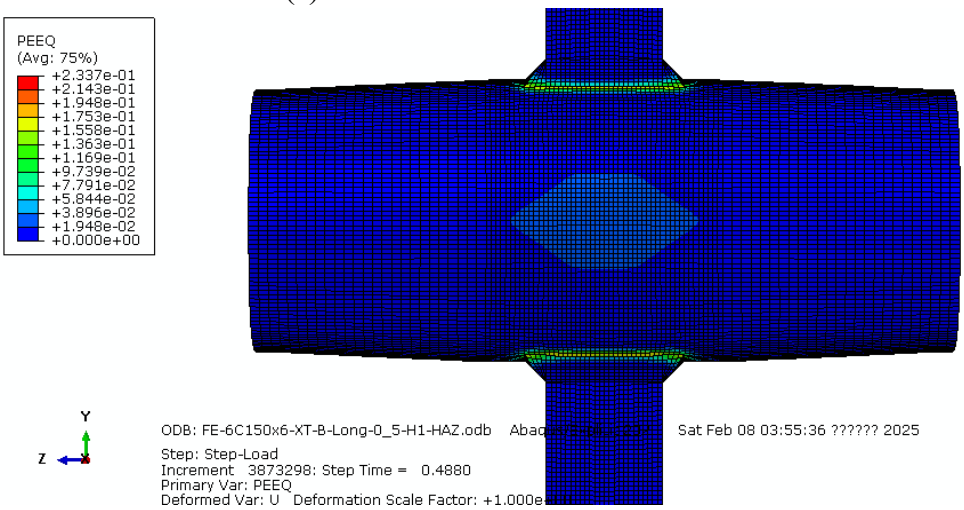

(b) PEEQ distribution of FE model

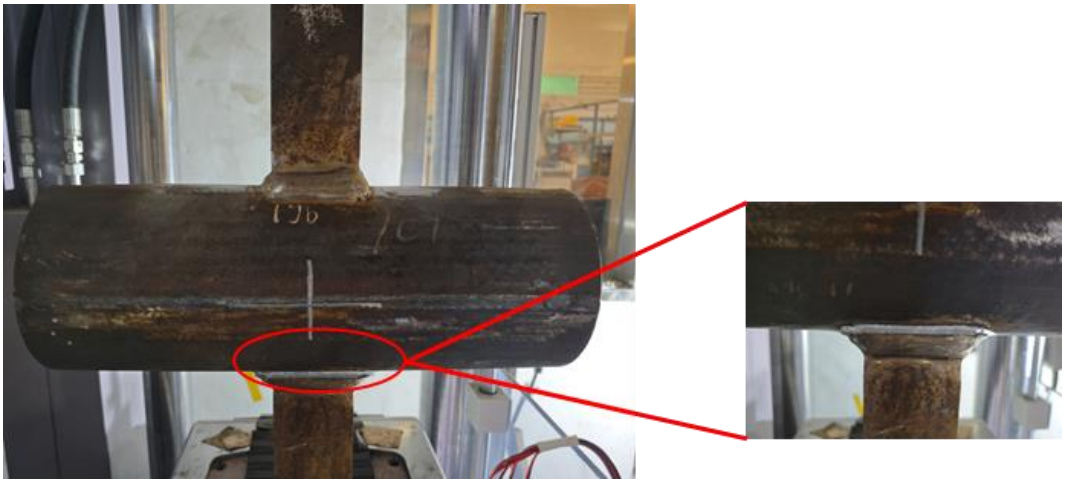

(c) Joint deformation at ultimate load

Figure 7.7 Comparison between experiments and numerical simulations for

9C150x5-XT-B-Long-0_5-M at ultimate load

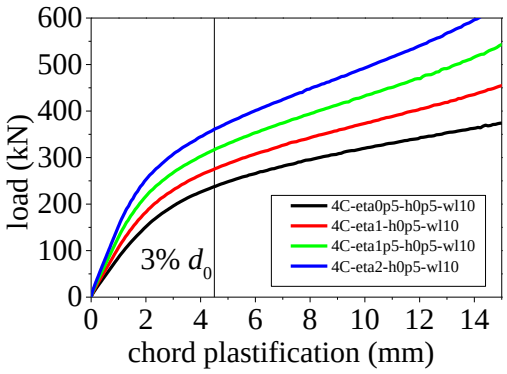

(a) Effect of η with w = 10 mm, t_1 = 20 mm and Q = 0.5 kJ/mm

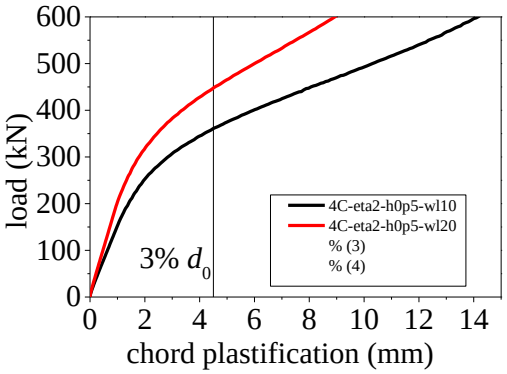

(b) Effect of w with η = 2.0, t_1 = 20 mm and Q = 0.5 kJ/mm

Figure 7.8 Influence of governing geometric parameters on the load-chord plastification curves for Q460 gusset plate to CHS X-joints under tension

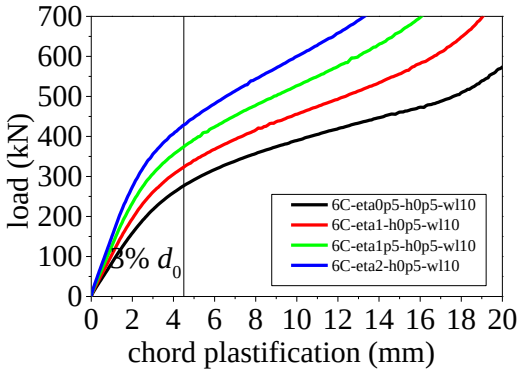

(a) Effect of η with w = 10 mm, t_1 =20 mm and Q = 0.5 kJ/mm

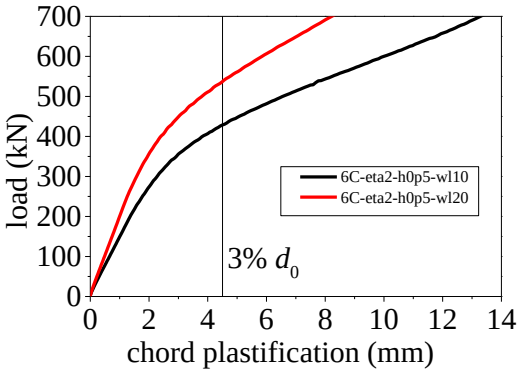

(b) Effect of w with η = 2.0, t_1 = 20 mm and Q = 0.5 kJ/mm

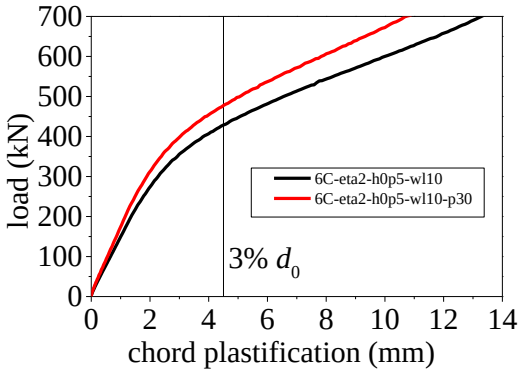

(c) Effect of t_1 with η = 2.0, w = 10 mm and Q = 0.5 kJ/mm

Figure 7.9 Influence of governing geometric parameters on the load-chord plastification curves for Q690 gusset plate to CHS X-joints under tension

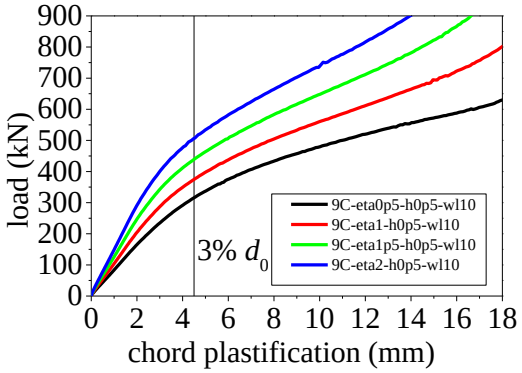

(a) Effect of η with w = 10 mm, t_1 =20 mm and Q = 0.5 kJ/mm

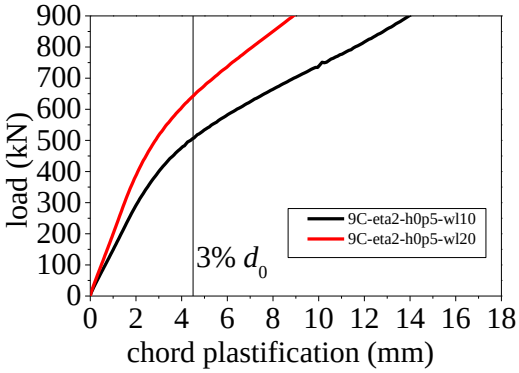

(b) Effect of w with η = 2.0, t_1 = 20 mm and Q = 0.5 kJ/mm

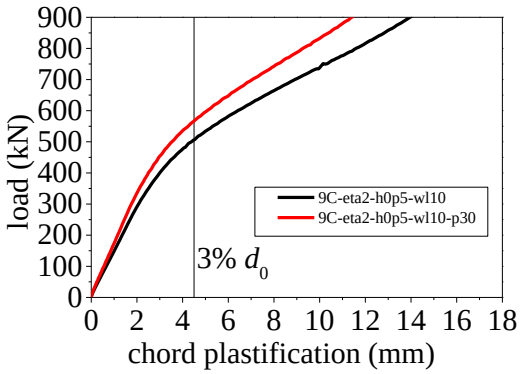

(c) Effect of t_1 with η = 2.0, w = 10 mm and Q = 0.5 kJ/mm

Figure 7.10 Influence of governing geometric parameters on the load-chord

plastification curves for Q960 gusset plate to CHS X-joints under tension

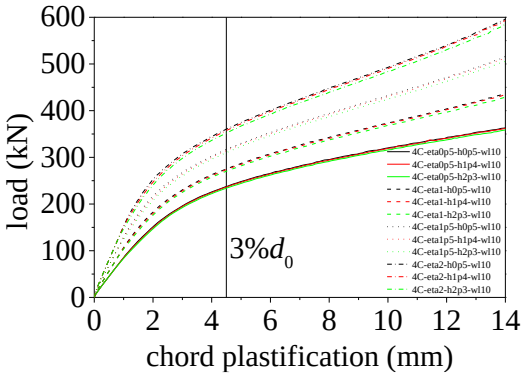

(a) Q460: Effect of Q with w = 10 mm and t_1 = 20 mm

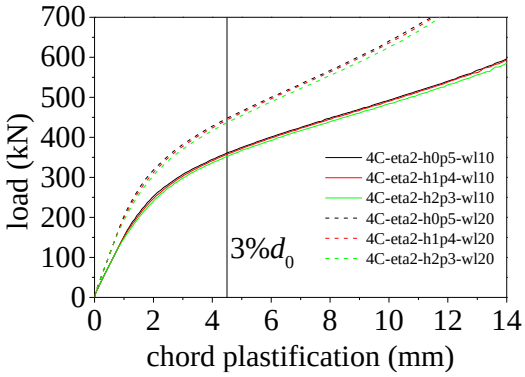

(b) Q460: Effect of Q with η = 2.0 and t_1 = 20 mm

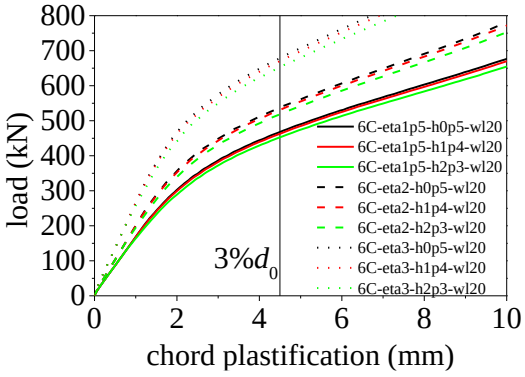

(c) Q690: Effect of Q with w = 20 mm and t_1 =20 mm

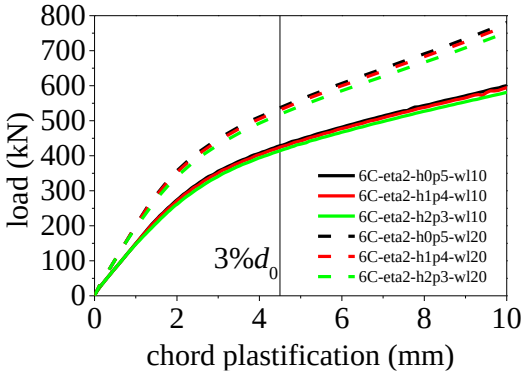

(d) Q690: Effect of Q with η = 2.0 and t_1 =20 mm

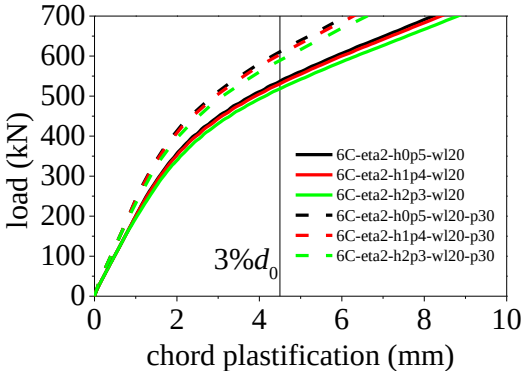

(e) Q690: Effect of Q with η = 2.0 and w = 20 mm

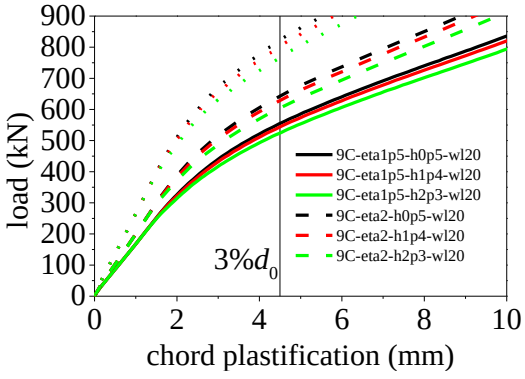

(f) Q960: Effect of Q with w = 20 mm and t_1 =20 mm

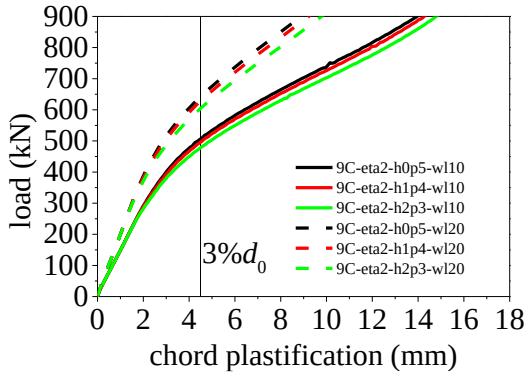

(g) Q960: Effect of Q with η = 2.0 and t_1 =20 mm

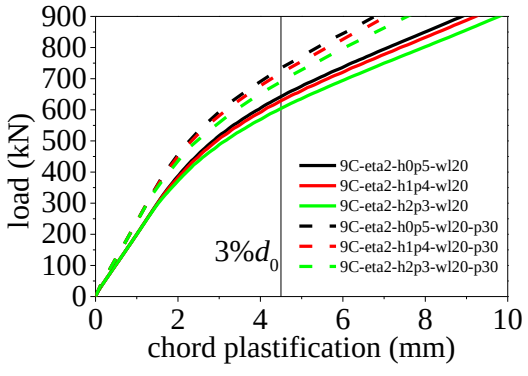

(h) Q960: Effect of Q with η = 2.0 and w = 20 mm

Figure 7.11 Influence of welding heat input on the load-chord plastification curves for HSS gusset plate to CHS X-joints under tension

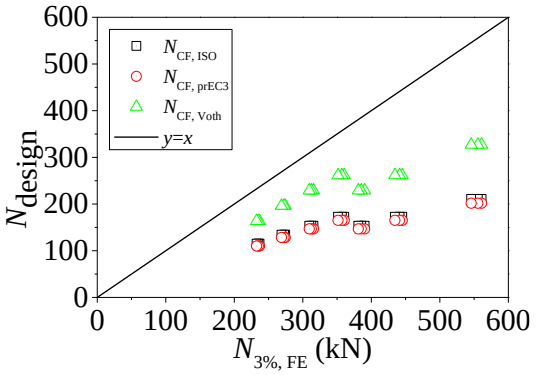

(a) Q460 without reduction factors

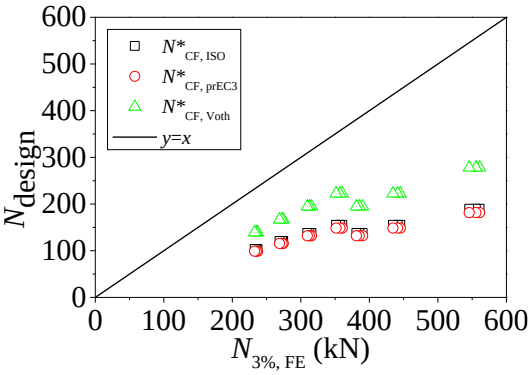

(b) Q460 with reduction factors

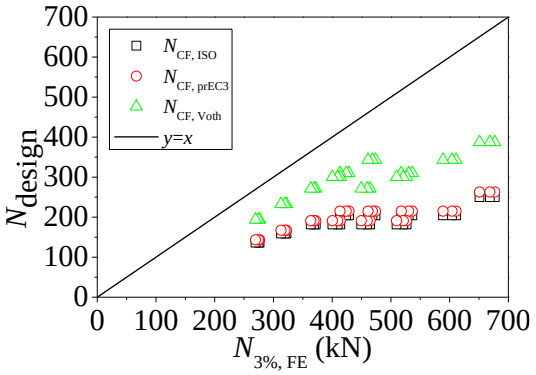

(c) Q690 without reduction factors

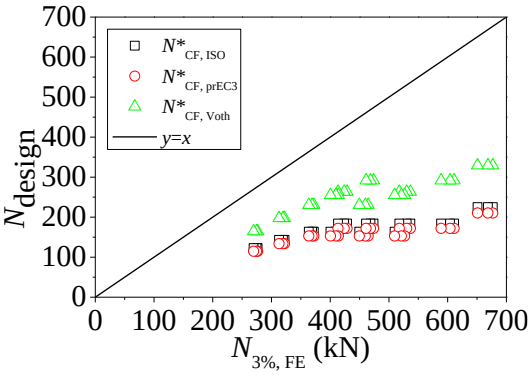

(d) Q690 with reduction factors

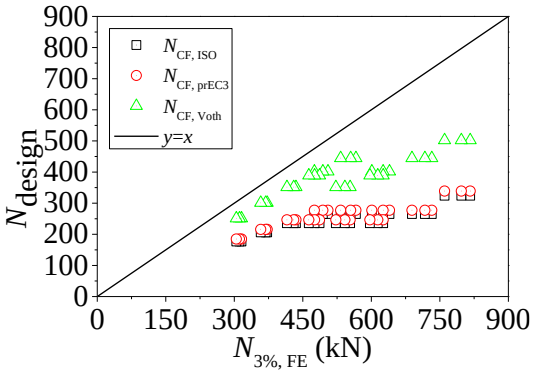

(e) Q960 without reduction factors

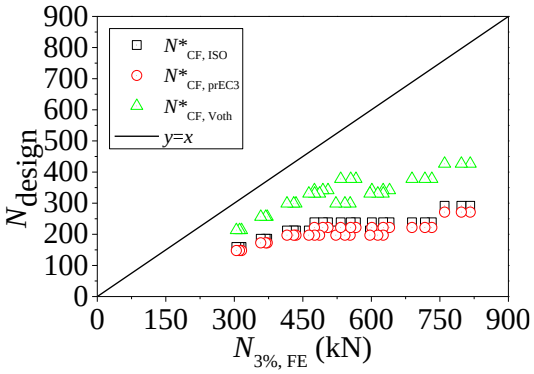

(f) Q960 with reduction factors

Figure 7.12 Comparison of joint strengths at 3% d deformation between parametric results and design equation predicting results

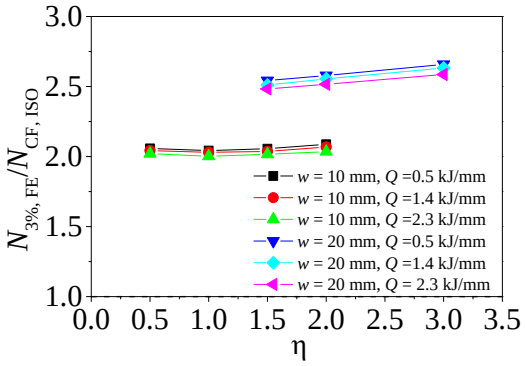

(a) ISO 14346

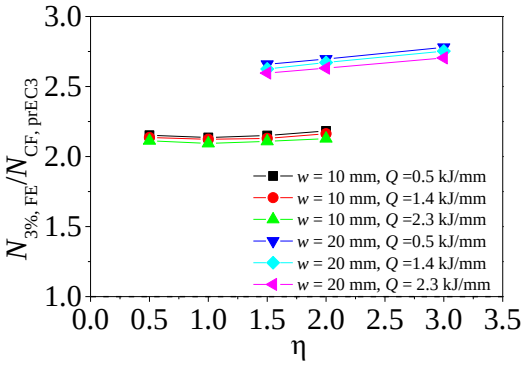

(b) prEN 1993-1-3

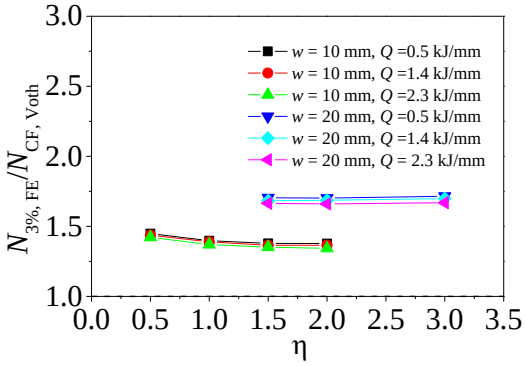

(c) Voth's design equation

Figure 7.13 Effect of critical parameters for the Q460 gusset plate to CHS X-joints under tension failed in chord plastification

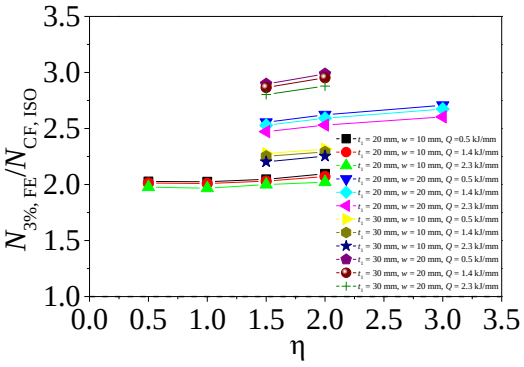

(a) ISO 14346

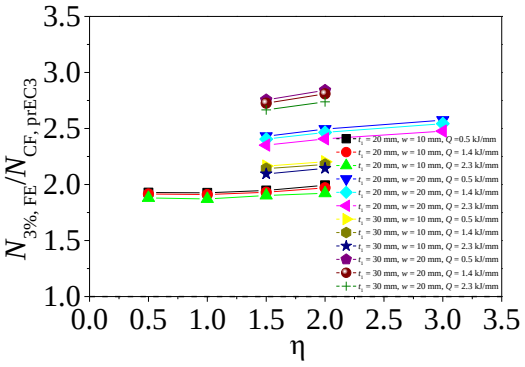

(b) prEN 1993-1-3

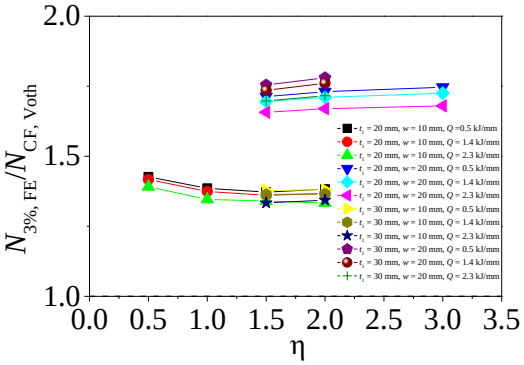

(c) Voth's design equation

Figure 7.14 Effect of critical parameters for the Q690 gusset plate to CHS X-joints under tension failed in chord plastification

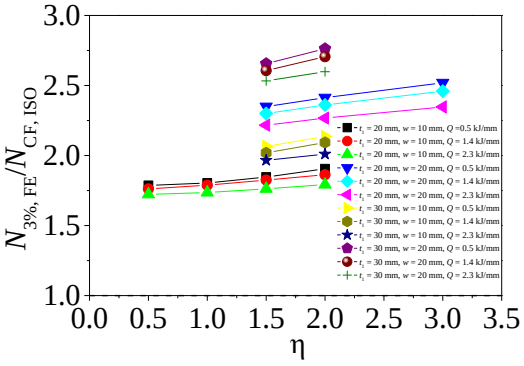

(a) ISO 14346

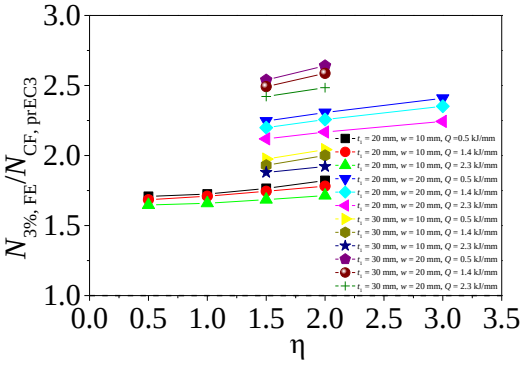

(b) prEN 1993-1-8

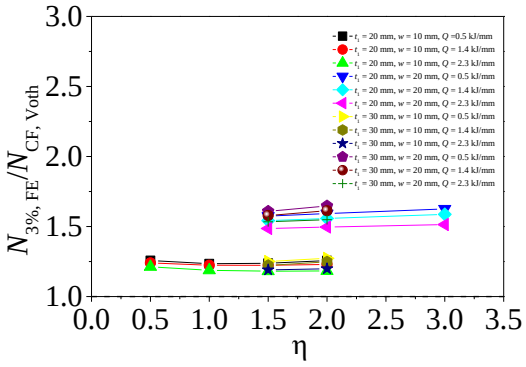

(c) Voth's design equation

Figure 7.15 Effect of critical parameters for the Q960 gusset plate to CHS X-joints under tension failed in chord plastification

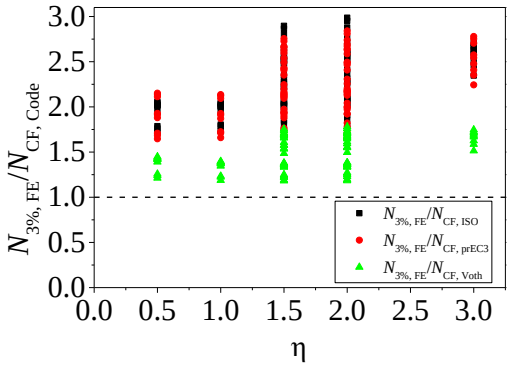

Figure 7.16 Comparison of different codes

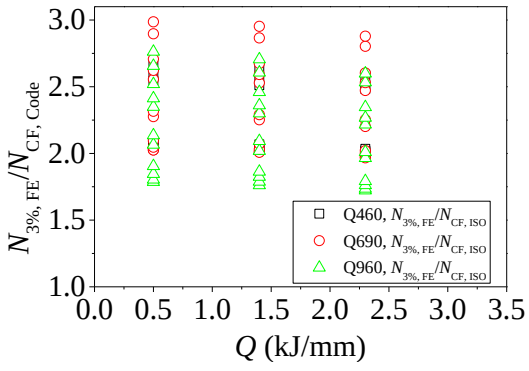

(a) ISO 14346

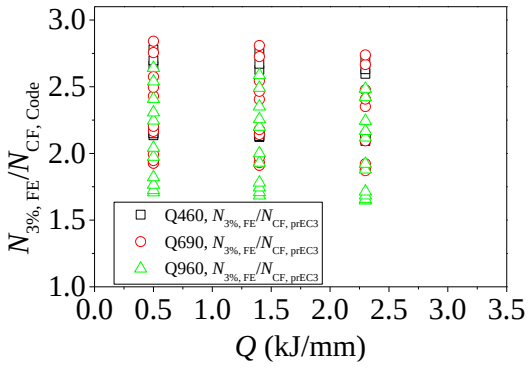

(b) prEN 1993-1-8

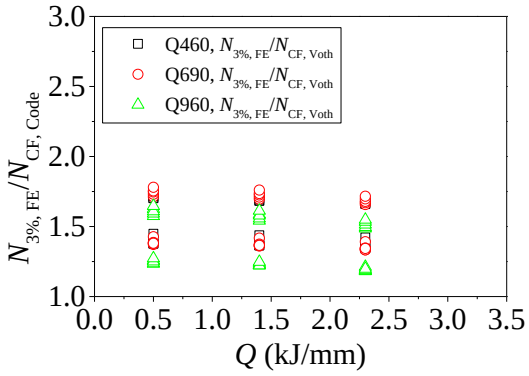

(c) Voth's design equation

Figure 7.17 Influence of Q for the HSS gusset plate to CHS X-joints under tension failed in chord plastification by different codes

Chapter 8 Conclusions

8.1 Introduction

This thesis presents the experimental and numerical investigations on the mechanical behaviours of HSS welded joints. The effect of welding on the joint behaviours was comprehensively studied. There were three kinds of HSS welded joints in this thesis, including butt-welded joints, single row T-stub joints and gusset plate to CHS X-joints. GMAW conducted by robotic arm was utilised to fabricate the Q460, Q690 and Q960 butt-welded joints with different heat inputs. Tensile coupons were cut from the butt-welded joints and tested. The hardness distributions were also obtained. The effect of heat inputs on the butt-welded tensile coupons was carefully discussion. Furthermore, the HAZ material properties were calibrated by an iterative experimental and numerical method based on the tensile coupon test results. And the polynomial regression models and linear regression models were developed respectively to predict the true stress-strain curves of HAZ.

For the single row T-stub joints, GMAW operated by two robotic arms were utilised to fabricate Q460, Q690 and Q960 specimens with three different heat inputs. Tensile tests were conducted to obtain load-displacement curves, and hardness tests were used to acquire hardness distribution along the flanges. The influences of not only heat inputs but also other parameters like end distance, steel grade and boundary condition were discussed with details. Based on the test results, current design equations were evaluated. In addition, numerical models for the tested T-stub joints were developed and validated. And a parametric study was implemented to reveal the effect of geometric dimensions (end distance and flange thickness) and welding heat inputs on the load-displacement curves for the HSS single row T-stub joints.

For the gusset plate to CHS X-joints, GMAW operated by robotic arm was utilised to

fabricate Q460, Q690 and Q960 specimens. 18 specimens in total were displacement-loaded until losing the ability to bear the load. The failure modes, load deformation curve, joint strength and deformation characteristics were carefully discussed. Based on the test specimens, FE models for the gusset plate to CHS X-joints were developed and validated. A comprehensive parametric study was conducted for the longitudinal joints. And the current design equations for the longitudinal joints were evaluated.

The following contents summarise the main conclusions of the thesis and propose the further research work.

8.2 HSS butt-welded joints

For the tested HSS butt-welded tensile coupons, there was a tendency that the fracture locations moved from the BM of the Q460, to the HAZ/BM interface of the Q690 and to the HAZ of the Q960 with the increase of steel grades from Q460 to Q960. Therefore, the influence of welding on the fracture initiation and damage evolution of the butt-welded joints got more significant for higher strength steels. The strengths of the butt-welded tensile coupons were affected by the heat input for HSS. $f_{y,\ Butt}$ decreased significantly for all the butt-welded tensile coupons regardless of the steel grades. In contrast, only for the Q960 butt-welded tensile coupons $f_{u,\ Butt}$ exhibited an obvious reduction while for the Q460 and Q690, $f_{u,\ Butt}$ remained close to $f_{u,\ BM}$. The ductility of the butt-welded tensile coupons was described by three indicators, including ε_u, elongation at fracture, and f_u/f_y. For each steel grade, ε_u and elongation at fracture showed a parabolic correlation with the heat inputs if abnormal values were excluded. Deformation characteristics of higher steel grades, for example, Q960, represented by ε_u and elongation at fracture, deteriorated more significantly under the same heat input. In addition, f_u/f_y was above 1.2 for almost all the butt-welded tensile coupons, conforming to the requirements that this ratio was recommended greater than 1.10, as listed in EN 1993-1-1.

According to the hardness test results, it was found that increasing the heat input could enlarge the HAZ widths for all steel grades. Linear regression models were developed to predict the HAZ width under specific heat input. However, the increase of heat input did not linearly related to the HAZ average hardness completely. Increasing heat input could lead to the increase of HAZ average hardness for Q460 while lead to the decrease of HAZ average hardness for Q690 and Q960 butt-welded joints. The HAZ divisions consisted of hardened zones and softened zones. For the Q460 butt-welded joints, the hardness of the hardened regions was greater than the BM hardness. But for Q690 and Q960 butt-welded joint, the hardness of the hardened part was slightly larger or close to the BM hardness.

An iterative experimental-numerical method combining with the Hollomon model was adapted to obtain the true stress-strain curves of the HAZ based on the butt-welded tensile coupon results. The HAZ material properties obtained from the method included $f_{\text{True, y, HAZ}}$, $f_{\text{True, u, HAZ}}$, K_{HAZ} and n_{HAZ}. The stress-strain curves obtained from butt-welded tensile coupons and numerical models were compared to determine these HAZ material properties. It was found that this iterative method was reliable to determine $f_{\text{True, y, HAZ}}$, $f_{\text{True, u, HAZ}}$, K_{HAZ} and n_{HAZ} for HAZ under various heat inputs and steel grades.

Based on the calibration results of HAZ material properties, two regression models were developed for $f_{\text{True, y, HAZ}}$, $f_{\text{True, u, HAZ}}$ and K_{HAZ}, one was polynomial regression model, the other was linear regression model. These two models were validated by HSS butt-welded tensile coupon tests by other researchers. The validation results exhibited that both regression models can be used to determine the HAZ material properties.

8.3 HSS single row T-stub joints

Four kinds of failure modes were observed from the HSS single row T-stub joint tests at the ultimate state: flange punching shear failure, bolt hole failure, complete yielding of flange with stripping out of nut, and a combination of bolt hole failure and weld toe cracking. Three stages were divided from the load-displacement curves: the elastic stage, plastic stage and second hardening stage. In the second hardening stage, significant membrane forces developed in the flange. The heat input could affect the joint behaviours. For the single row T-stub joints with e_1 = 80 mm, as the heat input increased, the load at the plastic stage decreased, especially for higher steel grade. For Q690 single row T-stub joints with 80 mm end distance, the failure mode switched from the bolt hole fracture to flange punching shear as the heat input increased. Besides, regardless of the steel grade and end distance, the plastic resistance decreased as the heat input increased, which may be attributed to the deterioration of HAZ. The influence of heat inputs on the ultimate loads was not consistent. It was observed that for the Q690 and Q960 single row T-stub joint, the ultimate load descended remarkably as the heat input increased.

The end distance could affect the single row T-stub joint behaviours. If the end distance increased, the failure mode tended to switch from the flange punching shear failure to bolt hole failure, especially for the Q460 and Q690 joints. For the Q960 single row T-stub joints, increasing end distance could lead to more severe cracks along the weld toe. Longer end distances could improve the initial stiffness but reduce the overall displacement of the joint. Meanwhile, reducing the end distances could enlarge the deformation ductility coefficients. In addition, increasing the end distance can enhance the plastic resistance. But for the ultimate load, the Q960 single row T-stub joint was an exception which showed higher ultimate load with shorter end distance. This phenomenon was attributed to the fact that the definition for the ultimate state was severe cracking along the weld toe for joints with e_1 = 80 mm, which neglected the

membrane action developed furthermore.

The single row T-stub joint was influenced by steel grades. The plastic resistance increased as the steel grade increased. However, under high heat inputs, the ultimate load could decrease as the steel grade increased. This fact implied that for the HSS single row T-stub joints, if the heat input was large, it would offset the advantage of HSS and cause strength degradation for the joints.

The hardness distributions of the flange of the single row T-stub joints within HAZ was not uniform. HAZ widths and average HAZ hardness were calculated based on the hardness distributions. Regression models were developed which could be utilised to predict the HAZ width based on the heat inputs. However, the HAZ average hardness did not completely reduce as the heat input increased, since for Q460, as the heat inputs increased, the average HAZ hardness increased.

The design equations in EN 1993-1-8 (CEN, 2005a) were introduced and evaluated. It was found that EN 1993-1-8 (CEN, 2005a) could give conservative predictions of both plastic resistance and ultimate resistance, because all the $F_{p,\,test}/\ F_{p,\,EC3}$ and $F_{u,\,test}/\ F_{u,\,EC3}$ were greater than unity. With the increase of heat inputs, the degree of underestimation for $F_{p,\,test}/\ F_{p,\,EC3}$ was reduced. This is because the $F_{p,\,test}$ dropped as the heat input increased. Besides, for the single row T-stub joints with higher steel grades but the same end distance, $F_{p,\,test}/\ F_{p,\,EC3}$ dropped under the same heat input level. Particularly, for the Q960 single row T-stub joint, $F_{p,\,test}/\ F_{p,\,EC3}$ was close to 1. In contrast, $F_{u,test}\ /\ F_{u,\,EC3}$ was much greater than unity, leading to a great conservative strength prediction for the ultimate load. This conservativeness was caused by the fact that design equations in EN 1993-1-8 (CEN, 2005a) are not applicable for the T-stub joint under large deformation, in which material strain hardening and membrane action were neglected.

A parametric study was conducted to reveal the effect of geometric dimensions (end distance and flange thickness) and welding heat inputs on the load-displacement curves for the HSS single row T-stub joints. It was found that for Q460 single row T-stub joints, the load-displacement curves were not significantly affected by varying heat inputs under the same end distance and flange thickness. For Q690 and Q960 single row T-stub joints, however, increasing heat inputs could decrease the plastic stage, as the plastic stage initiated when the flange near weld toe yielded where the HAZ existed. Furthermore, as the end distances increased, the degree of plastic stage degradation were reduced.

8.4 HSS gusset plate to CHS X-joints

A total of 18 HSS gusset plate to CHS X-joints were fabricated and tested by various steel grades including Q460, Q690 and Q960. According to the 3% d_0 deformation limit, most specimens failed by chord face failure. However, 6C200x6-XT-B-Tran-0_7-M, 9C200x5-XT-B-Tran-0_7-M, 6C200x6-XT-B-Tran-0_7-H1 and 9C200x5-XT-B-Tran-0_7-H1 failed before reaching to 3% d_0 deformation, known as chord punching shear failure. This fact proved that for HSS transverse plate to CHS X-joint under tension, the strength control could also determine the joint strength.

For the HSS gusset plate to CHS X-joints, the steel grades, heat inputs and geometric parameters can affect the joint strengths. The loads at 3% d_0 deformation enhanced with the increase of the steel grade since the higher steel grade could exhibit the longer elastic stage. In contrast, the peak loads corresponding to chord punching shear did not linearly increase as the steel grades increased, as the peak loads of the Q460 gusset plate to CHS joints were greater than that of the Q690 joints with the same configurations. On the one hand, the Q460 steel experienced less HAZ deterioration than the Q690 steel. On

the other hand, the Q460 joints could have the second hardening stage which improved the peak loads. Besides, the effect of heat inputs on the peak loads became significant when the steel grade increased to Q960, as a result of severe HAZ material deterioration caused by welding. As for the geometric parameters, β, η and γ all had effects on the joint strengths. Particularly, the Q460 transverse plate to CHS X-joint had longer elastic stage, larger stiffness, higher load at 3% d_0 deformation but reduced ductility compared to the Q460 longitudinal counterpart. However, the peak loads of both joints were approximate.

The ductility of the HSS gusset plate to CHS X-joints was influenced by the steel grade, heat input and geometric parameters. The ductility was represented by D_2/D_1 according to a bi-linear model. The larger the value was the better the ductility was. The ductility declined as the steel grades increased for both transverse and longitudinal joints. The influence of heat input, however, was obscure regardless of the plate skew angle: for the Q460 and Q960 joints, the ductility was reduced by enlarging the heat input; while for the Q690 joints, the ductility was enhanced as the heat input increased. As for the geometric parameters, β, γ, and η could all affect the joint ductility. Specially, the influence of the plate skew angle was quite mild as the skew angle increased from 0° to 90°, the D_2/D_1 of Q460 plate to CHS X-joints only reduced slightly from 3.886 to 3.639.

The plate surface stress distributions could indicate the position where the chord punching shear initiated. The plate surface stresses near the brace plate edge were usually higher than those in the plate centre under large load levels, therefore inducing the crack initiation at the chord saddle for the transverse joints and at the chord crown for the longitudinal joints due to the stress concentration.

The test strengths were compared with the design methods recommended by ISO 14346,

prEN 1993-1-8 and Voth. These design methods usually underestimated the load at 3% d_0 deformation for the HSS gusset plate to CHS X-joints without and with reduction factors. Therefore, incorporating the reduction factor was not necessary when calculating $N_{3\%}$. The mean values of the ratios between $N_{3\%}$ and the predicted load by the Voth's method were closest to unity and had small coefficient of variation (COV), which proved that considering the effect of plate thickness could improve the joint strength predictions. Besides, the design methods were not accurate and reliable when predicting the load corresponding to chord punching shear, because for some transverse joints failed by punching shear, the loads could be overestimated up to 30%. Finally, the COVs of the joints under higher heat input were greater that the counterpart under lower heat input. Therefore, the effect of the heat inputs should also be incorporated when designing the HSS gusset plate to CHS X-joints subjected to tension.

Apart from the experimental work, numerical simulations were conducted for the tested specimens. For each simulated gusset plate to CHS X-joints under axial tension, both the load-chord plastification curve and load-chord side wall deformation curve agreed well with the test curves. Besides, the experimental and numerical results of 6C200x6-XT-B-Tran-0_7-H1, 9C200x5-XT-B-Tran-0_7-H1, 6C150x6-XT-B-Long-0_5-H1 and 9C150x5-XT-B-Long-0_5-M at ultimate load were compared. The stress distribution, PEEQ distribution and joint deformation at the ultimate load all indicated that the numerical models could reproduce the joint behaviours of the test specimens. Therefore, the numerical models were validated and could be used for further parametric study.

The effect of HAZ on the tested gusset plate to CHS X-joints under tension was investigated by numerical simulations. It can be found that the joint initial stiffness was not affected by HAZ, because the Young's modulus of HAZ remained unchanged compared to BM. Therefore, the joint initial stiffness was only affected by its geometric dimensions. For the HSS transverse gusset plate to CHS X-joints under tension in this

experimental programme, the effect of HAZ was neglectable. In contrast, if the heat input was as high as 2.3 kJ/mm and high steel grades like Q690 and Q960 were adapted for the HSS longitudinal gusset plate to CHS X-joints under tension, the load-chord plastification curves were obviously affected by HAZ. The influence of HAZ on the joint strengths corresponding to 3% d deformation was existent but not significant unless the heat input was increased to 2.3 kJ/mm.

A comprehensive parametric study was implemented for the longitudinal HSS gusset plate to CHS X-joints. It showed that for all steel grades, increasing η, w and t_1 could improve the initial stiffness and joint strength corresponding to 3% d deformation. The influence of Q was illustrated as follows: for the Q460 joints, varying Q almost had no effect on the load-chord deformation curves; in contrast, as η increased, the load-chord plastification curves of Q690 and Q960 degraded. Furthermore, the higher Q was, the more degradation it was. Similarly, the effect of HAZ on the load-chord plastification curves enhanced with increasing w and t_1.

The design methods of the joint strengths corresponding to 3% d_0 were evaluated for the HSS longitudinal gusset plate to CHS X-joints under tension. These design methods included ISO 14346, prEN 1993-1-8 and design equations proposed by Voth. For all the design methods, the predicted joint strengths at 3% d_0 deformation were conservatively underestimated compared to the parametric counterparts with or without reduction factors. Besides, the effect of critical parameters on the values of $N_{3\%,\ FE}/N_{CF,\ code}$ was investigated. In ISO 14346 and prEN 1993-1-8, the weld leg size was not included into the design equations, thus the conservativeness which represented by the value of $N_{3\%,\ FE}/N_{CF,\ code}$ increased when w increased. In the design equations proposed by Voth, since the weld leg size effect was incorporated, the conservativeness was less significant.

8.5 Future works

Through extensive experimental and numerical investigations of three HSS welded joints, this thesis still has following limitations. First, the Hollomon model is applicable for the true stress-strain curve before necking. For the stress-strain curve after necking, the model to describe the relationship is not considered into this study. Second, the numerical models of butt-welded joints, T-stub joints and gusset plate to CHS X-joints did not incorporate the fracture initiation and damage evolution of the steel and corresponding HAZ. This neglection caused the deviations between test and FE results. Third, the design methods for the T-stub joint and gusset plate to CHS X-joint were only evaluated.

Based on these limitations, following suggestions on the future works are demonstrated.

Hollomon model is used to describe the true stress-strain curves of steel. Based on the HSS butt-welded tensile coupons, this thesis calibrated the HAZ material properties based on the Hollomon model. There are also other models to describe the true stress-strain curve, like Ramberg-Osgood model. The parameters of these models can be calibrated for HAZ based on the butt-welded tensile coupons, and the applicability of these models for HAZ should be investigated. Besides, the Hollomon model is only applicable for the part of true stress-strain curve before tensile coupon necking. For the true stress-strain curve of HAZ after necking, further research is imperatively needed.

All the butt-welded tensile coupons fractured at the end of tests. Since HSS structures are subjected to potential extreme loads which may lead to the fracture of HSS, like earthquake, explosion and vehicle impact, it is necessary to illustrate the fracture mechanism of welded HSS under different welding parameters. The fracture initiation and damage evolution of the HAZ under different heat inputs should be studied as it can form the basis for the further fracture-related research for HSS.

In this thesis, the design equations for HSS single row T-stub joint in EN 1993-1-8 were introduced and evaluated. However, there are still other design methods for this joint, like Piluso model, Faralli model and Tartaglia model. The applicability of these models should be further checked. Numerical models considering HAZ fracture under different welding parameters should also be developed for single row T-stub joints. Then a comprehensive parametric investigation considering fracture of T-stub joint can be implemented. The EN 1993-1-8 does not provide an accurate design method for the ultimate load. Design methods for the ultimate load of single row T-stub joint should also be proposed, as the single row T-stub joint may enter second hardening stage under extreme loads.

In this thesis, the HSS longitudinal gusset plate to CHS X-joints were deformation controlled when determining the joint strength. Therefore, fracture initiation and damage evolution were not included into the parametric investigations for this kind of joint. But for the HSS transverse gusset plate to CHS X-joints, the joint strength can be determined before reaching to the deformation limit. Consequently, the numerical models of this joint should incorporate the fracture initiation and damage evolution of HAZ. Research on this question that developing reliable tubular joint models considering HAZ fracture is still quite limited. The design methods of chord punching shear failure for both the transverse and longitudinal gusset plate to CHS X-joints will be proposed only when the corresponding comprehensive parametric study is finished.

References

AFKHAMI, S., BJöRK, T. & LARKIOLA, J. 2019. Weldability of cold-formed high strength and ultra-high strength steels. *Journal of Constructional Steel Research,* 158**,** 86-98.

AFKHAMI, S., JAVAHERI, V., AMRAEI, M., SKRIKO, T., PIILI, H., ZHAO, X.-L. & BJöRK, T. 2022a. Thermomechanical simulation of the heat-affected zones in welded ultra-high strength steels: Microstructure and mechanical properties. *Materials & Design,* 213.

AFKHAMI, S., JAVAHERI, V., AMRAEI, M., SKRIKO, T., PIILI, H., ZHAO, X.-L. & BJöRK, T. 2022b. Thermomechanical simulation of the heat-affected zones in welded ultra-high strength steels: Microstructure and mechanical properties. *Materials & Design,* 213**,** 110336.

AMRAEI, M., AFKHAMI, S., JAVAHERI, V., LARKIOLA, J., SKRIKO, T., BJöRK, T. & ZHAO, X.-L. 2020. Mechanical properties and microstructural evaluation of the heat-affected zone in ultra-high strength steels. *Thin-Walled Structures,* 157.

AMRAEI, M., AHOLA, A., AFKHAMI, S., BJöRK, T., HEIDARPOUR, A. & ZHAO, X.-L. 2019. Effects of heat input on the mechanical properties of butt-welded high and ultra-high strength steels. *Engineering Structures,* 198.

AMRAEI, M., SKRIKO, T., BJöRK, T. & ZHAO, X.-L. 2016. Plastic strain characteristics of butt-welded ultra-high strength steel (UHSS). *Thin-Walled Structures,* 109**,** 227-241.

AWS 2005. AWS A5.28/A5.28M: Specification for Low-Alloy Steel Electrodes and Rods for Gas Shielded Arc Welding. *Miami, Florida, USA: American Welding Society*.

AWS 2015. AWS D1.1/D1.1M: Structural Welding Code - Steel.

BALOGH, A., KIRK, S. & GöRBE, Z. 1999. Role of cooling time when steels to be welded requires controlled heat input. *GÉP, L. évfolyam***,** 44-50.

BHADESHIA, H. & HONEYCOMBE, R. 2017. *Steels: microstructure and properties*,

Butterworth-Heinemann.

CAI, W.-Y., WANG, Y.-B. & LI, G.-Q. 2022a. Experimental and numerical study on strength of high-strength steel double-V butt-welded joint. *Journal of Constructional Steel Research,* 196.

CAI, Y., CHAN, T.-M. & YOUNG, B. 2022b. Strength predictions of circular hollow section T-joints of steel grade 1100 MPa. *Journal of Constructional Steel Research,* 188.

CEN 2000. CR ISO 15608: Welding - Guidelines for a metallic material grouping system. *European Committe For Standardization*.

CEN 2001. EN 1011-2: Welding — Recommendations for welding of metallic materials, Part 2: Arc welding of ferritic steels. *European Committe For Standardization*.

CEN 2005a. Eurocode 3: Design of Steel Structures, Part 1-8: Design of Joints. *Brussels: European Committee for Standardization*.

CEN 2005b. Eurocode 3: Design of steel structures, Part 1–1: General rules and rules for buildings. *Brussels: European Committee for Standardization*.

CEN 2007. Eurocode 3: Design of steel structures, Part 1-12: Additional rules for the extension of EN 1993 up to steel grades S700. *Brussels: European Committee for Standardization*.

CEN 2024a. Eurocode 3 - Design of steel structures - Part 1-8: Joints. *Brussels: European Committee for Standardization*.

CEN 2024b. Eurocode 3: Design of Steel Structures, Part 1-8: Design of Joints. *Brussels: European Committee for Standardization*.

CHEN, C. 2019. *influence of welding on high strength steel butt joints* PhD, Nanyang Technological University.

CHEN, C., CHIEW, S.-P., ZHAO, M.-S., LEE, C.-K. & FUNG, T.-C. 2019. Welding effect on tensile strength of grade S690Q steel butt joint. *Journal of Constructional Steel Research,* 153**,** 153-168.

CHEN, C., ZHANG, X., ZHAO, M., LEE, C.-K., FUNG, T.-C. & CHIEW, S.-P. 2017. Effects of Welding on the Tensile Performance of High Strength Steel T-stub Joints.

Structures, 9**,** 70-78.

CHEN, Z., GAO, F., WANG, Z., LIN, Q., HUANG, S. & MA, L. 2023. Performance of Q690 high-strength steel T-stub under monotonic and cyclic loading. *Engineering Structures,* 277.

CHUNG, K.-F., HO, H.-C., HU, Y.-F., WANG, K., LIU, X., XIAO, M. & NETHERCOT, D. A. 2020. Experimental evidence on structural adequacy of high strength S690 steel welded joints with different heat input energy. *Engineering Structures,* 204.

COELHO, A. M. G. 2004. *Characterization of the ductility of bolted end plate beam-to-column steel connections.* PhD, Universidade de Coimbra.

CONSTRUCTION, A. I. O. S. 2022. Specification for Structural Steel Buildings, ANSI/AISC 360-22. American Institute of Steel Construction, Chicago, IL.

DUSAN ARSIC, R. N. 2015. optimal welding technology of high strength steel S690QL. *Materials Engineering,* 22**,** 33-47.

FERNANDEZ-CENICEROS, J., SANZ-GARCIA, A., ANTOñANZAS-TORRES, F. & MARTINEZ-DE-PISON, F. J. 2015. A numerical-informational approach for characterising the ductile behaviour of the T-stub component. Part 1: Refined finite element model and test validation. *Engineering Structures,* 82**,** 236-248.

FRANCAVILLA, A. B., LATOUR, M., PILUSO, V. & RIZZANO, G. 2015. Simplified finite element analysis of bolted T-stub connection components. *Engineering Structures,* 100**,** 656-664.

FRANCAVILLA, A. B., LATOUR, M. & RIZZANO, G. 2022. Ultimate behaviour of bolted T-stubs under large displacements: A mechanical model. *Journal of Constructional Steel Research,* 195.

GáSPáR, M. 2019. Effect of Welding Heat Input on Simulated HAZ Areas in S960QL High Strength Steel. *Metals,* 9.

GASPAR, M. & BALOGH, A. 2013. GMAW experiments for advanced (Q+T) high strength steels. *Production Processes and Systems,* 6**,** 9-24.

GHARIBSHAHIYAN, E., RAOUF, A. H., PARVIN, N. & RAHIMIAN, M. 2011. The effect of microstructure on hardness and toughness of low carbon welded steel using inert gas welding. *Materials & Design,* 32**,** 2042-2048.

GUO, H., LIANG, G., LI, Y. & LIU, Y. 2017. Q690 high strength steel T-stub tensile behavior: Experimental research and theoretical analysis. *Journal of Constructional Steel Research,* 139**,** 473-483.

HO, H.-C., CHUNG, K.-F., HUANG, M.-X., NETHERCOT, D. A., LIU, X., JIN, H., WANG, G.-D. & TIAN, Z.-H. 2020. Mechanical properties of high strength S690 steel welded sections through tensile tests on heat-treated coupons. *Journal of Constructional Steel Research,* 166.

HO, H. C., CHUNG, K. F., LIU, X., XIAO, M. & NETHERCOT, D. A. 2019. Modelling tensile tests on high strength S690 steel materials undergoing large deformations. *Engineering Structures,* 192**,** 305-322.

HOLLOMON, J. H. 1945. Tensile deformation. *Transactions of the Metallurgical Society of AIME*.

HU, J., DU, L.-X., WANG, J.-J. & GAO, C.-R. 2013. Effect of welding heat input on microstructures and toughness in simulated CGHAZ of V–N high strength steel. *Materials Science and Engineering: A,* 577**,** 161-168.

HU, Y.-F., CHUNG, K.-F., BAN, H. & NETHERCOT, D. A. 2022. Structural testing and numerical modelling of T-joints between cold-formed S690 circular hollow sections under brace in-plane bending. *Engineering Structures,* 250.

HU, Y.-F., CHUNG, K.-F., JIN, H., BAN, H. & NETHERCOT, D. A. 2021. Structural behaviour of T-joints between high strength S690 steel cold-formed circular hollow sections. *Journal of Constructional Steel Research,* 182.

IBRAHIM, I. A., MOHAMAT, S. A., AMIR, A. & GHALIB, A. 2012. The Effect of Gas Metal Arc Welding (GMAW) Processes on Different Welding Parameters. *Procedia Engineering,* 41**,** 1502-1506.

ISO 2013a. ISO 14346: Static Design Procedure for Welded Hollow-Section Joints –

Recommendations. *International Organization for Standardization*.

ISO 2013b. ISO 18265: Metallic materials - Conversion of hardness values. *International Organization for Standardization*.

ISO 2014. ISO 6506-1: Metallic materials - Brinell hardness test - Part 1: Test method. *International Organization for Standardization*.

ISO 2018. I.S. EN ISO 6507-1: Metallic materials - Vickers hardness test, Part 1: Test method *International Organization for Standardization*.

ISO 2019. BS EN ISO 6892 - 1: Metallic materials - Tensile testing, Part 1: Method of test at room temperature. *International Organization for Standardization*.

ISO 2023a. ISO 4545-1: Metallic materials - Knoop hardness test - Part 1: Test method. *International Organization for Standardization*.

ISO 2023b. ISO 6508-1: Metallic materials - Rockwell hardness test - Part 1: Test method. *International Organization for Standardization*.

JAVIDAN, F., HEIDARPOUR, A., ZHAO, X.-L., HUTCHINSON, C. R. & MINKKINEN, J. 2016. Effect of weld on the mechanical properties of high strength and ultra-high strength steel tubes in fabricated hybrid sections. *Engineering Structures,* 118**,** 16-27.

JIANG, J., PENG, Z. Y., YE, M., WANG, Y. B., WANG, X. & BAO, W. 2021. Thermal Effect of Welding on Mechanical Behavior of High-Strength Steel. *Journal of Materials in Civil Engineering,* 33.

KAPLAN, D. & MURRY, G. 2008. Thermal, Metallurgical and Mechanical Phenomena in the Heat Affected Zone. *Metallurgy and Mechanics of Welding.*

KARADENIZ, E., OZSARAC, U. & YILDIZ, C. 2007. The effect of process parameters on penetration in gas metal arc welding processes. *Materials & Design,* 28**,** 649-656.

KäSTNER;, T. & STROETMANN;, R. 2021. Influence of energy input on the strength and hardness of welded joints.

KHURSHID, M., BARSOUM, Z. & BARSOUM, I. 2015. Load Carrying Capacities

of Butt Welded Joints in High Strength Steels. *Journal of Engineering Materials and Technology,* 137.

KIM, J.-H., LEE, C.-H., KIM, S.-H. & HAN, K.-H. 2019. Experimental and Analytical Study of High-Strength Steel RHS X-Joints under Axial Compression. *Journal of Structural Engineering,* 145.

KIM, S.-H. & LEE, C.-H. 2020. Investigation of high-strength steel CHS X-joints loaded in compression including effect of chord stresses. *Engineering Structures,* 205.

LAN, X., CHAN, T.-M. & YOUNG, B. 2018. Structural behaviour and design of chord plastification in high strength steel CHS X-joints. *Construction and Building Materials,* 191**,** 1252-1267.

LAN, X., CHAN, T.-M. & YOUNG, B. 2019. Structural behaviour and design of high strength steel RHS X-joints. *Engineering Structures,* 200.

LAN, X., CHAN, T.-M. & YOUNG, B. 2021. Testing, finite element analysis and design of high strength steel RHS T-joints. *Engineering Structures,* 227.

LARSON, B. 2001. Ndt education resource center. *The Collaboration for NDT Education, Iowa State University, USA,* 2011.

LEE, C.-H. & KIM, S.-H. 2018. Structural performance of CHS X-joints fabricated from high-strength steel. *Steel Construction,* 11**,** 278-285.

LEE, C.-H., KIM, S.-H., CHUNG, D.-H., KIM, D.-K. & KIM, J.-W. 2017. Experimental and Numerical Study of Cold-Formed High-Strength Steel CHS X-Joints. *Journal of Structural Engineering,* 143.

LEE, S.-H., SHIN, K.-J., KIM, S.-Y. & LEE, H.-D. 2019. Numerical Study on the Deformation Behavior of Longitudinal Plate-to-High-Strength Circular Hollow-Section X-Joints under Axial Load. *Applied Sciences,* 9.

LIANG, G., GUO, H., LIU, Y., YANG, D. & LI, S. 2019. A comparative study on tensile behavior of welded T-stub joints using Q345 normal steel and Q690 high strength steel under bolt preloading cases. *Thin-Walled Structures,* 137**,** 271-283.

LIU, X., CHUNG, K.-F., HO, H.-C., XIAO, M., HOU, Z.-X. & NETHERCOT, D. A.

2018. Mechanical behavior of high strength S690-QT steel welded sections with various heat input energy. *Engineering Structures,* 175**,** 245-256.

LU, L. H., DE WINKEL, G. D., YU, Y. & WARDENIER, J. Deformation limit for the ultimate strength of hollow section joints. Tubular Structures VI, 1994 Balkerna, Rotterdam.

MA, X., WANG, W., CHEN, Y. & QIAN, X. 2015. Simulation of ductile fracture in welded tubular connections using a simplified damage plasticity model considering the effect of stress triaxiality and Lode angle. *Journal of Constructional Steel Research,* 114**,** 217-236.

MURAKAMI, Y. 2002. *Metal Fatigue: Effects of Small Defects and Nonmetallic Inclusions*, Elsevier Science Ltd.

NEUVONEN, R., SKRIKO, T. & BJöRK, T. 2021. Discretization and material parameter characterization for a HAZ in direct-quenched armor steel. *European Journal of Mechanics - A/Solids,* 89.

PACKER, J. & VOTH, A. 2008. *Parametric finite element study of branch plate-to-circular hollow section X-connections*, Tubular Structures XII.

PACKER, J. A., WARDENIER, J., ZHAO, X. L., VAN DER VEGTE, G. J. & KUROBANE, Y. 2009. *Design Guide for Rectangular Hollow Section (RHS) Joints Under Predominantly Static Loading,* Geneva, Switzerland, Comite' International pour le Developpement et l'Etude de la Construction Tubulaire (CIDECT).

PANDEY, M., CHUNG, K.-F. & YOUNG, B. 2021a. Design of cold-formed high strength steel tubular T-joints under compression loads. *Thin-Walled Structures,* 164.

PANDEY, M., CHUNG, K.-F. & YOUNG, B. 2021b. Numerical investigation and design of fully chord supported tubular T-joints. *Engineering Structures,* 239.

PANDEY, M. & YOUNG, B. 2019a. Compression capacities of cold-formed high strength steel tubular T-joints. *Journal of Constructional Steel Research,* 162.

PANDEY, M. & YOUNG, B. 2019b. Tests of cold-formed high strength steel tubular T-joints. *Thin-Walled Structures,* 143.

PANDEY, M. & YOUNG, B. 2021. Static resistances of cold-formed high strength steel tubular non-90° X-Joints. *Engineering Structures,* 239.

PAVLINA, E. J. & VAN TYNE, C. J. 2008. Correlation of Yield Strength and Tensile Strength with Hardness for Steels. *Journal of Materials Engineering and Performance,* 17**,** 888-893.

QIANG, X., SHEN, Y., JIANG, X. & BIJLAARD, F. S. K. 2020. Theoretical study on initial stiffness of thin-walled steel T-stubs taking account of prying force. *Thin-Walled Structures,* 155.

QIANG, X., ZHANG, Z., JIANG, X. & WANG, M. 2023. Study on initial stiffness of high strength steel T-stubs considering bending stiffness of bolts. *Journal of Building Engineering,* 76.

RAN, M.-M., SUN, F.-F., LI, G.-Q., KANVINDE, A., WANG, Y.-B. & XIAO, R. Y. 2019. Experimental study on the behavior of mismatched butt welded joints of high strength steel. *Journal of Constructional Steel Research,* 153**,** 196-208.

RODRIGUES, D. M., MENEZES, L. F., LOUREIRO, A. & FERNANDES, J. V. 2004. Numerical study of the plastic behaviour in tension of welds in high strength steels. *International Journal of Plasticity,* 20**,** 1-18.

SINGH, A. & SINGH, R. P. 2020. A review of effect of welding parameters on the mechanical properties of weld in submerged arc welding process. *Materials Today: Proceedings,* 26**,** 1714-1717.

SKRIKO, T. 2018. *Dependence of manufacturing parameters on the performance quality of welded joints made of direct quenched ultra-high-strength steel.*

ŚLODERBACH, Z. & PAJĄK, J. 2015. Determination of Ranges of Components of Heat Affected Zone Including Changes of Structure / Określenie Zakresów Składowych Strefy Wpływu Ciepła Uwzględniając Zmiany Struktury. *Archives of Metallurgy and Materials,* 60**,** 2607-2612.

SONG, H., ZHANG, S., LAN, L., LI, C., LIU, H., ZHAO, D. & WANG, G. 2013. Effect of direct quenching on microstructure and mechanical properties of a wear-

resistant steel. *ACTA METALLURGICA SINICA,* 26**,** 390-398.

SPERLE, J.-O., HALLBERG, L., LARSSON, J., GROTH, H., ÖSTMAN, K. & LARSSON, J. The environmental value of high strength steel structures (88044). Sperle Consulting, 2013.

SSAB Welding handbook: a guide to better welding of HARDOX and WELDOX.

STROETMANN, R. & KäSTNER, T. 2019. Influence of the execution parameters on the welds of high‐strength steels. *ce/papers,* 3**,** 707-712.

STROETMANN, R. & KäSTNER, T. 2021. A new design model for welded joints. *Steel Construction,* 14**,** 138-149.

STROETMANN, R., KäSTNER, T., HäLSIG, A. & MAYR, P. 2018. Influence of the cooling time on the mechanical properties of welded HSS-joints. *Steel Construction,* 11**,** 264-271.

SUN, F.-F., RAN, M.-M., LI, G.-Q., KANVINDE, A., WANG, Y.-B. & XIAO, R. Y. 2018a. Strength model for mismatched butt welded joints of high strength steel. *Journal of Constructional Steel Research,* 150**,** 514-527.

SUN, F., RAN, M., LI, G., XIAO, R. Y. & WANG, Y. 2018b. Experimental and numerical study of high-strength steel butt weld with softened HAZ. *Proceedings of the Institution of Civil Engineers - Structures and Buildings,* 171**,** 583-597.

SUN, F. F., XUE, X. Y., XIAO, Y., LE, Y. M. & LI, G. Q. 2018c. Effect of welding and complex loads on the high-strength steel T-stub connection. *Journal of Constructional Steel Research,* 150**,** 76-86.

SUN, J. & DILGER, K. 2023. Influence of preheating on residual stresses in ultra-high strength steel welded components. *Journal of Materials Research and Technology,* 25**,** 3120-3136.

TARTAGLIA, R., D'ANIELLO, M. & ZIMBRU, M. 2020. Experimental and numerical study on the T-Stub behaviour with preloaded bolts under large deformations. *Structures,* 27**,** 2137-2155.

TU, S., REN, X., HE, J. & ZHANG, Z. 2019. Stress‐strain curves of metallic materials

and post‐necking strain hardening characterization: A review. *Fatigue & Fracture of Engineering Materials & Structures,* 43**,** 3-19.

VOTH, A. P. 2010. *Branch plate-to-circular hollow structural section connections.* PhD, Toronto University.

WANG, Y.-B. & LI, G. Q. 2022. Strength of high strength steel butt welded connections with consideration of heat affected zone softening. *Journal of Building Structures,* 43**,** 26-35.

WARDENIER, J., KUROBANE, Y., PACKER, J. A., VEGTE, G. J. V. D. & ZHAO, X.-L. 2008. *Design Guide For Circular Hollow Section (CHS) Joints Under Predominantly Static Loading,* Geneva, Switzerland, Comite' International pour le Developpement et l'Etude de la Construction Tubulaire (CIDECT).

XIONG, M.-X. & LIEW, J. Y. R. 2020. Experimental study to differentiate mechanical behaviours of TMCP and QT high strength steel at elevated temperatures. *Construction and Building Materials,* 242.

YAN, R. 2023. *Heat-affected zone in welded cold-formed rectangular hollow section joints.* Doctor, Delft University of Technology.

YAN, R., EL BAMBY, H., VELJKOVIC, M., XIN, H. & YANG, F. 2021. A method for identifying the boundary of regions in welded coupon specimens using digital image correlation. *Materials & Design,* 210.

YAN, R., XIN, H., YANG, F., EL BAMBY, H., VELJKOVIC, M. & MELA, K. 2022. A method for determining the constitutive model of the heat-affected zone using digital image correlation. *Construction and Building Materials,* 342.

YUAN, H. X., HU, S., DU, X. X., YANG, L., CHENG, X. Y. & THEOFANOUS, M. 2019. Experimental behaviour of stainless steel bolted T-stub connections under monotonic loading. *Journal of Constructional Steel Research,* 152**,** 213-224.

ZHANG, Y., GAO, S., GUO, L., QU, J. & WANG, S. 2022. Ultimate tensile behavior of bolted T-stub connections with preload. *Journal of Building Engineering,* 47.

ZHAO, M. S., LEE, C. K. & CHIEW, S. P. 2016. Tensile behavior of high performance

structural steel T-stub joints. *Journal of Constructional Steel Research,* 122**,** 316-325.

ZHAO, M. S., LEE, C. K., FUNG, T. C. & CHIEW, S. P. 2017. Impact of welding on the strength of high performance steel T-stub joints. *Journal of Constructional Steel Research,* 131**,** 110-121.

ZHAO, X., HE, S. & YAN, S. 2021. Full-range behaviour of T-stubs with various yield line patterns. *Journal of Constructional Steel Research,* 186.